UNIVERSIDAD POLITÉCNICA DE MADRID

ESCUELA TÉCNICA SUPERIOR
DE INGENIEROS DE TELECOMUNICACIÓN

TESIS DOCTORAL

Desarrollo de estructuras nanofotónicas de campo cercano para intensificación localizada de luz en células solares de banda intermedia

Manuel João de Moura Dias Mendes

Licenciado en Física

Madrid, 2012

UNIVERSIDAD POLITÉCNICA DE MADRID

Instituto de Energía Solar

Departamento de Electrónica Física

Escuela Técnica Superior de Ingenieros de Telecomunicación

TESIS DOCTORAL

Near-field nanophotonic structures for localized light enhancement in intermediate band solar cells

(Desarrollo de estructuras nanofotónicas de campo cercano para intensificación localizada de luz en células solares de banda intermedia)

Autor: Manuel João de Moura Dias Mendes
Licenciado en Física

Directores: Ignacio Tobías Galicia
Profesor Titular ETSIT, UPM

Antonio Luque López
Profesor Catedrático ETSIT, UPM

Madrid, 2012

Tribunal nombrado por el Magfco. Y Excmo. Sr. Rector de la Universidad Politécnica de Madrid.

PRESIDENTE:

VOCALES:

SECRETARIO:

SUPLENTES:

Realizado el acto de defensa y lectura de la Tesis en Madrid,
el día ___ de _____ de 201__.

Calificación:

EL PRESIDENTE LOS VOCALES

EL SECRETARIO

A toda a minha família

"Se eu não morresse nunca
e eternamente buscasse e conseguisse a perfeição das coisas"
Cesário Verde (1855-1886)

Acknowledgements

It is not easy to thank in a few lines for all that I've lived and learned during the last four years as a PhD student in the Instituto de Energía Solar (IES). This has been the most productive time of my life, and all the knowledge that I gained here will define the course of my future. For that, I acknowledge everyone in IES since each person that I met here has contributed in a certain way to nourish my doctoral life.

My advisors, Prof. Ignacio Tobias and Prof. Antonio Luque, deserve a very special thanks for opening me the door to their scientific world, and for their great support and guidance throughout the work reported here. I also want to give a special acknowledgment to the other co-authors of this work: Prof. Antonio Martí and Dra. Estela Hernandez, who provided an enormous amount of assistance mainly in the experimental part of this thesis.

I am grateful to Professor Le-Wei Li, of University of Electronic Science and Technology of China, for providing the Mathematica numerical routines developed by his group [1].

I acknowledge the great assistance of Dr. José Maria Ripalda and Dr. Diego Alonso Álvarez, of IMM-CSIC, and Dra. Francesca Barbagini, of ISOM-UPM, with the atomic force microscopy measurements.

I appreaciate the assistance of Dr. David Pastor and Dr. Javier Olea, of the group "Láminas Delgadas y Microelectrónica" of Universidad Complutense de Madrid, with the profilometer measurements.

I thank Prof. Santiago Silvestre and Alfredo Boronat, of Universidad Politécnica de Catalunya, for their collaboration in the solar cell construction and testing.

I am grateful for all the advices and time dedicated by Miguel Gómez and Juan Carlos Zamorano in the repairs and mechanical work that had to be performed on the equipments used in our experiments.

I acknowledge the important help of David Fuertes, Esthér Lopez, Elisa Antolín, Pablo García-Linares, Enrique Cánovas, César Tablero, Irene Artacho, Ivan Garcia, Marta Victoria, Jasmin Hosfstetter, Ignacio Rey-Stolle, Ruben Nuñez and César Dominguéz in fruitful discussions and laboratory lessons; of Alex Mellor, who has improved my English skills considerably; and of all the other colleagues, professors and staff of IES.

Finally I want to leave a big hug to my friends of office 208, with whom I shared a work space and several unforgettable experiences during this PhD.

This thesis has been supported by the European Commission's IBPOWER project (Grant No. 211640), by the GENESIS FV project (Grant No. CSD2006-0004) of the Spanish program CONSOLIDER, by the Regional Government of Madrid within the NUMANCIA projects (Grants No. S-0505/ENE/0310 and S2009/ENE1477), and by the DENQUIBAND program (Grant No. PLE2009-0045) funded by the Spanish *Ministerio de Ciencia y Innovación*. The author also acknowledges the Portuguese Government grant No. SFRH/BD/21669/2005 of the *Fundação para a Ciência e Tecnologia* (*Ministério da Ciência, Tecnologia e Ensino Superior*) co-financed by the European program POPH/FSE; and the *Universidad Politécnica de Madrid* for the scholarship *Beca de Doctorado Homologada* (CH/007/2010).

Abstract

This doctoral thesis explores some of the possibilities that near-field optics can bring to photovoltaics, and in particular to quantum-dot intermediate band solar cells (QD-IBSCs). Our main focus is the analytical optimization of the electric field distribution produced in the vicinity of single scattering particles, in order to produce the highest possible absorption enhancement in the photovoltaic medium in their surroundings. Near-field scattering structures have also been fabricated in laboratory, allowing the application of the previously studied theoretical concepts to real devices.

We start by looking into the electrostatic scattering regime, which is only applicable to sub-wavelength sized particles. In this regime it was found that metallic nano-spheroids can produce absorption enhancements of about two orders of magnitude on the material in their vicinity, due to their strong plasmonic resonance. The frequency of such resonance can be tuned with the shape of the particles, allowing us to match it with the optimal transition energies of the intermediate band material. Since these metallic nanoparticles (MNPs) are to be inserted inside the cell photovoltaic medium, they should be coated by a thin insulating layer to prevent electron-hole recombination at their surface.

This analysis is then generalized, using an analytical separation-of-variables method implemented in Mathematica7.0, to compute scattering by spheroids of any size and material. This code allowed the study of the scattering properties of wavelength-sized particles (mesoscopic regime), and it was verified that in this regime dielectric spheroids perform better than metallic. The light intensity scattered from such dielectric spheroids can have more than two orders of magnitude than the incident intensity, and the focal region in front of the particle can be shaped in several ways by changing the particle geometry and/or material.

Experimental work was also performed in this PhD to implement in practice the concepts studied in the analysis of sub-wavelength MNPs. A wet-coating method was developed to self-assemble regular arrays of colloidal MNPs on the surface of several materials, such as silicon wafers, amorphous silicon films, gallium arsenide and glass. A series of thermal and chemical tests have been performed showing what treatments the nanoparticles can withstand for their embedment in a photovoltaic medium. MNPs

arrays are then inserted in an amorphous silicon medium to study the effect of their plasmonic near-field enhancement on the absorption spectrum of the material.

The self-assembled arrays of MNPs constructed in these experiments inspired a new strategy for fabricating IBSCs using colloidal quantum dots (CQDs). Such CQDs can be deposited in self-assembled monolayers, using procedures similar to those developed for the patterning of colloidal MNPs. The use of CQDs to form the intermediate band presents several important practical and physical advantages relative to the conventional dots epitaxially grown by the Stranski-Krastanov method. Besides, this provides a fast and inexpensive method for patterning binary arrays of QDs and MNPs, envisioned in the theoretical part of this thesis, in which the MNPs act as antennas focusing the light in the QDs and therefore boosting their absorption.

Resumen

Esta tesis doctoral explora las posibilidades que la óptica de campo cercano puede traer a la tecnología fotovoltaica y, en particular, a las células solares de banda intermedia con puntos cuánticos (del inglés, QD-IBSCs). El enfoque principal es la optimización analítica de la distribución de campo eléctrico alrededor de partículas aisladas dispersoras de luz, para producir el mayor incremento posible de la absorción en el medio fotovoltaico que rodea estas partículas. Las estructuras de dispersión de campo cercano se han fabricado en laboratorio, permitiendo la aplicación en dispositivos reales de los conceptos teóricos estudiados.

En primer lugar se examina el régimen de dispersión electrostático, sólo aplicable a partículas con un tamaño inferior a la longitud de onda. En este régimen se ha determinado que nano-esferoides metálicos pueden producir mejoras de hasta dos órdenes de magnitud en la absorción del material que los rodea, debido a su fuerte resonancia plasmónica. La frecuencia de la resonancia puede ajustarse variando la forma de las partículas, lo que permite optimizarla con las energías de transición del material de banda intermedia. Como las nano-partículas metálicas (en adelante MNPs) deben ser inseridas en el material de la célula fotovoltaica, ellas deben cubrirse con una fina capa aislante para prevenir la recombinación electrón-hueco en su superficie.

A continuación se generaliza el análisis para calcular la dispersión de luz causada por esferoides de cualquier tamaño y material. Para ello, se usa un método analítico de separación de variables implementado en Mathematica7.0. Este código permite el estudio de las propiedades de dispersión de las partículas del tamaño de la longitud de onda (régimen mesoscópico), y se ha verificado que en este régimen esferoides dieléctricos se comportan mejor que metálicos. La intensidad de luz dispersada desde estos esferoides dieléctricos puede ser dos órdenes de magnitud mayor que la intensidad incidente, y la región focal frente a la partícula puede ser modificada de distintas maneras cambiando la geometría y/o material de la partícula.

Además, el trabajo experimental realizado en esta tesis ha permitido implementar en la práctica los conceptos estudiados para el análisis de MNPs con tamaños inferiores a la longitud de onda. Se ha desarrollado un método de deposición de partículas en solución coloidal que autogenera redes regulares de MNPs en la superficie de varios materiales como obleas de silicio, láminas de silicio amorfo, arseniuro de galio y vidrio.

Se ha realizado una serie de pruebas térmicas y químicas que muestra que procesos las nano-partículas pueden resistir para su inserción en un medio fotovoltaico. Las redes de MNPs se insertan después en un medio de silicio amorfo para estudiar el efecto de su campo cercano plasmónico en el incremento del espectro de absorción del material.

Las redes de MNPs construidas en este trabajo experimental han inspirado una nueva estrategia de fabricación de IBSCs usando puntos cuánticos coloidales (del inglés, CQDs). Estos CQDs pueden ser depositados en monocapas auto-ensambladas, usando procedimientos similares a los desarrollados para la deposición de MNPs coloidales. El uso de CQDs para formar la banda intermedia presenta, desde el punto de vista práctico y físico, varias ventajas importantes frente a los puntos convencionales crecidos epitaxialmente por el método de Stranski-Krastanov. Además, supone un método rápido y barato para construir redes binarias de QDs y MNPs, previstas en la parte teórica de esta tesis, en las que los MNPs actúan como antenas enfocando la luz en los puntos cuánticos y, por tanto, estimulando su absorción.

Table of Contents

List of Figures

List of Tables

List of Symbols

$\mathbf{A}$	Vector potential
α_a	polarizability along the *a* axis
a_B	Bohr radius
C	Spheroid size parameter
C_{ext}	Extinction cross section
D	Diameter of spherical nanoparticle
e	Electronic charge
$\mathbf{E}$	Electric field vector
$\mathbf{E_0}$	Incident/illuminating electric field vector
$\mathbf{E_I}$	Internal electric field vector (inside the scatterer)
$\mathbf{E_S}$	Scattered electric field vector
$\mathbf{E_{Out}}$	External electric field vector (outside the scatterer)
$\mathbf{E_t}$	Total electric field vector
E_{CI}	Bandgap between intermediate and conduction band
E_{CV}	Bandgap between valence and conduction band
E_{IV}	Bandgap between valence and intermediate band
ϵ	Permittivity or dielectric function
ϵ_{FC}	Electron Quasi-Fermi level
ϵ_{FI}	Intermediate band Quasi-Fermi level
ϵ_{FV}	Hole Quasi-Fermi level
η	Spheroidal angular coordinate
ϕ	Scalar electric potential
$\mathbf{H}$	Magnetic field vector
H_{int}	Interaction Hamiltonean
I	Current
$\mathbf{J}$	Current density
K (or k)	Wavenumber
$\mathbf{K}$	Wavevector
k_r	Imaginary part of the relative refractive index
ξ	Spheroidal radial coordinate

L	Depolarization factor
L_Z	Width of the focal region along the z axis
λ	Wavelength
λ_{mn}	Eigenvalues of the spheroidal harmonics
m	Effective mass
μ	Permeability
N	Truncation number in the fields' expansions
N_m	Medium refractive index
N_p	Particle refractive index
N_r	Relative refractive index (partice/medium)
n_r	Real part of the relative refractive index
ω	Angular velocity
$\mathbf{P}$	Electric polarization vector
Q_{ext}	Extinction efficiency
R	Radius
R_{eq}	Volume-equivalent sphere radius
R_{mn}	Spheroidal radial harmonics
ρ	Charge density
$\mathbf{S}$	Poynting vector
σ	Conductivity
S_{mn}	Spheroidal angular harmonics
V	Voltage
Z	Impedance
Z_{MAX}	Distance in z from the focal point to the particle center

List of Abbreviations

a	amorphous
AFM	Atomic force microscopy
Ag	Silver
Al	Aluminum
APTMS	(3-Aminopropyl)trimethoxysilane
ARC	Anti-reflection coating
Ar	Argon
As	Arsenide
Au	Gold
BC	Boundary condition
CB	Conduction band
CQD	Colloidal quantum-dot
DMP	Dielectric mesoscopic particle
EA	Electrostatic approximation
EBL	E-beam lithography
EM	Electromagnetic
ES	Electrostatic regime
FDTD	Finite-difference time domain
FEM	Finite elements method
FS	Forward scattering regime
HCL	Hole-mask colloidal litography
IBSC	Intermediate band solar cell
In	Indium
IR	Infrared solar spectrum
ITO	Indium Tin Oxide
Ga	Gallium
GO	Geometrical optics
MEG	Multiple exciton generation
MNP	Metallic nanoparticle
NSL	Nano-sphere litography

PbS	Lead sulfide
PECVD	Plasma-enhanced chemical vapour deposition
PM	Point-matching method
PV	Photovoltaic
QD	Quantum dot
QFL	Quasi-Fermi level
RF	Radio-frequency
RTA	Rapid thermal annealing
SEM	Scanning electron microscopy
Se	Selenide
Si	Silicon
SiO_2	Silicon dioxide (silica)
SK	Stranski-Krastanov
SP	Surface Plasmon
TEM	Transmission electron microscopy
TFA	Thin-film annealing
UV	Ultra-violet solar spectrum
VB	Valence band
VIS	Visible solar spectrum

Chapter 1

Background

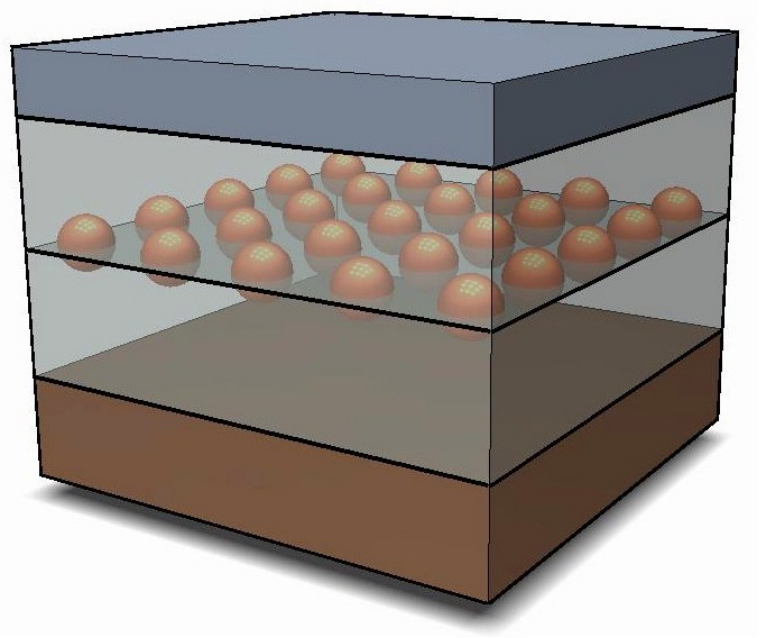

1.1 Introduction

Until the 1990's most of the literature on analytical solutions of scattering by particles was mainly concerned with the study of far-field quantities, such as electric field intensities at infinity and scattering cross sections [1-5]. Recent technological advances in the area of nano-optics have shifted the attention of the scientific community to near-field phenomena, leading to the growth of a new optics branch named near-field optics [6, 7] which studies the behavior of light fields in the vicinity of matter. This interest was sparked by novel techniques that probe (e.g. scanning near-field microscopy- SNOM) sub-wavelength structures, elucidating the optical properties of the near-field produced in their proximity; and also due to the appearance of a new range of nanotechnological applications that can benefit from the enhanced local fields in the vicinity of scattering particles: nanoscale processing of materials (by ablation [8, 9] or photo-etching [10]), high-resolution microscopy (e.g. for biomedical diagnostics [11, 12]), resonance spectroscopy (e.g. for amplification of Raman and fluorescence signals [13-15]), localized sensing techniques (e.g. enhancement of nanoparticles backscattering [16, 17]), optical data storage [18], transmission and manipulation of light [19], optical antennas [20], among others. In this thesis the authors are particularly interested in the implementation of near-field structures in photovoltaic devices, particularly in intermediate band solar cells (IBSCs) [21].

Near-field effects become particularly important at distances from the scattering object smaller or comparable to the incident illuminating wavelength (λ); therefore outside the macroscopic regime of geometrical optics (GO). Numerical grid-based approaches, such as finite difference time-domain (FDTD) [12, 14, 22] and finite elements methods (FEM) [16], are often employed to model the near-field distribution of complex structures. However, with mesh approaches it is usually difficult to resolve high field gradients that occur at the surface of particles that scatter highly resonantly with the incident light. In particular the optical properties of particles with sizes below or close to the wavelength are very dependent on their geometry, material and surrounding medium; so the design of each mesh must be well defined and refined for each particle structure. Therefore, whenever possible, it is preferable to use analytical techniques since the fields can be calculated everywhere without needing to cope with

finite mesh resolution errors. The main drawback of using analytical methods is that only “round shapes” can be considered [23], i.e. shapes without corners like ellipsoids, infinite cylinders, toroids, etc.

The numerical results presented in this thesis were obtained with analytical models able to determine the electric field distribution inside and outside scattering particles with an ellipsoidal shape. The aim is to explore the light focusing properties of the near-field produced by scatterers with nano/microscopic sizes (outside GO) for light trapping in a photovoltaic medium. The authors are particularly interested in developing arrays of such scattering particles to enhance the absorption of IBSC materials. Early experimental studies with prototype IBSCs demonstrated that this novel solar cell technology is in need of efficient light trapping mechanisms to compensate for its observed small absorption. That is the main purpose of the PhD work reported here.

1.2 The Intermediate Band Solar Cell concept

The photovoltaic (PV) material that constitutes conventional solar cells is a semiconductor whose energy bandgap determines the amount of current and voltage produced by the device. The generation of photo-current occurs when the incident photons have sufficient energy to pump an electron across the bandgap, from the valence to the conduction band of the semiconductor. Thus, high bandgap values produce low currents (few photons are absorbed) but high voltages, and vice versa. In 1961, W. Shockley and H. J. Queisser [24] determined that the maximum sunlight-to-electricity conversion efficiency (the sun assumed to be a blackbody with a temperature of 6000K) that can be attained by such conventional solar cells is 40.7%, having an optimal bandgap of 1.2 eV.

The Shockley-Queisser analysis can be applied to most of the current commercial photovoltaic technology, since these solar cells are composed of a single *p-n* junction with a unique bandgap. In the last decades intense research efforts have been undertaken to develop novel photovoltaic solutions in order to achieve grid parity in the final price of electricity generation. Such efforts are aimed not only at reducing the fabrication costs of the cells but also at achieving higher conversion efficiency (third-generation solar cells).

One of the technological schemes proposed to surpass the Shockley-Queisser eficiency limit is the intermediate band solar cell (IBSC), first introduced in 1997 by A. Luque and A. Martí [25]. The semiconductor material that constitutes this cell is characterized by the existence of an intermediate band (IB) located between the conventional semiconductor conduction band (CB) and valence band (VB) (see Figure 1.1) [25, 26]. Because of the IB, below-bandgap-energy photons can contribute to the cell photo-current by pumping electrons from the VB to the IB and from the IB to the CB. But, most importantly, since the IB is isolated from the CB and the VB by a zero density of states, carrier relaxation between bands becomes difficult and the carrier statistics in each band is described by its own quasi-Fermi level. Under this assumption, the recombination between bands is of a radiative nature and the voltage supplied by the cell is still limited by the high bandgap E_{CV} of the host semiconductor, and not by any of the lower bandgaps (E_{IV} or E_{CI} – represented in Figure 1.1c).

In an IBSC the optimum semiconductor bandgap (E_{CV}=1.95 eV) is higher than that previously referred for conventional single-gap cells (1.2 eV); and the corresponding optimum below-bandgap transition energies are: E_{CI}=0.71 eV and E_{IV}=1.24 eV. The maximum conversion efficiency that can be obtained by an IBSC having such optimal parameters is 63.2% (at maximum sunlight concentration), as compared with the Shockley-Queisser limit of 40.7% for a single-gap cell. This theoretical limiting efficiency of IBSCs is equivalent to that of triple junction solar cells, but it only requires a single *p-n* junction.

The main reason for the increased efficiency of the IBSC concept comes from the fact that this cell can absorb and produce current from a bigger portion of the solar energy spectrum, maintaining a high voltage. Conventional solar cell materials can absorb the high energy photons of the visible (VIS) and ultraviolet (UV) solar spectral range, since the energy of such photons is sufficiently above the material bandgap. However, most of the low energy photons in the infrared (IR) spectral range have energies below their bandgap and therefore pass through the cell material without generating any photo-current. Unlike these single-gap cells, the IBSC can exploit IR photons since the intermediate band acts as an “electronic footstep” that helps the low energy photons to pump electrons across the host semiconductor bandgap towards the conduction band.

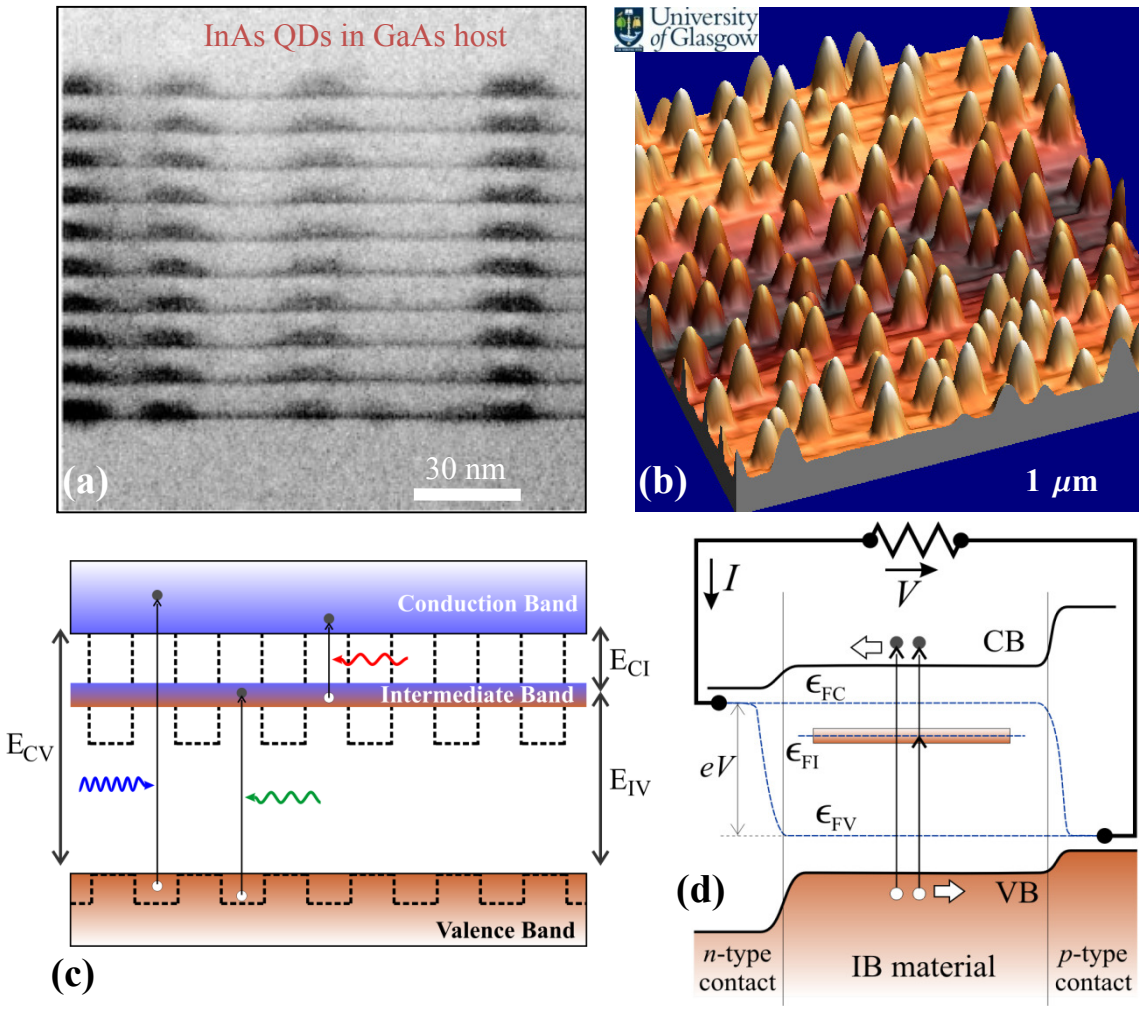

Figure 1.1: **a)** Transmission electron microscopy (TEM) image of a stack of 10 InAs QD layers grown in a GaAs cell [27]. **b)** Atomic force microscopy (AFM) image of InAs dots grown on the surface of GaAs (courtesy of Prof. Colin R. Stanley from University of Glasgow). **c)** Band diagram of an IB material, formed by the confined electronic states of the QDs, showing the single and double photon electron-hole generation. The predicted energy gaps for the particular structure shown in (a) are: E_{CI}=0.3 eV, E_{IV}=1.1 eV and E_{CV}=1.4 eV. **d)** Schematic of an IB solar cell showing the splitting of the Fermi level in three Quasi-Fermi levels (QFLs). The voltage (V) supplied by the cell is given by the separation between the hole (ϵ_{FV}) and electron (ϵ_{FC}) QFLs.

It has been demonstrated that the IB can be fabricated using nanotechnology, incorporating an array of quantum dots (QDs) in the cell semiconductor material (shown in Figure 1.1a,b) [28]. The IB is formed by the ground state (lowest energy level) of the quantum-confined wavefunctions of the electrons in the potential wells (QDs) in the conduction band (represented in Figure 1.1c by the dashed lines). The QD

ground states can be isolated from the CB by means of a zero density of states. This isolation results in the "phonon bottleneck" effect through which a transition from the CB to the IB is believed to the inhibited due to the low probability of simultaneous multi-phonon interactions needed to bridge the energy interval between the CB and IB.

If the confined electron wavefunctions are sufficiently delocalized (or there is a high enough QD density) they can overlap and form a "mini-band", which allows the mobility of carriers within the IB. This is advantageous (but not a necessary condition) for the IBSC, in order for the cell to be able to compensate for possible non-uniformities in the illumination or doping profiles [29].

Prototype QD-IBSCs have been fabricated with QDs epitaxially grown on semiconductor layers using the Stranski-Krastanov (SK) method [30], as shown in Figure 1.1a,b. Such devices are based, almost without exception, on III-V materials. The most common example is the case of Indium Arsenide (InAs) QDs epitaxially grown in a Gallium Arsenide (GaAs) host. The SK technique consists in an initial growth of a thin wetting layer of InAs over the GaAs substrate. When the wetting layer reaches a critical thickness (usually a few monolayers), the strain unbalance between the InAs and GaAs lattice constant causes the growth to proceed through the coalescence of InAs "islands" which constitute the QDs. Another layer of GaAs is deposited on top to embed the QDs in the host material (sometimes called the matrix). Additional QD layers can be built by repeating these steps as many times as the number of desired QD layers.

The IB material fabricated in this way is sandwiched between *p*- and *n*-doped layers to construct the solar cell (see band diagram in Figure 1.1d). The role of the *p* and *n* doped layers is to anchor the hole (ϵ_{FV}) and electron (ϵ_{FC}) Quasi-Fermi levels (QFLs) respectively, so that the output voltage of the cell is determined by the split between these quasi-Fermi levels. Ideally, the *p* contact only allows holes to pass through and the *n* contact only allows electrons. Besides, these doped layers also prevent the IB (with QFL ϵ_{FI}) from being short-circuited by the metallic contacts.

The quantum efficiency of the prototype IBSCs fabricated with this method reveals an extended response for photon energies below the GaAs bandgap, allowing the verification of the IB concept. However, the impact of the intermediate band effects on the cell performance is still marginal since the band structure experimentally produced with such technological approach is far from the optimal IB structure represented in

Figure 1.1c,d. In addition, the presence of the thin wetting layer below the QDs creates an effective reduction of the host material bandgap, and disrupts the three-dimensional electronic confinement required for the dots since it acts as an area of one-dimensional confinement (quantum well). Besides, the III-V QDs produced by the SK method have irregular and highly anisotropic shapes with in-plane dimensions considerably higher than the normal-to-plane dimension. The larger in-plane dimensions of these QDs cause the appearance of several discrete levels between the QDs ground state and the CB that enable the thermal (non-radiative) coupling between the IB and the CB, lowering the cell voltage. So, in practice, there is not a single IB level such as in the optimal case of Figure 1.1c. Instead, usually 3 or 4 confined levels can be experimentally observed, which do not allow a sufficient separation between the IB and the CB for the required phonon bottleneck effect to occur. Furthermore, there is a low photon absorption provided by the IB, which has been theoretically explained using a quantum mechanical four-band *k.p* method [31]. This is attributed to the low absorptivity of the QDs, which is experimentally observed to be more than one or two orders of magnitude lower than that of the host material [30, 32]. This is perhaps the most crucial issue of the QD-IBSCs fabricated up to now. The work presented in this thesis leads to solve this problem by studying near-field nano-photonic light trapping systems to enhance the IB absorption. The high electric field intensity amplification that can be achieved in the vicinity of scattering particles with sizes comparable to or below the wavelength can be used to enhance the absorption of QDs located in the particles' near-field. That is the main aim of the studies developed in this PhD.

1.3 Fundamentals of light scattering by particles

The theoretical work performed in this PhD thesis focuses on light scattering by individual particles, within the framework of classical electromagnetic theory, for potential application in light management structures in IBSCs. The basic problem is the interaction of light of arbitrary wavelength with a single particle which is embedded in an otherwise homogeneous medium [23]. By homogeneous it is meant that the atomic or molecular heterogeneity is small compared with the wavelength of the incident light. Although the particle may be complicated in shape and may have several homogeneous components, we assume that it is composed of matter that is at every point describable

in macroscopic terms. That is, the optical properties of a particle or regions thereof are completely specified by frequency-dependent optical constants. We also restrict our treatment to elastic scattering: the wavelength, λ, of the scattered light is the same as that of the incident light.

The logical point of departure is the Maxwell equations for the macroscopic electromagnetic field at interior points in matter, which in SI units are:

$$\begin{aligned} \nabla \cdot \mathbf{D} &= \rho, \\ \nabla \times \mathbf{E} + \frac{\partial \mathbf{B}}{\partial t} &= 0, \\ \nabla \cdot \mathbf{B} &= 0, \\ \nabla \times \mathbf{H} &= \mathbf{J} + \frac{\partial \mathbf{D}}{\partial t} \end{aligned} \tag{1.1}$$

where **E** is the electric field and **B** the magnetic induction. The electric displacement **D** and magnetic field **H** are defined by:

$$\begin{aligned} \mathbf{D} &= \varepsilon_0 \mathbf{E} + \mathbf{P}, \\ \mathbf{H} &= \frac{\mathbf{B}}{\mu_0} - \mathbf{M} \end{aligned} \tag{1.2}$$

where **P** is the electric polarization, **M** the magnetization, ϵ_0 the permittivity and μ_0 the permeability of free space. The charge density ρ and current density **J** are associated with the so-called "free" charges.

Equations (1.1) and (1.2) are not sufficient in themselves; they must be supplemented with *constitutive relations*, which have the form:

$$\begin{aligned} \mathbf{J} &= \sigma \mathbf{E}, \\ \mathbf{B} &= \mu \mathbf{H}, \\ \mathbf{P} &= \varepsilon_0 \chi \mathbf{E} \end{aligned} \tag{1.3}$$

where σ is the conductivity, μ the permeability, and χ the electric susceptibility. The phenomenological coefficients σ, μ and χ depend on the medium under consideration,

but are assumed to be independent of the fields (linear medium), independent of position (homogeneous medium), and independent of direction (isotropic medium).

The general time-harmonic electromagnetic fields are represented in complex form by a vector of the type: $\mathbf{F}_c = F_c e^{-i\omega t}$, where the subscript *c* denotes complex. There is some arbitrariness associated with the complex representation of a real field, so there are two possible choices for the time-dependent factor: $e^{-i\omega t}$ and $e^{i\omega t}$. It makes no difference which choice is made since the quantities of physical interest are real. But once a sign convention is chosen it must the used consistently in all the analysis. We shall take the time-dependent factor to be $e^{-i\omega t}$, which is the convention found in standard books [23, 33, 34]. If $e^{-i\omega t}$ is assumed for all fields, and the constitutive relations (1.3) are substituted into (1.1), we obtain:

$$\begin{aligned} &\nabla \cdot (\varepsilon \mathbf{E}_c) = 0, \\ &\nabla \times \mathbf{E}_c = i\omega\mu \mathbf{H}_c, \\ &\nabla \cdot \mathbf{H}_c = 0, \\ &\nabla \times \mathbf{H}_c = -i\omega\varepsilon \mathbf{E}_c \end{aligned} \tag{1.4}$$

where the complex permittivity is $\epsilon = \epsilon_0(1+\chi) + i\sigma/\omega$. Equations (1.4) are the usual starting point in scattering problems. However, for the sake of simplicity, we shall henceforth omit the subscript *c* from the complex fields.

The fundamental problem of scattering by individual particles is as follows: Given a particle of specified size, shape and optical properties that is illuminated by an arbitrarily polarized monochromatic wave, determine the electromagnetic field at all points in the particle and at all points of the homogeneous medium in which the particle is embedded. The field inside the particle is denoted by $(\mathbf{E_I}, \mathbf{H_I})$; the field outside in the medium surrounding the particle $(\mathbf{E_{Out}}, \mathbf{H_{Out}})$ is the superposition of the incident field $(\mathbf{E_0}, \mathbf{H_0})$ and the scattered field $(\mathbf{E_S}, \mathbf{H_S})$.

The fields must satisfy Maxwell equations (1.4) at all points where ϵ and μ are continuous. By applying the curl operator $(\nabla \times)$ to the left of the 2nd and 4th equations of (1.4), and using the vector identity $[\nabla \times (\nabla \times \mathbf{A}) = \nabla(\nabla \cdot \mathbf{A}) - \nabla \cdot (\nabla \mathbf{A})]$, we obtain:

$$\begin{aligned} \nabla^2\mathbf{E} + k^2\mathbf{E} &= 0, \\ \nabla^2\mathbf{H} + k^2\mathbf{H} &= 0 \end{aligned} \tag{1.5}$$

Thus, **E** and **H** satisfy the vector wave equation, where $k^2=\omega^2\epsilon\mu$. Any vector field with zero divergence that satisfies the vector wave equation is an admissible electric field; the associated magnetic field is related to the curl of the electric field through the 2nd equation of (1.4).

The electromagnetic field is required to satisfy the Maxwell equations at points where ϵ and μ are continuous. However, as one crosses the boundary between particle and medium, there is, in general, a sudden change in these properties. This change occurs over a transition region with thickness of the order of atomic dimensions. From a macroscopic point of view, therefore, there is a discontinuity at the boundary. At such boundary points (located at **x**) we impose the following conditions on the fields inside (I) and outside (Out) the particle:

$$\begin{aligned} \left[\mathbf{E}_{\mathbf{Out}}(\mathbf{x}) - \mathbf{E}_{\mathbf{I}}(\mathbf{x})\right] \times \hat{\mathbf{n}} &= 0, \\ \left[\mathbf{H}_{\mathbf{Out}}(\mathbf{x}) - \mathbf{H}_{\mathbf{I}}(\mathbf{x})\right] \times \hat{\mathbf{n}} &= 0, \end{aligned} \tag{1.6}$$

where $\hat{\mathbf{n}}$ is the outward directed normal to the surface of the particle. The boundary conditions (1.6) are the requirement that the tangential components of **E** and **H** are continuous across a boundary separating media with different properties.

The fundamental task, to solve the problem of scattering by a single particle, is to construct solutions to the Maxwell equations (1.4), both inside and outside the particle, which satisfy (1.6) at the boundary between particle and surrounding medium. If the incident electromagnetic field is arbitrary, subject to the restriction that it can be Fourier analyzed into a superposition of plane monochromatic waves, the solution to the problem of interaction of such a field with a particle can be obtained in principle by superposing fundamental solutions. That this is possible is a consequence of the linearity of the Maxwell equations and the boundary conditions. This is our justification for considering only scattering of plane monochromatic waves. An arbitrarily polarized wave can be expressed as the superposition of two orthogonal polarization states.

Therefore, we need only solve each scattering problem twice (for a given direction of propagation) in order to determine the scattering of an arbitrarily polarized plane wave.

A qualitative understanding of the physics of scattering by a single particle can be acquired without doing any calculations. Let's consider that our arbitrary particle is conceptually subdivided into small regions with sizes much smaller than λ. An applied electromagnetic wave induces a dipole moment in each region. These dipoles oscillate coherently at the frequency of the applied field and therefore scatter secondary radiation in all directions. In a particular point outside the particle, the total scattered field is obtained by superposing the scattered wavelets, where due account is taken of their phase differences. In general, these phase relations change for a different scattering direction; we therefore expect the scattered field to vary with scattering direction. If the particle is small compared with the wavelength, all the secondary wavelets are approximately in phase; for such a particle we do not expect much variation of scattering with direction away from the particle. As the particle size is increased, the number of possibilities for mutual enhancement and cancellation of the scattered wavelets increases. Thus, the larger the particle, the more peaks and valleys exist in the scattering pattern. Shape is also important: if the particle is distorted all the phase relations, hence the scattering pattern, are different. So, the phase relations among the scattered wavelets depend on the particle geometrical parameters, size and shape. The amplitude and phase of the induced dipole moments depend on the material of which the particle is composed.

The fields scattered by a single particle have very distinct properties in different regions. There are three zones of interest, defined in terms of the distance r to the particle [34]:

- near-field region, $r<<\lambda$
- intermediate/transition region, $r\sim\lambda$
- far-field region, $r>>\lambda$

In the near zone the fields have the character of static fields, with radial components and variation with distance that depend in detail on the properties of the particle (*i.e.* on the boundary conditions). In the far zone, on the other hand, the fields

are transverse to the radius vector and fall off as r^{-1}, typical of radiation fields. In between these regions, for $r \sim \lambda$, another zone is sometimes defined: the intermediate or transition zone where both longitudinal (parallel to the radius vector) and transverse fields coexist. In the quantum view of electromagnetic interactions, far-field effects are manifestations of real photons, whereas near-field effects are due to a mixture of real and virtual photons [35].

The application of scattering by individual particles as a light trapping mechanism to increase the absorption of a material is currently a very active research field, particularly promising for solar cell development. There are two types of schemes that can be employed which make use of either the near or the far scattered fields. Far-field approaches generally use scattering effects to bend the incoming light rays and redirect them along the layers of absorbing medium, thereby increasing the optical path length of the light in the cell material and, thus, the probability of photon absorption [36]. In this thesis we restrict ourselves to near-field approaches, which use the electric field produced in the near and intermediate regions close to scattering particles to concentrate the light on a medium in their proximity. It is in these regions where the secondary waves scattered by the particles can produce the highest peaks of constructive interference. So, these are the zones where one can locally achieve the maximum light concentration to enhance the absorption of a nearby photovoltaic material.

1.4 Longitudinal near-field light absorption – Semi-classical model

When accounting for absorption from the near-field, particular attention has to be paid to the polarization of the scattered light. The interaction between the scattered light and a material placed in the near-field of the scattering particle cannot be fully described classically such as with far-field radiation [37]. This is because the classical formalism can only accurately describe the light-matter interaction with purely transverse (electric field vector **E** orthogonal to the propagation direction **K**) electromagnetic waves, such as the waves that propagate far away from the source. However, the scattered electric near-field has a longitudinal component (parallel to its wavevector **K**) which can be dominant over the transverse component within distances from the scatterer smaller than the wavelength. A longitudinal field is a localized Coulomb field, with no

associated Poynting vector [6], that transmits electrostatic energy by means of scalar photons, as described by quantum electrodynamics [35].

In this section we describe a semi-classical formalism developed by our group to determine the energy absorption of an electronic system located in the longitudinal near-field of a sub-wavelength particle. The full details of this derivation are given in [38]; therefore in this section we shall only present a brief summary of the key concepts in the method and the main conclusions obtained.

Semi-classical approaches consider the radiation to be described by classical electrodynamics, but the absorbing medium is taken to be a quantized system of electrons (atom or quantum dot, for instance) [35]. The Hamiltonian for the interaction between the radiation and such system (each electron labeled by index *j*) is described by:

$$\mathcal{H}_{int} = \sum_j \left(\frac{e}{2m} (\mathbf{p}_j \cdot \mathbf{A}(\mathrm{r}_j) + \mathbf{A}(\mathrm{r}_j) \cdot \mathbf{p}_j) - e\phi(\mathbf{r}_j) \right) = \sum_j \mathcal{H}_{int,j} \qquad (1.7)$$

being **A** and ϕ the vector and scalar potentials, respectively, of the electromagnetic field incident at the position (**r**) of the electrons. This interaction Hamiltonian H_{int} is regarded as an energy perturbation to the rest state of the un-illuminated electronic system.

In the case of free (far-field) radiation there is no scalar potential $\phi(\mathbf{r}_j) = 0$ and **A** is transverse; so **A** commutes with $\boldsymbol{p}_\mathrm{j}$ and the Hamiltonian reduces to $\mathcal{H}_{int,j} = \frac{e}{m} \mathbf{p}_j \cdot \mathbf{A}(\mathrm{r}_j)$. In the case of a longitudinal electromagnetic field, such as the one scattered by nanoparticles, the scalar potential ϕ is non-zero but the vector potential **A** vanishes. This is because in the Coulomb or radiation gauge $\nabla \cdot \mathbf{A} = 0$, and therefore there is no longitudinal vector potential ($\mathbf{A} \cdot \mathbf{K} = 0$). Hence, the interaction Hamiltonian from a longitudinal field becomes: $\mathcal{H}_{int,j} = -e\phi(\mathbf{r}_j)$.

The absorption coefficient associated with an electronic transition from an initial state *i* to a final state *f* is determined by the transition probability, w_{if}, calculated with the Fermi Golden Rule:

$$w_{if} = \frac{2\pi}{\hbar} \left| < \psi_i \mid H_{\mathrm{int}} \mid \psi_f > \right|^2 g(E_f) \qquad (1.8)$$

where $g(E_f)$ is the density of available final states. For far-field transverse radiation the magnitude of H_{int} is proportional to that of the vector potential **A** which, in turn, is proportional to the electric field intensity **E**. Whereas for a longitudinal electrostatic field the magnitude of H_{int} is proportional to the scalar potential magnitude ϕ. Thus, according to (1.8), the absorption by a medium from a longitudinal field is proportional to $|\phi|^2$.

In the case of longitudinal light scattered by a particle, the scattered potential ϕ_S is affected by the particle geometrical polarizability factor that can increase the absorption by several orders of magnitude. As an example, we investigate in [38] scattering by spheroidal-shaped metal nanoparticles which, under favorable conditions, may provide near-field absorption enhancements almost as large as 10^4 and in many cases above 10. This is developed with further detail in the next chapter.

Chapter 2

Plasmonic light enhancement in the near-field of metallic nano-spheroids

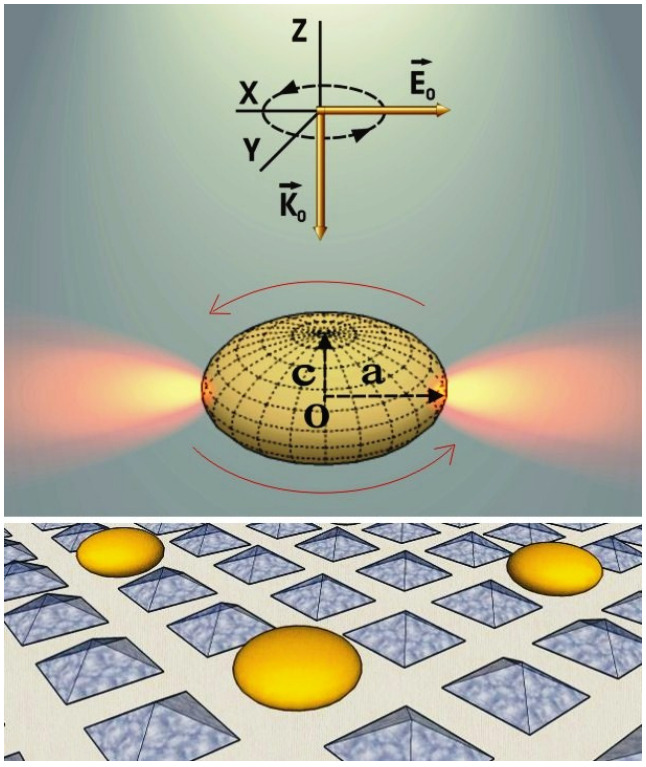

2.1 Introduction

In recent years there has been a growing interest in the optical properties of metal nanoparticles (MNPs) since they exhibit strong scattering resonance in the optical regime, at frequencies that can be tuned by engineering the particle size and shape. These resonances occur when the applied electromagnetic (EM) field frequency matches the frequency of the collective oscillations of the conduction electrons (plasmons) in the particle. The free electrons in MNPs are strongly bound to the particle surface, thus the particle geometry significantly influences the frequency at which they oscillate. Therefore, in MNPs these excitations are usually known as localized surface plasmons (SPs) [39].

At the SP resonance the pronounced polarizability of the MNP effectively draws the energy supplied by an incident EM wave into the particle. This produces a scattered near-field whose intensity can be several orders of magnitude higher than that of the incident field, up to a distance of about the particle size.

This effect can be useful for a wide variety of applications [6, 39], such as those listed in Section 1.1. Nevertheless, the authors are mainly interested in its implementation in quantum-dot intermediate band solar cells (QD-IBSCs) [21], to enhance the amount of light absorbed by the QDs forming the IB.

In this chapter the semi-classical model described in Section 1.4 is applied to estimate the absorption enhancement that SPs can produce in QDs placed in the vicinity of MNPs. The electrostatic approach is used to calculate the scattered potential in the near-field of uncoated and coated metallic nanoparticles with a spheroidal shape. In addition, we determine the optimal spheroidal geometries for light amplification at the sub-bandgap transition energies of QD-IBSCs.

The results show that the absorption enhancement produced at the surface plasmon frequency of the nanoparticles can be of several orders of magnitude in some cases.

2.2 Electrostatic Model

When an electric plane-wave impinges on a particle much smaller than its wavelength, the incident electric field and the field induced inside the particle can be

both assumed uniform [23]. This is the principle of the electrostatic approximation (EA), valid only if the following conditions are simultaneously fulfilled:

$$2\pi R_{eq} / \lambda << 1 \quad \text{and} \quad |N_r| 2\pi R_{eq} / \lambda << 1 \tag{2.1}$$

where R_{eq} is a characteristic length of the particle, taken as the radius of the volume-equivalent sphere [40], λ is the wavelength in the medium, and $N_r = N_p/N_m$ the complex refractive index of the particle divided by that of the surrounding medium.

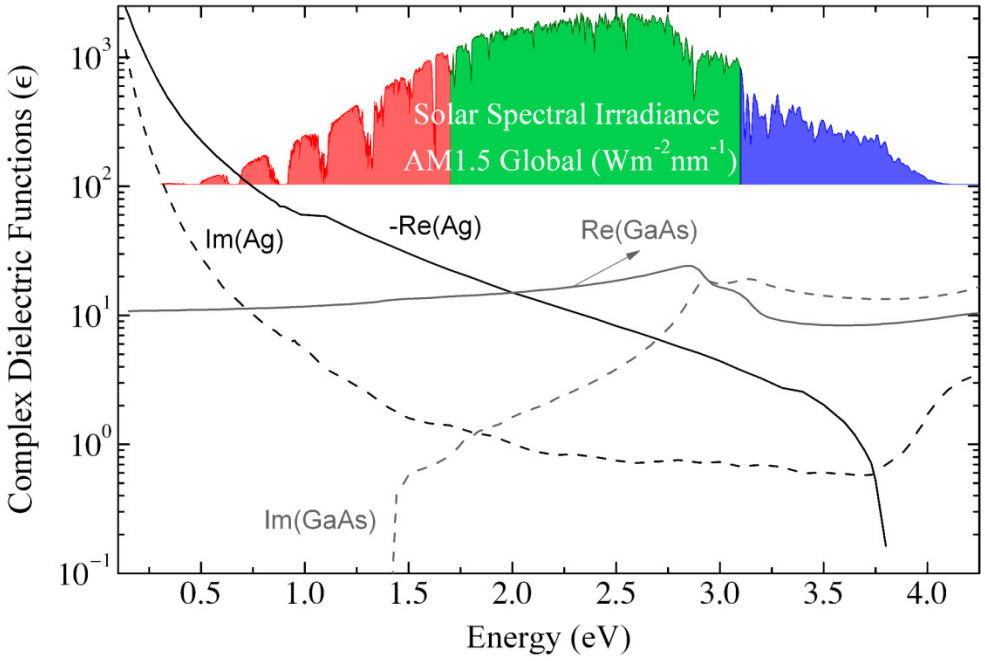

Figure 2.1: Dielectric functions (ϵ) of the particle (Ag) and the medium (GaAs) as a function of energy (in eV). The full lines correspond to the real parts (Re) and the dashed lines to the imaginary parts (Im) of ϵ. In Ag the real part is negative up to 3.8 eV, so we represent its symmetric in the *log* scale plot. The top inset represents the AM1.5 Global solar spectrum showing the infrared (IR, in red), visible (VIS, in green) and ultraviolet (UV, in blue) ranges. The absolute value of the dielectric function of Ag exceeds that of GaAs for energies below ~2 eV.

In this chapter we consider silver (Ag) MNPs in a gallium arsenide (GaAs) medium. The values of the refractive indices of these materials are obtained from interpolation of experimental data [41], and the corresponding dielectric functions ($\epsilon = N^2$) are plotted in Figure 2.1. Previous experimental and theoretical studies confirm

that nanoparticles composed by nobel metals, such as silver or gold, are those that exhibit the strongest plasmonic response [6, 42]. This is due to the relatively low imaginary part (associated to light attenuation) and high real part of their dielectric function in the infrared frequency range. The reason for the choice of GaAs as ambient medium is because most IBSCs have QDs epitaxially grown in a GaAs matrix, as referred in Section 1.2.

The maximum values that can be allowed for R_{eq} are those that set conditions (2.1) equal to unity. These are plotted in Figure 2.2a, for the first (black line) and second (red line) condition of (2.1), as a function of energy. At each photon energy, EA solutions can be considered rather accurate for particle R_{eq} up the lowest value of the two curves in Figure 2.2a [40].

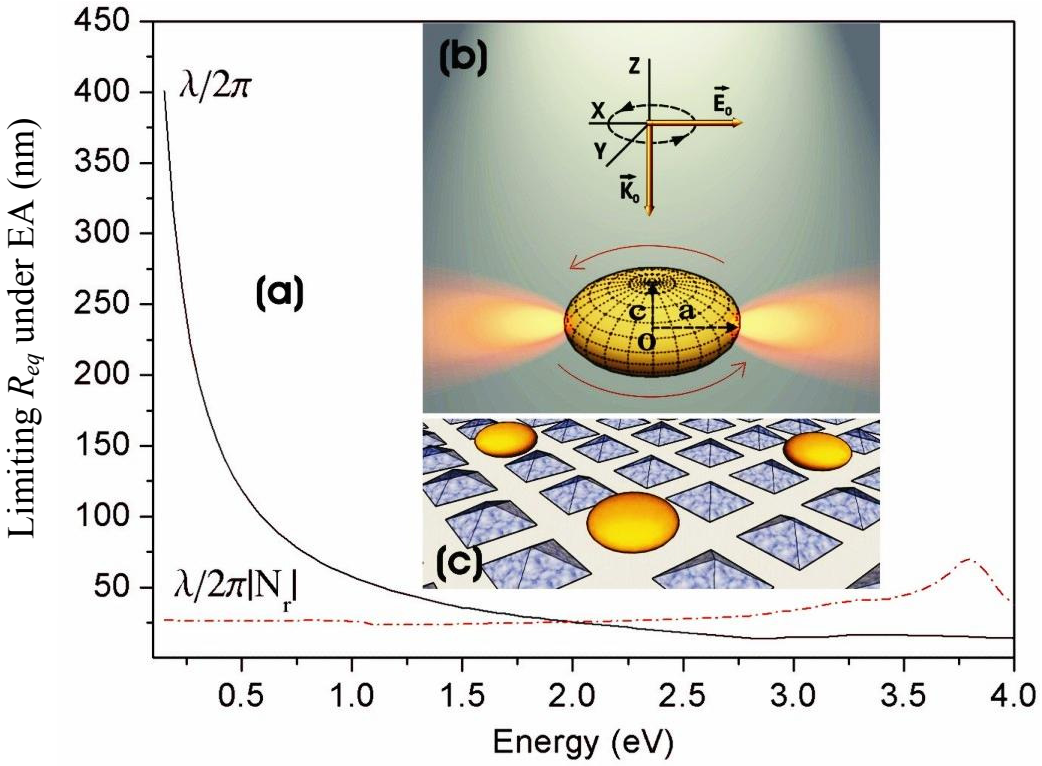

Figure 2.2: **a)** Maximum values of the particle equivalent radius R_{eq} under EA conditions (2.1) for Ag particles immersed in a GaAs medium. **b)** Coordinate system used. The illuminating plane-wave impinges on the particle with its electric field vector $\mathbf{E_0}$ along x. The origin (O) is at the particle center. The particle is a spheroid whose symmetry axis is collinear with the light propagation direction (z). **c)** Preferential position for inclusion of MNPs (yellowish spheroids) in the plane of the QDs (represented as pyramids).

Let us now consider a small [under conditions (2.1)] particle that is placed in a homogeneous and isotropic medium. Since the particle is so small relative to the wavelength, the incident electric field can be taken as uniform [$\mathbf{E_0}$=$E_0\,\hat{\mathbf{x}}$ - see Figure 2.2b] and all retardation effects can be neglected ($\partial/\partial t \to 0$). If the permittivities of the particle and medium are different, a charge will be induced on the surface of the particle. Consequently, the initially uniform field in the medium will be distorted by the presence of the particle.

In electrostatics, since retardation effects are not considered, the electric field is taken to be irrotational [$\partial\mathbf{B}/\partial t = 0$ in the 2nd eq. of (1.1)]; so it is possible to express it as the gradient of a scalar electrostatic potential ($\mathbf{E} = -\nabla\phi$). The potentials inside ϕ_I and outside ϕ_{Out} the particle are obtained from Laplace equation:

$$\nabla \cdot \mathbf{E} = 0 \Leftrightarrow \nabla^2\phi = 0 \tag{2.2}$$

subject to the boundary conditions at the particle surface: ϕ_I=ϕ_{Out} and $\hat{\mathbf{n}} \cdot \left[\varepsilon_p(\nabla\phi_I) - \varepsilon_m(\nabla\phi_{Out})\right] = 0$, where $\hat{\mathbf{n}}$ is the unit vector normal to the surface and ϵ_p and ϵ_m are the particle and medium dielectric functions.

The exact solution of $\mathbf{E}$ and ϕ everywhere can be analytically calculated for ellipsoidal particle geometries. As such, the MNPs are taken to be ellipsoids with semiaxes *a*, *b* and c directed along the *x*, *y* and *z* coordinate axes (depicted in Figure 2.2b).

Due to the unpolarized nature of sunlight, the incident field $\mathbf{E}_0$ can assume any orientation orthogonal to the propagation direction $\mathbf{K}_0$ (see Figure 2.2b). For our scatterer to respond equally to any such polarizations, the MNP must be a particular case of an ellipsoid: a spheroid with *a*=*b*, either oblate (*a*=*b*>*c*) or prolate (*c*>*a*=*b*) having the *c* axis along $\mathbf{K}_0$.

Although solar cells may receive sunlight with oblique incidence, even oblique rays become almost normal when entering the semiconductor due to its high refractive index. Thus, the analysis presented here is approximately valid for the case of oblique incidence.

The potential scattered (ϕ_S) by a spheroid oriented with the *a* semi-axis parallel to $\mathbf{E}_0$ is given by [23]:

$$\phi_S = -\phi_0 \psi_a(\xi)\alpha_a \quad \text{with}$$

$$\psi_a(\xi) = \frac{abc}{2}\int_{\xi}^{\infty} \frac{dq}{(a^2+q)f(q)} \quad \text{and} \qquad (2.3)$$

$$f(q) = \sqrt{(q+a^2)(q+b^2)(q+c^2)}$$

$$\alpha_a = \frac{\varepsilon_p - \varepsilon_m}{\varepsilon_m + L_a(\varepsilon_p - \varepsilon_m)}$$

where $\phi_0 = -E_0 x$ and $\psi_a(\xi)$ is a geometrical factor function of the spheroidal coordinate ξ. The surfaces ξ=constant are confocal ellipsoids and ξ=0 coincides with the particle surface[1]. α_a is the polarizability which depends on the difference in dielectric functions between particle and medium, and on the spheroid aspect ratio (a/c) through the depolarization factor $L_a = \psi_a(0)$.

2.3 Results for uncoated and coated Metal Nanoparticles

As mentioned in Section 1.4, the scattered near-field produced by an MNP is predominantly longitudinal (parallel to its wavector **K**). So, energy absorption from this field cannot be described classically such as with far-fields which are transverse (orthogonal to **K**) [35]. A longitudinal field is a localized Coulomb field, with no associated Poynting vector [6], that transmits electrostatic energy to the medium by means of scalar photons created by the scattered potential operator (ϕ_S), as described by quantum electrodynamics [35, 37]. The maximum absorption felt by the material in the near-field of an MNP is thus obtained by finding the particle aspect ratio that maximizes $|\phi_S|^2$ at each frequency [38]. For solar frequencies this maximum matches that of α_a and corresponds to the SP resonance [6].

[1] See Appendix A for more information on spheroidal coordinates.

However, there is a drawback in inserting metallic particles inside the active region of solar cells since metals may act as electron-hole recombination centers (carrier traps) causing photo-current degradation. Certain metals might form a Schottky barrier that prevents this to occur. Alternatively, the MNP can be enclosed in a shell of passivating coating with a wider bandgap than the medium. As the refractive index decreases with bandgap, this coating must have a lower refractive index than the host material and will quench the scattered field. Therefore, the thickness of the coating must be the minimum necessary to prevent photo-excited carriers (electrons and holes) to tunnel towards the metal core. Two coatings will be considered: SiO_2 (t=4.2nm; see inset in Figure 2.3), widely used in MOS technology, and $Al_{0.4}Ga_{0.6}As$ (t=15nm), a high bandgap III-V alloy that constitutes a good passivating layer for GaAs cells [43]. The values for the dielectric function of AlGaAs were taken from *http://refractiveindex.info*. Thicknesses are selected to produce a similar tunnel-leakage current to that acceptable in MOS technology [44], considering a metal/insulator/semiconductor rectangular barrier model.

In the electrostatic scattering of double layered ellipsoids the polarizability becomes [23]:

$$\alpha_a' = \frac{(\varepsilon_2 - \varepsilon_m)[\varepsilon_2 + (\varepsilon_1 - \varepsilon_2)(L_a^{(1)} - fL_a^{(2)})] + f\varepsilon_2(\varepsilon_1 - \varepsilon_2)}{[\varepsilon_2 + (\varepsilon_1 - \varepsilon_2)(L_a^{(1)} - fL_a^{(2)})][\varepsilon_m + (\varepsilon_2 - \varepsilon_m)L_a^{(2)}] + fL_a^{(2)}\varepsilon_2(\varepsilon_1 - \varepsilon_2)} \quad (2.4)$$

where ε_1 and ε_2 are the dielectric functions of the core metal and coating, respectively, as sketched in Figure 2.3. $L_a^{(1)}$ and $L_a^{(2)}$ are the corresponding depolarization factors and $f = c_1 a_1^2 / (c_2 a_2^2)$ is the fraction of the total volume occupied by the inner spheroid. This solution is valid for confocal spheroids, thus the coating thickness is not constant across the particle surface: it is maximal along the minor axis and minimal along the major. Henceforth, the coating thickness t refers to the value along the c axis (see inset in Figure 2.3).

For a fixed coating thickness there is an optimal core aspect ratio (a_1/c_1) that matches the SP resonance at each photon energy, maximizing the absolute value of (2.4) and ϕ_S. In other words, at each light frequency there is an optimal MNP aspect ratio that maximizes its polarizability and produces the highest possible scattering. This allows the tuning of the SP resonance with the particle geometry: increasing a_1/c_1 (higher

oblateness) shifts the SP frequency to lower energies (more to the infrared) and vice-versa.

These optimal aspect ratios are plotted in Figure 2.3 for coated Ag MNPs in a GaAs medium, using the maximum allowed values in Figure 2.2a for the R_{eq} of the Ag core [40]. It can be seen in the figure that the optimal SP aspect ratios decrease with photon energy.

The coatings considered here do not introduce significant additional restrictions to the EA conditions (2.1), due to their low refractive index (relative to metals) and thickness.

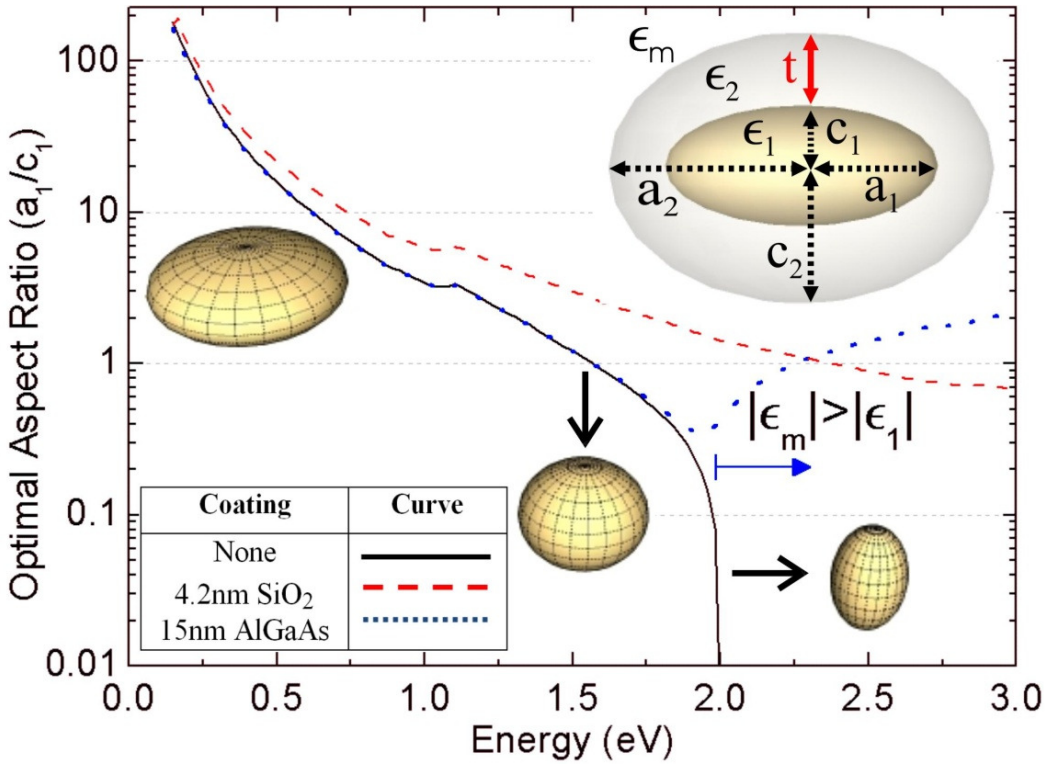

Figure 2.3: Spheroid aspect ratios that maximize the polarizability for uncoated (α_a) and coated (α_a') Ag MNPs in a GaAs medium. The lower the frequency the higher the absolute value of ϵ_1 (shown in Figure 2.1) and therefore the higher the optimal aspect ratio of the MNPs.

As described in Section 1.4, the increment in energy absorption by a system of electrons placed in the near-field of MNPs is given [38] by the quantity $\left|\phi_S / \phi_0\right|^2$, represented in Figure 2.4 at the surface of coatead and uncoated Ag nanoparticles in GaAs.

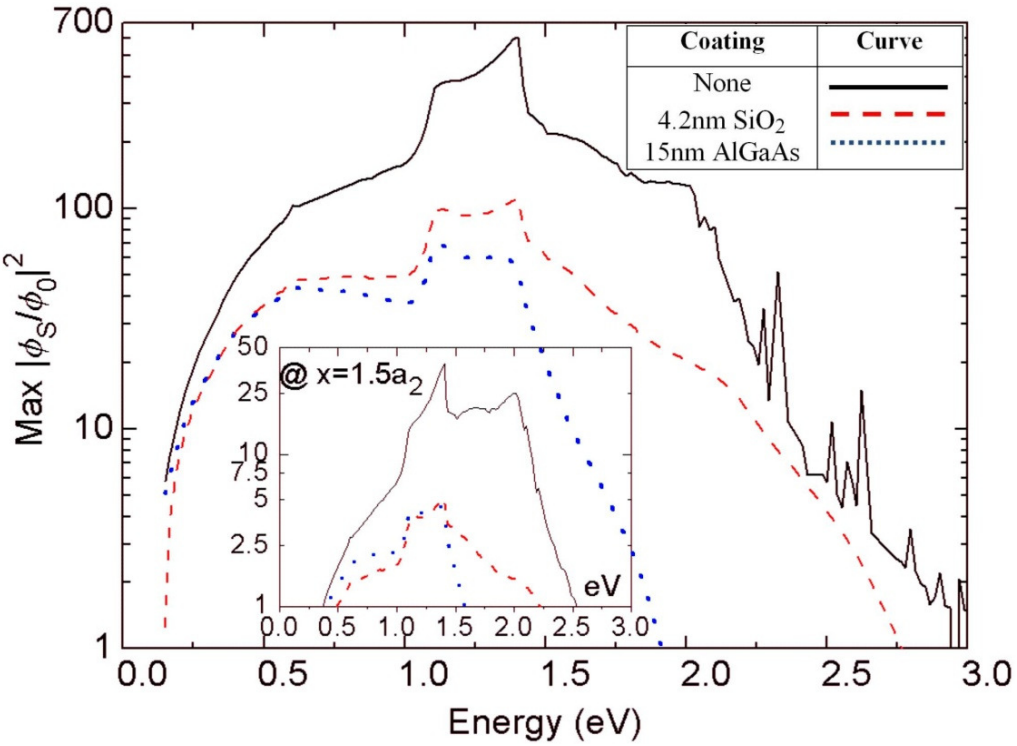

Figure 2.4: Scattered potential $|\phi_S|^2$, in units of $|\phi_0|^2$, at the particle surface (ξ=0 or $x=a_2$) for the SP shapes in Figure 2.3. The inset shows the value of this quantity at $x=1.5a_2$ which corresponds approximately to the spot where a QD would be located according to the array sketched in Figure 2.2c.

This quantity is constant along ellipsoidal surfaces confocal with the particle. Close to oblates it decays roughly with r^{-6} and becomes less than unity after a distance of about twice the particle size ($r = 2a_2$) in the oblate plane. In the inset of Figure 2.4, the value of $\left|\phi_S / \phi_0\right|^2$ is represented at a distance of $1.5a_2$ in this plane, which corresponds to the spot where a QD would be located according to the distribution sketched in Figure 2.2c. It can be seen in Figure 2.4, that the absorption enhancement produced by the MNPs is only remarkably high (> 10) at energies up to ~2 eV, i.e. mostly in the IR spectral range. In the VIS and UV solar range the scattering performance of MNPs is poor and no absorption enhancement is expected at those energies.

The electric field intensity is even more enhanced in the IR region, reaching $2\times10^5 E_0^2$ at 0.2 eV at the uncoated MNP surface (plotted in Figure 2.5). This is on the same order of the intrinsic electric field between the *p* and *n* regions in QD-IBSCs [27], therefore the tilt in the QDs band structure caused by the MNPs scattered field is not

expected to significantly affect the device performance. In the inset of Figure 2.5, the polar plot for the sphere case (E=1.56 eV) was computed with exact Mie theory [23, 33]; and the values precisely match the EA for sizes within the limits (2.1) plotted in Figure 2.2a. Comparing this with the oblate polar plot at E=1 eV it can be seen that the higher is the aspect ratio the more unidirectional the scattered field becomes along $\mathbf{E_0}$ (less angular spread), and the higher is the peak intensity. The SP near-field magnitude decreases nearly monotonically with photon energy, but evanesces as r^{-3} whereas the far-field evanesces as r^{-1}.

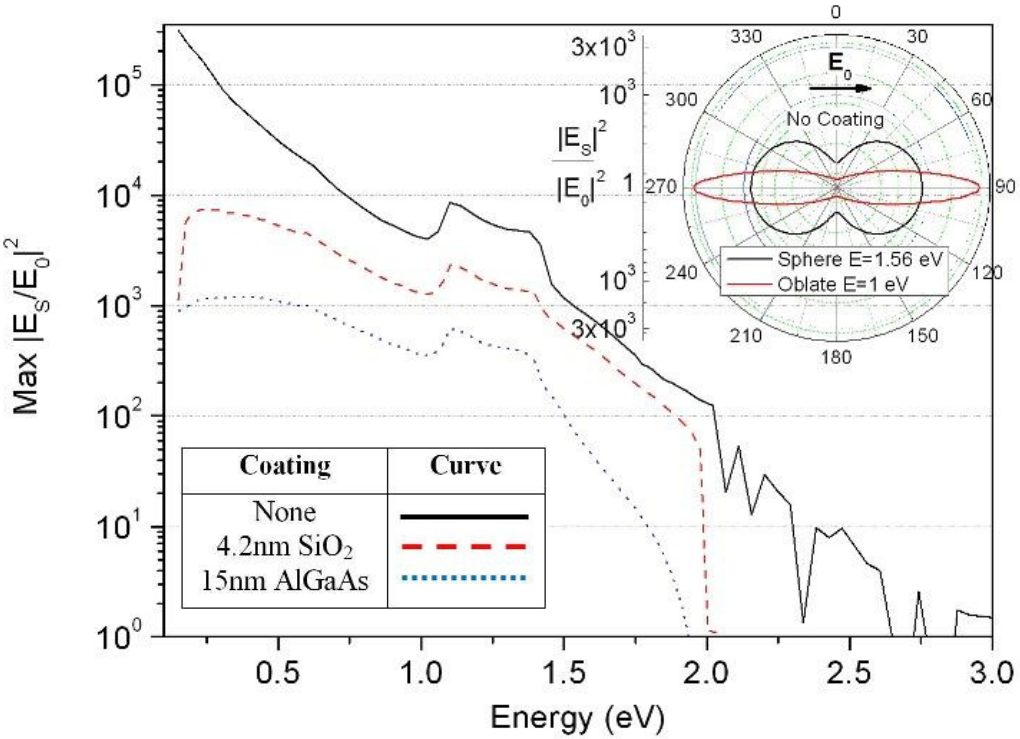

Figure 2.5: Scattered electric intensity $|\mathbf{E_S}|^2$, in units of $|\mathbf{E_0}|^2$, calculated at the point of maximum field strength $x=a_2$ for the SP shapes in Figure 2.3. The field enhancement is only significative up to about 3 eV for uncoated MNPs and 2 eV for coated ones. The inset shows a polar plot of the scattered intensity at the uncoated MNP surface for the two particular shapes sustaining SPs at 1 eV (oblate with a/c=3.4) and 1.56 eV (sphere).

The sub-gap absorption bands in InAs/GaAs QD-IBSCs are located at about 1 eV and 0.3 eV, as indicated in Figure 1.1c. Figure 2.6 shows the spectral absorption enhancement at the surface of MNPs optimally shaped for those energies. The SP shape

corresponding to 1 eV is also optimal for 1.12 eV (due to the feature in the permittivity of Ag – see Figure 2.1), leading to the broad double peak.

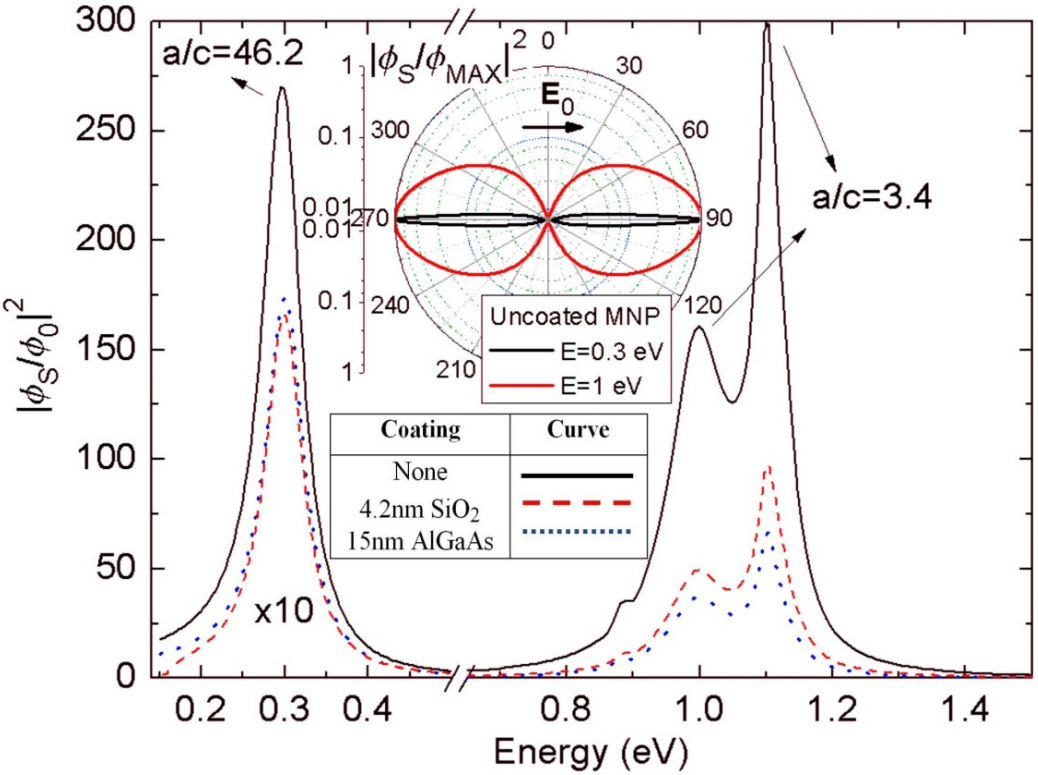

Figure 2.6: Absorption enhancement for spheroids optimally shaped for 0.3 and 1 eV. The curves for the 0.3 eV case are multiplied by 10 for better visualization. The SP shape corresponding to 1 eV is also optimal for 1.12 eV (see corresponding feature in Figure 2.1 and Figure 2.3). The inset is a polar-plot of the scattered potential ϕ_S angular distribution at the uncoated MNP surface in the *xz* plane, normalized by its maximum at 90º, for the 0.3 and 1 eV shapes.

The polar plot in the inset of Figure 2.6 shows the directionality of the scattered potential, typical of a near-field dipolar scattering pattern. As can be seen, the spots of maximum potential (and electric field) intensity are those located in the direction of the $\mathbf{E_0}$ vector. In the case of incident sunlight (unpolarizad), $\mathbf{E_0}$ constantly rotates in a plane orthogonal to $\mathbf{K_0}$, so the MNPs produce absorption enhancement at any point close to their equator. This is why it is preferable to integrate the QDs array on the same plane as the MNPs, in such a way that each QD is close to the equator of at least one MNP, as shown in Figure 2.2c.

2.4 Discussion of results

The results presented in this chapter demonstrate some of the potentialities of the application of plasmonic near-field structures for localized light trapping in solar cells, which is specially promising for the enhancement of their infrared light absorption. This concept is of interest not only for implementation in quantum dot solar cells, but also in other third generation photovoltaic devices able to generate photocurrent from infrared photons, such as multijunction III-V cells.

The electrostatic model was used to calculate the scattering pattern of sub-wavelenght metallic nanoparticles. Such scatterers produce a dipolar near-field angular pattern, which indicates that the particles should be preferentially placed inside the solar cells active region, side-by-side with the QDs, since the maximum enhancement is felt in the plane of the particles (orthogonally to the light propagation direction) close to their surface.

However, metallic surfaces can cause severe carrier recombination in the semiconductor material of the cells, so the MNPs should be coated with a passivating layer having a higher bandgap than the host semiconductor. Insulating coatings such as SiO_2 are preferable to high bandgap semiconductors (e.g. AlGaAs) because they can shield electron tunnelling as well with less coating thickness.

It was concluded that absorption enhancements on the order of 100 can be expected for QDs placed in the vicinity of uncoated MNPs in the 1 eV absorption band, and around 10 with any reasonable coating. For the 0.3 eV band the enhancement, achieved with a set of MNP of much more elongated shape, is smaller but still significant in a close vicinity of the particle. Thus, this alternative is most effective if the IBSC mechanism is based on energy transfer through photons absorbed in valence band (VB) to IB transitions [45]. Closely related mechanisms were found to be important in multiple exciton generation materials [46].

For an MNP shape resonant at a certain photon energy E, the field amplification is significant in an energy interval of $E \pm 0.1$ eV, larger in the 1 eV band.

Within the EA, the magnitude of the enhancement is size independent. However, its *range* is proportional to the MNP size. Thus, the bigger the MNP is the better (under conditions (2.1) of EA) because the absorption enhancement is felt within a larger

volume of PV medium. MNP sizes in the range of 10-100 nm fulfill the conditions and should behave adequately.

Chapter 3

Scattering by wavelength-sized dielectric spheroids

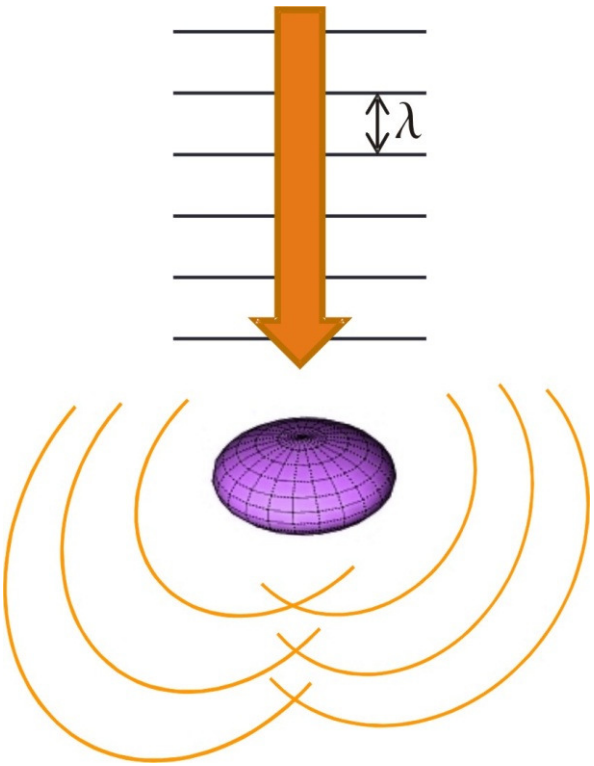

3.1 Introduction

The electrostatic approximation used in the previous chapter can only be applied to scattering by particles much smaller than the illuminating wavelength. However, high field enhancements can also be obtained with bigger particles, outside of the validity limits (2.1) of the electrostatic/dipolar model. That is the size regime that is explored in this and in the following chapter.

In the wavelength-size regime, metallic particles do not perform well as scatterers. Due to the high imaginary part of their refractive index, they mainly shade the incoming light producing weak near-field scattered intensities. According to extensive studies performed by the authors [47, 48], it has been observed that dielectric scatterers with sizes comparable to the wavelength and a real refractive index can exhibit a much stronger scattering behavior, comparable to that of sub-wavelength metallic nanoparticles (MNPs). Furthermore, dielectric scatterers cause much less electron-hole recombination inside a semiconducting medium than metallic ones. This constitutes a crucial advantage for their implementation in PV devices, since they can be embedded in the cell photoactive region without the need of having a passivating coating shell such as that considered in Section 2.3 for MNPs.

In this chapter, we present a theoretical study of electric field scattering by wavelength-sized dielectric spheroids [47]. The incident, internal and scattered fields are computed analytically by a spheroidal coordinate separation-of-variables solution, assuming axially incident monochromatic illumination. The main sources of possible numerical errors are identified and an additional point-matching procedure is implemented to provide a built-in test of the validity of the results.

3.2 Theoretical Background

The analysis of electromagnetic (EM) wave scattering by spheroidal particles has been of increasing interest since the geometry of many objects of practical use can be approximated by a spheroidal shape, and the fields can be obtained analytically.

The exact analytical solution of Maxwell's equations for the plane-wave scattering by a homogeneous sphere of arbitrary size was obtained by Mie [49], using the method

of separation of variables. This problem was first fully solved for the more general case of an homogeneous spheroid by Asano and Yamamoto [2], for any angle of incidence. Their approach consists in separating the vector wave equations (1.5) in spheroidal coordinates and expanding them in terms of the spheroidal wave functions. The conditions of continuity (1.6) of the tangential fields across the surface of the spheroid generate a set of simultaneous linear equations that can be solved for the set of unknown expansion coefficients. The coefficients are determined using the orthogonality integrals approach, similar to the method used here [1].

Theoretically, the solution obtained in this way is exact. However, this does not happen in practice as it is not possible to include terms of infinite order in the series expansions, and due to unavoidable computational inaccuracies. These issues become more significant when considering particles with sizes close or above the illuminating wavelength. In this chapter the main sources of numerical error in the method are identified, and the best ways to reduce them are described based on previous literature and our empirical tests. In addition, a simple built-in test procedure is described to check on the validity of the computed results. This makes use of a boundary condition point-matching strategy that can refine the initial solution.

So far most of the analyses of EM scattering aimed at near-field applications consider objects that are either so small compared to the wavelength that the electrostatic approximation becomes applicable (such as performed in the previous chapter), or particles with a spherical geometry that can be treated with Mie theory [6]. Studies that go beyond these limitations, dealing with non-spherical objects with sizes on the order of or bigger than the wavelength, usually employ numerical grid-based approaches such as finite difference time-domain (FDTD) [14] and finite elements methods (FEM) [50]. However, with mesh approaches it is usually difficult to resolve high field gradients that occur at the surface of particles that scatter highly resonantly with the incoming light. Therefore, the design of each mesh must be well defined and refined for each particle structure. In particular the optical properties of particles with sizes close to the wavelength are very dependent on their geometry, material and surrounding medium. Thus, to model the optical response of particles in the size ranges of interest in this work, it is beneficial to use analytical technique since the fields can be calculated everywhere without needing to cope with finite mesh resolution errors.

The solution of EM scattering by objects which are small compared to the wavelength becomes highly simplified, relative to the full arbitrary-size solution, since retardation effects can be neglected and only one scattering mode – the dipole mode - is excited. Therefore, scatterers in this regime produce very similar field patterns (dipolar-like), independently of their geometry [21, 23], as seen in Chapter 2.

When the particle size approaches the wavelength, higher order modes are excited producing additional features in the field pattern which are highly dependent on the scatterer geometry. In this and in the following chapter we provide a numerical study of scattering by spheroidal particles with sizes comparable to the wavelength, which are able to produce scattered fields with magnitudes significantly higher than the incident field. It is observed that, as the particle size increases from small to comparable to the wavelength, the peak scattered field intensity shifts from the side (dipolar pattern) to the front (forward scattering) of the particle. Besides, unlike sub-wavelength particles in the dipolar regime, the position and extension of the field enhancement can be controlled according to the particle geometry.

In this chapter we study how the electric field pattern is influenced by the scatterer size and shape for prolate and oblate spheroids with a real refractive index of 1.33 relative to that of the ambient medium [47]. This refractive index is chosen to allow comparison between results obtained here and previous studies presenting scattering patterns of spheroids calculated by distinct methods [1, 2, 14, 33, 51, 52]. Such relative refractive index has been widely adopted since it corresponds to that of water drops in air, and therefore the computed results can be used for atmospheric simulation. Nevertheless, these results can also be useful for any of the applications referred in Section 1.1 by making an appropriate choice of the scatterer material. For instance, the relative index of germanium (or lead chalcogenide) particles in a gallium arsenide (or silicon) medium is close to 1.3 in the solar infrared range, which can be of interest for implementation in photovoltaic devices.

Furthermore, in Section 3.4 different size regimes are identified for the distinct types of near-field distributions produced. Particular attention is drawn to the polarization characteristics in each regime. It is important to distinguish between the polarization components longitudinal (parallel to the wavevector **K**) and transverse (orthogonal to **K**) when considering the interaction between the scattered light and a material in the near field of the scattering particle [38], as described in Section 1.4.

3.3 Description of the separation-of-variables method

We consider the scattering of a plane, linearly polarized monochromatic wave by a spheroidal particle of arbitrary size whose axis of revolution is oriented along the incident wave direction. Both the particle material and the surrounding medium are homogeneous, isotropic and nonmagnetic. The exact solution is obtained by expanding the incident, scattered and internal fields in terms of an infinite sum of spheroidal vector wave functions whose coefficients are determined from the boundary conditions at the spheroid-medium interface [47].

Here we adopt a development [1, 4] of the method of Asano and Yamamoto [2], mentioned in the previous section, that employs a formulation where the column matrix of the series coefficients of the scattered field is obtained from the matrix of the series coefficients of the incident field by means of a matrix transformation. The coordinate system used is either prolate or oblate spheroidal, depending on the scatterer geometry. The definition of the spheroidal coordinates (η,ξ,ϕ) is given in Appendix A. These are orthogonal curvilinear coordinates which allow the separation of variables to obtain the eigenfunctions of the scalar potential wave equation. In the prolate system these eigenfunctions are [53]: $\psi^{(i)}_{\substack{e\\o}mn}(C;\eta,\xi,\phi) = S_{mn}(C,\eta)R^{(i)}_{mn}(C,\xi)\begin{matrix}\cos(m\phi)\\ \sin(m\phi)\end{matrix}$, where $S_{mn}(C,\eta)$ is the spheroidal angular harmonic of first kind, with order *m* and degree *n*, and $R^{(i)}_{mn}(C,\xi)$ the spheroidal radial harmonic of i$^{\text{th}}$ kind. The $\phi-$dependence is equal to the product of either a cosine (even) or a sine (odd), indexed by the subscripts *e* and *o* respectively. The spheroid size parameter (*C*) is defined by:

$$C = \frac{Kd}{2} \tag{3.1}$$

where *K* is the wavevector magnitude in the corresponding medium and *d* the particle interfocal distance. From the eigenfunctions $\psi^{(i)}_{\substack{e\\o}mn}$ we can obtain [1, 53] the spheroidal

vector wave functions $\mathbf{M}_{\substack{e\\o}mn}^{q(i)} = \nabla \times \left[\psi_{\substack{e\\o}mn}^{(i)} \hat{\mathbf{q}} \right]$ and $\mathbf{N}_{\substack{e\\o}mn}^{q(i)} = K^{-1} \nabla \times \mathbf{M}_{\substack{e\\o}mn}^{q(i)}$, being $\hat{\mathbf{q}} = \hat{\mathbf{x}}, \hat{\mathbf{y}}, \hat{\mathbf{z}}$. When the incident light direction is collinear with the symmetry axis of the spheroid, the series coefficients vanish for $m \neq 0$ for the expansions of the polarized waves in terms of vector functions with $q=x,y$. Whereas the coefficients of the expansions in $q=z$ functions are only non-zero for $m=1$ [53]. Thus, the summation over m in the fields' expansions reduces to a single m term. The expansions are therefore represented by a single sum over the degree n [5]. The expressions of the vector wave functions used here are given in Appendix A.

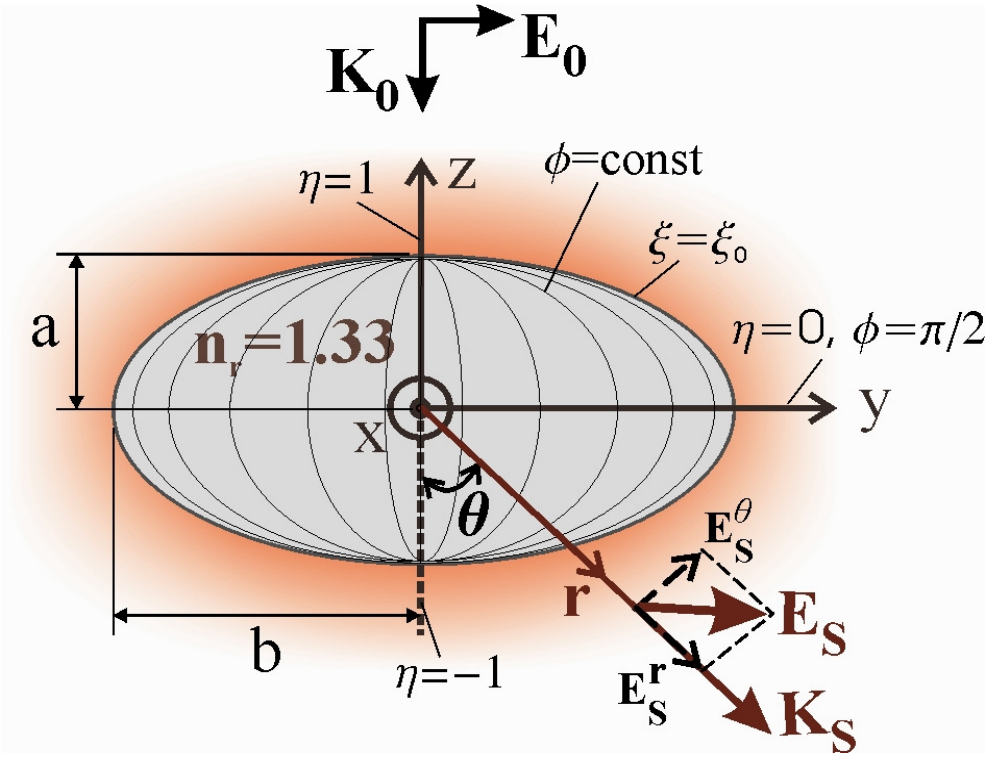

Figure 3.1: Coordinate system for scattering by a spheroid. The particles considered in this work are dielectric with an index of refraction of $n_r=1.33$ relative to the surrounding medium. The surfaces ξ=constant are spheroids confocal with the particle, and ξ_0 coincides with the particle surface. The direction of illumination ($\mathbf{K_0}$) is collinear with the spheroid axis of symmetry (z). A scattered wave in the zy plane is shown, making an angle θ with the negative z axis. It propagates along $\mathbf{K_S}$ (the radial direction $\mathbf{r}$) and its electric field ($\mathbf{E_S}$) can have a component longitudinal ($\mathbf{E_S^r}$) and transverse ($\mathbf{E_S^\theta}$) relative to the propagation direction.

Figure 3.1 shows a schematic of the coordinate system used here. At axial incidence the exciting plane wave can be resolved by a single polarization component, by virtue of symmetry. This wave is then assumed to propagate along the negative *z* direction with the electric field $\mathbf{E_0}$ parallel to *y,* and magnetic field $\mathbf{H_0}$ along the positive *x*-axis. The electric field unit considered in this work is E_0. As such, the illuminating wave has unitary electric field amplitude and can be described by [53]:

$$\mathbf{E_0} = \frac{1}{K_0}\sum_{n=0}^{\infty} A_n \mathbf{M}_{e0n}^{x(1)}(C_0;\eta,\xi,\phi) \;\; ; \;\; \mathbf{H_0} = \frac{i}{K_0 Z_0}\sum_{n=0}^{\infty} A_n \mathbf{N}_{e0n}^{x(1)}(C_0;\eta,\xi,\phi) \tag{3.2}$$

where $K_0=2\pi/\lambda$ (λ being the wavelength in the medium outside the particle), $C_0= K_0 d/2$ and $Z_0 = \sqrt{\mu_0/\varepsilon_0}$ is the characteristic impedance of free space. The coefficients A_n of the incident wave expansion are: $A_n = \dfrac{2i^{n-1}S_{0n}(C_0,1)}{\int_{-1}^{1} S_{0n}(C_0,\eta)^2 d\eta}$.

The scattered field is described by vector wave functions of the 4th kind to satisfy the radiation condition at infinity [5]:

$$\begin{aligned}
\mathbf{E_S} &= \sum_{n=0}^{\infty}\left[\alpha_n \mathbf{M}_{e0n}^{+(4)}(C_0;\eta,\xi,\phi) + \beta_{n+1}\mathbf{M}_{e1,n+1}^{z(4)}(C_0;\eta,\xi,\phi)\right], \\
\mathbf{H_S} &= \frac{i}{Z_0}\sum_{n=0}^{\infty}\left[\alpha_n \mathbf{N}_{e0n}^{+(4)}(C_0;\eta,\xi,\phi) + \beta_{n+1}\mathbf{N}_{e1,n+1}^{z(4)}(C_0;\eta,\xi,\phi)\right]
\end{aligned} \tag{3.3}$$

where $\mathbf{M}_{e0n}^{+(i)}(C;\eta,\xi,\phi) = \frac{1}{2}\mathbf{M}_{e0n}^{x(i)}(C;\eta,\xi,\phi)$ and $\mathbf{N}_{e0n}^{+(i)}(C;\eta,\xi,\phi) = \frac{1}{2}\mathbf{N}_{e0n}^{x(i)}(C;\eta,\xi,\phi)$.

Finally, the transmitted field inside the spheroid ($\xi<\xi_0$) can be expressed as [1]:

$$\begin{aligned}
\mathbf{E_I} &= \sum_{n=0}^{\infty}\left[\gamma_n \mathbf{M}_{e0n}^{+(1)}(C_I;\eta,\xi,\phi) + \delta_{n+1}\mathbf{M}_{e1,n+1}^{z(1)}(C_I;\eta,\xi,\phi)\right], \\
\mathbf{H_I} &= \frac{i}{Z_I}\sum_{n=0}^{\infty}\left[\gamma_n \mathbf{N}_{e0n}^{+(1)}(C_I;\eta,\xi,\phi) + \delta_{n+1}\mathbf{N}_{e1,n+1}^{z(1)}(C_I;\eta,\xi,\phi)\right]
\end{aligned} \tag{3.4}$$

where $C_1=n_rC_0$, n_r being the ratio of the refractive indices of the particle and the medium. The expressions given in this section are written with respect to the prolate coordinate system, but they are identical for the oblate system with the interchanges: $c\rightarrow -ic$ and $\xi\rightarrow i\xi$.

The sets of unknown expansion coefficients α_n, β_{n+1}, γ_n and δ_{n+1}, in the expressions (3.3) and (3.4) for the scattered and internal fields, can be determined by applying the boundary conditions (BCs) at the surface ($\xi=\xi_0$). These require the continuity of the tangential electric and magnetic field components (1.6):

$$\xi=\xi_0:\begin{cases} E_0^{\eta}=E_I^{\eta}-E_S^{\eta} & (3.5a)\\ E_0^{\phi}=E_I^{\phi}-E_S^{\phi} & (3.5b)\\ H_0^{\eta}=H_I^{\eta}-H_S^{\eta} & (3.5c)\\ H_0^{\phi}=H_I^{\phi}-H_S^{\phi} & (3.5d)\end{cases}$$

The 4 sets of unknowns are of infinite number and coupled to each other; therefore in practice it is impossible to obtain the exact solution. However, sufficient computational accuracy can be achieved by properly choosing the truncation number (N) in the fields' expansions (3.2)-(3.4). In this work we take:

$$N=\text{Integer}(K_0\alpha+4) \qquad (3.6)$$

α being the longest semi-axis of the spheroidal particle. This was seen to be the most reasonable choice based in literature [1, 4, 5] and empirical tests performed by the authors.

3.3.1 Determination of the expansion coefficients by the Orthogonality Integrals approach

The following methodology [1, 4, 5] is used to find the unknown coefficients α_n, β_{n+1}, γ_n and δ_{n+1}:

1) The ϕ dependence of the BCs (3.5) is removed by applying the orthogonality properties of the trigonometric functions. However, in the particular case of axial incidence this is not necessary since all vector wave functions in (3.5a) and (3.5d) have a sin(ϕ) factor, and those in (3.5b) and (3.5c) have a cos(ϕ) factor, which can therefore be readily eliminated.

2) The η dependence from the BCs is removed by making use of the angular functions (S_{mn}) orthogonality properties. The $S_{mn}(C,\eta)$ are expansions of Legendre functions, so their orthogonality comes from the Legendre Polynomials orthogonality relations. The approach consists in writing N+1 equations for each BC in (3.5), each equation being multiplied by a distinct $S_{0,n}$ term (where n=0,1,2,…,N). The 4(N+1) equations constructed in this way are then integrated in η over its domain (from -1 to 1); the orthogonality properties are applied to compute the integrals.

3) The system of 4(N+1) equations, now independent of ϕ and η, is solved for the 4(N+1) unknowns (the expansion coefficients). This system can be written in matrix form:

$$\mathsf{Q}\mathbf{A} = \mathsf{R}\mathbf{X} \tag{3.7}$$

where Q is a 4(N+1)×(N+1) matrix with the values of (3.2) that multiply the incident field coefficients A_n and the calculated integrals in η from the previous step. The A_n coefficients are included in the (N+1) column vector **A**. Matrix R has dimension 4(N+1)×4(N+1) and contains the values in eqs. (3.3) and (3.4) that multiply the unknown coefficients with the integrals in η evaluated at $\xi=\xi_0$. The unknowns α_n, β_{n+1}, γ_n and δ_{n+1} are included in **X**, arranged in a column vector of dimension 4(N+1). Vector **X** is determined by inverting the R matrix:

$$\mathbf{X}=R^{-1}Q\mathbf{A} \tag{3.8}$$

The computational environment used to perform the calculations is Mathematica7.0; suitable due to its symbolic and high-precision numerical capabilities, as well as its large library of built-in routines that include packages for computation of spheroidal harmonics [1, 54, 55].

The results presented in this work were generated in an Intel Duo Core CPU machine with 2.33GHz, 2GB of RAM. The total time needed to calculate the expansion coefficients with the method described is mainly dependent on the number of orders (N) used. For a low truncation number ($N \leq 7$) the total time, in minutes, is roughly equal to N/2. For higher N it scales approximately with $N^{2.6}$ for prolates and N^3 for oblates. Most of this time is spent in the computation of the overlap integrals in step 2).

3.3.2 Identification of possible numerical error sources

Once the coefficients vector **X** is obtained the problem is formally solved, since the **E** and **H** fields are known everywhere [eqs. (3.2)-(3.4)]. This result should give an accurate solution for the fields as long as the number of orders N is sufficiently high. However in practice this may not happen, no matter how big N is, due to computational inaccuracies that can occur at every step of the program. These errors tend to become more significant for higher orders, which may cause severe problems when attempting to consider particle sizes close or above the illuminating wavelength. In order to prevent such issues, particular attention should be paid to the following important points in the method:

1) Determination of the eigenvalues $\lambda_{mn}(C)$ of the spheroidal angular and radial harmonics - There are several methods that can be used to evaluate the eigenvalues [1]; among these the one found to be more precise, for any size parameter *C*, and consistent with tabulated published results [53, 54, 56] is the Tridiagonal Matrix method [55, 57]. This is the method employed by the Mathematica7.0 routine *SpheroidalEigenvalue*.

2) Calculation of the spheroidal harmonics S_{mn} and R_{mn} – According to our numerical tests and comparison with literature results, both functions can be accurately computed with the Mathematica7.0 built-in routines based on Falloon code [54]. However, the calculation of the S_{mn} functions becomes relatively slow for large and complex size parameters (C). The routine used in this work, based in the code developed by Li *et al.* [1, 55], calculates the angular functions considerably faster maintaining a high numerical precision, as shown in Figure 3.2.

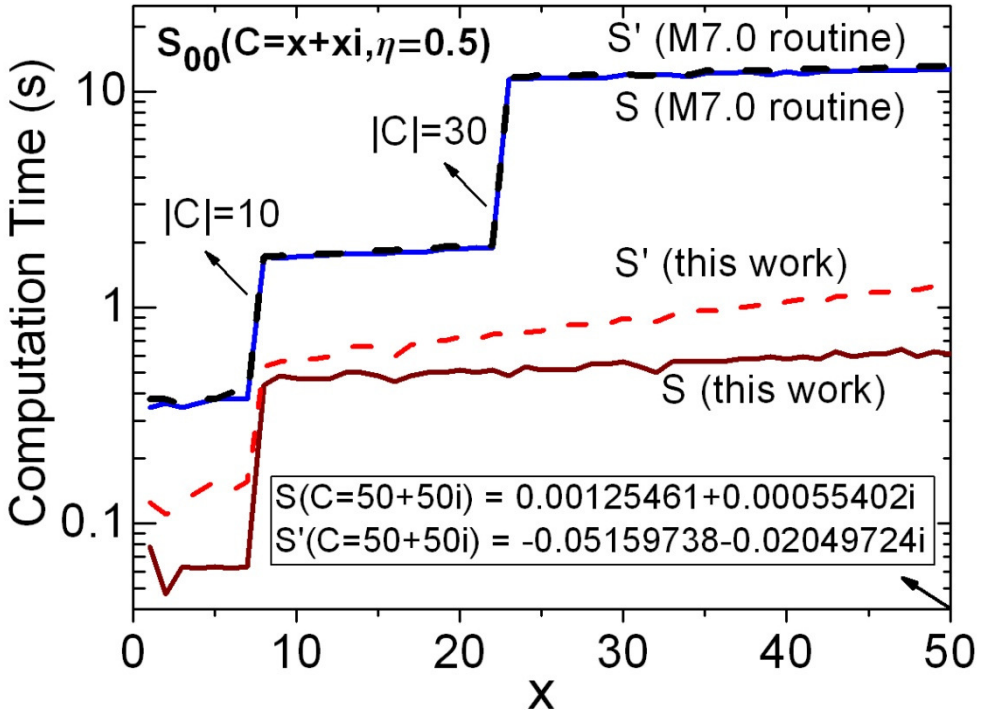

Figure 3.2: Computational time to calculate the angular harmonics $S_{mn}(C,\eta)$ and $S'=dS/d\eta$, with $m=n=0$, $\eta=0.5$ and $C=x+xi$, as a function of x. The calculations were performed using the Mathematica7.0 built-in routine and the routine used in this work. For all x values both codes give the same results for S and S' up to the 14th decimal place. The inset shows the results for $x=50$, which match those presented in [1].

3) Inversion of the matrix R in eq. (3.8) – For problems involving large particles that hence require many N orders [according to (3.6)], the matrix R can become very sparse with values spanning several orders of magnitude. In such cases a simple inversion routine performed by a standard algorithm (such as Gaussian elimination or others) may not provide a sufficiently accurate result. Therefore an iterative correction algorithm, that refines the output of the matrix inversion, should be used.

The algorithm given in Section 2.5 of Numerical Recipes [58] was implemented here. This routine iteratively reduces the value of the inversion error defined as $\varepsilon = \left\| \mathsf{R}\mathsf{R}^{-1} - \mathsf{I} \right\|$, with I being the identity matrix. Typically ϵ can be reduced by one or two orders of magnitude with as few as 5 iterations, being the total computational time practically negligible (on the order of 0.1 seconds).

3.3.3 Boundary Point-matching test

Further error can be induced by the limited precision of any computer calculation. Therefore, it is advisable to implement an additional routine able to check the correctness of the solution of (3.8) and, if possible, to refine it. As such, we included in the code a simple iterative refinement cycle based on boundary condition point-matching (PM) [3, 59, 60].

An alternative way of determining the 4(N+1) expansion coefficients α_n, β_{n+1}, γ_n and δ_{n+1} to that described in Section 3.3.1 would be to directly solve the BCs (3.5) for the tangential components of the fields at a set of M points picked along the spheroid surface. The number of points chosen has to be at least $M_{min}=2(N+1)$, to ensure that the number of obtained equations is equal to the number of unknown coefficients in the expansions.

To avoid ill-conditioned BC matrixes with PM, it is important that the M points are well distributed along the surface. The authors in [61] found it advantageous to place more points near the spheroid axis ($\eta=\pm1$) and fewer at $\eta\approx0$; while others [62] implemented an additional algorithm to determine the optimal points positions. The most favorable location of the points depends on the spheroid geometry; therefore it is advantageous to use more than the minimum number of points ($M>M_{min}$) and solve for the coefficients providing the minimum mean square error over the point set – the least-squares solution [3, 63]. The more points are used the more the error is reduced, and the less sensitive the solution becomes to the chosen positions of the points. In our code the points are positioned at equally spaced intervals from $\eta=-1$ to $\eta=1$, as in [52], half of them at $\phi=0$ and the other half at $\phi=\pi/2$. The total number of fitting points M was taken to be about twice the number of minimum points M=4(N+1), as suggested in previous applications of the method [3]. For each point the tangential internal and scattered vector wave functions in eqs. (3.3) and (3.4) are calculated, and the values inserted in a

matrix A with dimension 2M×4(N+1). According to the BCs (3.5), this matrix multiplied by the solution of (3.8) should satisfy:

$$\mathsf{A}\mathbf{X}=\mathbf{B} \tag{3.9}$$

where **B** is a vector of dimension 2M determined by the two tangential components of the incident field at the picked surface points. Equation (3.9) is, in general, not exactly fulfilled due to possible errors in the computation of **X**. The correct equation is therefore:

$$\mathsf{A}(\mathbf{X}_{\text{correct}}+\mathbf{X}_{\text{error}})=\mathbf{B}+\mathbf{dB} \tag{3.10}$$

where $\mathbf{X}_{\text{error}}$ is the error in **X** which we want to find. The vector **dB** is the error on the right-hand side of eq. (3.9) and can be calculated: $\mathbf{dB}=\mathsf{A}\mathbf{X}-\mathbf{B}$. From (3.9) and (3.10) we get:

$$\mathsf{A}\mathbf{X}_{\text{error}}=\mathbf{dB} \tag{3.11}$$

Since A and **dB** are known, $\mathbf{X}_{\text{error}}$ can be determined from the least-squares solution of eq. (3.11). Then finally a more correct solution $\mathbf{X}_{\text{correct}}$ is obtained by:

$$\mathbf{X}_{\text{correct}}=\mathbf{X}-\mathbf{X}_{\text{error}} \tag{3.12}$$

This solution is further refined in an iteration cycle which improves the least-squares operation. At each iteration, the result of (3.12) is taken as the new initial **X** solution; it is inserted back into eq. (3.9) and the previous calculations are repeated. The iterations then proceed until convergence is achieved.

From the tests performed, the authors have concluded that the final $\mathbf{X}_{\text{correct}}$ solution does not bring a considerable improvement to the initial **X** solution from (3.8) if **X** is determined with the advisable amount of N (or more) orders given in (3.6). When fewer orders are used, this additional PM refinement can improve the result. However, for particle sizes on the order of or bigger than the wavelength, the improvement is never as good as that which would be obtained with the correct number of N orders in (3.6), no matter how many M points are used. Therefore, the addition of this PM algorithm should not be used to compensate for using a lower number of N orders than (3.6) in the method of Section 3.3.1. The main reason why it was implemented in the program is because it provides an automatic check on the correctness of the expansions coefficients result. The computational time required for this PM test is on the same order of the time

spent in calculating the expansion coefficients with the orthogonality integrals approach described in Section 3.3.1.

3.4 Main scattering regimes

The way in which the scatterer geometry influences the field around it changes considerably according to the size of the particle relative to the illuminating wavelength, λ. Three main scattering regimes can be distinguished: the "small particle" or electrostatic (ES) regime, the "big particle" regime described by macroscopic geometrical optics (GO), and in between an intermediate regime for particle sizes on the order of λ. This intermediate regime, defined by some authors as the domain of physical optics [64], is the focus of this chapter using the previously described numerical code.

Most of the literature on analytical solutions of EM scattering by spheroidal particles, with sizes comparable to λ, mainly analyzes far-field quantities. However, the internal and near-field around such particles contain additional physically rich features worth analyzing in more detail [14, 51].

The length unit used is λ, making the results given here dimensionless and therefore independent of the particular wavelength of illumination.

3.4.1 Numerical verification

The EM code used in this work was extensively checked with known analytic and numerical solutions available in the literature. Some examples of such comparisons are given along the presentation of the results. In the next sub-section we start by looking at the electric field distribution around a small sphere in the ES regime, which is compared in Figure 3.3 with the analytic electrostatic approximation [23]. In the following sub-sections, results are shown for bigger spheroids with certain shapes selected to illustrate the main characteristics of the intermediate regime. These are compared with curves obtained numerically by Asano and Yamamoto [2] in Figure 3.4 to Figure 3.7. Finally, the inset of Figure 3.10 shows a comparison with Mie theory [49] considering a prolate with $a \approx b = \lambda$. In all cases the numerical results obtained by us match the known solutions.

3.4.2 Electrostatic case

As referred in Section 2.2, particles much smaller than λ act as electric dipoles generating an internal and scattered field parallel to the incident field. This is known as the electrostatic or non-retarded regime, and occurs when the particle size is sufficiently small to satisfy both Rayleigh limit conditions [23]:

$$2\pi R_{eq} / \lambda << 1 \quad \text{and} \quad |n_r| 2\pi R_{eq} / \lambda << 1 \tag{3.13}$$

where R_{eq} is a characteristic length of the particle. For spheres it is simply the radius, and for spheroids R_{eq} is taken as the radius of the volume-equivalent sphere [40]. The refractive index of the particle relative to the medium is taken to be n_r=1.33.

Even though the present method can accurately calculate scattering by absorbing spheroids (with a non-zero imaginary part in n_r), a purely real refractive index is considered since it facilitates comparison with previous literature results. Furthermore, it has been verified that the inclusion of a small imaginary part (on the order of 0.001i) in n_r does not significantly change the results and conclusions given here.

As long as conditions (3.13) are fulfilled, the scattered field pattern is the same regardless of the particle size. Figure 3.3 shows the field distribution inside and in a close vicinity outside a sphere with radius much smaller than λ. The plot on the left is the magnitude squared of the total field ($\mathbf{E_t}$); given by $\mathbf{E_t}=\mathbf{E_I}$ in the interior of the particle and $\mathbf{E_t}=\mathbf{E_S}+\mathbf{E_0}$ in the exterior. The central and right plots of Figure 3.3 depict the magnitude squared of the longitudinal (along **r**) and transverse (orthogonal to **r**) components of $\mathbf{E_t}$, respectively. If the particle shape were oblate or prolate the only practical change that would occur in Figure 3.3 would be in the scale values. The characteristics which we are mainly interested, such as the peak electric field position and polarization, are shape-independent in the ES regime.

As a dipole, the field inside the particle is uniform and along $\mathbf{E_0}$. The external field is highest close to the surface in that direction, being the longitudinal component dominant there. The longitudinal field is evanescent; it decays very rapidly, roughly with $1/r^3$, r being the distance from the particle center. Since the magnitude of the transverse component only decays with $1/r$ this becomes the dominant component in the far-field.

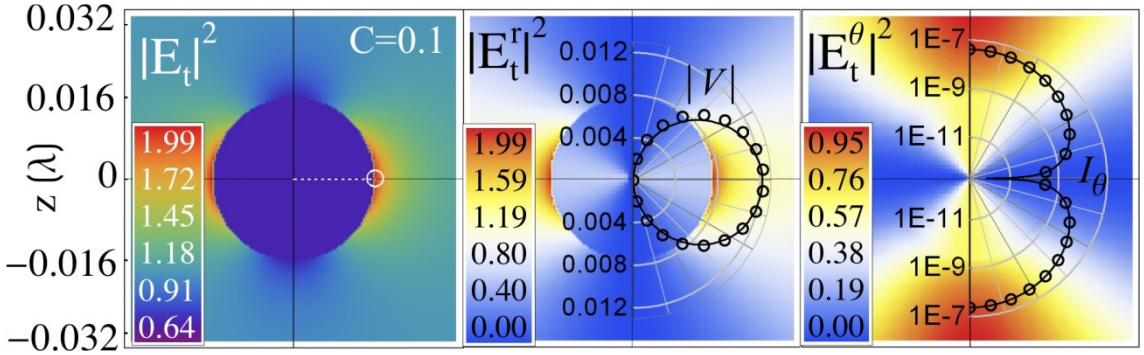

Figure 3.3: Electric field distribution in the *yz* plane of a sphere with n_r=1.33. **Left** – Total field ($\mathbf{E_t}$) magnitude squared. For spheres the size parameter is $C=2\pi R/\lambda$, where R is the radius. The white circle is at the spot of maximum intensity. **Center** – Squared magnitude of the longitudinal component ($\mathbf{E_t}^r$). The polar plot depicts the electrostatic potential magnitude ($|V|$) at the particle surface (r=R). **Right** – Squared magnitude of the transverse component ($\mathbf{E_t}^\theta$). The polar plot shows the far-field intensity function I_θ [Eq. (3.14)]. In the plots of $|V|$ and I_θ the circular dots correspond to the values obtained with the electrostatic (or Rayleigh) approximation [6, 23].

In the field distributions shown in this chapter the longitudinal and transverse components are represented separately since they have a distinct physical nature, as explained in Section 1.4. A transverse EM field is a propagating wave; whereas a longitudinal field is, at some time t, an instantaneous localized Coulomb field associated to a static charge distribution [35]. This is important to take into account when modeling the interaction between scattered light and a material placed in the near-field. For instance, when considering the transference of energy from the scattered beam to a medium, one can use the classical Poynting vector $\mathbf{S}=\mathbf{E}\times\mathbf{H}$ for the energy flux of the transverse part of the field (the only component present far away from a scatterer). However, the concept of Poynting vector is not applicable to a non-propagating longitudinal field since it is not an EM wave, as defined classically [65].

Only semi-classical formalisms can account for a reasonable interpretation of light-matter interaction by the longitudinal component [35]. In this way it has been derived (see Section 1.4 and [38]) that the rate of energy absorption from a longitudinal field, such as that in the near-field of scatterers, should be proportional to the squared magnitude of the scalar potential $V(r)=-\int_0^r \mathbf{E}\cdot\mathbf{dr}$. Therefore, the plots of the

longitudinal E_t^r component distributions shown in this work include a polar plot of the magnitude of *V(r)* at the surface of the particle. In Figure 3.3 it can be seen that, in the ES regime, the spot of maximum field intensity coincides with that of maximum potential at the particle surface. The same is not verified for particles with bigger sizes.

The far-field pattern is usually analyzed by calculating the intensities of the scattered light at infinite distances from the scattering object. In this limit one can take $C_0\xi \to \infty$ and neglect terms with ξ^{-2} and higher-order inverse powers of ξ in expression (3.3). By doing so, the longitudinal/radial terms (E^{ξ} and H^{ξ}) vanish and the scattered wave becomes a purely transverse wave. Besides, the angular coordinate $\eta \to \cos(\theta)$ becomes a function of θ only. As such, the squared magnitude of the scattered (electric) far-field vector in the plane of $\mathbf{E}_0$ ($\phi=\pi/2$) reduces to [1]: $\left|\mathbf{E}_S(\phi=\pi/2)\right|^2 = \dfrac{I_\theta(\theta)}{(K_0 r)^2}$, where I_θ is the intensity function on the scattering plane given by:

$$I_\theta(\theta) = \left| \sum_{n=0}^{\infty} -i^n \pi \alpha_n S_{0,n}(C_0, \cos\theta) \right|^2 \tag{3.14}$$

A polar plot of this quantity is included in the $|\mathbf{E_t}^{\boldsymbol{\theta}}|^2$ plots presented in this chapter, in order to compare the transverse component in the near and far fields. For a small scatterer (see Figure 3.3) the I_θ pattern is approximately proportional to $\cos^2(\theta)$ with equal back and frontal lobes - typical of scattering in the Rayleigh limit [2, 23]. This is similar to the distribution of $|\mathbf{E_t}^{\boldsymbol{\theta}}|^2$ in the near-field.

Another typical characteristic of the ES regime that can be observed in Figure 3.3 is that all quantities are perfectly symmetric with respect to the *y* axis. This means that in this regime there is no *K* dependence in the scattering; it only depends on the incident electric field vector $\mathbf{E}_0$ [23]. The opposite occurs for particles with large sizes relative to λ, as shall be shown in the following sub-sections, where scattering becomes mainly $\mathbf{K}_0$ dependent.

3.4.3 Transition regime

When the scatterer size is not much smaller than λ the field is no longer uniform in its interior due to the appearance of retarded potentials. In the model, this behavior

arises due to the excitation of higher order modes in the fields' expansions (3.2)-(3.4). The bigger the particle the more modes come into play (3.6), causing the appearance of quadrupolar, octopolar and other features in the field patterns that are highly dependent on the particle geometry.

As explained in the previous sub-section, in the small particle (ES) limit the highest scattered field magnitude occurs in the $\mathbf{E}_0$ direction at the particle surface. For spheroids with $R_{eq}>\lambda$ the peak field magnitude is on the axis of propagation ($\mathbf{K}_0$), which is known as forward scattering (FS) [33]. Between the ES and FS cases there is a transition regime for particles with R_{eq} sizes above those set by conditions (3.13), but still smaller than λ.

This transition regime has unique characteristics since the peak scattered field can lie in between the $\mathbf{E}_0$ and $\mathbf{K}_0$ axes, depending on the particle size and shape. This can be well illustrated by spheroidal particles with a size parameter C=2 [as defined in (3.1)]. Figure 3.4 and Figure 3.5 show the field distributions produced by an oblate and prolate spheroid, respectively, with size parameter and aspect ratio equal to 2. Similar calculations were performed for spheroids with higher aspect ratios and the same size parameter. Due to their lower volume (R_{eq}) it was observed that the more elongated the spheroid is the more its field distribution resembles that of a dipole in the ES regime.

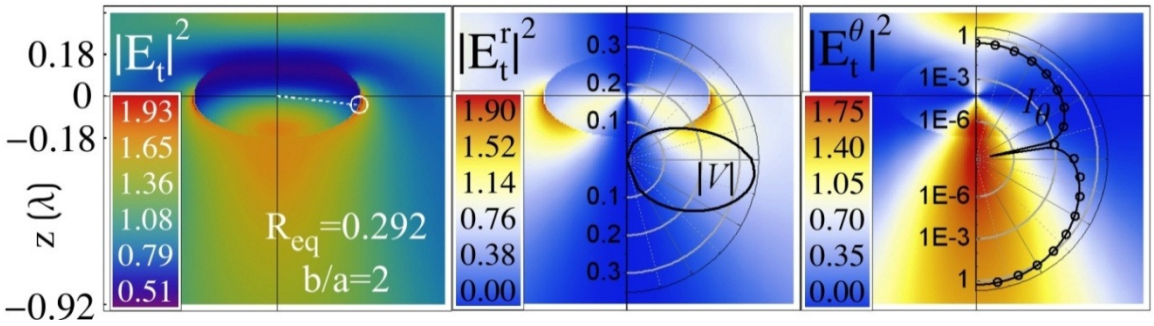

Figure 3.4: Electric field distributions in the *yz* plane of a n_r=1.33 oblate spheroid with size parameter C=2 and aspect ratio b/a=2. In the I_θ curve the circular dots correspond to the values obtained by Asano and Yamamoto [2], shown for comparison.

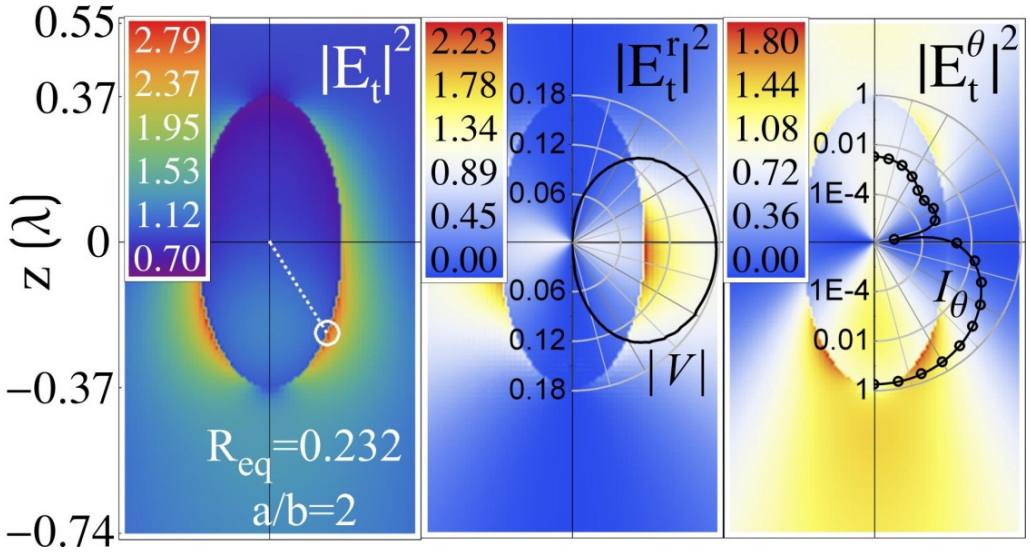

Figure 3.5: Same as Figure 3.4 but for a prolate spheroid with aspect ratio *a/b*=2.

The near and far field quantities in the plots of Figure 3.4 and Figure 3.5 are no longer symmetric with respect to the *y* axis; hence exhibiting a certain *K* dependence that was not present in the ES case. The longitudinal field and potential do not peak in the horizontal $\mathbf{E}_0$ direction, but move down slightly closer to the vertical $\mathbf{K}_0$ axis. In the case of the oblate in Figure 3.4 the maximum of the transverse component E_t^{θ} is almost as intense as that of the longitudinal E_t^r, and occurs in the forward direction. However, for the prolate in Figure 3.5 the E_t^{θ} near field distribution has a dominant quadrupolar feature with two frontal lobes peaking at angles of ±32.2º with the negative *z* axis. Such feature is not present in the far-field I_θ pattern.

3.4.4 Forward scattering regime

In the forward scattering (FS) regime, spheroids whose indices of refraction are real and higher than the medium focus the light in the forward direction, producing scattered fields along their axes of revolution that can be more than one order of magnitude higher than the incident field.

Figure 3.6 and Figure 3.7 show the field distribution for spheroids with a size parameter *C*=7, in the FS regime. Inside the particles, retarded potentials cause the appearance of standing waves. The transverse component E_t^{θ} of these electric waves propagates into the far-field causing the distinct lobes in the I_θ plot. In this size range this component plays the main role even in the near-field, since the spot of maximum

$|E_t|$ is transverse polarized. This does not occur in the previous regimes for smaller particles where the longitudinal component has the highest intensities close to the scatterer.

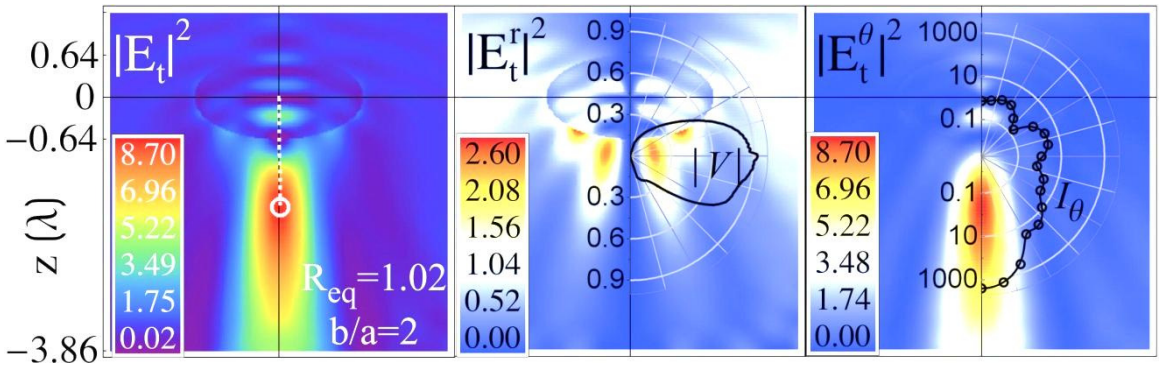

Figure 3.6: Electric field distributions in the *yz* plane of a n_r=1.33 oblate with size parameter C=7 and aspect ratio b/a=2. In the I_θ curves the circular dots correspond to the values obtained by Asano and Yamamoto [2].

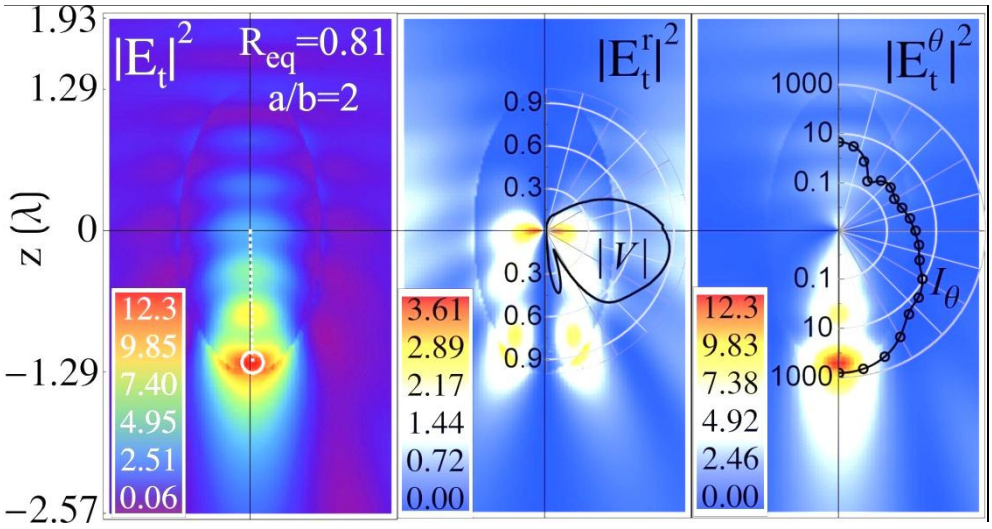

Figure 3.7: Same as Figure 3.6 but for a prolate with aspect ratio a/b=2.

The spots of strongest E_t field are quite distinct for the oblate and prolate shapes of Figure 3.6 and Figure 3.7, respectively. The field enhancement achieved with the prolate is higher than with the oblate of the same size, but it is confined to a smaller region at the prolate front edge. The "bright region" in the oblate case is positioned away from the particle surface and extends through a distance in the negative *z* direction much higher than the particle R_{eq} (about 10 times higher as is shown below in Subsection 3.5.2).

The curves of the potential $|V|$ at the surface present additional features to those of smaller particles, owing to the peaks of the radial, electric field component, E_t^r. Some of these peaks now appear close to the incidence direction, but right at the z axis there is always a minimum in the longitudinal field no matter how big the particle is.

Both spheroids in Figure 3.6 and Figure 3.7 have an aspect ratio of 2. Spheroids with the same size parameter C=7 but an aspect ratio of 5, for instance, have smaller R_{eq}. As a result, the field distributions of such elongated particles present the characteristics of the transition regime described in Subsection 3.4.3. Therefore, it is better to compare field distributions of particles with different aspect ratios that have the same $R_{eq.}$

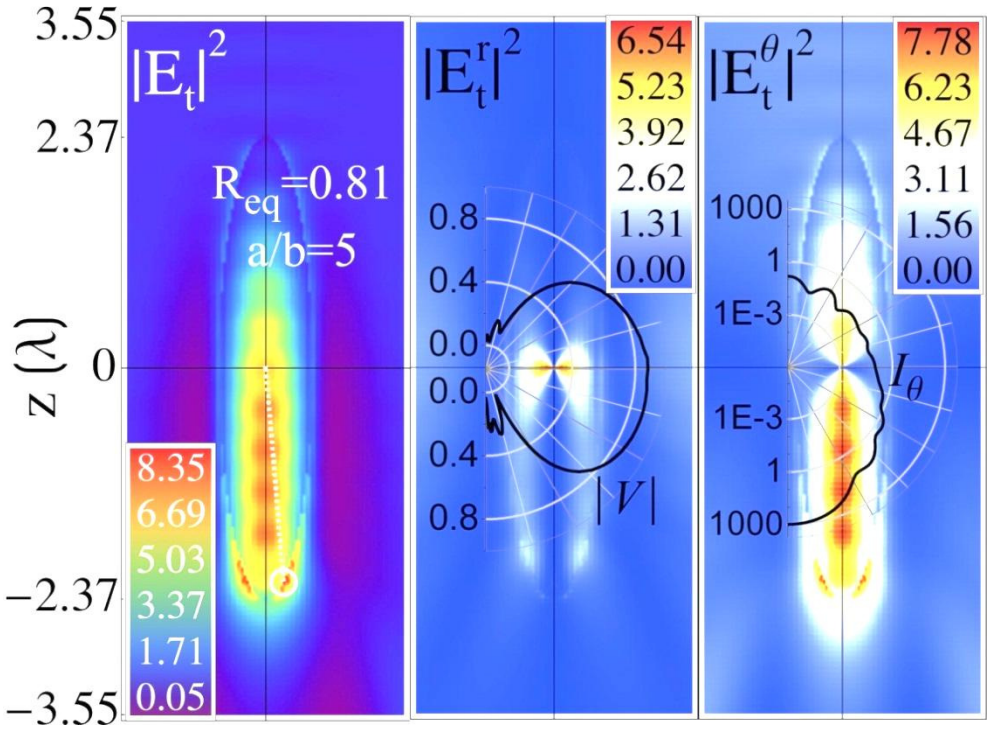

Figure 3.8: Electric field distribution in the yz plane of a n_r=1.33 spheroid with size parameter C=14.6. This is an elongated prolate with aspect ratio a/b=5 and the same R_{eq} as the prolate in Figure 3.7.

Figure 3.8 shows the results of a prolate with the same R_{eq} as that of Figure 3.7 but more elongated (a/b=5). In this case the light enhancement occurs mainly in the interior of the particle and in a localized region close to the surface. The spatial extension of the maximum field peak (signaled with the white circle) is even smaller than in Figure 3.7.

The plot of the total field $|\mathbf{E_t}|^2$ is almost identical to that of $|\mathbf{E_t}^{\theta}|^2$; the longitudinal component only being relevant in a small dipole-like feature close to the particle center.

3.5 Discussion of Results

3.5.1 Direction of maximum scattering

The field distributions shown in Figure 3.4 to Figure 3.8 correspond to a few selected geometries that illustrate the particularities of light scattering by spheroids with sizes on the order of the incident wavelength λ. In this section, these characteristics are analysed in more detail. We start by looking at the θ-angle at which the highest field intensity occurs (θ_{MAX}). This quantity is a good indicator of the distinct scattering regimes described in Section 3.3, as can be seen in the plot of Figure 3.9. The plot represents the value of θ_{MAX} as a function of the spheroid size R_{eq}.

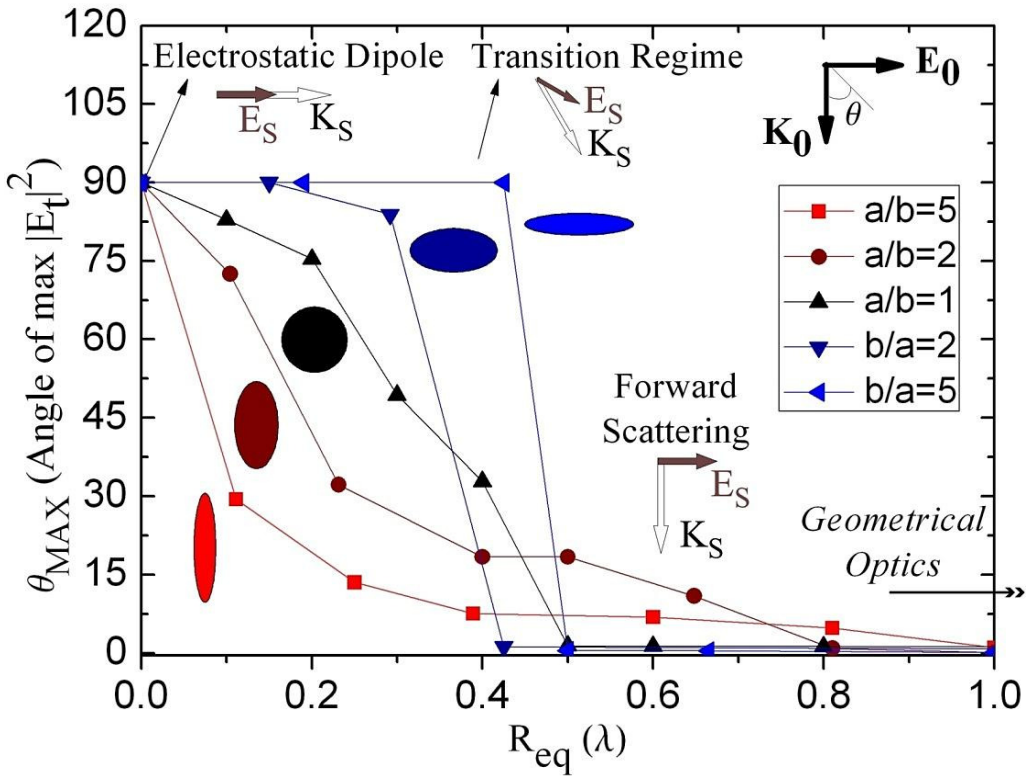

Figure 3.9: Angle θ (in degrees) between the incidence direction and the position of maximum field intensity. In the plots of Figure 3.3 to Figure 3.8 this is the angle between the white dashed line and the negative z axis. The schematic $\mathbf{E_S}$ and $\mathbf{K_S}$ vectors represent the polarization of the scattered field at the spot of maximum field intensity. From the dipole to the forward scattering regime the polarization

goes from being purely longitudinal to transverse, passing by a transition regime where it has both a longitudinal and transverse component.

In the electrostatic (ES) case, the direction of highest field strength is always the same as the incident E-field direction (θ_{MAX}=90º), independently of the scatterer parameters. Spheroids with $R_{eq} \cong \lambda$, or higher, also have a fixed peak scattering direction which is the incidence direction (θ_{MAX}=0º), regardless of their shape – the forward scattering (FS) regime. Between these extremes there is a transition regime where the direction of highest field enhancement switches according to the spheroid size and shape. This interval of particle sizes where θ_{MAX} can lie between 90º and 0º is broader for prolate spheroids and narrower for oblates. The more elongated the oblate the more abrupt is the transition from θ_{MAX}=90º to θ_{MAX}=0º.

Figure 3.9 also shows the case of spheres (*a/b*=1) calculated with Mie theory. The transition regime for spheres occurs between $R_{eq} << \lambda$ and $R_{eq} \approx \lambda/2$; and in that interval θ_{MAX} decreases roughly linearly with R_{eq}.

The peak scattered field in the dipole case is dominantly longitudinal and occurs at the particle surface. This longitudinal component evanesces rapidly with distance from the particle, so in the far-field only the transverse part of the scattered wave is present.

As the particle size increases and we approach the FS regime, the transverse component becomes progressively more dominant relative to the longitudinal even in a close proximity of the particle. So for big sizes the scattered field is mainly transverse both in the near and far regions, as illustrated by Figure 3.6 to Figure 3.8. In the transition regime the longitudinal and transverse components have similar magnitudes in the near-field, as observed in Figure 3.4 and Figure 3.5.

3.5.2 Extension of focal region

Spheroidal particles with a real index of refraction higher than that of the surrounding medium act as lenses in FS regime, concentrating the light in a “bright region” which can be located inside or outside the particle but always in the incidence axis.

According to the principles of physical optics [64], a particle in this regime acts as a resonator (cavity) for the light that is transmitted to its interior. Inside the particle some of that light is internally reflected, bouncing back and forth at distinct angles with

the surface. This produces the appearance of an interference pattern both in the internal and external field, as can be seen in the images of Subsection 3.4.4. The electric field peaks occur at the spots where the light rays interfere more constructively.

Figure 3.10 shows the spatial extension of the bright focal region of field concentration, where the maximum E_t is located, for spheroids with the aspect ratios analyzed in this work and R_{eq} sizes close to λ. The curves in the figure correspond to the values of $|\mathbf{E}_t|^2$ along the radial line starting at the particle center and passing by the point of maximum field intensity (represented in the images of Section 3.4 by a white circle).

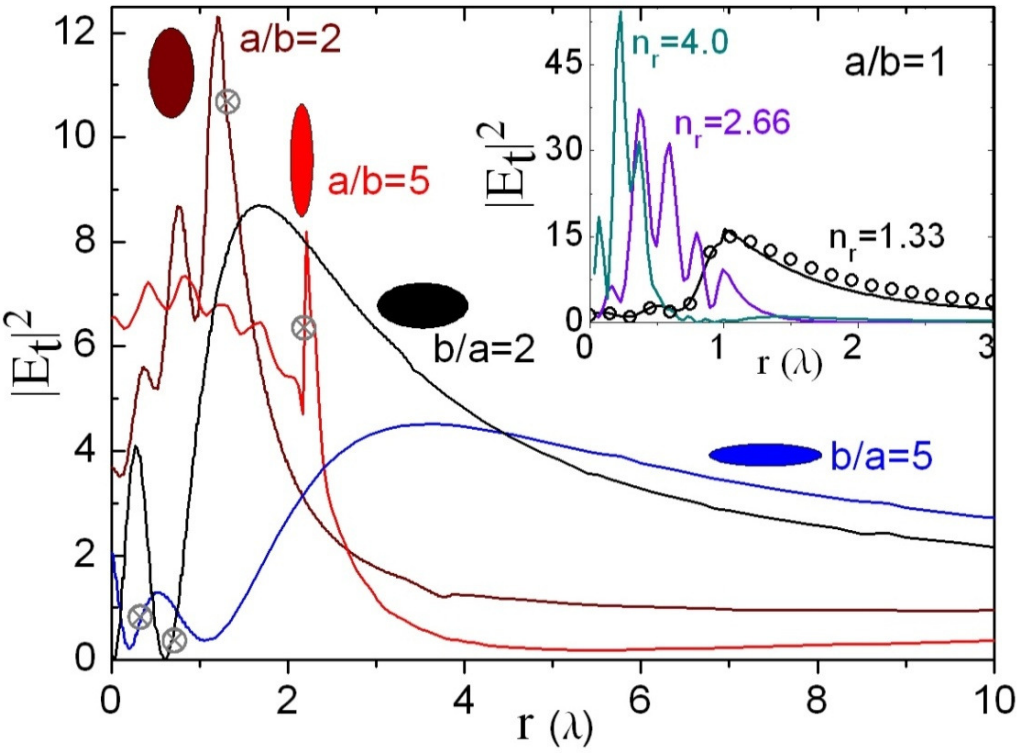

Figure 3.10: $|\mathbf{E}_t|^2$ profiles along the radial direction of maximum field (θ_{MAX}), represented by the white dashed line in the plots of Section 3.4, for particles with size close to λ. *r* is the distance to the particle center, in units of λ. The spheroids with aspect ratio 2 correspond to those in Figure 3.6 and Figure 3.7. The prolate with *a/b*=5 (red curve) corresponds to Figure 3.8. The oblate with *b/a*=5 (blue curve) has the same R_{eq} as the oblate with *b/a*=2. The gray crossed circles represent the intersection with the particle surface. The inset shows similar $|\mathbf{E}_t|^2$ profiles for spheres with radius $R=\lambda$ but distinct refractive indices n_r, computed with Mie theory. The curve for n_r=1.33 is compared with that (circular dots) calculated with our separation-of-variables method described in Section 3.3 using an almost spherical prolate (a/b=1.001).

It can be observed that prolates produce more localized focal regions, positioned inside the particle and on the outside close to the surface. In the exterior of the prolate, this region of field enhancement decays very rapidly with distance, and the higher the elongation of the prolate the more rapidly it decays. On the other hand, the peak scattered intensity produced by oblates is located outside the particle away from the surface, and decays very slowly with distance. For instance, the focal region close to the oblate with b/a=2 extends to a distance above 10 times the particle R_{eq}. The higher is the oblate aspect ratio the lower is the slope of the E_t decay.

The spheroids considered in this work have a real index of refraction of 1.33 relative to the medium. Increasing the particle refractive index causes more bending of the light rays transmitted to the particle material, increasing the interference in its interior. Therefore, the higher the particle real refractive index the higher the peak field magnitude is expected to be. This is shown in the inset of Figure 3.10 for spheres with radius equal to λ and distinct relative refractive indices. It can be seen that bigger indices cause an increase of the maximum E_t and shift the field enhancement closer to the particle center.

3.6 Conclusions

A separation of variables method was used to solve the scattering problem of a spheroidal particle illuminated by an axially incident plane-wave. This method can be extended to the case of an arbitrary excitation beam using generalized Lorenz-Mie theory (GLMT) [66].

Depending on the characteristic size of the scattering particle (R_{eq}) relative to the illumination wavelength, three different regimes can be distinguished: electrostatic ($R_{eq}<<\lambda$), intermediate ($R_{eq}\sim\lambda$) and geometrical optics ($R_{eq}>>\lambda$). In this chapter we focus on the intermediate regime for particles with a real index of refraction of 1.33 times that of the surrounding medium. It was seen that this regime can be subdivided into two: the transition and forward scattering regimes.

The internal and near fields around spheroids in these size regimes exhibit peculiar characteristics that can be of interest for distinct technological applications. According to the particle size and shape, the internal field and external near-field can achieve intensities one or more orders of magnitude higher than the incident intensity.

Furthermore, the spatial location of the field enhancement can be controlled with the spheroidal geometry. This possibility does not exist in any of the other size regimes: small particles in the electrostatic case produce a peak scattered field in the direction of the incident field and at the particle surface, and big particles scatter the light mainly in the direction of incidence. However, with wavelength-sized spheroids the maximum intensity direction can be located anywhere between the directions of the previous two cases, and it can occur closer to the particle center for prolates and away from it for oblates.

The spatial extension over which the field enhancement is felt is another parameter that can be switched according to the spheroid geometry. In the forward scattering regime, prolate shapes produce confined focal regions in their interior or in the vicinity of the surface. Whereas oblates exhibit peak scattered fields in their exterior which can extend to a distance several times higher than its size (see Figure 3.10).

As seen in the previous chapter, metallic scatterers sustaining localized surface plasmons can also produce high light amplification in the electrostatic regime [21, 38]. However, in the intermediate regime the performance of metallic particles for near-field enhancement is deteriorated because their absorption becomes higher than their scattering power, so they mainly shade the incoming light. Therefore, in this size regime, dielectric scatterers with a real index of refraction higher than the medium perform better. In the cases analyzed here, high field enhancements are observed with dielectric scatterers having only a 33% difference between particle and medium refractive indices. This is a crucial advantage of working with dielectric particles in this size regime, since for certain applications it may be beneficial to have the lowest material contrast as possible. For instance, for solar cell applications [21] the embeddement of metallic scatterers in their semiconducting medium can generate severe electron-hole recombination, degrading the generated photo-current (such as occurs with MNPs [42, 67]). Also, for biological applications, like cancer ablation [9] or in-vivo imaging, the introduction of dielectric particles may cause less harm to the organism than metallic ones.

Chapter 4

Optimization of near-field scattering by dielectric mesoscopic spheroids

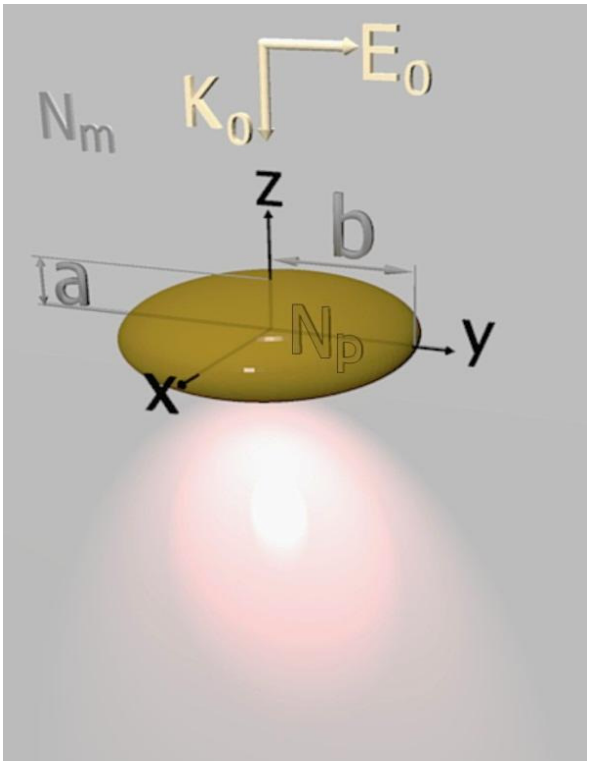

4.1 Introduction

The way in which the scatterer geometry influences the field around it changes considerably according to the size of the particle (R_{eq}) relative to λ. In Chapter 2 it was described how the field distribution produced by objects with sizes much smaller than λ can be obtained with the electrostatic approximation (EA) [23]. Scatterers in this electrostatic size regime (ES) produce dipolar-like (first order) near-field patterns independently of their geometry or material. In Chapter 3 it was observed that, as the particle size approaches λ, higher order modes (quadrupolar, octopolar, etc.) are excited producing additional features in the field pattern which are highly dependent on the scatterer physical parameters (size, shape, material and surrounding medium) [23, 68].

Figure 4.1 portraits the main characteristics of the electric field distributions inside and in the near-field outside the particles, as their size is increased [69]. The material of the particles and the coordinate system used is the same as in the previous chapter, shown in Figure 3.1. Optically small particles (see $R_{eq}=\lambda/20\pi$ in Figure 4.1) act as electric dipoles (ES regime) producing an external peak field intensity on the $\mathbf{E_0}$ axis (at $y=\pm b$) attached to their surface. As the scatterer size increases and approaches λ (see $R_{eq}=\lambda/\pi$ in Figure 4.1) the peak field intensity moves along the surface from the $\mathbf{E_0}$ axis to the forward direction ($\mathbf{K_0}$). Particles with sizes close to or above λ (see $R_{eq}=\lambda$ in the figure) produce transverse polarized scattered fields focused along its axis of revolution z (forward scattering). Such scatterers act as optical cavities and its near-field distribution is a standing wave pattern in which the electric energy is removed from the regions of destructive interference and concentrated in those of constructive interference.

The work presented in this chapter is entirely focused on particles with sizes on the order of λ, such as those in the bottom plots of Figure 4.1. Such scatterers lie in a scattering regime between EA and GO, known as the mesoscopic regime. This regime is still rather unexplored, since the solution of electromagnetic (EM) scattering by mesoscopic objects requires the detailed calculation of the full set of Maxwell's equations [7, 47].

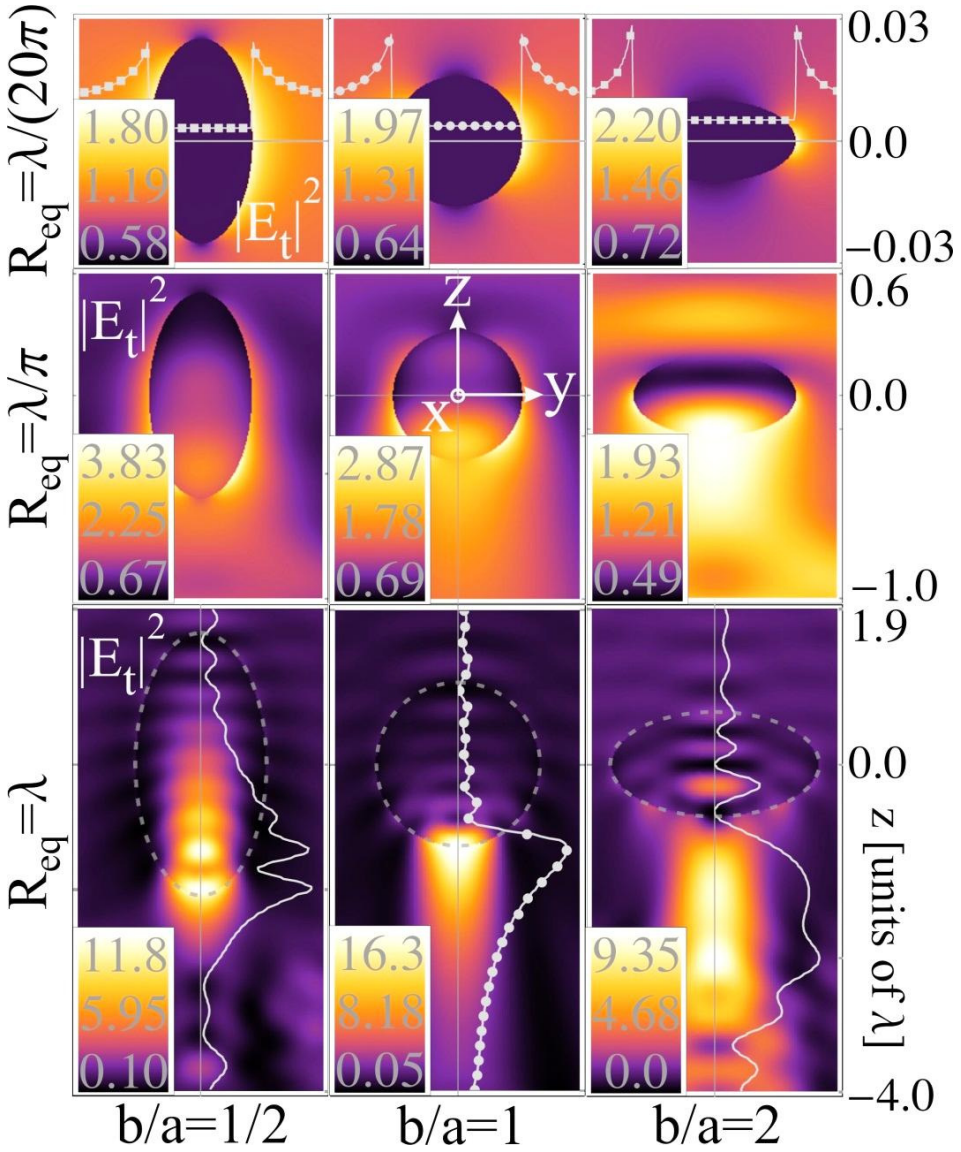

Figure 4.1: Total electric field intensity $|\mathbf{E_t}|^2$ distribution, in units of the incident field intensity $|\mathbf{E_0}|^2$, produced by spheroidal particles with distinct sizes (R_{eq}) and shapes (b/a). The field distributions were computed on a vertical cross-section through the center of the particle, coplanar with the yz plane defined by the incident wave ($\mathbf{K_0}$,$\mathbf{E_0}$). The coordinate system is depicted in Figure 3.1. The refractive index is N_r=1.33 for all particles. The solid gray curves on the top/right of each image correspond to $|\mathbf{E_t}|^2$ along the y/z axis. In the top images the values of $|\mathbf{E_t}|^2$ along the horizontal y axis obtained with our numerical code (gray curves) are compared with those obtained with the EA (square dots). The gray curves on the bottom plots correspond to $|\mathbf{E_t}|^2$ on the z axis. In the central plots for spheres (b/a=1) the curves are compared with Mie theory (circular dots).

Most of the analytical studies published so far on light scattering by mesoscopic particles use Mie theory [8, 10, 17, 23, 33, 70], which is valid for any particle size but restricted to perfectly spherical shapes. In the present work, a spheroidal coordinate

separation-of-variables solution is used to study the near-field scattering properties of spheroidal particles with arbitrary size and shape [1, 15, 47].

Using Mie theory, dielectric spheres and cylinders have been shown [8, 12, 14, 16, 70-73] to produce remarkably intense electric fields close to their shadow-side surface. They act as near-field lenses concentrating the light in a jet-like region located along the incidence axis; which has already been corroborated experimentally by direct imaging [74]. The laws of such focusing are quite distinct from those of macroscopic GO lenses [8, 10, 72, 75]. In the mesoscopic regime the diffraction pattern is dictated by EM wave interference mechanisms which distribute the energy from the regions of destructive interference to those of constructive interference [76], as is discussed below in Section 4.4.

In most cases of practical interest scatterers are non-spherical and can be better approximated by a spheroidal shape. However, accurate light-scattering computations for mesoscopic spheroids are complex and time consuming, and the literature in which such calculations are reported is rather scarce. The work presented in this and the previous chapter contributes to fill this gap. The near-field light focusing properties of dielectric spheroids with arbitrary size, aspect ratio and complex refractive index are analyzed; and important additional possibilities are found relative to the particular case of spheres. In this chapter, a small imaginary part is considered in the materials' refractive index in order for the results to meet conditions attainable in practice.

The possibility to concentrate light in the near-field of dielectric mesoscopic particles (DMPs) is still little explored [10, 75]. This is partly due to the fact that usually only their far-field scattering properties are studied [1, 2, 64, 77]. Besides, the high energy concentration occurs only in specific cases when there is an optimized set of physical parameters that allow a pronounced constructive interference in the diffraction pattern. In any application, the absorptive nature of scatterers and the high confinement of their near-field substantially limit the parameter space where near-field structures can provide exceptional improvements to the properties of the surrounding receiving materials (emitters or absorbers depending on the application) [68]. Therefore, a theoretical study involving a computational optimization is crucial prior to any practical implementation. In this work, an optimization algorithm was developed that iteratively searches for the DMP parameters that provide the highest possible forward scattered field intensities along a certain region of the external medium [48, 69].

Previous works on scattering by mesoscopic spheroids already investigated some properties of their near-field distributions [14, 15, 47, 51]. However, this is the first time, to our knowledge, that an optimization study has been presented which seeks the best electric energy focusing characteristics that can be produced by such particles [48]. The evolution of the optimization process towards convergence provides important insight about the role that each DMP parameter (size, aspect ratio and material contrast) plays on the characteristics of the near-field distribution. For particular parameter sets the field outside the particle can achieve intensities more than two orders of magnitude higher than the incident intensity. Furthermore, the spatial location and extension of such field enhancement can be controlled [47], allowing distinct types of field patterns ranging from highly confined and intense focal spots to less intense but widely spread focal regions.

This can be of interest for several applications such as nanoscale processing of materials (by ablation [8] or photo-etching [10]), high-resolution microscopy (e.g. biomedical diagnostics [11, 12]), resonance spectroscopy (e.g. amplification of Raman and fluorescence [14, 78] signals), localized sensing techniques (e.g. enhancement of nanoparticles backscattering [16, 17]), cancer ablation [9], optical data storage [18], optical antennas [20], among others. Nevertheless, the authors are particularly interested in its implementation in photovoltaic devices [21]. The incorporation of DMPs as "mesoscopic lenses" in a solar cell could lead to locally enhanced optical absorption and an overall increase in the power conversion efficiency [22, 69]. The increased strength of the optical interactions with the PV material would also allow the use of a thinner (thus less expensive) photo-active region.

4.2 Separation-of-variables method and definitions

We consider the EM interaction between a spheroidal particle and a monochromatic plane-wave incident along the spheroid symmetry axis. The particle and the surrounding medium are taken to be homogeneous, isotropic, and non-magnetic. The theoretical model used is a spheroidal coordinate separation-of-variables solution [1] that allows the computation of the EM fields inside and outside of a spheroid with arbitrary size, shape and complex refractive index.

The details of the method are already described in the previous chapter and in [47]. In short, by applying the separation of variables to the scalar Helmholtz equation the spheroidal harmonics of EM waves can be obtained [53, 55]. The solution of the vector Helmholtz equations for the incident (0), internal (i) and scattered (s) electric (**E**) and magnetic (**H**) fields is determined by expanding the fields in spheroidal vector wave functions[2] obtained from the corresponding scalar spheroidal harmonics. The boundary conditions (BCs) of continuity of the tangential fields across the spheroid surface generate a set of simultaneous linear equations that can be solved for the set of unknown expansion coefficients. The solution of this system of equations is obtained by choosing a suitable truncation number (N) for the fields expansions and then employing the orthogonality integrals approach [1, 2, 15]. The value of N is chosen to be sufficiently large for convergence of the solution. In each calculation an initial set of expansion coefficients is obtained with the truncation number N=Integer($K_0\alpha$+4). Being $K_0=2\pi/\lambda$ and α the longest semi-axis of the spheroid [1, 47]. The continuity of the fields' tangential components is then checked at a set of points along the particle surface. If there is not enough rigor in maintaining the BCs in the computed solution, the value of N is progressively increased until an accurate match is obtained between the internal and external tangential fields at the surface.

The total computational time is roughly proportional to N^3. Most of this time is spent in the determination of the orthogonality integrals to obtain the expansion coefficients. However, these calculations can be parallelized, scaling down the computational time almost proportionally to the number of CPUs used in parallel. The computational environment used to perform the calculations was Mathematica7.0; suitable due to its high-precision numerical capabilities and its packages for computation of spheroidal harmonics [1, 47, 55].

Figure 4.2 is a schematic drawing of the coordinate system used, which is the same as that of the previous chapter. At axial incidence the illuminating wave ($\mathbf{K_0}$,$\mathbf{E_0}$) can be resolved by a single polarization component, by virtue of symmetry. This wave propagates along the negative z direction with the electric field $\mathbf{E_0}$ parallel to y.

As in the previous chapter, the electric field magnitude is given in units of the incident field amplitude (E_0). The length unit used is λ, making the results given here independent of the particular wavelength of illumination.

[2] The expressions of the vector wave functions are given in Appendix A.

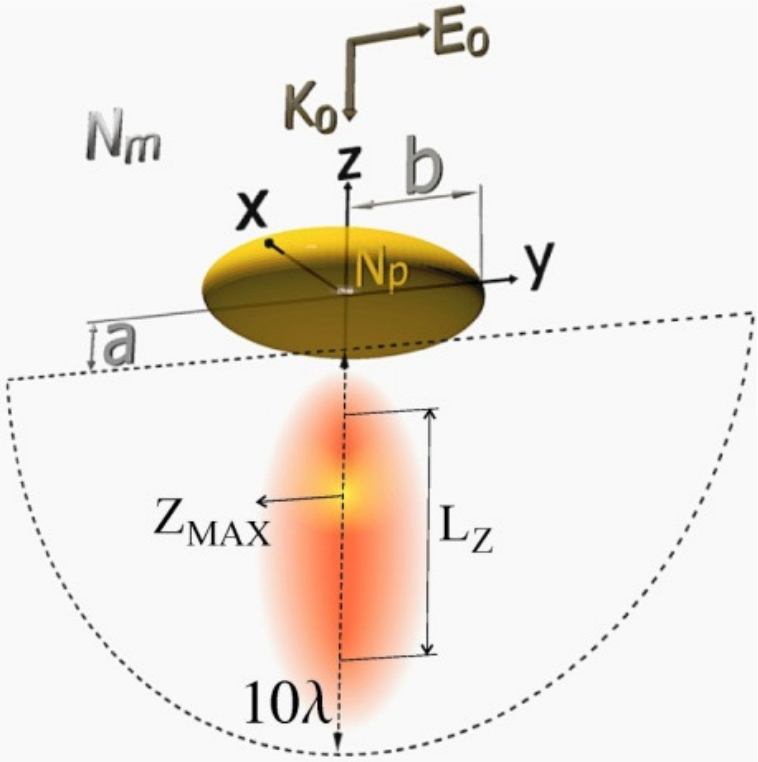

Figure 4.2: Coordinate system with origin at the center of the spheroidal particle. The spheroid has semi-axes *a* (*z* axis) and *b* (*xy* plane). Its refractive index (N_p) is higher than that of the surrounding medium (N_m). The direction of illumination ($\mathbf{K_0}$) is collinear with the spheroid axis of symmetry (*z*). The scattered light can form a forward-directed lobe extending away from the particle shadow-side surface. The point of highest electric field intensity ($|\mathbf{E}|^2_{MAX}$) outside the particle is located on the *z* axis at a distance Z_{MAX} from the origin. L_Z is the width of the focal peak along the *z* axis, corresponding to the distance in *z* where the external field intensity remains above $|\mathbf{E}|^2_{MAX}/e^2$.

The physical parameters involved are the size of the spheroid, its aspect ratio (*b/a*), and the relative refractive index given by the ratio between the refractive index of the particle and that of the ambient medium ($N_r=N_p/N_m$). The spheroid size parameter (*C*) used in the separation-of-variables method is defined in terms of its inter-focal distance *d* [1, 53]:

$$C = \frac{Kd}{2} \tag{4.1}$$

where K is the wavevector magnitude in the corresponding medium. Inside the particle the size parameter is $C_i=N_rC_0$, being C_0 the size parameter in the external medium. Our method allows the computation of the spheroidal harmonics with complex arguments. So, a complex refractive index $N_r=n_r+ik_r$ is considered; enabling us to account for light absorption in the media [23]. The spheroid size parameter defined in (4.1) is not a measure of the spheroid size alone, but rather of the size times the eccentricity of the particle. Therefore, for non-spherical scatterers it is usual to adopt the volume-equivalent-sphere radius (R_{eq}) as the characteristic particle size [21, 47, 77].

4.3 Numerical limits and computational verification

The main computational challenge of the separation-of-variables approach is the accurate calculation of the spheroidal harmonics for large and complex C values. The method used here [1, 47, 55] is able to accurately determine the angular harmonics for any C, and for high number of orders N. However, the computation of the radial harmonics is limited by numerical cancelation and slow convergence. At present, there appears to be no method that is completely satisfactory for the calculation of these functions for large and complex C [79]. In this work the well-known Wronskian relation was used to check the correctness of the computed radial functions [80]. It was verified that the Wronskian relation is satisfied for absolute values of C below 60. For $|C|>60$ the results may not be accurate enough in some cases. Therefore, the present study is restricted to particles with $|C_i|<60$ in order to avoid possible computational errors associated with the radial functions.

The code used in the work presented in this chapter was extensively checked with known analytic and numerical solutions available in the literature. In the previous chapter the results obtained by our code are shown to match [47]:

- ✓ The electrostatic approximation (EA) for a particle size much smaller than λ
- ✓ Mie theory for a wavelength-sized sphere
- ✓ Far-field scattering patterns of wavelength-sized spheroids presented in [2].

In this chapter, further comparisons with Mie theory are given in Figure 4.3.

4.4 Portrait of physical parameters

The field distribution produced by a mesoscopic scatterer is dictated by interference phenomena, and can be understood by using a qualitative description like the one mentioned in Section 1.3. The scattering particle can conceptually be pictured as an array of dispersion points (or little regions much smaller than λ), for instance the atoms in a solid [76]. As the incident light beam propagates through the particle material, planes of points transverse to the beam are progressively illuminated in phase and scattered spherical waves radiate from every point. For each point in a plane radiating spherical waves there is another point in the same plane, separated by a distance of $\lambda/2$, that scatters in opposite phase; and the waves radiated from these two centers cancel in the transverse direction. Thus, in a particle with dimensions comparable or larger than λ almost no light is scattered laterally. However, these waves interfere constructively along the direction of propagation and add up to a larger wave inside the particle which propagates along the direction of the illuminating beam, and overlaps with it. When the total internal wave reaches the bottom surface of the particle part of its energy is transmitted to the external medium, and the other part is reflected back to the particle material interfering with itself and undergoing further reflections and refractions at the particle walls.

The transmitted waves in the external medium propagate along the forward direction and interfere with the waves scattered from the borders of the particle. If the particle has a circular cross-section relative to the incoming light (such as the spheroids considered in this work - see Figure 4.2) the path-length difference between the transmitted wave and the scattered waves coming from the circular perimeter of the particle can only lead to constructive interference at a region along the symmetry axis (z). This can originate jet-like "focal regions" of high electric field magnitude located close to the shadow-side surface of dielectric mesoscopic particles (DMPs) [8, 10, 12, 14, 15, 70, 72-74].

Figure 4.3 displays the total electric field ($\mathbf{E_t}$) intensity distribution produced by DMPs with the same size (R_{eq}=1.5λ) but distinct shape (b/a) and material (N_r). The total field inside the particle is equal to its internal field ($\mathbf{E_t}$=$\mathbf{E_i}$) and outside it is the sum of the scattered and incident fields ($\mathbf{E_t}$=$\mathbf{E_S}$+$\mathbf{E_0}$). A small imaginary part is considered in the

relative refractive index (k_r=0.01i) to account for light attenuation losses of realistic dielectric materials.

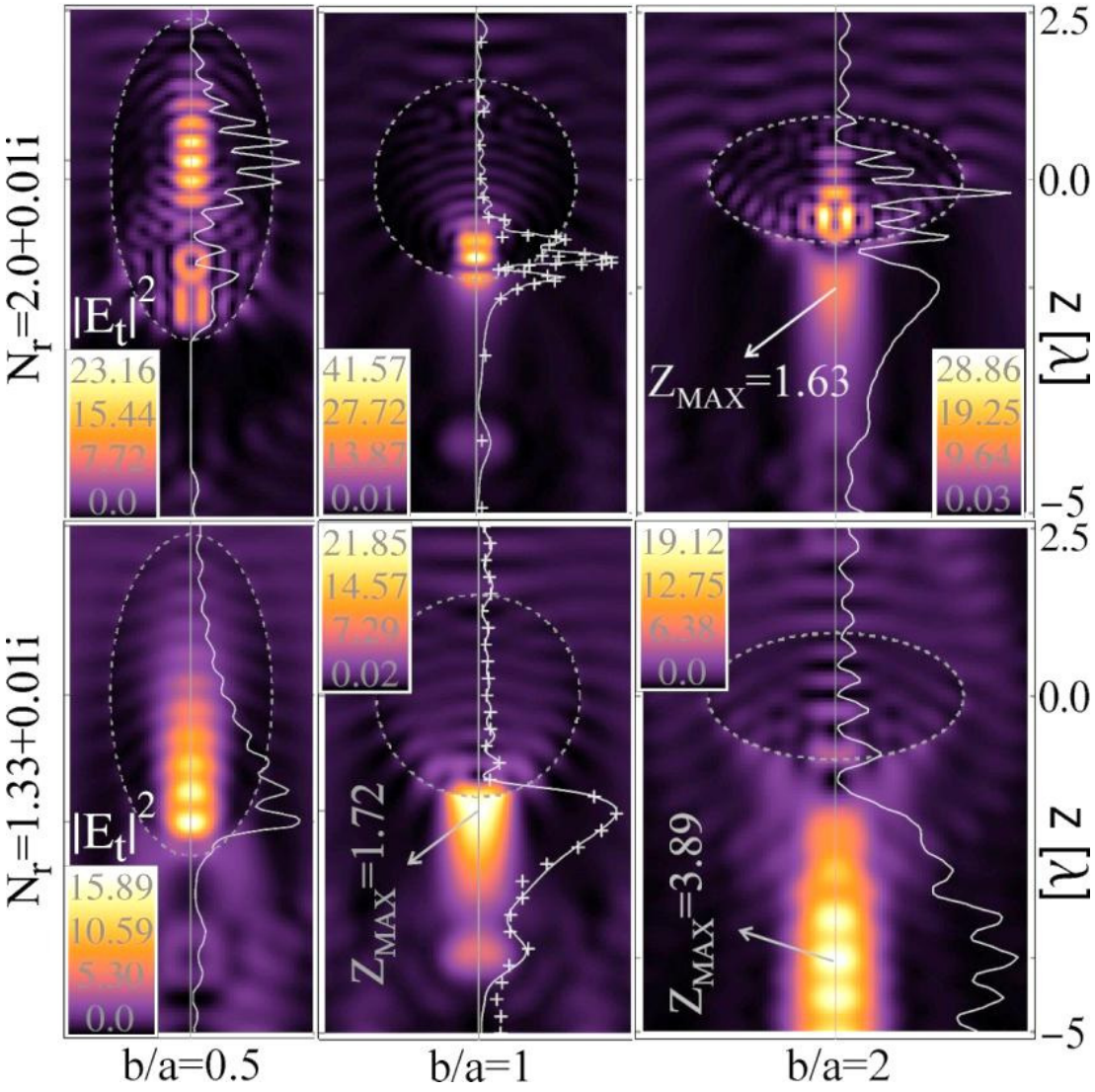

Figure 4.3: Total electric field intensity $|\mathbf{E_t}|^2$ distribution, in units of the incident field intensity $|\mathbf{E_0}|^2$, produced by DMPs (outlined with a gray dashed line) with the same size (R_{eq}=1.5λ) but distinct aspect ratio (b/a) and real part of the relative index (n_r). The length unit is λ. The field distributions were computed on a vertical cross-section through the center of the particle, coplanar with the yz plane defined by the incident wave ($\mathbf{K_0}$,$\mathbf{E_0}$). The solid curve on the right of each image corresponds to $|\mathbf{E_t}|^2$ along the vertical z axis. The fields in the central plots for spheres (b/a=1) were computed with Mie theory. For comparison, the cross dots in these plots correspond to the values obtained with our spheroidal separation-of-variables method considering spheroids with b/a=1.0001.

In the central plots of spheres (b/a=1) it can be seen that there is a good match between our spheroidal code and Mie theory. The bottom plots (N_r=1.33+0.01i) with b/a=0.5 and b/a=2 are similar to those in figures 13 and 14 of [15], respectively, which consider lossless materials (k_r=0) and slightly different R_{eq}.

The field patterns of Figure 4.3 present two main types of modes. The dominant mode outside the particle is the previously described transverse (**E**⊥**K**) wave that propagates in the forward $\mathbf{K_0}$ direction towards the far-field. This mode leads to intensity maxima that can be located inside or outside the particle but always on the z axis. The spot of maximum field ($|\mathbf{E_t}|_{MAX}$) outside the particle is called the focal point, located at a distance Z_{MAX} from the particle center (see Figure 4.2). An increase in Z_{MAX} leads to a broadening of the focal region, and to a general decrease in the scattered field intensities. This is observed in the central and right plots of Figure 4.3. The more the focus is separated from the particle surface the larger is its waist and width along the z axis (L_Z) [14, 73]. This occurs because the region of peak constructive interference outside the particle becomes less localized, thus resulting in a wider but less intense focus.

Besides the dominant transverse modes, longitudinal (**E**//**K**) modes are also observed close to the particle surface – the whispering gallery modes [22, 73, 75]. These modes originate from the total internal reflection of the light inside the particle, making it circulating around its curved surface and interfering with itself. This interference causes discrete peaks around the edge of the particle. The leakage of these peaks outside the particle walls originates longitudinal field maxima in the external medium which evanesce very rapidly ($1/r^3$) with distance (r) from the surface. The solutions obtained from Helmholtz equation do not allow the existence of these longitudinal fields on the vertical z axis, but that is not the case in other directions.

4.5 Lens-like focusing

Interference effects can lead to regions with significant light concentration in front of the particle; as in the sphere (b/a=1) and oblate (b/a=2) cases of Figure 4.3. A smaller volume of constructive interference implies a brighter focus since there is a higher density of electric energy. This resembles the focusing effect of a macroscopic biconvex lens. However, the characteristics (i.e. intensity, position, spatial extension) of such

focal spots are distinct from those predicted by geometrical optics (GO) [8, 10, 75]. The conventional GO focusing by a lens gives focal spots whose dimensions cannot be confined below the wavelength. With DMPs there is not an explicit focus; instead there is a jet-like tail of the scattered intensity along the forward direction which can have sub-wavelength dimensions [14, 17, 70, 72, 73]. In GO, the focal distance f of a biconvex lens much larger than λ is obtained with the lensmaker equation [33]:

$$f = \frac{n_r R_c^{\,2}}{2(n_r - 1)} \cdot \frac{1}{a + n_r(R_c - a)} \tag{4.2}$$

where R_c is the lens curvature radius, which is equal to b^2/a at the points on the symmetry axis ($z=\pm a$) of a spheroid. It was verified by [70, 75] that the values obtained with (4.2) only match Mie theory for spheres with radius $R>20\lambda$, and the lower is R the higher is the discrepancy. Hence, as expected, eq. (4.2) is not applicable in the mesoscopic size regime; but it can be useful in a qualitative way to elucidate the dependence of the focal distance with the particle parameters. It is straightforward to deduce from (4.2) that f decreases with n_r and increases with the spheroid aspect ratio (b/a). The same tendencies are observed (see Figure 4.3) relative to Z_{MAX} with mesoscopic spheroids [15]. However, the values of Z_{MAX} in the mesoscopic regime are lower than those of f resulting from (4.2). This GO lens equation therefore constitutes an upper limit which can be useful for a rough first-order prediction of a DMP focal distance [8, 10].

4.6 Application in photovoltaics

The focusing characteristics of the near-field produced by DMPs can be of interest for light management in a growing list of applications, as referred in Section 4.1. The authors are particularly interested in the implementation of arrays of optimally designed DMPs in photovoltaic (PV) devices [22, 42, 69]. The aim is to use such scatterers as "mesoscopic lenses" to improve absorption in the photo-active layers of solar cells. This would enable a reduction in the amount of expensive PV material, an improvement in the conditions for charge carrier collection and a raise in the efficiency by virtue of the concentrated energy density in the PV medium [81]. This is particularly suited for light

trapping and concentration in novel solar cell concepts using quantum dots (e.g. intermediate band solar cells [21, 38], hot carrier cells, all-silicon tandem cells, etc.). DMPs should allow a significant enhancement in the absorption of a single layer of dots within a broad sunlight wavelength range.

Depending on the particular cell architecture, different strategies can be used to position the DMP array in order to take most profit from its forward scattered light. The easiest and cheapest design for practical implementation is to place the particles on the top surface of the cell [22, 81]. However, a higher interaction (photocurrent generation) between the PV medium and the scatterers' near-field can be achieved by placing the particles inside the cell material [21, 67], for instance in the depletion region of the cell *p-n* junction. It is also possible to have several layers of DMP arrays positioned over distinct layers of a PV device, each array composed of particles designed to concentrate light the way that best suits each layer.

It is important to target the light focusing properties of these structures to the lower energy part of the solar spectrum, the infrared (IR); since the lower energy photons are harder to absorb by typical PV semiconductor materials. The higher energy photons of the visible (VIS) and ultraviolet (UV) range are easily absorbed in the first micrometers of the solar cell material, since their energy is sufficiently higher than the semiconductor bandgap. For these reasons, the complex refractive indices N_r considered in this chapter have values that are physically attainable by common dielectric/semiconductor materials in the IR range. In the optimization studies presented in the next section, the domain of the real part n_r was restricted between 1 and 4; and the imaginary part was taken to be k_r=0.01. Nevertheless, the main results are also given for a smaller k_r=0.001 to analyze the effect of lower light attenuation.

When accounting for absorption from the near-field, particular attention has to be paid to the polarization of the scattered light as discussed in Section 1.4. If the scattered electric field $\mathbf{E_S}$ is longitudinal, energy absorption from this field cannot be determined classically such as with far-fields which are transverse [38]. A longitudinal field is a localized Coulomb field, with no associated Poynting vector [6], that transmits electrostatic energy by means of scalar photons, as described by quantum electrodynamics [35]. This is especially important for particles with sizes much smaller than λ (electrostatic regime) whose peak $\mathbf{E_S}$ is longitudinally polarized [21]. However, as the particle size increases and becomes comparable or larger than λ, the transverse

component of the region of highest E_S becomes progressively more dominant relative to the longitudinal [47]. So, in the mesoscopic regime the scattered light outside the particle is mostly transverse, having the same polarization as the incident wave [17]. Hence, the classical formalism for light absorption in the far-field can be used here for the absorption produced in the medium located in the DMP near-field. The absorption enhancement due to scattering is therefore given by the ratio between the intensities of the total and incident field ($|\mathbf{E_t}|^2/|\mathbf{E_0}|^2$). This is the quantity represented in the field distributions displayed in this chapter.

PV applications also have to account for the unpolarized nature of the illuminating sunlight. The incident field $\mathbf{E_0}$ can take any orientation orthogonal to the propagation direction $\mathbf{K_0}$. Therefore, it is important to have a scatterer shape that allows a response independent of such orientations. That is the case of the spheroids considered here, whose symmetry axis is $\mathbf{K_0}$ (see Figure 4.2).

4.7 Results of optimization studies

A Nelder and Mead optimization algorithm was implemented in the analytical EM code described in Sections 3.3 and 4.2, enabling an iterative search for the spheroid parameters that allow a maximum in a certain function of the scattered field. The details of the algorithm are given in Appendix B. Three parameters are used as variables: the spheroid size (R_{eq}), aspect ratio (b/a) and real part of the relative refractive index (n_r). The imaginary part of the relative refractive index is kept fixed (k_r=0.01). Two particular functions were considered for optimization that maximize at quite distinct near-field patterns; thus providing a good illustration of the different ways in which DMPs can be used for light concentration. The results obtained for each function are given in the following Sections 4.7.1 and 4.7.2.

4.7.1 Optimization of local electric field intensity

The first function to be optimized is the maximum of the scattered field intensity ($|\mathbf{E_S}|^2/|\mathbf{E_0}|^2$) at any point in the external medium in front of the particle. Three particular cases are considered:

- Sphere (b/a=1), using R and n_r as variables

- Spheroid with n_r=1.33, using R_{eq} and b/a as variables
- General spheroid using R_{eq}, b/a and n_r as variables

The results obtained in each case are presented in the following sub-sections and summarized in Table 4.1. For the three cases the optimization converged to localized focal regions at the bottom surface of the particle in the z axis ($Z_{MAX}=a$). That is the spot where the focus can be more confined outside the particle; thus allowing the highest possible field magnitude in the external medium.

Table 4.1: Characteristics of the optimal spheroids that maximize the scattered field intensity. The values in green are the parameters that remained fixed. The optimizations were performed with a fixed k_r=0.01; however $|\mathbf{E_t}|^2_{MAX}$ is also given for the case of k_r=0.001 with the same spheroid parameters.

Optimization of Scattered Intensity	Optimal Parameters			$\|\mathbf{E_t}\|^2_{MAX}$ (at z=-a)		L_Z Focal Width[a]
	n_r	R_{eq}	b/a	$\boldsymbol{k_r}$**=0.01**	k_r=0.001	
Sphere	1.733	5.785	1.0	**92.06**	328.3	1.39λ
Spheroid with n_r=1.33	1.33	3.446	0.773	**46.79**	99.21	2.71λ
General spheroid	4.0	1.415	1.461	**110.7**	176.4	0.13λ

[a] width of the $|\mathbf{E_t}|^2$ peak along the z axis measured outside the particle (distance from the particle surface at z=-a to the end of the focus at the point where $|\mathbf{E_t}|^2=|\mathbf{E_t}|^2_{MAX}/e^2$).

4.7.1.1 Sphere case

We start by presenting the results for the maximization of the scattered intensity produced by spherical particles (b/a=1) with variable radius R and n_r. Since the geometry is spherical, the fields were computed with Mie theory to save computational time.

For a given R, the lower is n_r the higher is the distance of the focus to the particle center, as predicted by the lens eq. (4.2). The focus can therefore be located inside or outside the particle, depending on the value of n_r. As observed in [70, 75], the maximum field intensity outside the particle always occurs for the n_r index that sets the focal point right at the particle surface ($Z_{MAX}=R$). According to (4.2), for macroscopic spheres the value of n_r that sets $f=R$ is n_r=2.0. With mesoscopic spheres such n_r value is too high since it places the maximum intensity inside the particle [10, 70], as shown in

the central top plot of Figure 4.3. A smaller n_r=1.33 (see central bottom plot of Figure 4.3) is already too low because it sets the maximum E_t outside the particle separated from its surface. The optimal values of n_r that place the focus exactly at z=-R are plotted in Figure 4.4a (dashed line) for R ranging from 0.5λ to 10λ. The optimal n_r is around $\sqrt{3}$ within such mesoscopic sizes, and tends to 2.0 as the size approaches the macroscopic GO regime [10, 70].

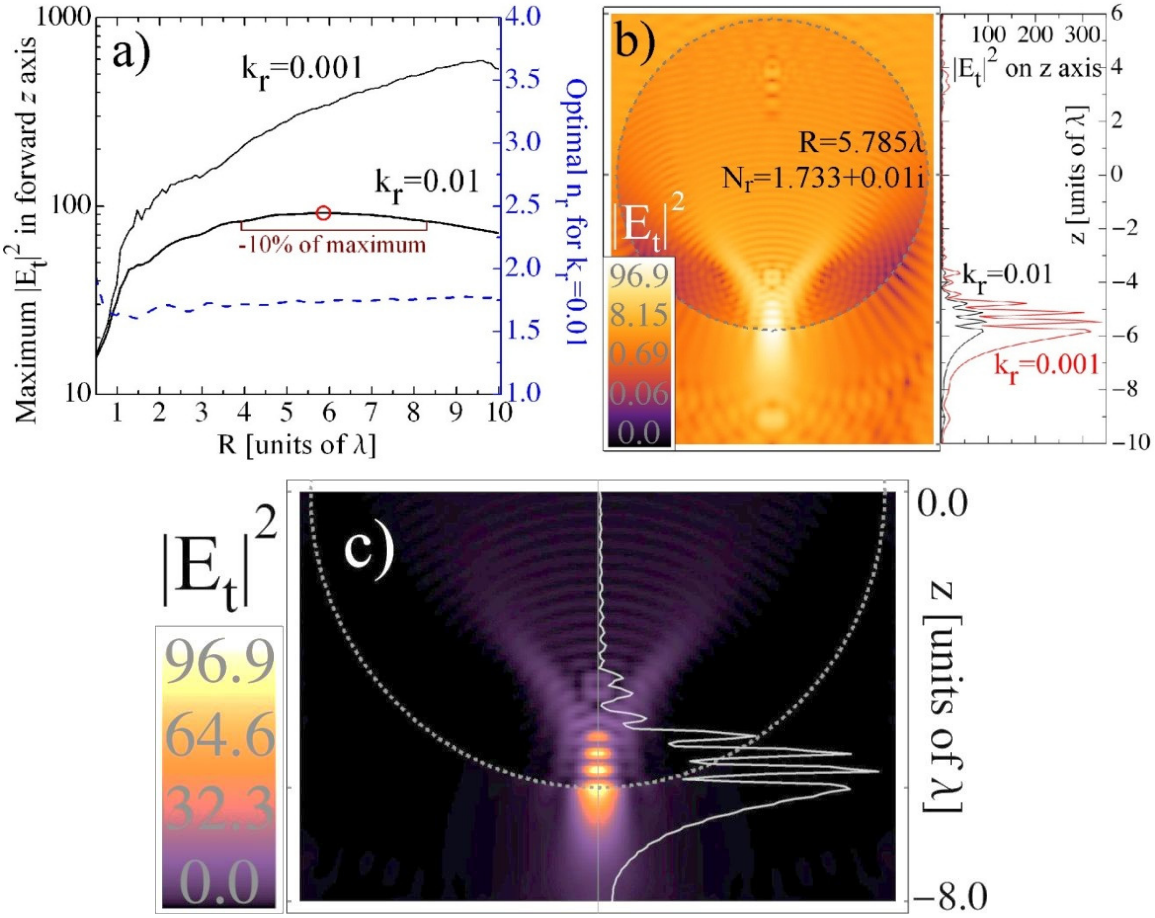

Figure 4.4: **a)** *Left axis* (black curves) - Maximum values of $|\mathbf{E_t}|^2$ (in units of $|\mathbf{E_0}|^2$) outside the particle, as a function of the sphere radius (R), for k_r=0.01 and k_r=0.001. The red circle is at the value obtained with the optimization algorithm considering k_r=0.01. The line segment beneath the circle marks the interval where $|\mathbf{E_t}|^2$ remains within a 10% difference from the maximum value. *Right axis* (blue curve) - Optimal n_r values computed with k_r=0.01. Similar values are obtained with k_r=0.001. **b)** *Left* - $|\mathbf{E_t}|^2$ distribution, in logarithmic scale, for the optimal sphere parameters (R,n_r) indicated in the plot. The distribution is computed on the same yz plane as those of Figure 4.3. *Right* - $|\mathbf{E_t}|^2$ along the z axis, in linear scale, for k_r=0.01 (black line) and k_r=0.001 (red). **c)** Zoom of the field distribution on the left plot of (b), but represented in linear scale. The gray line corresponds to $|\mathbf{E_t}|^2$ along the vertical z axis.

The field intensities at the focal point ($|\mathbf{E_t}|^2_{MAX}$) are shown in Figure 4.4a for k_r=0.01 and k_r=0.001 (solid lines) using the optimal n_r. The attenuation index k_r has a quite significant impact in the peak field magnitudes that can be obtained in these optimal cases. If absorption were neglected (k_r=0), the bigger the sphere size the stronger could be the focal point intensity. The effect of absorption opposes this tendency, because the bigger the particle the more energy is dissipated in its volume and thus the less energy is available for the focus. As shown in the solid curves of Figure 4.4a, for low sizes $|\mathbf{E_t}|^2_{MAX}$ increases with R. However, for sufficiently big R, the effect of absorption dominates over scattering and $|\mathbf{E_t}|^2_{MAX}$ starts decreasing with the size. The higher is k_r the lower is the optimal R value at which the maximum in the curves occurs. For k_r=0.01 such maximum is at R_{opt}=5.785λ which matches the result obtained with the optimization algorithm. The electric field intensity distribution of this case is plotted in Figure 4.4b. At the particle surface (z=-R) the intensity is $|\mathbf{E_t}|^2_{MAX}$=92.06, but with lower k_r=0.001 it is about 3.5 times higher ($|\mathbf{E_t}|^2_{MAX}$=328.3).

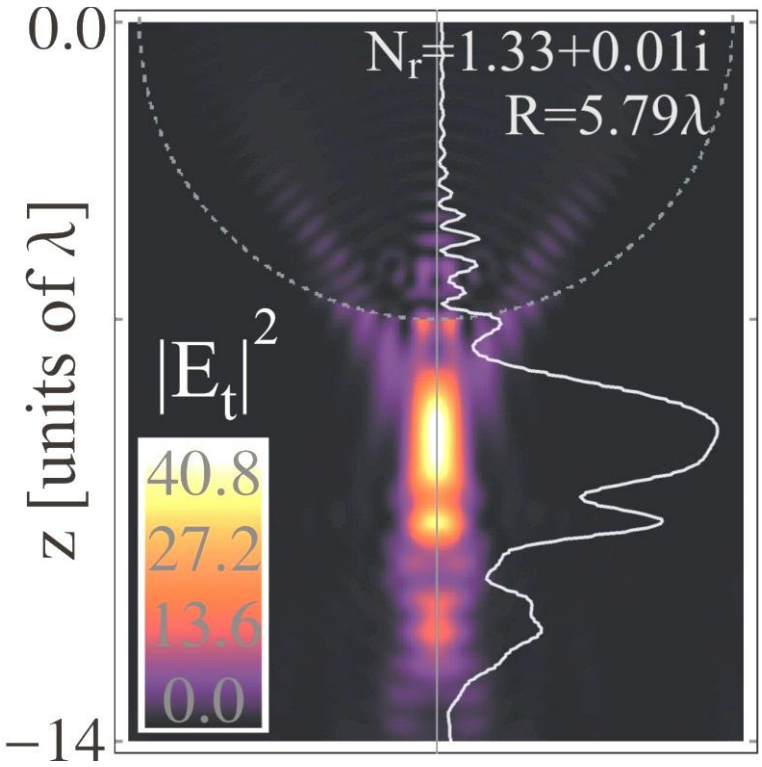

Figure 4.5: Same as Figure 4.4c but for a lower (non-optimal) refractive index N_r.

For comparison, in Figure 4.5 it is shown the field distribution produced by a sphere with $R=R_{opt}$ but a refractive index (N_r=1.33+0.01i) lower than the optimal. It can be seen that a lower N_r spreads the focal region and moves it away from the particle bottom surface. The spreading of the focus results in lower maximum field intensities in the external medium.

A DMP fabricated with the optimal parameters of Figure 4.4b would produce a focal intensity above $0.9|\mathbf{E_t}|^2_{MAX}$ for any wavelength within $\lambda \pm 0.3\lambda$. This broad frequency width is due to the fact that the k_r=0.01 curve in Figure 4.4a is rather flat around R_{opt} (as marked by the line segment beneath the curve), and n_r remains approximately constant in that interval.

4.7.1.2 Spheroid with n_r=1.33

A relative refractive index of 1.33 is often adopted in theoretical studies of particle scattering [1, 2, 14, 15, 23, 77, 78]. This is the refractive index of water in air, but can also match other possible particle/medium material combinations. For instance, a germanium particle in a gallium arsenide or silicon medium corresponds to a relative index close to that value in the infrared, which can be interesting for PV applications. In this case there is a small imaginary part in the refractive index on the order of k_r=0.01i, as considered in the calculations presented in this chapter.

In this sub-section we present the optimization of the scattered intensity produced by spheroidal particles with a fixed refractive index (N_r=1.33+0.01i) but tunable size (R_{eq}) and aspect ratio (b/a). The optimal geometry is plotted in Figure 4.6. The maximum field intensity ($|\mathbf{E_t}|^2_{MAX}$=46.8) occurs at the bottom point of the particle (z=-a), such as in the previous sphere case. With lower attenuation (k_r=0.001) the maximum field at that spot increases to about twice this value ($|\mathbf{E_t}|^2$=99.2), as shown in the right plot of Figure 4.6.

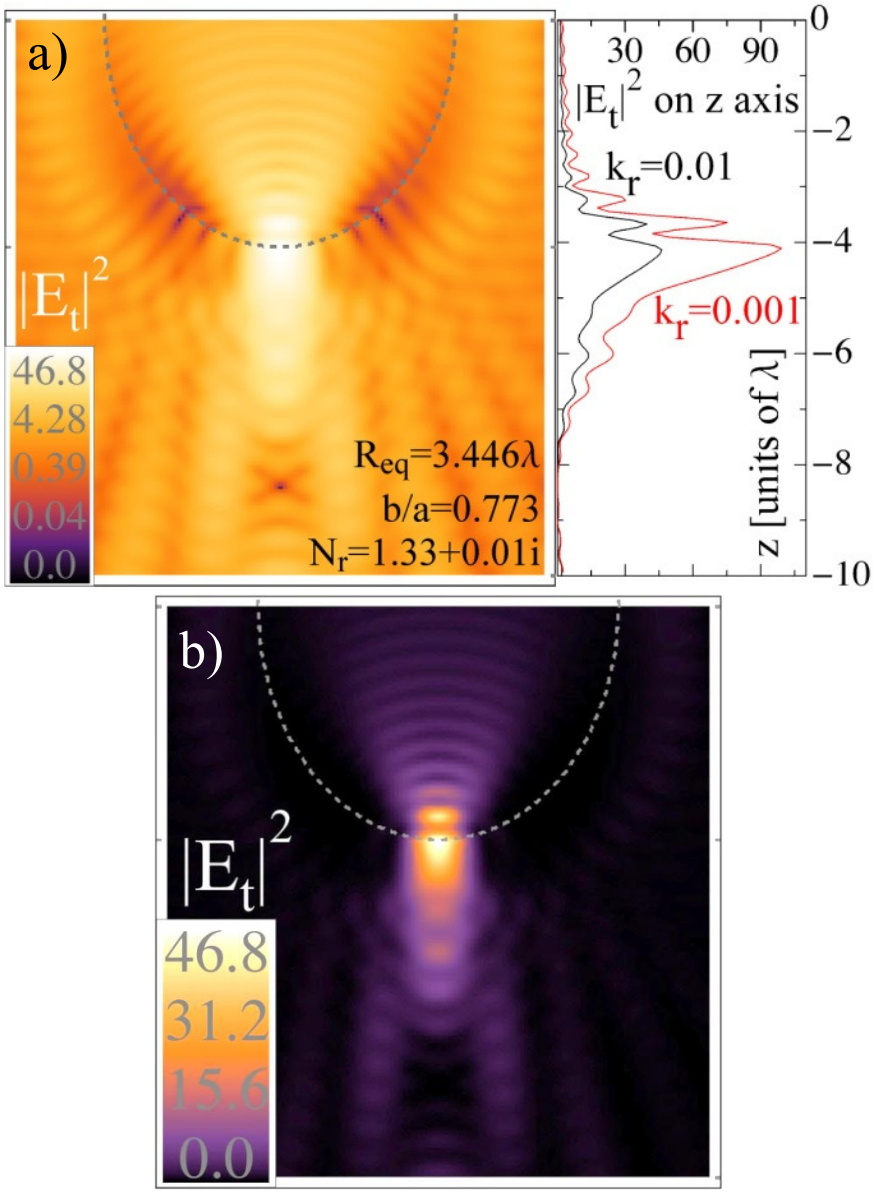

Figure 4.6: **a)** Same as Figure 4.4b but for the optimal spheroid geometry with a fixed n_r=1.33 and variable R_{eq} and b/a. The dimensions of the spheroid semi-axes are: a=4.093λ and b=3.162λ. **b)** Same as (a) but represented in linear scale.

The optimization converged to a prolate geometry since only with b/a<1 could the focus be positioned at the particle surface given such low n_r. If the shape were spherical or oblate the focal region would be located away from the surface (see bottom plots of Figure 4.3) exhibiting higher length but lower peak intensity. For comparison, the maximum intensity produced by a sphere with the same R_{eq} and N_r as the prolate of Figure 4.6 is $|\mathbf{E_t}|^2$=33.9 at Z_{MAX}=4.29λ.

4.7.1.3 General spheroidal case

The optimization is now extended to the general case of a spheroidal particle with variable size (R_{eq}), aspect ratio (b/a) and real part of the relative index (n_r). The domain of variation of n_r was restricted to $n_r \leq 4.0$, since most pure or compound dielectric materials have refractive indices lower than such limit at low optical frequencies, as referred in Section 4.6. The imaginary part of N_r is kept fixed (k_r=0.01).

As in the previous cases, the optimization converges to spheroid parameters that locate the focal spot at the particle bottom surface (z=-a). In addition, the search moves towards the highest allowed n_r value (n_r=4.0). A higher n_r increases the optical interference inside the spheroid, since the internal light waves have smaller wavelength and suffer more refraction and reflection with the particle walls. The combination of these effects raises the intensities associated with the concentrated field at the spots of constructive interference [11, 20].

Increasing n_r also shifts the maximum field intensity towards the particle interior. Therefore, usually DMPs with big n_r exhibit high internal fields but small scattered intensities in the external medium. This is, for instance, the case of spheres with any n_r above the optimal values given in Figure 4.4a. Nevertheless, with spheroids there is an additional degree of freedom, the aspect ratio, which enables to keep the focus outside the particle while still using a high refractive index. This constitutes one of the main advantages of spheroids for near-field light concentration, and a key point of this chapter. As displayed in Figure 4.3, the effect of the aspect ratio on the location of the focal spot is opposite to the effect of n_r. Thus, the focus can be kept at the bottom point of the particle (Z_{MAX}=a) if b/a is increased together with n_r. This possibility allows the achievement of near-field intensities of more than two orders of magnitude (relative to the incident intensity) and with spheroid sizes lower than those of Sections 4.7.1.1 and 4.7.1.2.

In the present case, the optimization converged to an oblate (b/a>1) shape, since otherwise the maximum $|\mathbf{E_t}|^2$ would be inside the particle for such high n_r=4.0. The corresponding field pattern is given in Figure 4.7. As shown in the right plot, the curve corresponding to k_r=0.001 has a maximum $|\mathbf{E_t}|^2$=176.4, which is 1.6 times higher than the peak value of k_r=0.01. The ratio between the values of $|\mathbf{E_t}|^2_{MAX}$ for k_r=0.001 and k_r=0.01 is lower in this case than in the previous cases of Figure 4.4b and Figure 4.6 (see Table 4.1). This is due to the fact that a smaller spheroid size reduces the effect of

light absorption by the particle material. For the same reason, the ratio between the $|\mathbf{E_t}|^2_{MAX}$ in Figure 4.6 is smaller than that in Figure 4.4b.

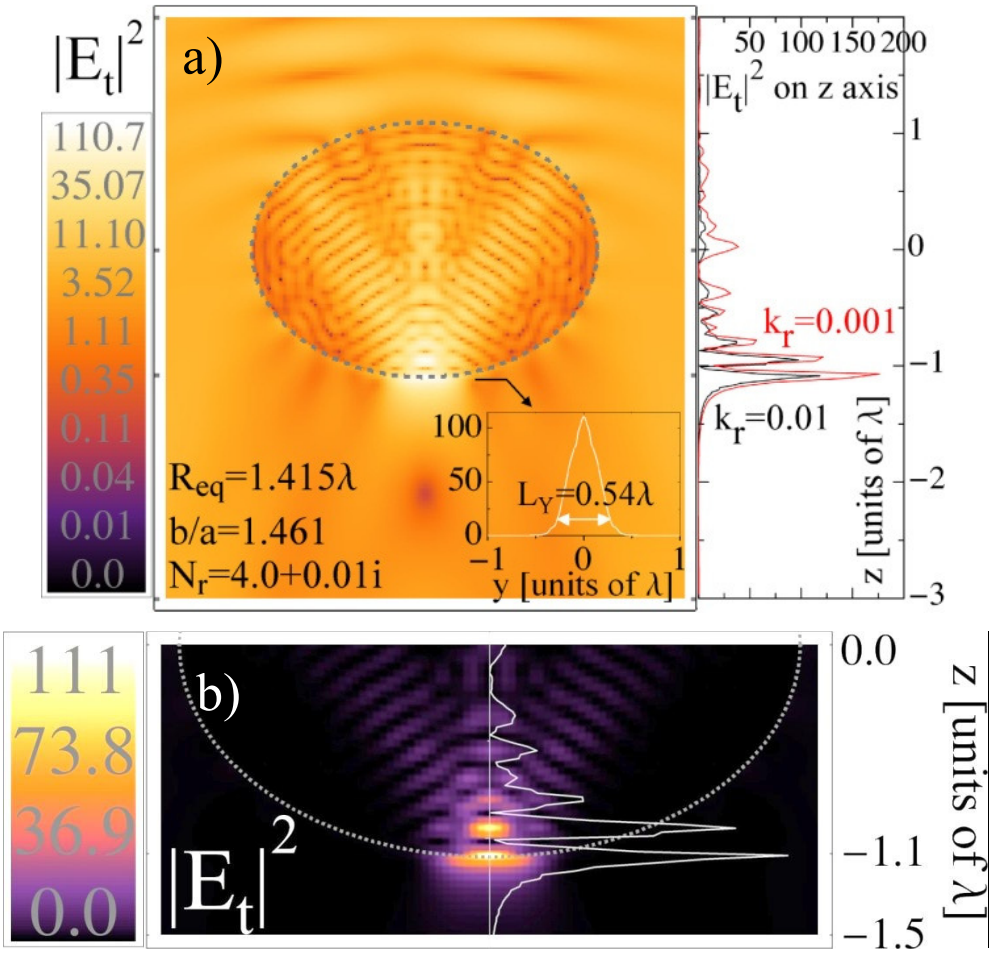

Figure 4.7: **a)** Same as Figure 4.4b but for the optimal spheroid parameters obtained with tunable R_{eq}, b/a and n_r. The dimensions of the spheroid semi-axes are: a=1.099λ and b=1.605λ. The bottom inset shows the peak $|\mathbf{E_t}|^2$ along y at the bottom of the particle (z=-a). L_Y is the peak full width at $|\mathbf{E_t}|^2_{MAX}/e^2$. **b)** Zoom of the field distribution in (a), but represented in linear scale. The gray line corresponds to $|\mathbf{E_t}|^2$ along the vertical z axis.

The pronounced interference caused by this high n_r=4.0 results in a more confined focal spot than that of the field distributions in Figure 4.4b and Figure 4.6 (see L_Z values in Table 4.1). The focal peak is extremely localized in this case, having sub-wavelength dimensions both in the z (L_Z=0.13λ) and y (L_Y=0.54λ - see inset in Figure 4.7) directions. Spherical DMPs can also produce external focal regions that are sub-wavelength confined in the transverse xy directions, but not along the forward z axis when illuminated by a plane-wave [10, 70, 71, 73, 74]. With oblate DMPs having a high

n_r it is possible to achieve sub-wavelength confinement with plane-wave illumination both in the transverse and forward directions.

4.7.2 Optimization of electric intensity over near-field region

A second class of optimizations was performed to find the spheroid parameters that maximize the integral of the scattered intensity over the near-field region in front of the particle. The aim here is not to achieve a high field magnitude at a certain point, like in the previous cases, but rather to find the highest possible scattered field distribution with a broad focal region in front of the particle. This can be of interest for applications, such as PV, that can benefit from a wide region of light concentration extending throughout the volume of a nearby absorbing medium. The near-field zone around a scatterer with size close to λ extends up to a distance on the order of 10λ. Therefore, the function to be optimized (P) integrates the scattered intensity, normalized by $|\mathbf{E_0}|^2$, along a semi-circular region in front of the particle, in the *yz* plane, of radius $R_M=10\lambda$:

$$P(R_{eq}, b/a, n_r) = \frac{1}{\pi ab} \iint \frac{|E_S|^2}{|E_0|^2} f(\eta,\xi) d\eta d\xi \tag{4.3}$$

Here η and ξ are the spheroidal angular and radial coordinates, respectively; and the factor $f(\eta,\xi)d\eta d\xi$ is the area element in spheroidal coordinates. The region of integration is outlined by the dashed semi-circle in Figure 4.2. The radius of this region (R_M) is on the order of the thickness of the main photocurrent generation zone in most solar cell designs, considering $\lambda \approx 1\mu$m (near-IR). As such, function P is an example of an optimization function suited to find the best spheroid parameters for implementation in PV devices. DMPs can be incorporated either on the surface of solar cells or embedded in their PV material, depending on the cell architecture and the preferred relative refractive index. In any case, the particles size should be as small as possible since their material always constitutes a disturbance in the PV medium which only serves for optical concentration purposes but cannot contribute (and most of the times deteriorates) to the current generation. If DMPs designed to focus IR light are placed on top of a cell the bigger their size the more significant becomes their attenuation of the lower wavelengths (VIS and UV), reducing the cell response to the higher energy part

of the solar spectrum. This issue can be avoided if DMPs are placed inside the PV material. Nevertheless, in such case the bigger the DMP size the more volume of PV medium is occupied and the higher is the charge carrier trapping that may occur at the particle-medium interface.

In view of the above, the area integral in (4.3) is normalized by the *yz* area of the particle (πab), in order to beneficiate smaller sizes (R_{eq}) in the optimization procedure.

In the following sub-sections we present the results obtained with the optimization of (4.3) considering the same 3 cases (sphere, spheroid with n_r=1.33 and general spheroid) of Section 4.7.1. The main results are summarized in Table 4.2.

Table 4.2: Characteristics of the optimal spheroidal parameters that maximize function P. The values in green correspond to the parameters that remained fixed. The optimizations were performed with a fixed k_r=0.01.

Optimization of Function P	Optimal Parameters			P_{MAX}	$(\pi ab)P_{MAX}$	L_Z Focal Width[a]
	n_r	R_{eq}	b/a			
Sphere	1.287	1.195	1.0	**15.35**	68.86	2.19λ
Spheroid with n_r=1.33	1.33	1.642	3.380	**36.28**	204.7	7.71λ
General spheroid	4.0	0.741	28.75	**278.8**	157.1	8.04λ

[a] Width of the focal peak along the *z* axis (see Figure 4.2).

4.7.2.1 Sphere case

As in Subsection 4.7.1.1, the calculations for spherical particles were performed with Mie theory for faster computation. In this case the aspect ratio is fixed (b/a=1), so the quantity P [eq. (4.3)] becomes a function of only two parameters: R and n_r. As before, the imaginary part of the refractive index is kept fixed (k_r=0.01).

The two parameters can be viewed as the coordinates of a bi-dimensional space in which P(R,n_r) is to be maximized. Figure 4.8a shows the values of P for every (R,n_r) point within the search domain of the optimization algorithm. There are several local maxima in the function whose intensity becomes progressively lower with increasing R and n_r. The decrease of P with R is mainly due to the normalization factor $(\pi ab)^{-1}$ multiplying the integral in (4.3). As previously referred, our aim here is to find the scatterer parameters that achieve the highest possible electric field integral with a particle that occupies the least possible volume; as an exercise for possible PV

applications. Nevertheless, the values of the integral alone ($\pi ab P_{MAX}$) are also given in Table 4.2 for the optimal parameters. The P peaks decrease with n_r because the focal region moves towards the particle interior, thus reducing the scattered intensity in the external medium in front.

The global P maximum obtained with the optimization is marked by a white circle in Figure 4.8a. This peak is rather flat along the R axis close to the optimal value $R_{opt}=1.2\lambda$, as in the curve of $k_r=0.01$ in Figure 4.4a. Therefore, a sphere fabricated with the optimal parameters produces a P value above $0.9P_{MAX}$ at any wavelength within $\lambda\pm0.2\lambda$.

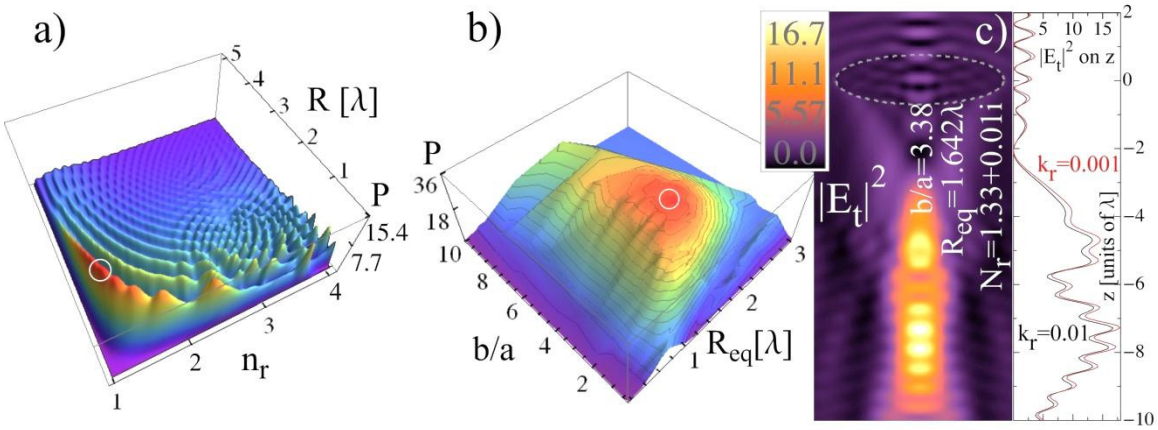

Figure 4.8: **a)** 3D plot of the optimization function P(R,n_r) for spheres. The white circle is at the spot of maximum P obtained with the optimization algorithm. **b)** Same as (a) but for the optimization of spheroids with fixed n_r=1.33 and tunable R_{eq} and b/a. **c)** $|\mathbf{E_t}|^2$ distribution, in linear scale, corresponding to the optimum spheroid parameters indicated by the white circle in (b). The spheroid semi-axes are: a=0.729λ and b=2.464λ.

4.7.2.2 Spheroid with n_r=1.33

The present case with a low relative refractive index N_r=1.33+0.01i can be interesting for applications that would benefit from a small material contrast between scatterer and surrounding medium. That is the case of PV applications in which the particles are embedded inside the PV medium. In that situation the lower is N_r the less charge carrier trapping and recombination can occur at the particle surface.

Figure 4.8b represents the function P(R_{eq},b/a), of the present optimization, in a region around its maximum value obtained with the optimization algorithm. Function P decreases with R_{eq} due to the normalization of the integral in (4.3) by the spheroid area.

The aspect ratio (*b/a*) shifts the position and spatial extension of the focal region. High aspect ratios not only reduce the overall scattered intensities but can also place the jet-like focus too far in *z*, outside the integration region limited by the dashed line in Figure 4.2. If *b/a* is too small the focus moves close to the particle and becomes more spatially confined; which may produce higher peak intensities at the focal spot (such as in Figure 4.6) but a lower value of the integral of E_S over the chosen semi-circular region.

The maximum P occurs for the field distribution displayed in Figure 4.8c. The R_{eq} width of the peak P in Figure 4.8b, within -10% of the maximum, allows a wavelength variation of $\lambda \pm 0.21\lambda$; which is close to that reported in the previous subsection. It can be seen in the right plot of Figure 4.8c that there is a quite small difference between the $|\mathbf{E_t}|^2$ profile of k_r=0.01 and k_r=0.001, as compared with the previous case of Section 4.7.1.2.

4.7.2.3 General spheroidal case

The optimization of P considering the variation of all 3 parameters (R_{eq},*b/a*,n_r) achieves a value (P_{MAX}=278.8) considerably higher than the previous two cases, as indicated in Table 4.2.

As in Section 4.7.1.3, the algorithm converges to the highest allowed refractive index (n_r=4.0) since the higher is n_r the higher can be the scattered field outside the particle. However, the increase of n_r has to be accompanied by an increase in *b/a* or else the focal region moves too close to the particle (or even to its interior) and loses its extension over the near-field region in front. Keeping the highest possible n_r=4.0 and large *b/a*, the algorithm converges to small particle sizes ($R_{eq}<\lambda$) in order to achieve a high value of the integral in (4.3) with a low value of the spheroid *yz* area (πab) in the denominator.

The spheroid parameters that allow a maximum in P(R_{eq},*b/a*,n_r) produce the field distribution shown in Figure 4.9. An oblate with such extreme elongation presents a long forward scattering lobe; quite distinct from the point focus obtained with the moderately elongated oblate in Figure 4.7. It can be seen in the right plot of Figure 4.9 that there is almost no difference between the field intensities with k_r=0.01 and k_r=0.001, due to the small particle size.

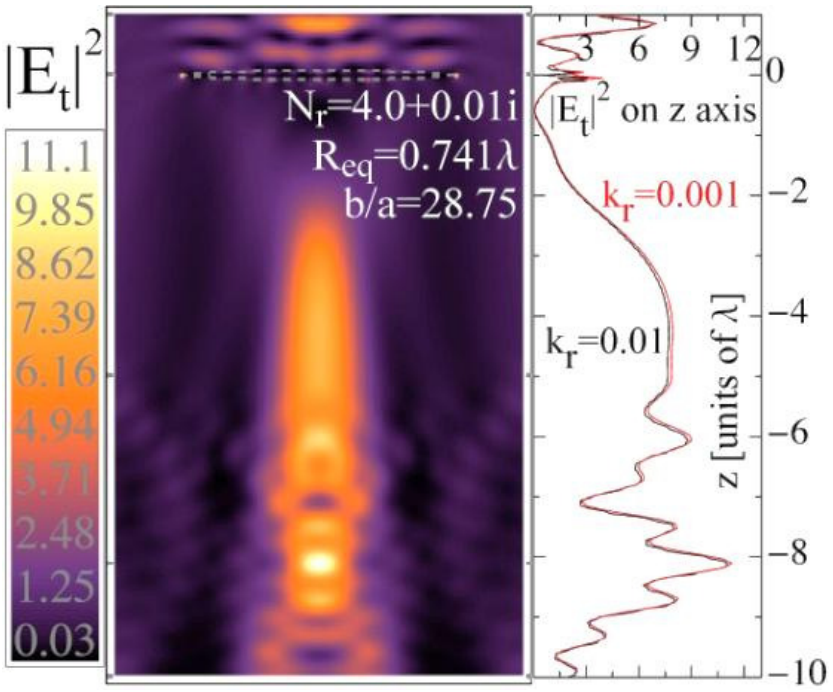

Figure 4.9: *Left* - $|\mathbf{E_t}|^2$ distribution for the optimal parameters that maximize function P(R_{eq},b/a,n_r). The spheroid semi-axes are: a=0.079λ and b=2.271λ. *Right* - $|\mathbf{E_t}|^2$ profiles along the z axis for k_r=0.01 (black line) and k_r=0.001 (red).

Even higher P values could be achieved with higher values of the size parameter C_i. As referred in Section 4.3, the maximum allowed value of $|C_i|$ was limited to 60 in order to avoid inaccuracies in the calculation of the radial spheroidal harmonics.

4.8 Conclusions

The relation between the geometry and material of a spheroidal scatterer and its resulting field distribution may be very complex; especially in the mesoscopic regime where it can only be analytically determined by fully solving Maxwell's equations using the boundary conditions of continuity across the particle surface. This can be accomplished by the spheroidal coordinate separation-of-variables method used here, described in Section 4.2 and further detailed in Section 3.3 [1, 47].

The results of this chapter illustrate the capabilities of spheroidal DMPs for use as "mesoscopic lenses" in PV or in several other applications (listed in Section 4.1). For the first time, an optimization algorithm was coupled to the analytical EM code to iteratively search for the scatterer parameters that allow the maximization of a certain function of the scattered field [48]. Two different quantities were considered for

optimization: 1) the value of the scattered intensity at any point outside the particle (Section 4.7.1); 2) the integral of the scattered intensity over a semi-circular region in front of the particle of radius 10λ (Section 4.7.2). These two particular functions chosen here converge to quite distinct near-field distributions.

With the first function, the maximum intensity in the external medium is achieved by placing the focus right at the point of intersection between the particle surface and the *z* axis. The higher n_r the more intense and confined can the focus be. However, the particle oblateness has to increase with n_r or else the light would be focused in the interior of the particle. An optimal adjust of *b/a* and n_r can lead to electric field intensities at the particle surface of more than 2 orders of magnitude higher than the incident intensity, with a particle size close to λ (see Figure 4.7). Such pronounced intensities are achieved due to a sub-wavelength confinement of the focal peak in all directions, which is possible in plane-wave illumination with an oblate geometry and high n_r. This is one of the main advantages of going beyond the simple spherical geometry with the use of spheroidal DMPs; and can be interesting for applications with localized absorbing centers, such as quantum-dot solar cells [21].

The second function converges to wide focal regions extending several λ along the *z* axis. The electric intensities are not as high as in the previous case, since the energy is distributed in a bigger volume of the external medium. This situation can be advantageous for certain applications that benefit from an extended region of field enhancement covering a broad portion of the surrounding absorbing medium, such as thin-film [42] or nano-rod/wire solar cells [82].

Pronounced near-field light amplification can also be achieved in the electrostatic regime using the surface plasmon (SP) resonance of metallic nanoparticles (MNPs) much smaller than λ [21, 42, 68, 81]. As shown here, the electric intensity enhancement that can be obtained with mesoscopic spheroids is as high as that predicted at the surface of MNPs sustaining SPs ($\sim 100E_0^2$) in the infrared (see Section 2.3). Nevertheless, DMPs may be more suited for certain applications, such as PV, due to the following additional advantages [47]:

- First, since they are composed of dielectric material their inclusion in the interior of the photo-active medium of a solar cell should cause less current degradation

(due to charge carrier recombination at the particle surface) than MNPs [22, 81]. Dielectric materials are, in this sense, more *PV-friendly* than metals.

- Secondly, the scattering pattern produced by MNPs has a single dipolar (first-order) mode. DMPs excite additional higher-order modes thereby allowing very distinct near-field profiles which can be adapted to different structures of the device absorber. The intensity, spatial extension and position of the peak field intensity can be adjusted by tuning the particle parameters, as explained in this chapter.

- Thirdly, besides higher spatial extension there is also a higher frequency extension of the electric field peaks produced by DMPs. The SP resonance produces sharp intensity peaks having a HWHM of about 0.05λ. With DMPs the peaks can be broader in wavelength; the examples analysed here have half widths of 0.2-0.3λ relative to only −10% of the maximum. This comparison is illustrated in Figure 4.10 for the particular case of a peak field intensity located at λ=1μm.

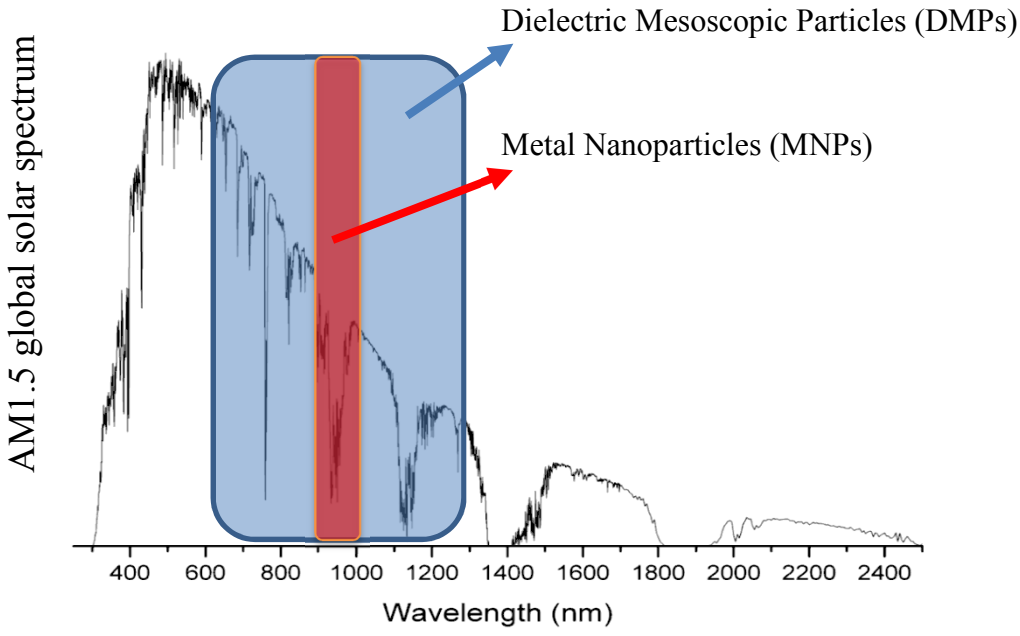

Figure 4.10: Schematic comparison between the spectral widths of the peak field enhancement produced by MNPs and DMPs optimally shaped for the case of λ=1μm. With DMPs, the spectral width of the peak intensity achieved can cover the wavelength interval represented in blue. This spectral width is much bigger

than that achieved at the sharp plasmonic resonance of MNPs (represented in red). This constitutes a crucial advantage of DMPs, relative to MNPs, for PV applications.

Nevertheless, there are also a few drawbacks that can limit the application of DMPs in practical devices. One of the disadvantages is that the precise conditions (size, shape and material) that allow DMPs to perform optimally as light concentrators may be hard to fabricate. There are also challenges related with the construction of an array of spheroidal particles on a device material. Due to the aspherical shape of the particles, colloidal deposition techniques such as spin or dip-coating may not be feasible since it is hard to control the orientation of the particles upon deposition. Possible mass-production alternatives are litographical techniques for large-scale patterning, such as hole-mask colloidal litography (HCL) [83] or hollographic litography (HL) [84]. However, perhaps the main disadvantage is the complexity of the calculations required to model their optical response; requiring considerable computational time and resources. That is the reason why the mesoscopic size regime hasn't been much explored beyond Mie theory studies limited to spherical geometries. This introduces challenges to new optical approximations [10, 64, 77, 85] and motivates the development of more efficient numerical models to improve the speed and accuracy of the computed EM solutions [1, 47, 51].

Chapter 5

Colloidal metal nanoparticles in photovoltaic materials

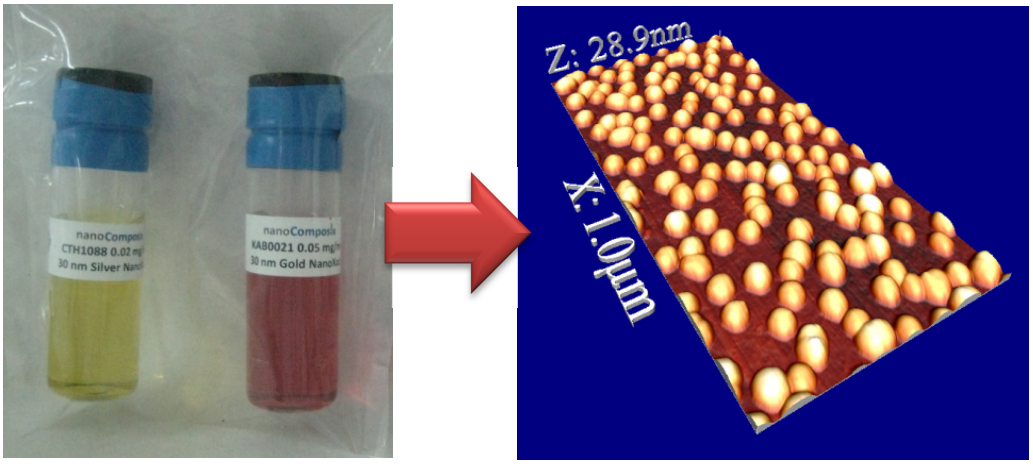

5.1 Introduction

The main focus of the work developed in this PhD thesis was the computational studies described in the previous chapters. However, in the course of such work, we have also devoted some time developing experimental procedures to manufacture plasmonic light-trapping structures in solar cells, such as those theoretically studied in Chapter 2.

In the IBSC design proposed in Chapter 2, a plasmonic light-trapping near-field structure, composed of an array of metal nanoparticles (MNPs), is incorporated in the QDs volume. The MNPs are embedded inside the active region of the solar cell and positioned side-by-side with the quantum dots (QDs). This is sketched in Figure 2.2c and in Figure 5.1 below. Each MNP acts as an optical antenna, bringing the incident energy from its surroundings and focusing that energy in their localized near-field. This allows a pronounced concentration of light in the dots volume relative to the usual case where no MNPs are present (such as in conventional QD-IBSCs shown in Figure 1.1a,b).

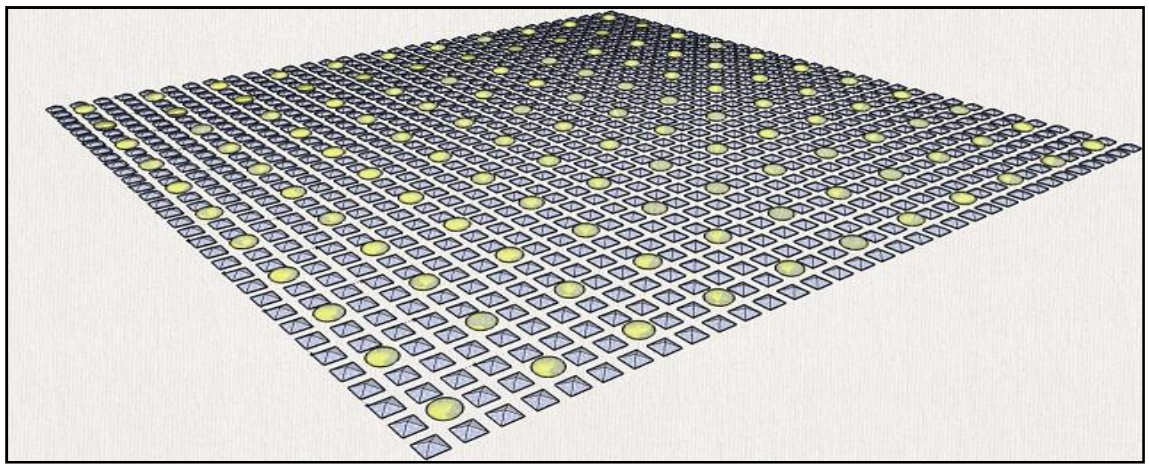

Figure 5.1: Sketch of a binary array of MNPs (yellowish spheroids) and QDs (gray pyramids). As described in Chapter 2, the highest scattered field occurs in a vicinity of the MNPs surface, along their equator plane orthogonal to the light propagation direction. Therefore, the QDs should be located in between the MNPs, in such a way that each QD is positioned close to a MNP surface.

Plasmonic light-trapping structures exploit the light concentration effects produced by the high electric field scattered by MNPs sustaining surface plasmons (SPs) [42].

Nowadays there has been an increasing interest in introducing plasmonic structures in photovoltaic devices such as thin-film [86], silicon [87, 88] or organic [89] solar cells. Mainly due to fabrication difficulties, most of these experimental approaches place the MNPs on top or in the bottom of the cell. In these approaches the internal photo-active layers of the cell are only illuminated by the far-field that is scattered by the MNPs, but cannot "feel" their strong near-field since it is significant only up to a very small distance (of about the particle size) from the particle surface. It has been theoretically and experimentally observed that in these configurations the effect of the MNPs is similar to that of an anti-reflection coating (ARC) or a rear mirror layer. So, a better choice is just to use such conventional layers instead of the MNPs, since the MNPs always exhibit more dissipation (light absorption) at energies away from their plasmonic frequency [90, 91]. In other words, the easiness of the application of MNPs on the top or bottom surface of the cell does not make a case for their use in this configuration.

According to the authors, the implementation of MNP arrays in solar cells can only be significantly profitable if they are embedded in the photo-active region of the cell [67, 92]. The reason being that only in this configuration it is possible to exploit the intense near-field light produced in the MNPs' vicinity. In our work we are particularly interested in exploiting such near-field to concentrate the light in the QDs at the appropriate photon energies of the IBSCs transitions. To do so, the first task is to study the best procedure to embed the MNPs in the host semiconductor material of the IBSCs. This is the main goal of the experimental efforts reported in this chapter, aimed at developing efficient methods for the fabrication and embedment of MNPs in semiconductor materials. This can be realized in practice by spreading the MNPs onto the surface of a certain semiconductor wafer/film and then growing a capping layer on top of the MNPs of the same material as the wafer/film, as illustrated in Figure 5.2.

The embedment of MNPs in semiconductor media is still a rather unexplored topic in the literature. So, the work presented in this chapter not only contributes to fill this gap, but also constitutes the first steps towards the incorporation of MNPs in QD-IBSCs. The knowledge gained in overcoming the experimental challenges faced in this work can be of interest to the incorporation of MNPs not only in typical semiconductor materials used for solar cells (*e.g.* Si, a-Si, GaAs), but also in other materials for distinct applications.

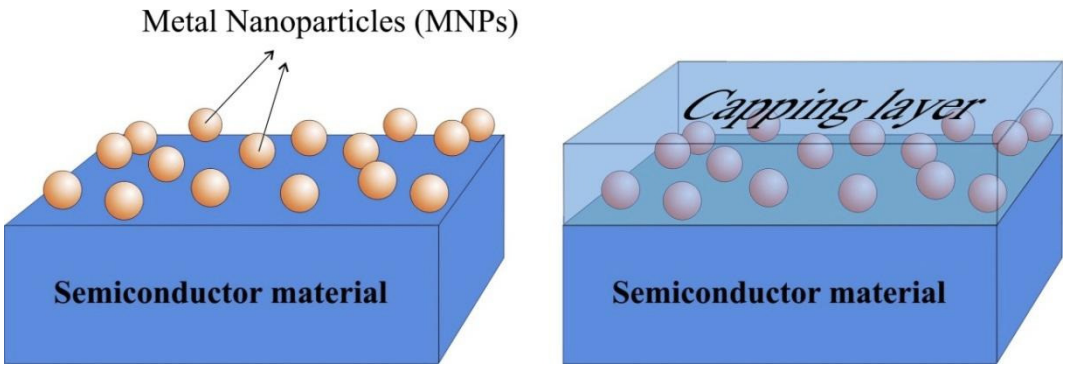

Figure 5.2: **Left** – Colloidal MNPs deposited on the surface of a semiconductor material (for instance, a Si or GaAs wafer or an amorphous thin-film supported on a glass substrate). **Right** – A capping layer, of the same semiconductor material, is grown on top to immerse the MNPs in the photovoltaic medium.

In all experiments we used spherical metal nanoparticles synthesized in colloidal solution, as described in the following Section 5.2. The first task of our experimental work consisted in developing a colloidal deposition technique able to pattern MNPs dispersed in solution onto the surface of semiconductor wafers of different materials. The deposition conditions were optimized to achieve a uniform bi-dimensional array of individual MNPs all over the wafers' surface, as explained in Section 5.3 and further detailed in Appendix C. The deposited MNPs were then submitted to a series of thermal and chemical tests to study their "resistance" to the conditions required for the growth of a capping layer on top by standard deposition methods, as detailed in Section 5.4 and in Appendix C. Such capping layer was deposited in our laboratory using radio-frequency (RF) magnetron sputtering, as described in Section 5.5.

The SP frequency of MNPs is dependent on their size, shape, material and surrounding dielectric environment. This frequency can be experimentally determined by analyzing the maximum in the absorption spectra of samples containing the MNPs array, as shown in Section 5.6. Such spectra can be analytically modeled by calculating the extinction efficiency of individual MNPs. In Section 5.6 the extinction efficiency of spherical MNPs, embedded in different media, is computed using an exact analytical solution known as Mie theory. The computed results allow us to predict the optical response of embedded arrays of MNPs fabricated in practice.

5.2 Fabrication of colloidal metals

The preferable MNP sizes for plasmonic near-field light enhancement in solar cells are on the order of 10-100nm, as determined in Chapter 2. One way of patterning arrays of MNPs with such dimension is using e-beam lithography (EBL) followed by metal evaporation [93]. EBL is currently the most accurate physical deposition method, allowing nanometer precision in the control of the geometry and inter-particle spacing of the patterned objects. However, this technique is expensive, time consuming (it would take several days to pattern a small 2 inch wafer) and hardly scalable [94]. Therefore, most of the works that attach MNPs to the surface of solar cells use techniques such as thin-film annealing (TFA) [91] or nano-sphere lithography (NSL) [95] which are more suited for large area devices. The TFA method is perhaps the simplest approach for MNP patterning, but there is a high non-uniformity in the size, shape and distribution of the MNPs fabricated in this way. With NSL there is good control on the MNP distribution, but is limited in terms of the MNPs geometries that can be constructed.

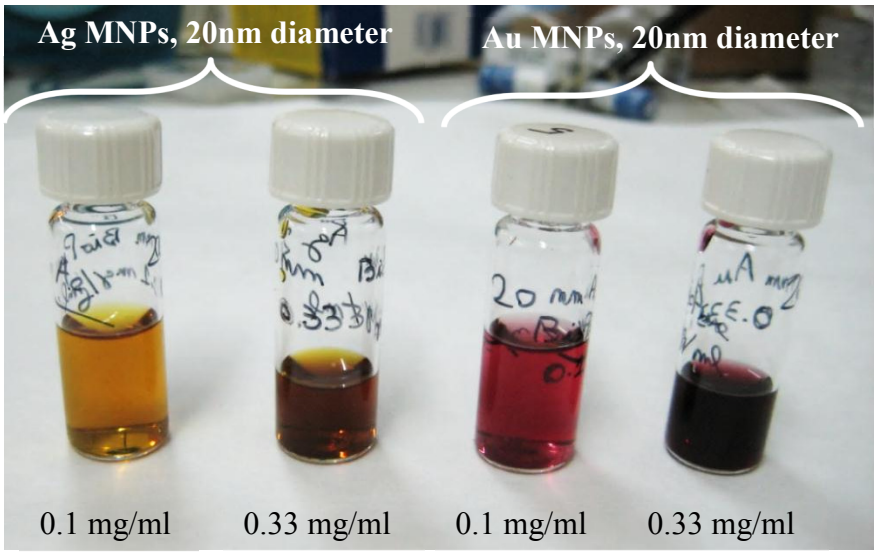

Figure 5.3: Examples of aqueous dispersions containing silver (Ag) or gold (Au) colloids produced by *nanoComposix*, with different particle concentrations (expressed in mass of metal per volume of solution).

In this work an alternative process was developed, using a bottom-up wet coating method [96] to incorporate MNPs in photovoltaic materials. It consists in dip-coating colloidal MNPs dispersed in solution onto the materials' surface, as shall be explained

in Section 5.3. This is a scalable and inexpensive method, as TFA or NSL, which allows good control over the distribution of the patterned MNPs and, more importantly, provides a remarkable precision on the particles' size.

It is possible to synthesize MNP dispersions of spherical particles with well-defined diameters; however, it is still difficult to controllably engineer the shape of non-spherical objects such as spheroids. For application in IBSCs, oblate spheroidal MNPs are preferable since their SP resonance is located deeper in the infrared than spheres, as calculated in Chapter 2 and [21]. However, currently there is still no known method to fabricate colloidal MNPs with oblate geometries in solution phase. Therefore, our experimental studies are limited to spherical MNPs; which do not provide the optimum scattering properties required for light enhancement in QD-IBSCs, but can still be useful to develop the preliminary fabrication steps to incorporate MNPs in the host material of these cells.

Colloidal MNPs can be dispersed in pure water. For our studies, we used aqueous dispersions bought from specialized companies, such as *nanoComposix* and *British Bio Cells*. These solutions exhibit distinct colours depending on the material, size and concentration of the dispersed nanoparticles, as seen in the photo of Figure 5.3.

Figure 5.4 shows typical size distributions of a colloidal solution with silver nanoparticles, obtained with both transmission electron microscopy (TEM) and atomic force microscopy (AFM).

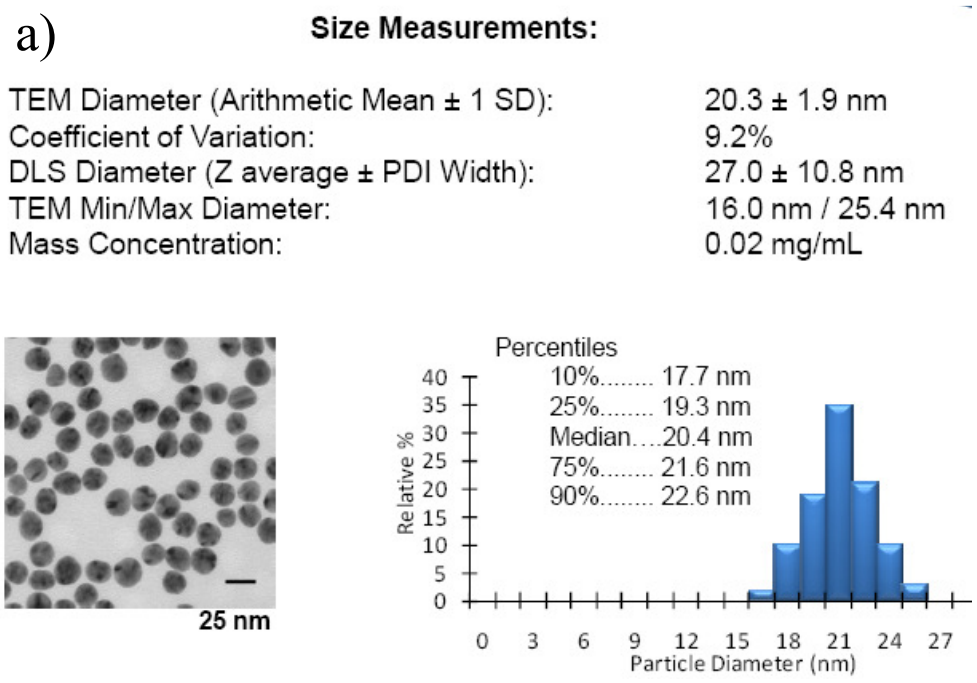

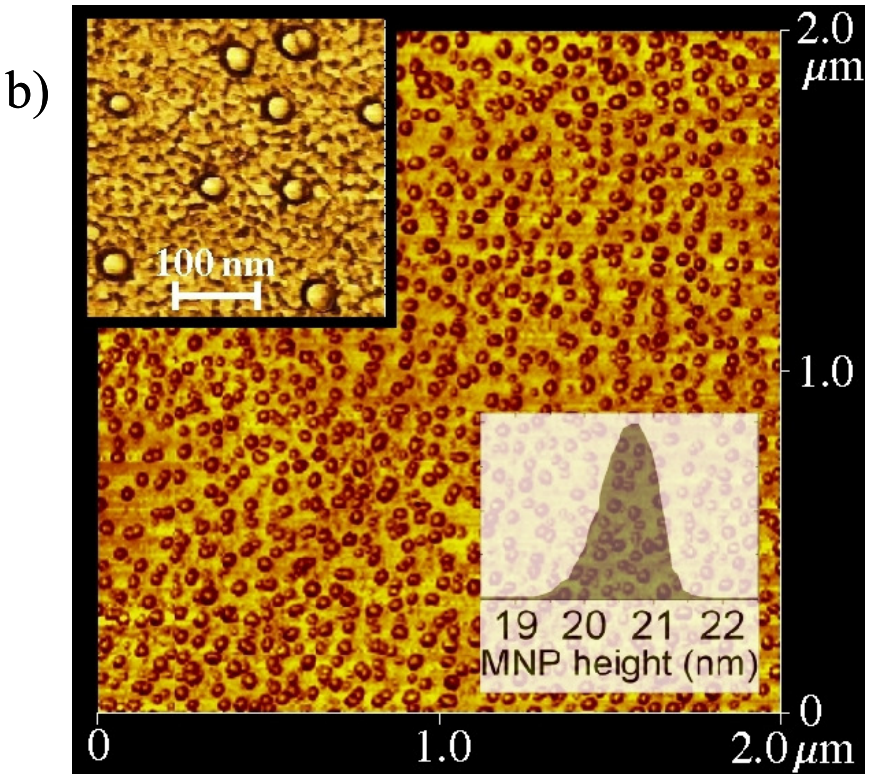

Figure 5.4: Size distributions of a solution containing colloidal Ag nanoparticles produced by *nanoComposix*. The MNP diameters are within the range of 20±2nm. **a)** The diameter distribution on the right was obtained by *nanoComposix* using TEM images such as that shown on the left. **b)** AFM phase image of Ag MNPs deposited on the surface of a GaAs wafer, taken by us using the equipment of the *Centro de Microscopía* of *Universidad Complutense de Madrid*. The bottom inset is an histogram of the particles diameter (measured height), which matches that in (a) obtained with TEM analysis. The top inset shows the MNPs in more detail.

As referred in Section 2.2, the metals which exhibit the strongest plasmonic scattering at solar frequencies are noble metals such as silver (Ag) and gold (Au) [6]. Therefore, those were the nanoparticle materials used in our experiments. Usually colloidal nanoparticles made of Au are better to work than those made of Ag. This is because Au MNPs can be synthesized with more homogeneous diameters, and they remain stabilized in solution (i.e. without aggregating in clusters) for a longer time.

The common synthesis methodology of gold nanoparticles is based on Frens's method [97]. Typically a starting solution of 100ml of 2.2mM trisodium citrate ($C_6H_8O_7Na_3 \cdot 2H_2O$) as a reductant is heated to boil, and 40ml of 0.815mM $HAuCl_4$ ($HAuCl_4 \cdot 4H_2O$) is added with rapid mixing. The solution is then heated to boil for 15 minutes. It initially develops a pale yellow color and then a gray color, which changes to lavender and then transforms into red in 1–3 minutes.

This procedure forms Au nanoparticles whose surface is passivated with a monolayer of citric acid, or citrate [$C_3H_5O(COO)_3^{3-}$]. These citrate molecules passivate the MNPs' surface and are known as the "capping agent" of the nanoparticles. Such molecules attach on one end to the MNP surface dangling bonds and on the other end to the water molecules. They carry a negative charge which causes the MNPs to repeal each other in solution, preventing their aggregation/agglomeration.

Besides citrate, other organic compounds can also be used as capping agents; for instance tannic acid is also commonly applied. Different capping agents provide differing levels of stability to salt, light, heat, pH, and solvents other than water. However, such aspects are outside the scope of the present thesis.

5.3 Self-assembled nanoparticle arrays on various substrates

This section summarizes the controlled assembly procedure that we developed to pattern uniform arrays of MNPs on distinct substrates. The two most standard methods used to deposit colloidal particles onto flat surfaces are by dip-coating or spin-coating.

In dip-coating, the sample is immersed in the colloidal solution and the particles deposit onto its surface by adsorption. It usually takes a few hours for the particles to cover the entire surface.

In spin-coating, a small volume of the colloidal solution is dropped on top of the sample surface and the sample is rotated fast (usually at a speed on the order of 1000 rpm), for just a few minutes, to spread the solution over the entire surface and remove the excess amount of liquid [98]. The spin-coating method is considerably faster than dip-coating; however it requires the solution to wet the sample surface; i.e. if the solvent is water the surface must be hydrophilic. Otherwise the colloids are deposited non-uniformly over the surface area, resulting in areas with big agglomerations of particles and other areas with no particles at all. In Appendix D the spin-coating method is described in more detail, together with practical advices from our extensive experience.

In any wet-coating method, the colloidal MNPs can only get attached to a sample if its surface is charged oppositely to the nanoparticles. If there is no electrostatic force that attracts the particles to the sample then they just remain dispersed in the liquid and do not get adsorbed onto the surface. As referred in Section 5.2, the MNPs have a

negatively charged surface due to the presence of the capping molecules that stabilize them in solution. So, the sample should have a positive surface charge in order to attract the MNPs onto it. However, no such charge is naturally present in the surface of semiconductor materials if they are not chemically treated (functionalized).

The only way to force the particles to deposit onto an untreated surface is by covering it with a drop of colloidal solution and then evaporating all the water [99]. This was actually the initial process that we employed to deposit the MNPs before learning about the functionalization mechanisms. In Figure 5.5 and Figure 5.6 we show scanning electron microscope (SEM) images of depositions that were obtained by evaporating the water from the MNP solution. At first, we tried to deposit the MNPs simply by drying a drop of the colloidal solution onto the wafer surface. As the water evaporates from the drop, there is an outward flow of colloids suspended in the liquid that pushes them to the borders of the drop, resulting in the well-known coffee-stain deposition pattern. This results in a highly heterogeneous distribution of deposited particles over the sample surface, with some regions having no particles at all and other regions (those in the coffee-stain boundaries) having big MNP agglomerates as shown in Figure 5.5.

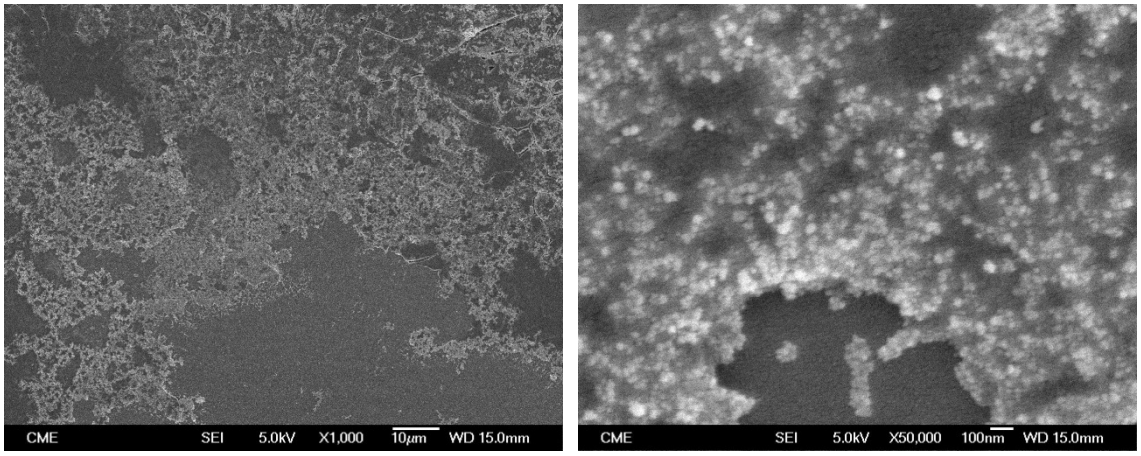

Figure 5.5: SEM images of Au MNPs agglomerates deposited in a Si wafer by drop drying. Here a drop of the aqueous colloidal solution was placed on sample surface and the water was evaporated in oven, leaving only the nanoparticles. The Si surface was not chemically functionalized.

Left – image of a large MNP agglomerate obtained on the borders of the coffee-stain drying pattern of the drop. **Right** – magnified image of the agglomerate where the individual MNPs can be distinguished.

Afterwards we started employing spin-coating and evaporated the water from the colloidal solution while the sample was spinning. Several spin-coating tests were performed to try to optimize the spinning conditions (rotation speed, time, solution concentration, heating during spinning, etc.) in order to achieve a homogeneous surface coverage with a uniform array of individual MNPs (see Appendix D for further instructions on spin-coating). These tests yielded a better surface coverage than that of Figure 5.5, which was obtained by simple drop-drying. However, with this process we could never achieve a homogeneous deposition over the entire sample with a uniform array of equally-spaced MNPs. Figure 5.6 shows SEM images of a typical deposition of Au MNPs using this method of drying the colloidal solution during the spin-coating, without surface functionalization. Most of the sample is covered with small clusters of MNPs, separated by large empty areas. On the sample borders there are big MNP agglomerates due to the inevitable coffee-stain effect.

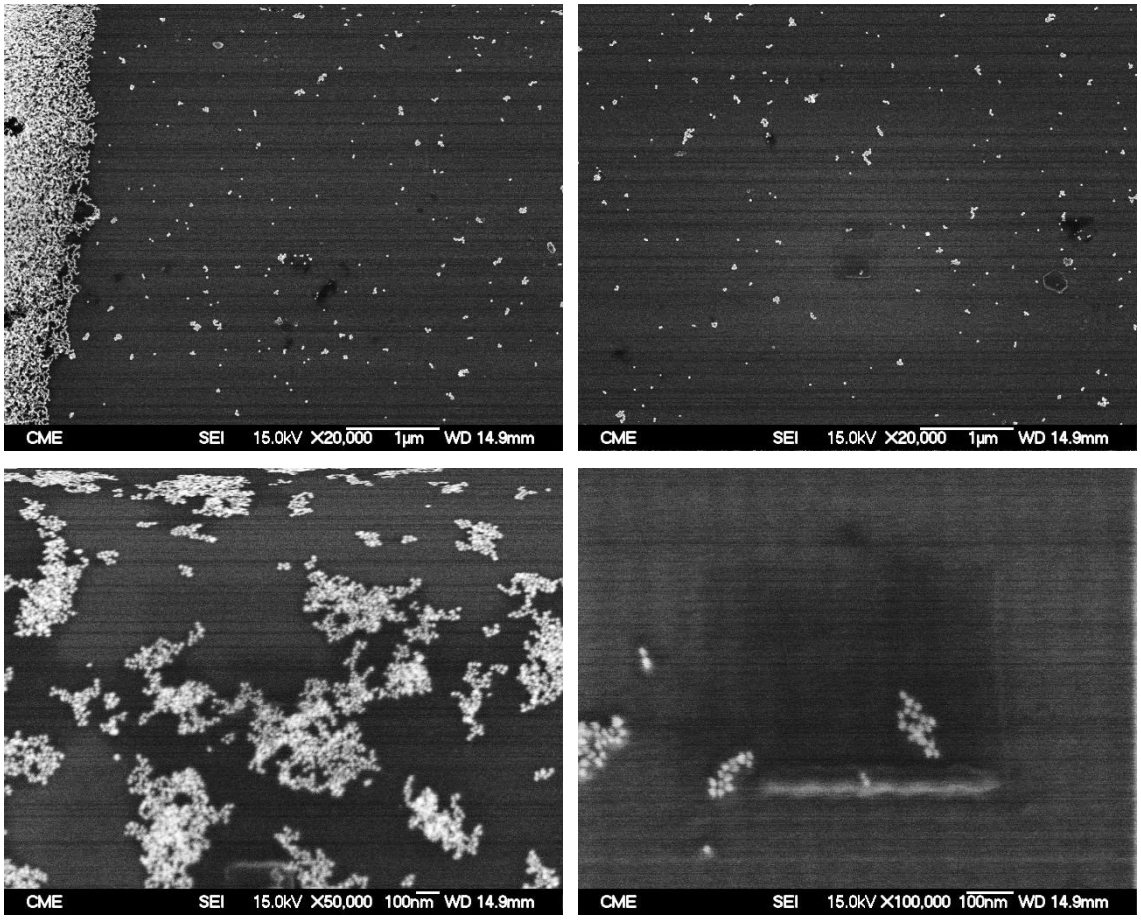

Figure 5.6: SEM images of a deposition of Au MNPs on a Si wafer by evaporating the water from the colloidal solution during spin-coating. The Si surface was not functionalized. The top left image was taken on the border of the sample, where big

MNP agglomerates are formed due to the drying pattern of the colloidal solution (coffee-stain effect). Away from the borders the sample is covered by small MNP clusters separated by large empty areas, as shown in the top right image. The bottom images show such MNP clusters with more magnification.

It can be clearly noted in Figure 5.6 that the MNP distributions obtained in this way are quite unsatisfactory. It is important that the MNPs are individually deposited on the surface, with a constant inter-particle separation distance throughout the sample. That could only be achieved by chemically functionalizing the surface with a positive surface charge in order to allow the deposition of the negatively-charged nanoparticles, as sketched in Figure 5.7. Such functionalization is achieved by covering the surface with a molecular linker, such as DNA or other organic molecules, which act as a "glue" for the nanoparticles. The molecular linkers attach to the dangling bonds of the sample surface on one of its ends, and the other end provides a positive charge that attracts the particles in solution (see Figure 5.7). Some of the substances that are commonly used as organic linkers for patterning monolayers of MNPs onto Si wafers are AEAPTMS [N-(2-Aminoethyl)-3-aminopropyl-trimethoxysilane] [100], APS [101], APTMS [102] or APTES [103]. The procedure followed by us is described in detail in Appendix C and uses an APTMS organic linker to functionalize the samples. Even though in the literature such functionalization is usually exclusively applied to Si surfaces, we have realized in the course of the experimental work that it could also be used for the proper functionalization of other materials such as GaAs, amorphous silicon (a-Si) and glass. This is an important advantage of the current functionalization procedure, since it is not limited by the surface material.

It is worth underlining that the previously referred functionalization treatment is an essential step in any wet-coating deposition method. If the sample is not functionalized with a surface charge opposite to that of the MNPs capping agent, the colloids remain dispersed in the water solvent and they don't adhere to the surface.

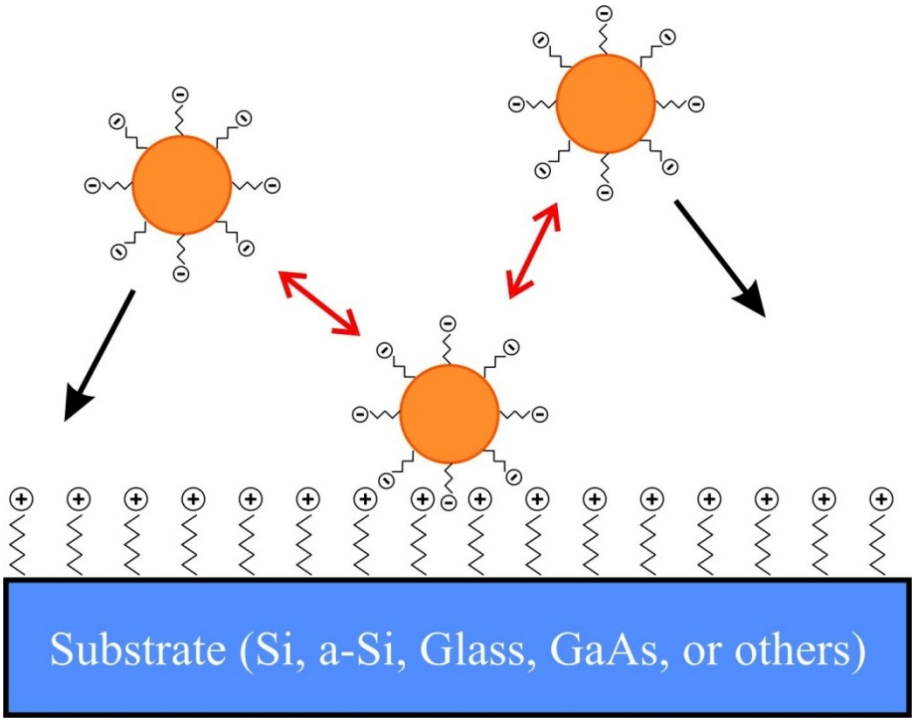

Figure 5.7: Self-assembled deposition of colloidal MNPs. The negative surface charge of the MNPs' capping agent causes the particles to repeal each other in solution (red arrows). They are attracted to the substrate (black arrows) if its surface is functionalized with molecules (e.g. APTMS) that have a positive charge on their end group. The electrostatic repulsion between the MNPs keeps them separated by a certain distance upon deposition. Such separation distance depends on the MNPs surface charge density and on the pH of the solution.

[*Image not to scale* - the length of the organic molecules (zig-zag lines) is exaggerated for better visualization]

With the functionalization method we were able to obtain the required uniformity in the deposited MNPs array, simply by immersing the sample in the colloidal solution for some hours. No spin-coating or water evaporation was necessary because the MNPs are electrostatically driven to the surface, due to the positive charge of the APTMS, and self-assemble with a constant inter-particle spacing (*d*) due to the electrostatic repulsion caused by their capping molecules (see Figure 5.7 and Figure 5.8). This is a quite effective dip-coating procedure that can pattern, with a remarkable degree of order, indefinitely large sample areas (even entire solar panels at once). Besides, it allows a high degree of control over the density (i.e. spacing) of the deposited MNPs. The separation distance *d*, represented in Figure 5.8, can be tuned by adjusting the electrostatic repulsion force between the MNPs. This can be done, for instance, by changing the pH of the solution, the solvent liquid, or the organic capping agent.

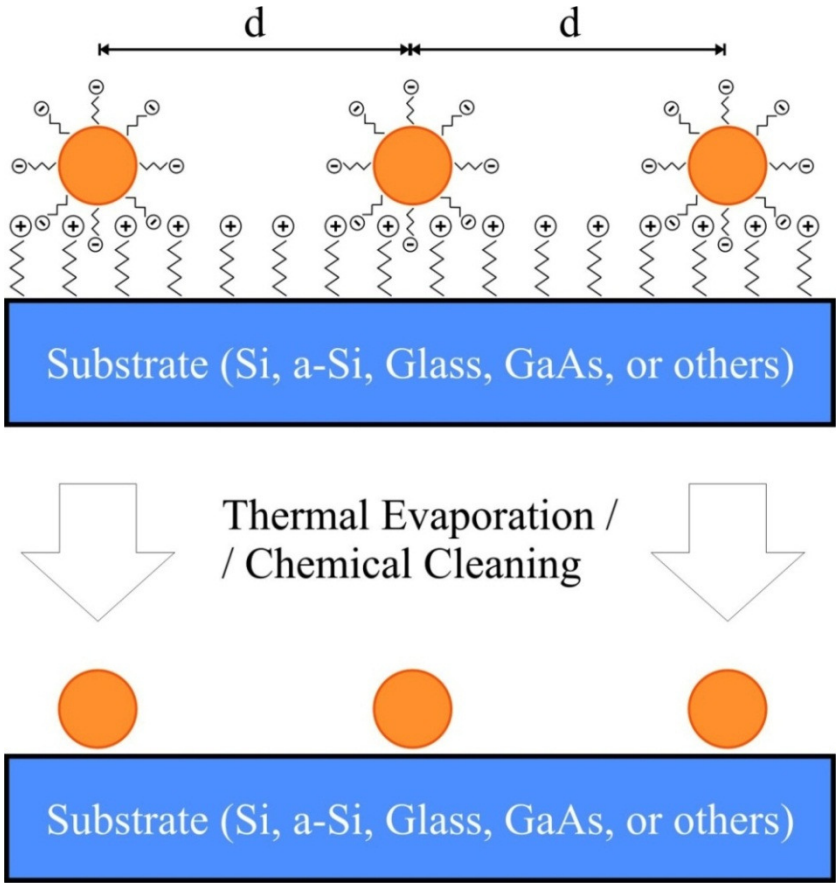

Figure 5.8: Sketch of a deposited array of self-assembled MNPs obtained with the APTMS functionalization procedure. The inter-particle separation distance (*d*) is mantained throughout the sample. All the organic species (APTMS + capping agent) can later be removed by thermal evaporation and/or chemical cleaning, leaving only the MNPs array on the surface.

[*Image not to scale* - the length of the organic molecules (zig-zag lines) is exaggerated for better visualization]

As referred in Chapter 2, the near-field region of pronounced light enhancement is located within a distance from the MNP surface of about its size. Therefore, in order to have complete in-plane near-field coverage, with the minimum number of scatterers, the MNPs should be ideally spaced by a distance *d* of about twice its diameter.

After the deposition of the MNP array, the APTMS and the capping molecules can later be removed either by thermal evaporation or chemical cleaning, as sketched in Figure 5.8. Appendix C provides more information on this. The removal of such organic species is particularly important prior to the growth of the capping layer that will embed the MNPs in the sample material, as shall be referred in the following section.

Figure 5.9 shows an example of one of the distributions obtained with this approach, for the case of Au MNPs deposited on a Si sample.

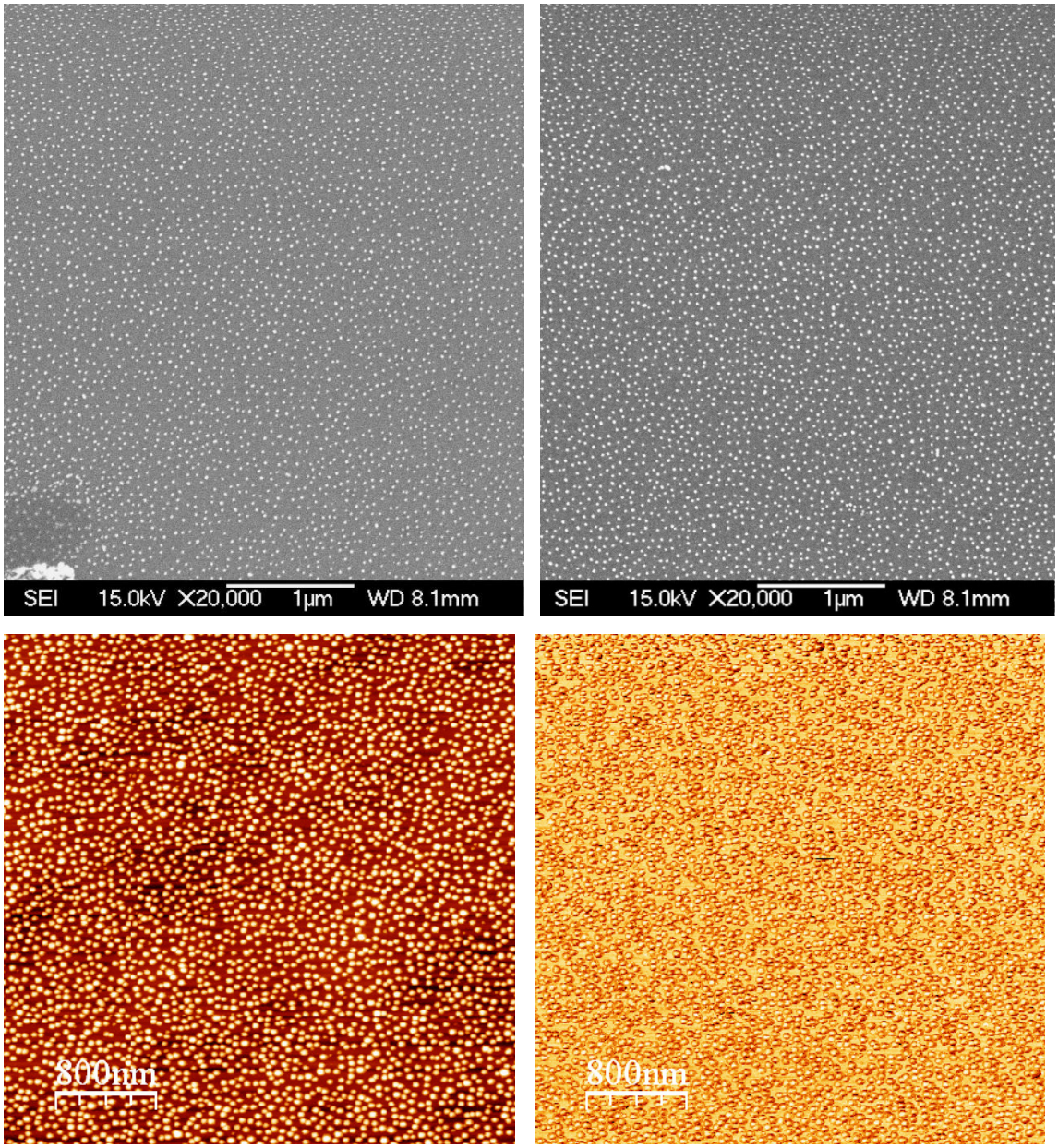

Figure 5.9: Array of 20nm Au MNPs deposited on a Si wafer functionalized with APTMS, following the procedure described in Appendix C.

Top – SEM images taken at two different spots of the surface. The deposited MNP pattern is the same throughout the entire sample surface, no matter how big the sample is.

Bottom – AFM images of the MNP array. The left image shows the height profile, and the right image shows the phase (related with differences in materials). In the height image it can be seen that the MNP sizes are well monodispersed since the colloids' diameter distribution is quite sharp (of 20±2nm).

Using this method we were also able to deposit uniform arrays with particles of distinct sizes and on various substrate materials (Si, a-Si, Glass and GaAs), as shown in the examples of Figure 5.10. It can be seen that the higher the particle size the higher is the inter-particle spacing *d*, since there is a stronger electrostatic repulsion force between the MNPs.

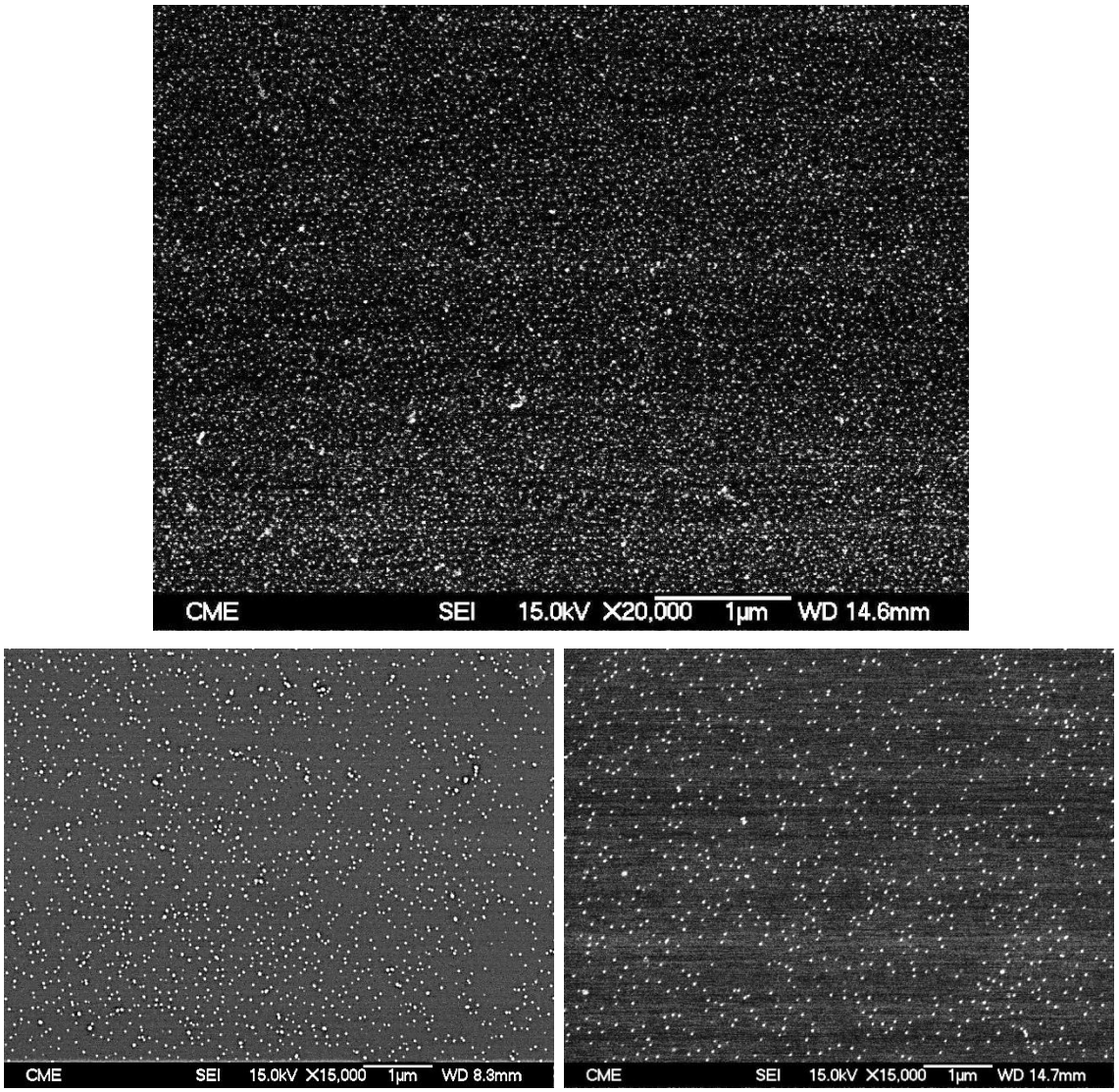

Figure 5.10: SEM images of Au MNPs of distinct sizes self-assembled onto various substrates, using the APTMS functionalization. In all the samples the MNP distribution is uniform throughout the entire sample surface.

Top – 15nm Au MNPs deposited in GaAs

Bottom left – 20nm Au MNPs deposited in an a-Si layer (glass substrate)

Bottom right – 30nm Au MNPs deposited in GaAs

Arrays of Ag MNPs were also deposited with this procedure, since Ag is one of the materials with strongest plasmonic resonance at solar frequencies. However, as previously mentioned, Ag is not such a stable colloid as Au and it aggregates into clusters more easily. Therefore, as can be seen in the examples of Figure 5.11, the obtained patterns of Ag MNPs are not as good as those of Au MNPs shown in the previous images. In view of this, we decided to restrict our experiments to Au MNPs.

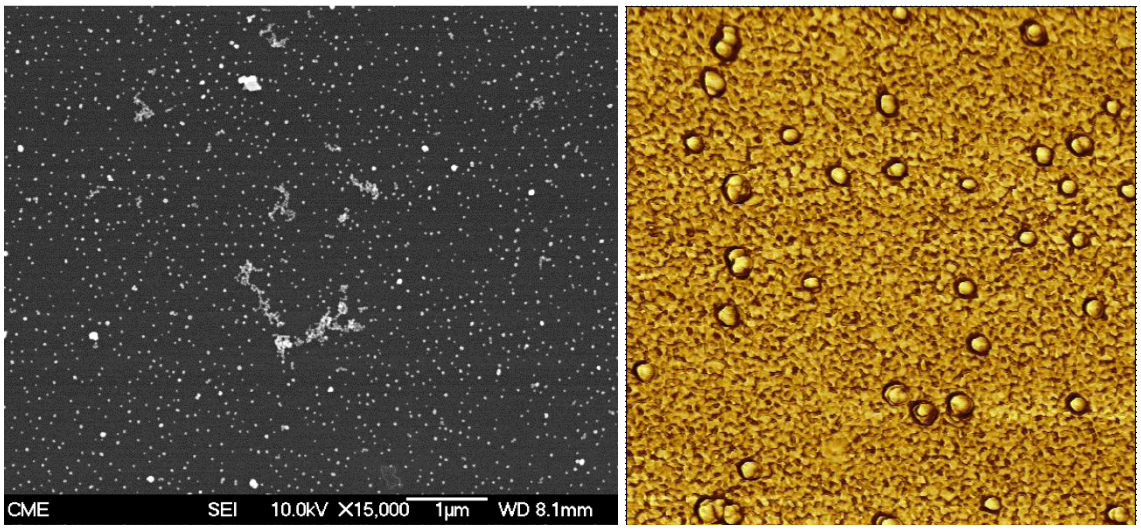

Figure 5.11: Ag MNPs deposited in APTMS functionalized surfaces. These nanoparticles are not so stable in solution as Au MNPs, and they agglomerate into clusters, as can be seen in these images.

Left – SEM image of 40nm Ag MNPs deposited in an a-Si layer

Right – AFM Phase image of 20nm Ag MNPs deposited in GaAs. Image taken with a 5420 AFM system of *Agilent* company.

5.4 Thermal tests on deposited metal nanoparticles

In the previous section it was described how to construct uniform arrays of MNPs onto the surface of various materials. In this section we study the possibility of embedding such arrays by growing a capping layer, on top of the deposited particles, of the same material of the layer in which they were deposited (as depicted in Figure 5.2). The capping layer deposition can be performed by processes such as chemical vapour deposition, molecular beam epitaxy, or sputtering. For GaAs growth these processes can use temperatures up to the range of 500-600ºC; whereas for Si growth the temperatures

can go higher than that (up to around 1000ºC) depending on the process used and the required degree of crystallinity.

In order to verify if the MNPs can withstand the deposition of such capping layer, we conducted a series of thermal tests to determine the maximum temperature that the nanoparticles can support without suffering any structural deformation. Four different MNP dispersions were deposited on distinct GaAs and Si substrates. The four dispersions were composed of Ag and Au particles with diameters of 20nm and 30nm.

A *Solaris SSI* Rapid Thermal Annealing (RTA) equipment was employed to heat all the samples at distinct temperatures between 200ºC and 1000ºC, during 20min, under an inert atmosphere of forming gas (90% N_2 + 10% H_2) at atmospheric pressure.

After the RTA all the samples were inspected by AFM, at distinct spots along their surface, to see if there was any change in the deposited MNPs diameter (measured height). It was observed that no size change occurs in the MNPs deposited in GaAs up to 500ºC. Above this temperature we cannot tell by AFM what occurs to the particles, since the arsenide starts to desorb from the substrate leaving an excess of gallium on its surface [104]. This causes the appearance of holes on the surface and small droplets formed by the excess of Ga [105], which mask the MNPs and prevent us from accurately measuring their sizes.

Si substrates are more thermally stable since their surface remains smooth up to 1000ºC. From the AFM measurements of MNPs deposited on Si, we concluded that the 20nm and 30nm Ag MNPs suffered no changes up to 700ºC, and the Au MNPs up to 800ºC. At higher temperatures the particles start vanishing, and at 1000ºC practically no particles are present. It is not possible to tell by AFM which physical mechanisms (sublimation, melting or diffusion into the substrate) are responsible for the disappearance of the MNPs; however, there are several other literature contributions that investigate this in further detail. Thermodynamic models assuming isolated spherical MNPs yield a linear relationship between the melting temperature and the reciprocal of the particle size [106, 107]. It is predicted that isolated Ag and Au MNPs with diameters above 15nm should have a melting point very close (within 10% difference) to that of the bulk crystal (960ºC for Ag and 1063ºC for Au). However, most of these models do not consider the interaction with the substrate, which plays a crucial role on the thermal behavior of the deposited MNPs [108]. This surface interaction reduces the melting point of the nanoparticle, relative to that predicted for isolated

particles, and can determine the physical mechanism responsible for the MNP size reduction with temperature.

The thermal limits of 700-800ºC observed here for MNP stability are well above the maximum GaAs deposition temperatures (500-600ºC). Thus, the MNPs should not suffer any deformation during the GaAs capping layer growth. As for the Si capping layer growth, a deposition process should be chosen that keeps its temperature below the MNPs' thermal stability limit.

The studies performed in this thesis used uncoated MNPs. However, MNPs coated with a dielectric shell (for instance, silica) should have a better thermal and electrical performance. Silica-coated MNPs were observed to withstand higher temperatures without structural changes [109]. This is because the shell creates a barrier between the MNP and the substrate, reducing the surface effects on the particle thermal deformation. Besides, the dielectric shell acts as a passivation coating on the MNP, preventing electron-hole recombination at the metal surface. As determined in Section 2.3, a silica shell a few nanometers thick should prevent current degradation due to recombination and still allow a sufficiently high scattered field intensity [21].

5.5 Sputtering of capping layer

The growth of the material embedding the nanoparticles was performed with RF magnetron sputtering, since our group recently purchased a sputtering equipment from *Vaksis*. Figure 5.12 (left) shows a typical a-Si layer deposited by this method in a glass substrate. Since the substrate is constantly rotating during the deposition process, the layer thickness is uniform over the entire surface. The quality of the deposition can be appreciated in the photograph, attending to the fact that the a-Si layer is homogeneously reflective in its entire surface. The surface roughness of the deposited layers is usually below 10nm, as measured by AFM (see right image of Figure 5.12).

Since the equipment was new, we first had to calibrate our sputtering conditions to achieve the desired deposition rate. For that, we deposited a series of a-Si films onto Si wafers and measured their thicknesses with a *Sloan Dektak* mechanical profilometer and with an MM-16 elipsometer of *Horiba-JY* company. Figure 5.13 shows SEM vertical profiles of one of such samples used for calibration. The values of the a-Si film

thickness obtained with the profilometer and the elipsometer match those determined by SEM.

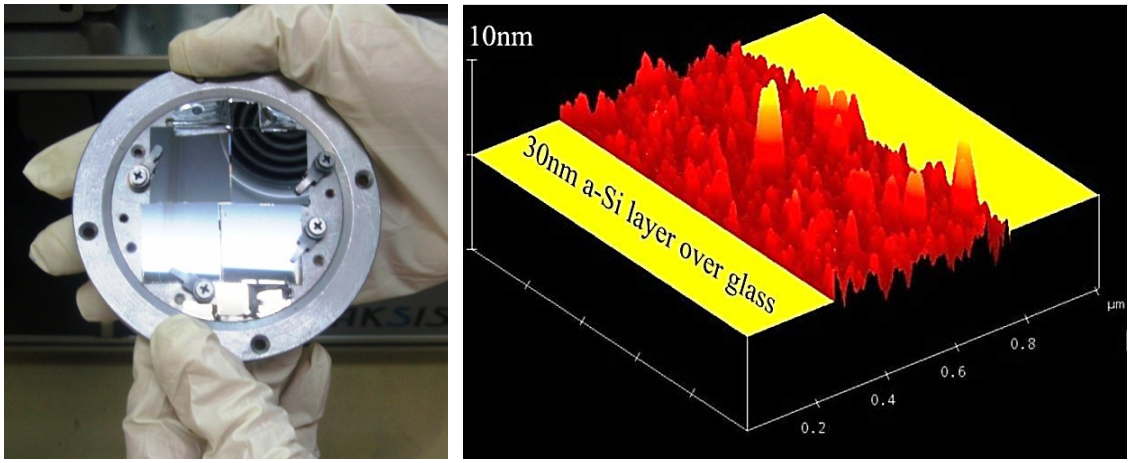

Figure 5.12: **Left** – 300nm thick a-Si layer deposited on glass substrates using RF magnetron sputtering with the *Vaksis* equipment of the group of *Estudios Fundamentales*. In this photo it can be seen that, even though the deposited material is amorphous, its surface is mirror-like smooth due to the good quality of the deposition. **Right** – AFM height image of the surface of one of the deposited a-Si layers. Its roughness is of about 5-10nm height.

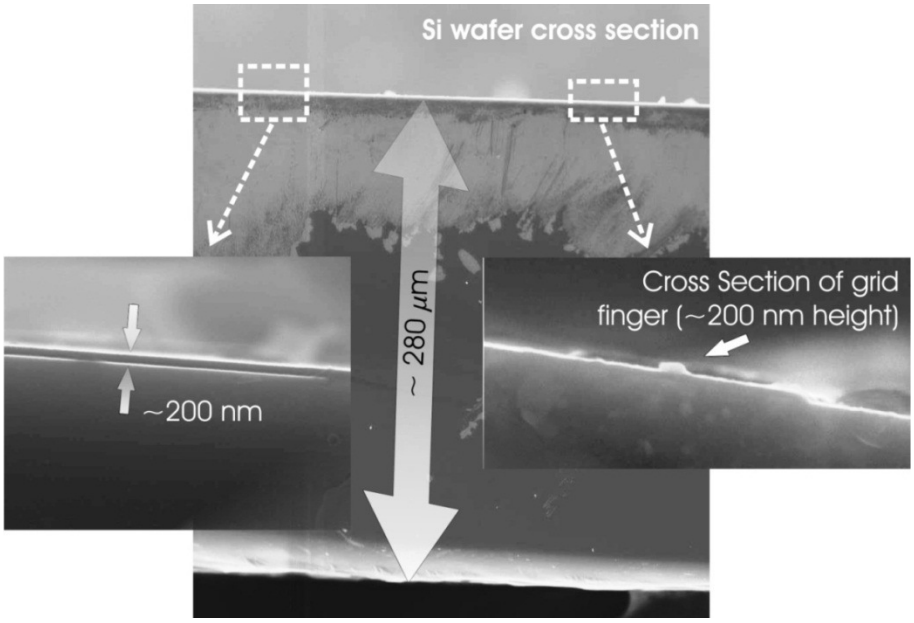

Figure 5.13: SEM images of a vertical cross-section of a Si wafer having a 200nm a-Si layer deposited on top by RF sputtering. The thickness of the deposited a-Si layer measured by SEM is close to that measured with profilometry and elipsometry.

The results of the calibration tests are represented in Figure 5.14 which shows the values of the a-Si film thickness as a function of the deposition time. The conditions indicated in the figure provide a deposition speed of ~9nm/min, which is a quite satisfactory rate. Those were the conditions used for the sputtering depositions performed with our equipment.

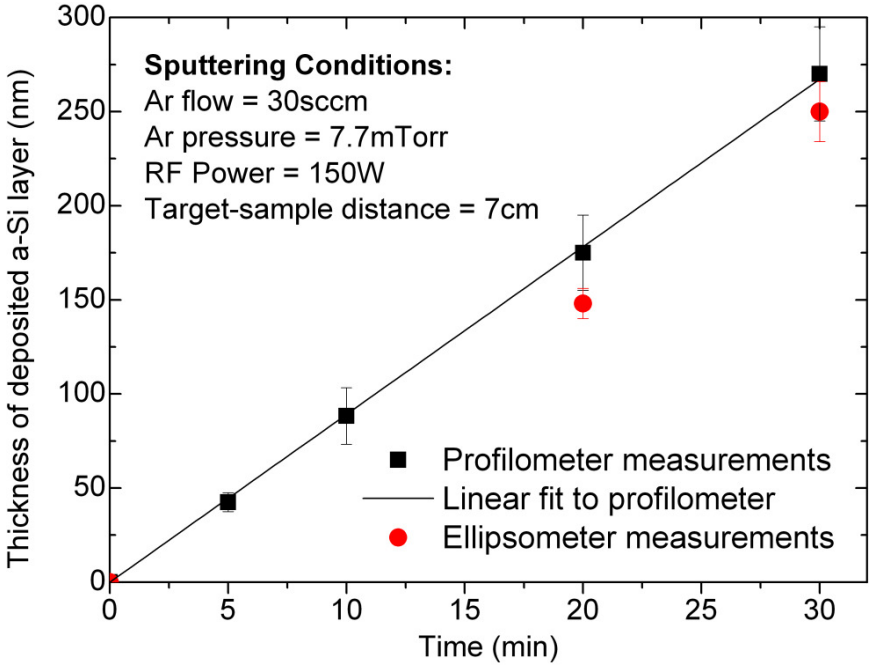

Figure 5.14: Calibration results of the sputtering of a-Si films over Si wafers, measured with the profilometer of the "Láminas Delgadas y Microelectrónica" group of *Univ. Complutense de Madrid* and with the elipsometer of our institute. The sputtering deposition conditions and indicated on the top left. The chamber is filled with Argon (Ar) and the sample holder rotates at a constant speed during the deposition. With these conditions the deposited layer thickness is uniform and increases proportionally to the deposition time at a rate of ~9nm/min.

5.6 Plasmon-enhanced light extinction in various media

Extinction is the attenuation of an electromagnetic wave by scattering and absorption as it traverses a particulate medium. The irradiance of a beam of light is exponentially attenuated from I_0 to I_t in traversing a distance t through a particulate medium:

$$I_t = I_0 \exp(-\alpha_{ext} t) \quad , \quad \alpha_{ext} = \rho C_{ext} \tag{5.1}$$

being ρ the number of particles per unit volume, and $C_{ext}=C_{sca}+C_{abs}$ the extinction cross section of each particle which is the sum of the scattering and absorption cross sections [23]. This assumes that multiple scattering or any other inter-particle effects are negligible. In physics, it is usually more common to work with the efficiencies (instead of the cross sections) for extinction, scattering, and absorption: $Q=C/A$, where A is the particle cross-sectional area projected onto a plane perpendicular to the incident light beam.

In homogeneous media, with no embedded particles, the dominant attenuation mechanism is usually only absorption. So the extinction coeffient is equal to the absorption coeffient ($\alpha_{ext} \approx \alpha_{abs}$) and expression (5.1) becomes the well-known Lambert-Beer law.

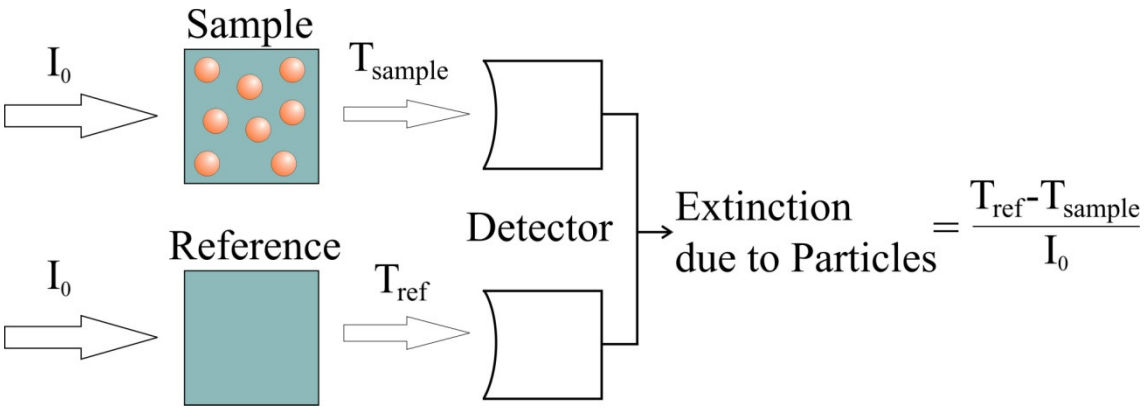

Figure 5.15: Schematic representation of a transmission measurement performed with a spectrophotometer. The output is the light intensity that is extinct (absorbed + scattered) due to the presence of the particles in the sample.

Scattering by individual spherical particles, such as the colloidal MNPs used in our experimental work, can be computed analytically with Mie theory [49]. This is a separation-of-variables method that determines the exact solution of Maxwell's equations for the plane-wave scattering by a homogeneous sphere of arbitrary size. In the case of particles much smaller than the wavelength of incident light, the simplified electrostatic approximation (EA, see Section 2.2) can be used [23]. Any of these methods allows the calculation of the extinction efficiency $Q_{ext}= C_{ext}/A$ of a particle

embedded in a homogeneous medium. This quantity is directly proportional to the extinction coefficient α_{ext}, according to eq. (5.1), which can be experimentally determined by measuring the amount of light transmitted (T) through a particulate sample using spectrophotometry. Figure 5.15 illustrates the steps of a typical measurement performed with this technique, such as those presented in this section.

This is the most standard procedure used by the manufacturing companies of colloidal MNPs to analyze the quality of their synthesized solutions (apart from TEM analysis as in Figure 5.4a). The values of the SP frequencies obtained in this way are usually quite accurate and can match well what would be expected by electromagnetic modeling (Mie theory), as shown in Figure 5.16.

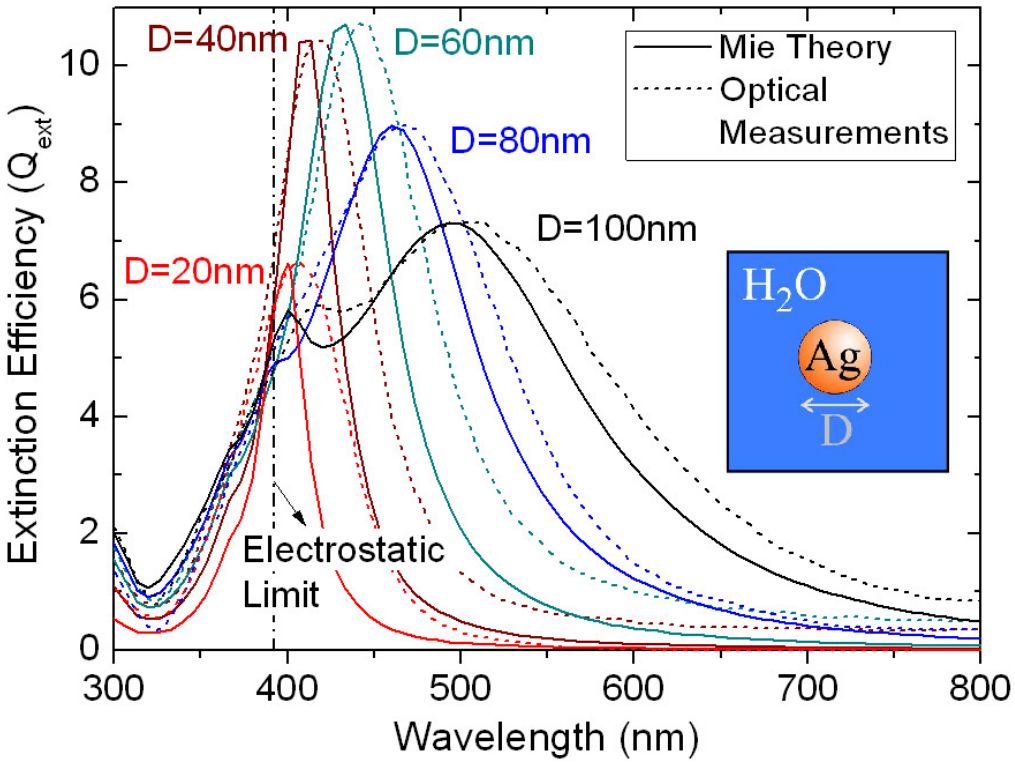

Figure 5.16: Extinction efficiency (solid lines) of individual Ag spheres in water with distinct diameters (D), computed with Mie theory. These are compared with extinction measurements (dashed lines) performed by *nanoComposix* on their MNPs solutions, containing particles such as those shown in Figure 5.4. The units of the measured extinction are arbitrary; so the dashed curves were normalized to the corresponding Q_{ext} maximum, for better visualization.

The vertical dash-dot line (electrostatic limit) corresponds to the SP resonance of particles much smaller than the wavelength, calculated with the EA. That is the minimum SP wavelength that can be achieved with Ag spheres in water.

The dashed lines of Figure 5.16 correspond to the extinction spectra of several aqueous solutions containing silver (Ag) nanospheres of distinct diameters (D). The observed extinction peaks occur at the mean particles' SP frequency. These spectra can be modeled with Mie theory, by computing the extinction efficiency (Q_{ext}) of an isolated Ag sphere immersed in a water medium. The Q_{ext} curves calculated in this way are the solid lines in Figure 5.16. The refractive index of the water medium was taken to be n_m=1.33, and that of Ag was interpolated from experimental data [41].

The optical response of the smaller (D<80nm) MNPs is predominantly dipolar in nature, but as the particle size is increased retarded potentials cause the field inside the particle to become less uniform. This leads to the excitation of higher-order modes (quadrupolar, octopolar, etc.) with different scattering characteristics and higher resonance frequencies [110]. For instance, in the spectrum of 100nm MNPs (black lines) of Figure 5.16, two clear peaks are present corresponding to the dipolar (at λ≈500nm) and quadrupolar (at λ≈400nm) modes.

In our work we are interested in analyzing the scattering of MNPs immersed in photovoltaic media, such as Si or GaAs. If the particles are embedded in a GaAs or Si medium the SP frequencies are red-shifted relative to those in water, since the refractive index of these materials is higher (around 3.5 in the infrared). This is shown in the computed Q_{ext} plots of Figure 5.17a, for the case of a GaAs medium, where it can be seen that the MNPs' resonance appears close to the GaAs bandgap (1.43eV) for diameters below 40nm. The Q_{ext} spectra of MNPs with D>50nm presents additional higher-order peaks besides the dipolar SP resonance. As the particle size increases the magnitude of these peaks increases relative to that of the dipole mode. In the case of 100nm MNPs in GaAs (black line) it is no longer the dipolar peak that corresponds to the maximum Q_{ext}.

In Figure 5.17b it can be seen that the dipolar SP resonance occurs at very similar frequencies for Ag and Au MNPs in GaAs and Si. The SP frequency is mostly dependent on the geometry of the particle, and less on the materials, as long as the absolute value of the MNP dielectric function is much higher than that of the medium. Differences in the maximum Q_{ext} are only observed for big particles when higher-order modes become dominant.

These results provide a preliminary theoretical insight on the optical response of embedded arrays of MNPs.

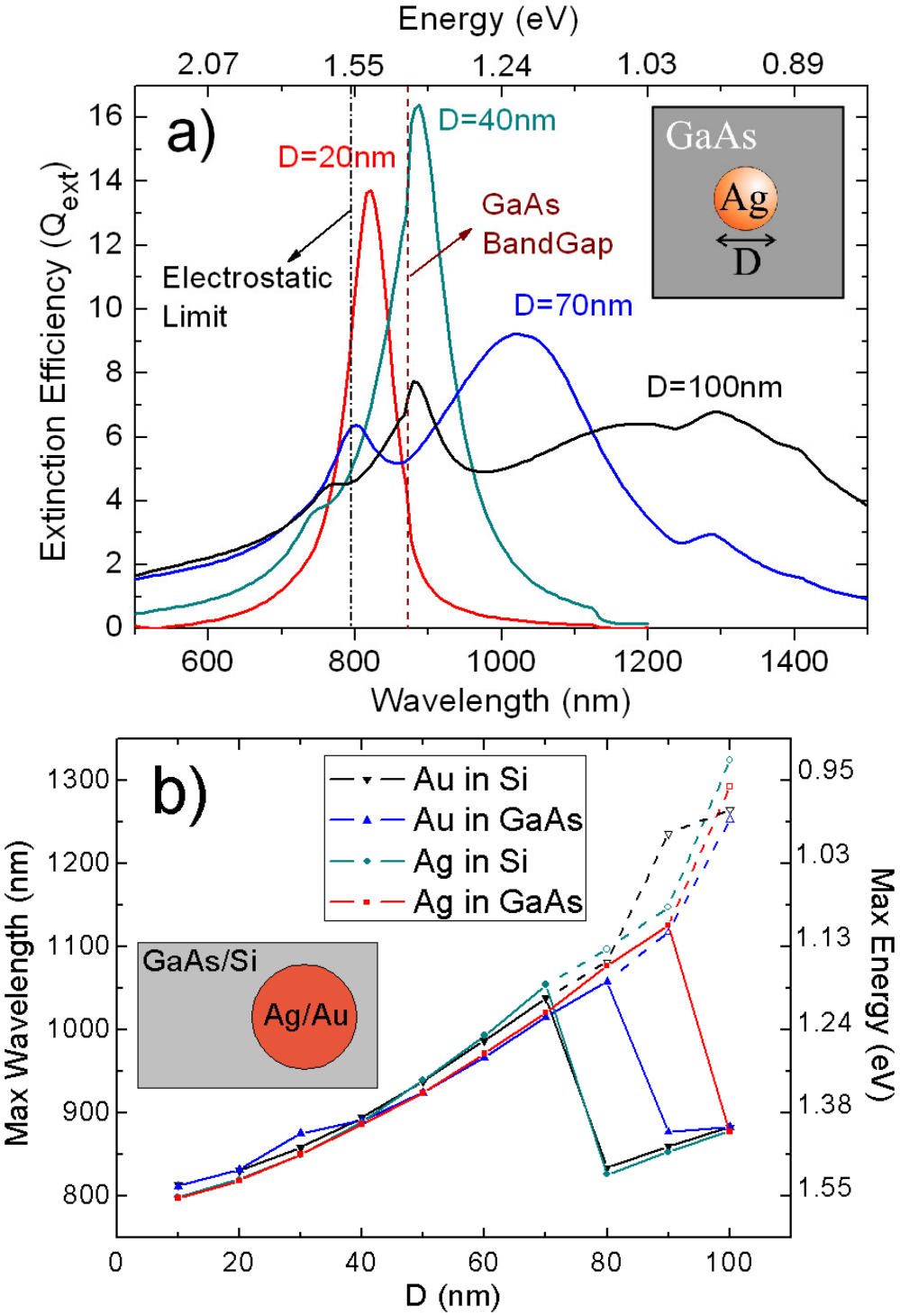

Figure 5.17: **a)** Extinction cross section spectra of Ag spheres inside GaAs, computed with Mie theory. The vertical dash-dot line corresponds to the SP wavelength calculated with EA. The refractive index of Ag and GaAs were taken from interpolation of experimental data [41]. **b)** Maximum Q_{ext} wavelengths, as a function of MNP diameter, for Ag and Au MNPs embedded in GaAs or Si. For big sizes the Q_{ext} maxima no longer occur at the dipolar resonances (shown along the

dashed-lines) but switch to higher-order modes, such as in the case of D=100nm in (a).

In the following paragraphs we analyze some of the main results obtained from the spectrophotometry measurements performed on the samples fabricated by us with the processes described in this chapter. All the measurements were performed with a Spectro 320 spectrophotometer of *Instrument Systems,* that allows the measurement of the light intensity transmitted (T) through a sample for a wavelength range of 350-1700nm. The light extinction in the sample is determined according to the procedure depicted in Figure 5.15. To simplify the analysis the measured T intensity comes in units of I_0 (i.e. I_0=1).

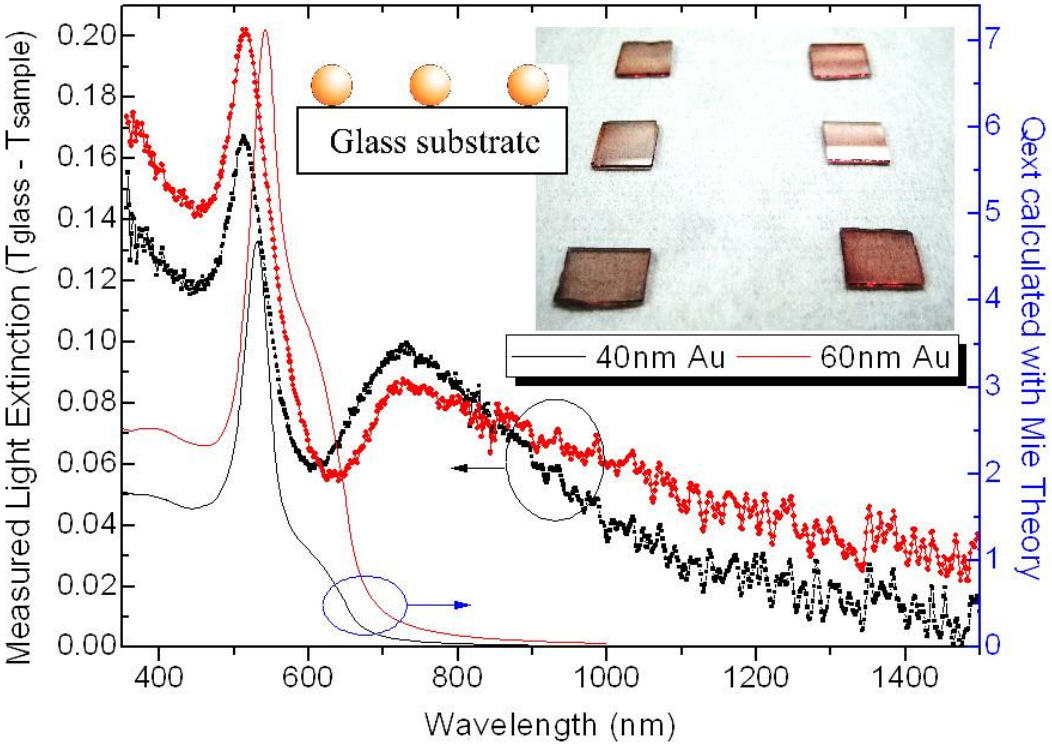

Figure 5.18: Measured light extinction (*left axis*, in units of I_0) of MNP arrays on glass, and extinction efficiency (*right axis*) of an MNP inside a homogeneous glass medium calculated with Mie Theory. The reference sample used for the measurements was a simple glass slide without MNPs.

The simplest way of measuring the optical response of deposited MNPs is by patterning them onto the surface of glass slides, following the procedure detailed in Section 5.3 and Appendix C. Several samples were prepared in this way by coating

different glass slides with Au MNPs of distinct diameters. Figure 5.18 shows the measured light extinction from two of such samples containing arrays of 40nm and 60nm Au MNPs. The deposited MNP arrays give a redish tone to the glass surfaces (shown in the photo of Figure 5.18) similar to the color of the corresponding MNP solutions as seen in the third vial of Figure 5.3. This indicates that the MNPs did not aglomerate into clusters after deposition, and remain well individualized on the samples' surface just as they were when dispersed in solution.

The measured extinction curves are compared with the Q_{ext}, calculated with Mie theory, of a single MNP assumed to be immersed in a uniform glass medium. In our samples the MNPs are not immersed in a uniform medium, but are deposited on the surface of a glass substrate in air. So, the effective medium that is "seen" by the deposited MNPs has an effective refractive index between that of air (N_m=1) and glass (N_m=1.5). This explains the redshift of the Q_{ext} maxima relative to those of the measured curves, since the SP frequency decreases with increasing N_m. The wavelenghts corresponding to the maximum points of the SP peaks appearing in Figure 5.18 are indicated in Table 5.1.

In both measured curves a secondary peak is present close to 730nm, which does not appear in the Q_{ext} spectra. This peak is associated to the interference between the MNPs electric field and the substrate surface. When an MNP is close to an interface there is an extra field incident on the MNP, in addition to the illuminating field coming from above. That extra field comes from the light that is backreflected from the surface which is not necessarily in phase with the illuminating light and, thus, also not in phase with the dipolar field inside the MNP. So, the field coming from the surface modifies the driving field incident upon the MNP originating retarded potentials that change the MNP internal field and polarizability [111]. This results in the appearance of dispersive lineshapes in the measured spectra, such as those observed in the secondary peaks of Figure 5.18. The minima in the lineshapes (around 600-650nm) occur when the driving field coming from the substrate surface interferes destructively with the dipolar field inside the MNP, and the maxima in the lineshapes (around 730nm) correspond to constructive interference [68]. Since destructive interference is associated with a reduction of the radiative decay rate, the dispersive lineshapes are always present at wavelengths above the SP dipolar resonance.

Wavelenghts of plasmon peaks of MNPs arrays	*MNPs over glass substrate* (Figure 5.18)		*MNPs over a-Si layer on glass* (Figure 5.19, left)		*MNPs embedded in a-Si on glass* (Figure 5.19, right)	
Au MNP diameter	**40nm**	**60nm**	**40nm**	**60nm**	**40nm**	**60nm**
Measured Extinction peaks	513 nm	516 nm	530 nm	531 nm	567 nm	579 nm
Calculated Q_{ext} peaks	531 nm	541 nm	-	-	916 nm	996 nm

Table 5.1: Positions of the peaks in Figure 5.18 and Figure 5.19 corresponding to the SP resonance of the 40nm and 60nm diameter MNPs. The values of the Q_{ext} peaks, calculated with Mie theory, assume that the MNP is embedded in a homogeneous medium. The values given here have an associated error of ± 5nm due to the finite number of plotted points.

In another set of experiments, MNPs of various diameters (15, 20, 30, 40, 60 and 80nm) were patterned onto 30nm a-Si layers deposited on glass slides. The a-Si films were deposited by RF Sputtering, following the method described in Section 5.5. The light extinction measured in these samples is shown on the left plot of Figure 5.19. Comparing this plot to Figure 5.18, it can be seen that the presence of a higher-index material below the MNPs significantly increases the height, width and wavelength of the lineshape peak associated to the interaction with the substrate surface. The plasmonic dipolar peaks also shift to higher wavelengths, as indicated in Table 5.1.

The right plot of Figure 5.19 shows the light extinction of the same samples after depositing an additional layer of 30nm a-Si on top on the MNPs array. Here the reference sample was a glass slide with two layers of 30nm a-Si deposited on top. A significant enhancement is observed in all the extinction peaks corresponding to the plasmon resonances, after the deposition of the capping layer of a-Si. Such enhancement indicates that the MNPs' scattered near-field is effectively increasing the light absorbed by the a-Si medium at the SP frequency.

In all the samples of Figure 5.19 it was verified that the measured transmission was similar whether the light was shining from above or below the sample. This tells us that the light scattered from the MNPs, responsible for the observed absorption enhancement in the medium, is independent of such illumination direction. This is a unique characteristic of scatterers in the electrostatic regime, as described in Section 3.4, whose scattering pattern depends on the direction of the incident electric field vector ($\mathbf{E_0}$) but not on the direction of illumination ($\mathbf{K_0}$).

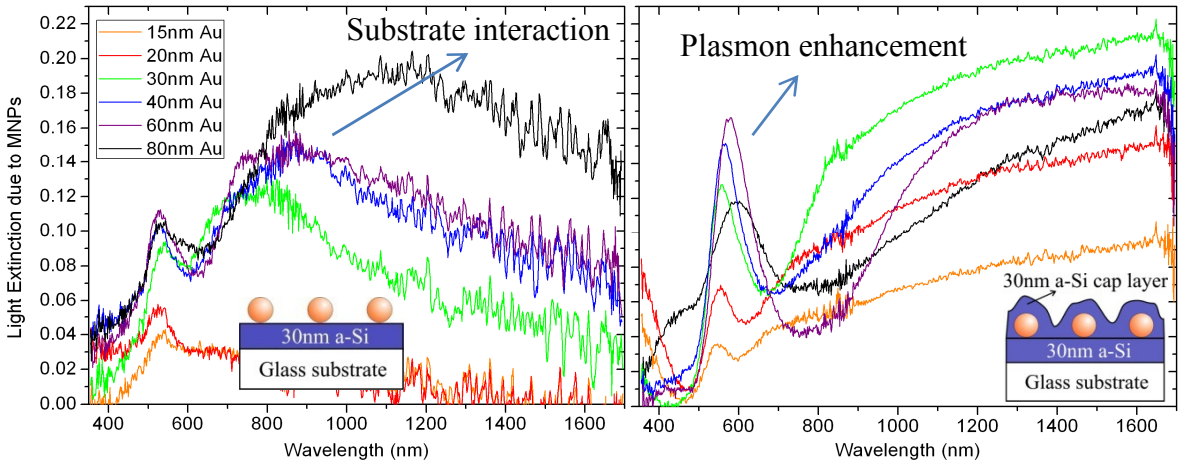

Figure 5.19: **Left** - Measured extinction spectra of MNPs with different diameters deposited on a 30nm a-Si layer over a glass substrate. The reference sample used here was a glass slide with a 30nm a-Si layer on top, without MNPs. **Right** – Measurements of the same samples after being capped with an additional 30nm a-Si layer deposited on top. The reference sample was the same as that of the left, but with an additional 30nm a-Si layer on top.

The measured extinction curves can be compared with the Q_{ext}, calculated with Mie theory, of a single MNP assumed to be immersed in a uniform a-Si medium. These curves are shown in Figure 5.20, and the positions of some of the peaks are indicated in Table 5.1. The calculated plasmonic resonances are significantly redshifted relative to those in the measured curves of Figure 5.19. That is because the a-Si layers surronding the MNPs are very thin, and therefore the MNPs cannot be assumed to be immersed in a uniform and isotropic a-Si medium. If the a-Si layers were thicker it would be difficult to measure the light transmitted through the samples in the wavelength range of interest.

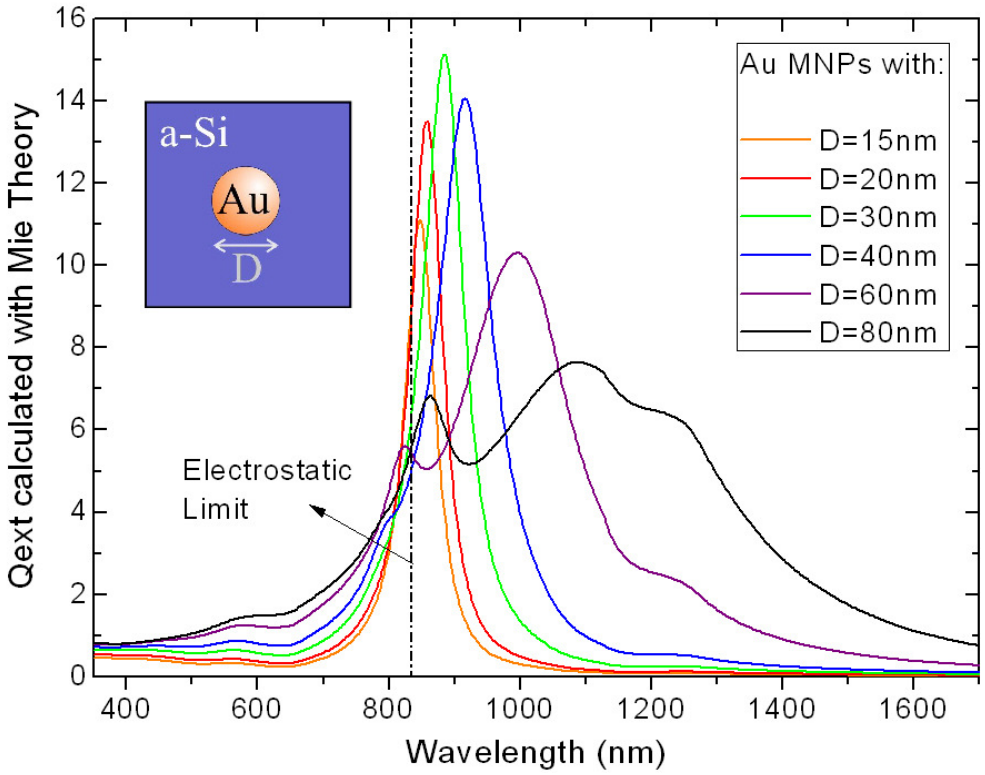

Figure 5.20: Extinction efficiency of an MNP inside an homogeneous a-Si medium, calculated with Mie theory, for the same MNP diameters of Figure 5.19. The refractive index of a-Si was taken from http://refractiveindex.info/.

The light extinction studies presented in this section reveal that colloidal MNPs can produce a considerable amount of absorption enhancement in their surrounding material, particularly at their dipolar SP resonance. However, given the spherical shape of these particles, it is difficult to tune such resonance to the infrared range and achieve a considerable amount of absorption enhancement for wavelengths above ~1μm (i.e., for energies below ~1.24eV). Therefore, spherical colloidal MNPs are not adequate to enhance the absorption of the sub-bandgap transitions in QD-IBSCs (see Figure 1.1). Instead, oblate (disk-like) MNPs should be used, as shown in Section 2.3. Oblate geometries are harder to fabricate in colloidal solution; however it is possible to synthesize other types of flattened MNPs, such as triangles or hexagons [112], which can also sustain SP resonances at the desired infrared energies.

Chapter 6

Colloidal quantum-dot intermediate band solar cells

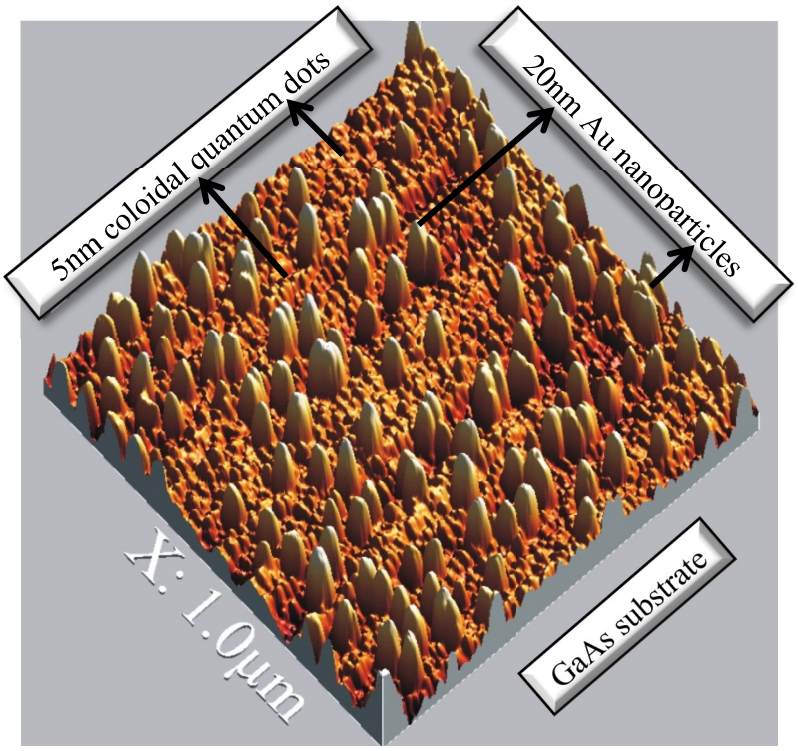

6.1 Introduction

In the previous chapter we reported the successful construction of metallic nanoparticle arrays on various substrates using a colloidal self-assembling process. The process yielded a remarkable degree of order and uniformity across the surface of arbitrarily large samples, demonstrating the high-throughput potential of colloidal wet-coating techniques. Such achievement led the authors to consider applying a similar procedure to the fabrication of quantum dot arrays composed of colloidal semiconductor nanoparticles. This could lead to the construction of novel quantum-dot intermediate band solar cells in which the quantum-dots would no longer be epitaxially grown on the substrate material, but rather deposited via colloidal chemistry.

As referred in Section 1.2, one may implement an intermediate band in a solar cell by constructing in its material a superlattice of QDs having a bangap lower than that of the host semiconductor (matrix) in which they are embedded. The offsets of the conduction or valence band, together with the quantum confinement provided by the QDs, give rise to a region with finite density of states within the matrix bandgap.

Quantum-dot intermediate band solar cells (QD-IBSCs) are usually fabricated with QDs epitaxially grown on semiconductor layers using the Stranski-Krastanov (SK) method [30]. Such devices are based, almost without exception, on III-V materials. The quantum efficiency of the prototype IBSCs fabricated with this method reveals an extended response for photon energies below the host material bandgap, allowing the verification of the IB concept. However, the impact of the intermediate band effects on the cell performance is still marginal since the band structure experimentally produced with such technological approach is far from the optimal IB structure represented in Figure 1.1c. First of all, the presence of the thin wetting layer below the QDs creates an effective reduction of the host material bandgap, and disrupts the three-dimensional electronic confinement required for the dots since it acts as an area of one-dimensional confinement (quantum well). Besides, the III-V QDs produced by the SK method have irregular and highly anisotropic shapes with in-plane dimensions considerably higher than the normal-to-plane dimension. The larger in-plane dimensions of these QDs cause the appearance of several discrete levels between the QDs ground state and the conduction band (CB) that enable the thermal (non-radiative) coupling between the IB

and the CB, lowering the cell voltage. So, in practice, there is not a single IB level such as in the optimal case of Figure 1.1c,d. Instead, usually 3 or 4 confined levels can be experimentally observed, which do not allow a sufficient separation between the IB and the CB for the required phonon bottleneck effect to occur [113]. Furthermore, there is a low photon absorption provided by the IB. This is attributed to the low absorptivity of the QDs which is observed to be more than one order of magnitude lower than that of the host material. Such shortcomings have been theoretically modeled with a quantum mechanical four-band *k.p* method [31] developed by our group; and they constitute the most crucial issues of the QD-IBSCs fabricated up to now.

The novel QD-IBSC proposed in this chapter can potentially solve the aforementioned problems, by adding important modifications related to the manufacturing of the QDs and to the incorporation of a plasmonic light trapping system to enhance the IB absorption. The main characteristic of such QD-IBSC is that its IB is formed by an array of semiconductor nanoparticles produced by means of colloidal synthesis in a solvent medium [114].

In recent years there has been a rapid advance in the synthesis of such nanoparticles, also called colloidal quantum dots (CQDs), which has led to a high degree of control over their size, shape, and composition [115]. Owing to their small dimensions, their band structure can be tuned with the particle size. This fact, coupled with the flexibility and high throughput of chemical synthesis, makes them attractive candidates for nanostructured PV materials [116, 117]. CQD arrays can be assembled in any substrate through inexpensive patterning processes such as spin-coating, dip-coating and inkjet printing, which offer the additional advantage of being highly scalable for the fabrication of large-area electronic devices such as entire PV modules.

It is well known that the establishment of PV systems in the energy market requires a combination of low cost and high efficiency in order to overcome balance-of-systems costs. A significant fraction of the overall production cost of wafer-based solar cells (such as the prototype IBSCs epitaxially grown by the SK method) is associated to the material requirements, in particular the substrate which constitutes more than 97% of the cell volume. Unlike SK grown QDs, CQDs do not require a lattice constant close to the host semiconductor since they are not fabricated epitaxially. So, CQDs can be virtually integrated in any matrix material, allowing the fabrication of thin-film IBSCs supported on top of inexpensive substrates such as glass, plastic or any kind of flexible

material. Besides, the size-effect bandgap tuning of CQD structures also enables the use of inexpensive, Earth-abundant semiconductors, both for the dot and host material, otherwise unsuited for PV.

6.2 Infrared-emitting colloidal quantum dots

During the last decade, research on CQDs has been growing exponentially. CQDs have been integrated not only in several different types of solar cell architectures (Schottky solar cells [118], depleted heterojunction cells [119], organic cells [120], dye-sensitized cells, etc.) but are also being explored in other optoelectronic applications (photodetectors [120-122], light emitting diodes, transistors [123], lasers [124], optical amplifier media [115], etc.), and as biological fluorescent tags for noninvasive optical imaging [125, 126].

Quantum confinement provides a promising alternative for bandgap engineering, preferable to the conventional ternary and quaternary stoichiometric tuning employed in thin-film or multi-junction solar cells composed of bulk materials. Most semiconducting materials in the 1-20nm size range exhibit quantum confinement effects which determine their electronic properties and cannot be described by classical theories. Such effects occur when the size of the nanoparticle is smaller than the bulk-exciton Bohr radius (a_B) of the semiconductor, and result in a blue-shift (energy increase) of the absorption peaks due to an increase in the effective bandgap.

The Bohr radius is given by:

$$a_B = \frac{4\pi\hbar^2\varepsilon}{e^2}\left(\frac{1}{m_e}+\frac{1}{m_h}\right) \tag{6.1}$$

where e is the electronic charge, ϵ is the dielectric constant and m is the effective mass of electrons (e) and holes (h).

Most of the work carried out up to the end of the 20th century on the synthesis and applications of semiconductor nanoparticles dealt with materials emitting in the visible spectral range. Over the last decade there has been a growing shift of attention towards IR emitting CQDs, due to their increasing range of applications such as in PV devices [115]. Those are the CQDs of interest for application in IBSCs.

Figure 6.1 shows the positions of the bulk bandgaps and effective bandgap energies of CQDs with 10nm and 3nm size, for a selection of semiconductors absorbing in the IR range.

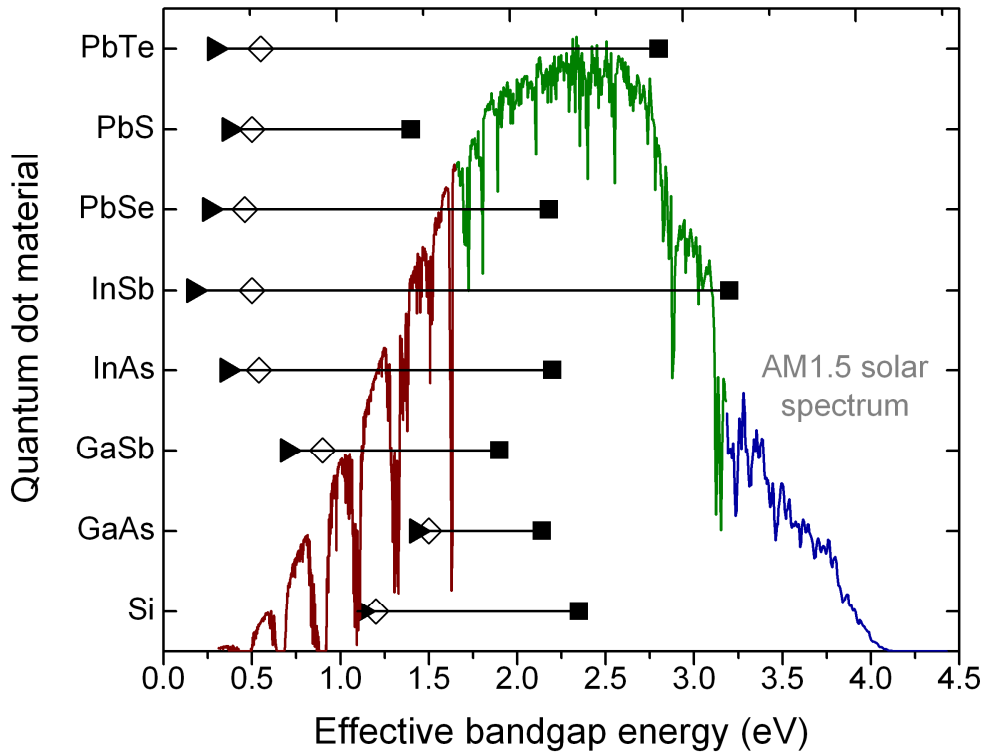

Figure 6.1: Size-dependent bandgap energies of several semiconductor quantum dots [115, 127]. The bandgaps are shown for bulk materials (▸) and for a nanocrystal diameter of 10nm (◇) and 3nm (■). As the particle diameter is reduced the energy gap is blue-shifted due to the quantum-confinement effect. Also shown for reference is the AM1.5G solar spectrum composed of infrared (shown in red), visible (in green) and ultraviolet (in blue) photons. The effective bandgap of most of the quantum dot materials represented here can be size-tuned over the solar infrared range and in part of the visible.

Among the range of IR-emitting CQDs, those that exhibit the best properties are the IV-VI series of semiconductors: the lead chalcogenides, also known as lead salts (PbS, PbSe and PbTe). This is not only due to their small bandgap but also due to a set of unique characteristics that these semiconductors possess [115]:

- large optical dielectric constants (e.g. 17.6 and 22.1 in the IR for PbS and PbSe, respectively, as compared to 11.9 for Si)

- the effective masses of the electron (m_e) and hole (m_h) are small and approximately equal (e.g. m_e=m_h≈0.1m_0 and 0.04m_0 for PbS and PbSe, respectively, as compared to m_e=0.26m_0 and m_h=0.36m_0 for Si; where m_0 is the electronic mass), and the Bohr radii (a_B) are large (e.g. a_B=18nm and 46nm for PbS and PbSe, respectively, as compared to 4.3nm for Si)
- are naturally occurring minerals which crystallize in the highly symmetrical sodium chloride structure
- have direct bandgap transitions at the *L*-point of the Brillouin zone

The large Bohr radii of the exciton shared almost equally between both the electron and the hole in lead chalcogenide CQDs allows for the study of quantum confinement effects in the sense of both charge carriers being confined, in contrast to most II-VI and III-V materials. Particle volume to Bohr radii ratios of 0.04 are attainable with the lead salts as opposed to 0.16 with the much-studied classical CdSe nanoparticle system (a condition that applies to all the II-VI and III-V materials, with the possible exception of InSb) [115]. The large Bohr radius of lead salts enables a wide tunability of their bandgap according to the particle size, which allows the production of CQD bandgaps at any energy in the IR range with particles of a few nanometers diameter [128]. Besides, it also delocalizes the carries, establishing greater electronic coupling between the QDs since the wavefunctions of the carriers spill outside the volume of the QDs enabling exchange interactions. This can reduce the effect of the nanoparticle surface traps and therefore facilitate charge transport [116, 117].

By far, the most varied literature studies and synthetic approaches in the synthesis of lead chalcogenide nanoparticles have been applied to PbS and PbSe CQDs [115]. There are fewer reported methods for the preparation of PbTe, and its absorption spectra displays a much broader series of transitions than those of PbS and PbSe. For these reasons, the preferential materials for the CQDs of the IBSCs considered in this chapter are PbS or PbSe.

Another interesting possibility of these CQDs that is being investigated is the production of the multiple exciton generation (MEG) effect, also known as carrier multiplication (CM) [129]. The efficient formation of more than one photo-induced electron-hole (*e*-*h*) pair upon the absorption of a single photon is a potentially important process in any opto-electronic device. This process has been observed in the generated

photocurrent of bulk PV materials (sometimes termed impact ionization). However, in bulk semiconductors it is not an efficient process since the threshold photon energy required is many multiples of the bandgap energy (E_G). For instance, in bulk Si, MEG does not become measurable until the photon energy exceeds 3.5 eV, an ultraviolet energy threshold that is beyond the solar spectral range. However, in semiconductor QDs the generation of multiple *e-h* pairs becomes much more efficient and the threshold energy can approach values as low as twice the bandgap energy, corresponding to the visible or near-IR spectral region. This occurs because the rates of excited state exciton cooling can be slowed down in quantized semiconductor structures due to the existence of discrete energy levels. This arises because the energy separation between quantized levels in QDs can be many times the typical phonon energy, thus originating a "phonon bottleneck" effect [129]. A quantum yield of 300% (3 excitons per photon) was already reported for PbSe CQDs at a photon energy of $4E_G$ [26].

6.2.1 Synthesis and chemical surface treatments

Colloidal semiconductors are synthesized from precursor compounds dissolved in solution. The solvent medium is usually organic and the particles are stabilized in solution by capping ligands/agents that attach to their surface, in the same way as the colloidal metal nanoparticles (MNPs) referred in Section 5.2. Such ligands are also typically organic molecules which fulfill three main tasks:

1. provide solubility of the particles in the solvent medium,
2. prevent particle aggregation, and
3. passivate the surface dangling bonds of the particle core.

The ligands play an important role in the observed physical properties of CQDs, particularly in the electric characteristics of CQD arrays deposited on a surface (CQD films). Nevertheless, several chemical treatments allow the manipulation of such capping agents enabling, for instance, the replacement of a certain organic ligand by another organic compound while the CQDs are in solution phase or even after they are deposited on a surface.

As an example, lead chalcogenide CQDs are usually synthesized in solution using octylamine (oleic acid) as the capping agent. Several studies on such oleate-capped CQDs have reported efficient fluorescence and absorption spectra, clearly revealing the

signature of the first excitonic states. This indicates that trapping processes are ineffective and that the surface is well-passivated with oleic acid [130, 131]. Nevertheless, several other organic compounds [128, 132] have also been reported as efficient ligands for this type of CQDs: formic acid, DNA, methylamine, butylamine, hydrazine [123], pyridine, dithiols such as 1,2-ethanedithiol (EDT) [118, 133, 134] and benzenedithiol (BDT), among others.

The length of the organic ligand molecule is an important parameter to consider, since it controls the spacing between the CQDs when they are deposited onto a flat surface. In the example of lead chalcogenides capped with oleic acid, the films of deposited CQD arrays maintain an inter-dot distance of ~2.5 nanometers. However, this distance can be changed by chemically replacing the oleic acid ligands by another capping agent with longer or shorter molecular length. For instance, soaking the deposited CQD films in an EDT solution reduces the inter-dot spacing to ~1 nanometer because the length of the EDT ligand is shorter than the oleic acid molecule that originally dispersed the CQDs in the as-synthesized solution [134]. It has been consistently verified in the literature of CQDs that these ligand exchange treatments do not alter the QD size, which is favorable.

Due to their small molecular weight, these organic ligands are volatile and may be readily removed under thermal annealing after depositing the CQDs. This is important for the fabrication process of the CQD-IBSC described in this chapter, since the ligands are insulating and can therefore severely decrease the mobility (charge transport) of the photo-generated carriers in the IB material.

Apart from organic ligands, CQD surface passivation can also be accomplished by enclosing the dot in a thin semiconductor material of wider bandgap, called the shell. The shell material can be epitaxially grown during the colloidal chemical synthesis around the QD core, offering one potential solution to overcome the limitations of molecular ligands. This solution can improve the air stability and luminescence emission intensity appreciably, as demonstrated for instance for lead chalcogenide core/shell CQDs [124].

6.2.2 Absorption spectra of colloidal QD thin films

To test the stability of CQDs outside solution, we measured the extinction spectra of PbS dots after being deposited on a glass slide for several days. For these

experiments we used three solutions, bought from *Evident Technologies*, of PbS nanoparticles dispersed in 1-octanol with diameters of 2.3, 3.4 and 5.1nm. In these solutions the CQDs were stabilized in octanol by oleic acid molecules that are ~2nm long.

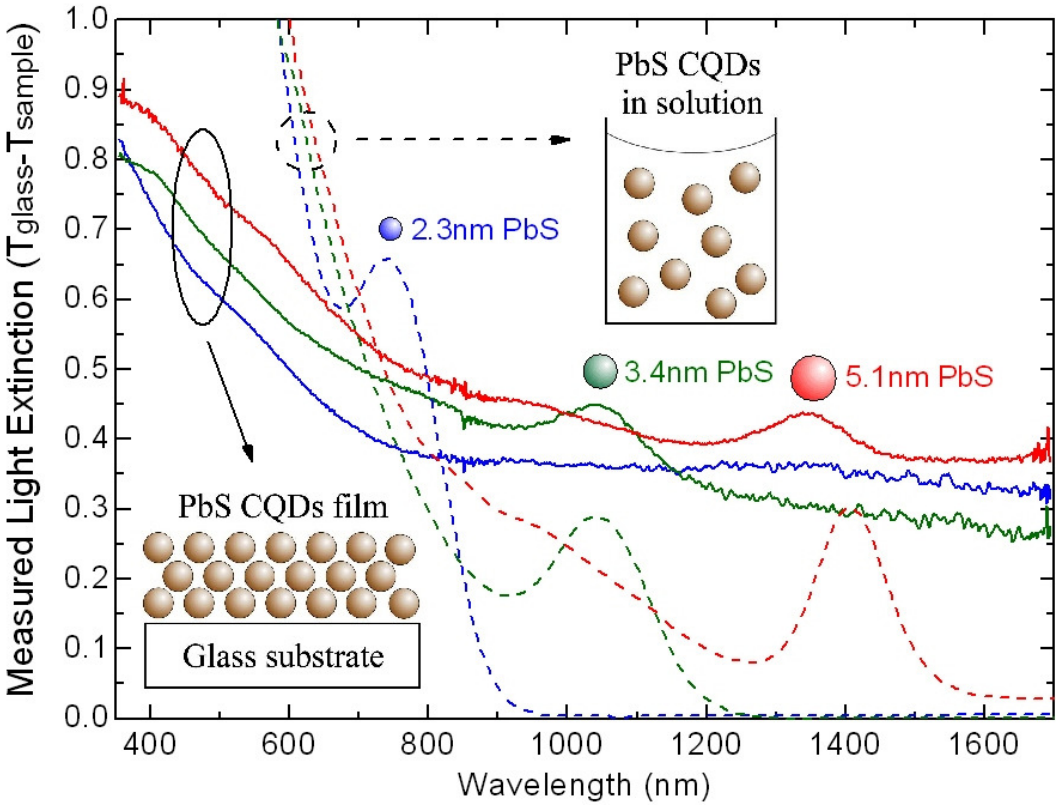

Figure 6.2: Measured light extinction of ~1μm thick films (solid lines) composed of PbS CQDs stacked on glass slides. The three films contain CQDs with distinct diameters from the three solutions bought from *Evident Technologies*. For comparison, we show the absorption spectra of the CQDs in solution (dashed lines, in arbitrary units) taken by *Evident*.

The extinction spectra of the CQDs was measured using the spectrophotometry technique described in Section 5.6. For that, thin-films of stacked CQDs were fabricated by controlled drop-drying of small volumes of the colloidal solution on glass slides. The films constructed in this way are composed of several layers of dots on top of each other, and have thicknesses in the range of 0.1-1μm as measured with a *Dektak* mechanical profilometer.

The solid lines in Figure 6.2 correspond to the extinction spectra of three films fabricated with CQDs of distinct diameters. The dashed lines in the figure are the

spectra of the CQDs in solution, before deposition. The peaks in the curves correspond to the CQDs ground-state (effective bandgap). These peaks are present in the extinction spectra of films with 3.4 and 5.1nm dots, and appear close to the peaks of the CQDs in solution. This indicates that these dots remain well stabilized by their capping molecules even after several days outside solution. However, the same may not occur with the 2.3nm CQDs, because films assembled with these dots do not show any absorption peak as can be seen in the solid blue line of Figure 6.2.

The total light extinction in CQD films is due to absorption inside the CQDs plus light dispersion (scattering) in the CQDs array. The effect of absorption originates the observed peaks (at the dots ground-state level) and is also responsible for the increase of the curves with lower wavelengths (absorption at the higher-energy levels of the dots). Since CQDs do not exhibit any significant resonant scattering properties, the effect of light dispersion in the film is only responsible for the vertical shift in the curves by a value of about 0.25-0.35.

6.3 Feasible light trapping with metal nanoparticles

Early experimental studies with prototype IBSCs formed with SK-grown QDs demonstrated that this cell technology is in need of efficient light trapping mechanisms to compensate for the observed low absorption in the QD arrays, as previously mentioned. In Chapter 2 it was shown that the intense electric near-field produced by the MNPs, when the incoming light matches their surface plasmon (SP) frequency, can enhance the absorption of QDs by a factor on the order of 10 or, in special cases of 100.

One of the interesting possibilities of the CQD-IBSCs proposed here [114] is that it allows an effective way of realizing the structure considered in Chapter 2 (depicted in Figure 2.2c and Figure 5.1), using an MNP array to enhance the absorption of light by the QDs. Since both MNPs and CQDs can be synthesized in colloidal solution, the fabrication of binary arrays of MNPs and CQDs can be achieved by low-cost wet-coating techniques able to pattern large-scale devices such as entire PV modules. In the next section further details are provided relative to the construction of such binary nanoparticle arrays.

6.4 Description of a thin-film CQD-IBSC

In this section we describe one way of realizing in practice an efficient CQD-IBSC device [114], composed by an array of CQDs and colloidal MNPs embedded in an inorganic or organic matrix material – see Figure 6.3. The ground-state confined energy levels of the CQDs form an IB in between the valence and conduction band of the host semiconductor, as shown in Figure 1.1. The colloidal metal nanoparticles sustaining plasmon resonances are used as a light trapping mechanism, concentrating the incoming light in the dots thereby increasing their absorption. Both the CQDs and MNPs have a shell material which acts as a potential barrier for the charge carriers and passivates the particles' surface. In addition, the shell around the CQDs has an optimal potential height to extend the spectral response of the absorption associated with electronic transitions from the IB to the conduction band up the minimum energy of the valence to IB transitions, as shall be described in Subsection 6.4.2.

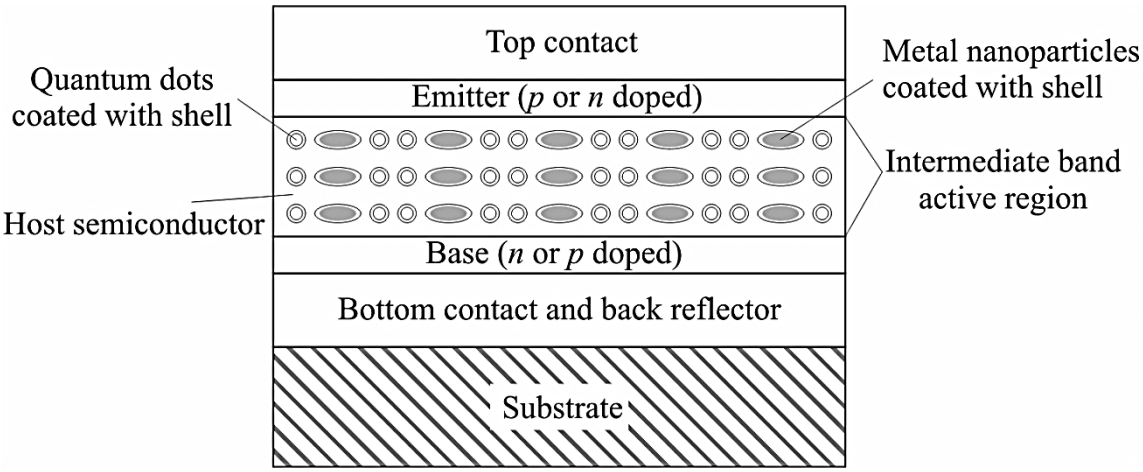

Figure 6.3: Representation of a simplified layer structure for the proposed CQD-IBSC. It consists of an IB-semiconductor (active region) sandwiched between two doped semiconductor layers (base and emitter). If the emitter is chosen to be *n*-doped then the base has to be *p*-doped, and vice-versa. The thickness of these doped layers should be small, in the range of 10-50 nanometers, and its material should preferentially be the same as the IB host semiconductor. The light enters in the cell from the top contact. The bottom contact is a regular metal that also acts as a mirror to provide additional light confinement in the active region. The entire structure is supported on a substrate which can be made of a rigid or flexible material.

The device can be composed by the layer structure shown in Figure 6.3. It consists of an IB semiconductor material sandwiched between *p*- and *n*-doped layers. The doped layers are made of a semiconducting material and they anchor the hole and electron quasi-Fermi levels respectively, so that the output voltage of the cell is determined by the split between these quasi-Fermi levels (see Figure 1.1d). The *p*-doped layer should only allow holes to pass through and the *n*-doped layer should only allow electrons. Besides, these layers also isolate the IB material, preventing it from being short-circuited by the metallic contacts.

The cell is illuminated from the top contact which can be constituted by a transparent conductive layer [such as Indium-Tin-Oxide (ITO)] or a metallic contact grid. The light that is not absorbed in a first pass through the cell material is reflected back into the cell from the bottom metallic contact. This contact can be made of aluminum and, apart from extracting the photo-generated current, it acts as a back reflector (mirror) thus contributing to the light confinement in the cell active region.

The whole cell structure is mounted on a substrate that acts solely as a mechanical support and can be composed either of a rigid (typically glass or a low-cost wafer) or flexible material (e.g. plastic foil). The cell layer structure can be mounted on top of the substrate, following the arrangement shown in Figure 6.3, or beneath the substrate if the substrate is transparent. In the latter configuration the substrate is termed superstrate, acting as window for the illumination and as part of the cell encapsulation.

In addition to the mentioned layers, additional layers can exist for different purposes as, for example, the inclusion of buffer layers between the doped layers and the contacts to passivate surface defects and ease the current extraction.

Concerning the IB active layer, it should be composed of a host semiconductor material with a bandgap close to the optimal value of E_{CV}=1.95eV (see Section 1.2) in which an array of QDs and MNPs, both previously synthesized in colloidal solution, is embedded. The role of the embedded colloidal particles is to extend the absorption and consequent photo-current generation of the host material to energies below E_{CV}, through the creation of an IB. Since the IB is electrically isolated, the generated current is delivered to the contacts through the host material. Therefore, the host has to allow sufficiently high carrier mobility so that the energy of the photo-excited electrons and holes is not lost during transport.

6.4.1 Host semiconductor of intermediate band material

The host material of the IB region should be composed by a semiconductor with a bandgap close to the optimal value of E_{CV}=1.95 eV. It may be a low-cost inorganic or organic semiconductor typically used in thin-film technology, in order to allow the inexpensive fabrication of the device. Three types of materials are proposed here for the host semiconductor material of the IB region: hydrogenated amorphous silicon, a multinary chalcopyrite compound, or a conjugated conductive polymer. These are described in the following subsections.

6.4.1.1 Hydrogenated amorphous silicon host

Hydrogenated amorphous silicon (a-Si:H) is the most widely used material in thin-film solar cells. In addition to reduced fabrication cost, a-Si:H provides the advantage of increased light absorptivity, which allows the reduction of the solar cell thickness [135]. Since less material is required for a-Si:H films, the devices composed by such material can be lighter (especially important for space application) and less expensive.

The role of the hydrogen in the amorphous silicon material is to decrease the amount of defect states in the amorphous network, which cause current loss due to carrier trapping and recombination. This occurs because the hydrogen binds to the dangling bonds of the a-Si, passivating its defects.

Integration of CQDs into a-Si:H is facilitated by the fact that a-Si:H can be grown using low-temperature techniques that are gentle enough to preserve the integrity of the nanoparticles. It has been verified by [118] that, by directly depositing a-Si:H on top of a CQD layer, a good electronic coupling can be achieved at the CQD/a-Si:H interface. In addition, the encapsulation of the CQD array inside a-Si:H isolates the CQDs from the external environment, preventing oxidation and other adverse effects, which is essential for the stability of the devices.

A low processing temperature also allows the deposition of a-Si:H on a wide range of low-cost substrates which can be rigid (e.g. glass, metal sheet), flexible (e.g. plastic) or roll-away types (e.g. polymer foil). Currently, the highest quality technique for deposition of a-Si:H thin-films is by Plasma-Enhanced Chemical Vapor Deposition (PECVD), which enables deposition over large areas. Another commonly used technique is by radio frequency magnetron sputtering. It was demonstrated [118] that

these techniques are compatible with CQD integration in a-Si:H, which is an encouraging aspect for the large-scale production of CQD-IBSC devices.

Once deposited, a-Si:H can be doped in a fashion similar to conventional crystalline Si, to form the *p*-type or *n*-type layers of the IBSC structure (see Figure 6.3). However, doped a-Si:H has two or three orders of magnitude larger defect density in comparison to intrinsic a-Si:H. The diffusion length of charge carriers in doped aSi:H is very small compared to crystalline silicon. For this reason, a-Si:H solar cells cannot function successfully as a *p*-*n* junction, but a relatively defect-free intrinsic layer has to be inserted between the *p*-type and *n*-type layers. Since the underlying processes of the photovoltaic effect (absorption of light and separation of photo-generated carriers) take place in the intrinsic layer, this layer is called the active layer in a-Si:H cells. In our cell design (see Figure 6.3) such layer is formed by the IB region.

Amorphous alloys of silicon and carbon (amorphous silicon carbide, also hydrogenated, a-$Si_{1-x}C_x$:H) are an interesting variant. The introduction of carbon atoms adds extra degrees of freedom to control the bandgap of the material. Increasing concentration of carbon in the alloy widens the bandgap. This can be used to tune the bandgap of the compound from a minimum value of 1.75 eV without carbon (x=0) to about 3 eV with SiC (x=1). Therefore, the optimal value for the host material bandgap (E_{CV}=1.95 eV) can be achieved with hydrogenated amorphous silicon carbide having an appropriate carbon concentration.

6.4.1.2 Chalcopyrite host

The host material can also be made of a multinary chalcopyrite compound. It may be a derivative of the type (Cu,Ag)(Al,Ga,In)$(S,Se,Te)_2$ obtained from the deviations in the stoichiometry that provide an alloy having a bandgap close to the optimum E_{CV}=1.95 eV. Examples of suitable multinary chalcopyrite semiconductors of the type (Cu,Ag)(Al,Ga,In)$(S,Se,Te)_2$ are: $CuAlTe_2$, In_2S_3, $AgInS_2$, $AgGaSe_2$ and $CuGaSe_2$ with bandgaps of 2.1, 2.0, 1.9, 1.8 and 1.7 eV, respectively [136, 137].

6.4.1.3 Conjugated polymer host

Another alternative to the IB host material can be realized with a conjugated conductive polymer. In contrast to traditional semiconductors, conjugated polymers

made with organic materials provide ease of processing, low cost, physical flexibility, large area coverage, lightweight, and are potentially disposable.

The integration of CQDs in organic polymers is considerably more facilitated than in inorganic semiconductors since the CQDs can be mixed together with the polymer in solution-phase before depositing them. In particular, lead chalcogenide CQDs have been successfully assembled in a polymer matrix by the authors in [120], and it was verified that the CQDs were able to extend the photocurrent spectrum of the polymer host to photon energies below its forbidden bandgap.

Polymers of the type PPV- (poly[p-phenylene vinylene]), PT- (polythiophene) and PF- (polyfluorene) have bandgaps around 2eV, therefore close to the optimum host bandgap of 1.95 eV. Typical examples are the well-known compounds: MEH-PPV (poly[2-methoxy-5-(2'-ethyl-hexyloxy)-1,4-phenylene vinylene]), PT and P3HT (poly[3-hexylthiophene]) whose bandgaps are 2.2, 2 and 1.9 eV, respectively [138]. Nevertheless, several synthetic approaches can be used to conjugate other organic compounds and fine-tune their bandgaps. The bandgap of polymers can be manipulated, for instance, by changing its substituents and/or introducing side groups. In this way, a wide range of derivatives can be chemically fabricated with bandgaps engineered to match 1.95 eV, such as the case of polyfluorene-based alternating polymers: PFR3-S (poly[9,9- dioctylfluorene- 2,7- diyl- *alt*- 2,5- bis(2- thienyl- 1- cyanovinyl)- 1- (2′- ethylhexyloxy)- 4- methoxy- benzene- 5″,5″- diyl]) and PFR4-S (poly[9,9- dioctylfluorene- 2,7- diyl- *alt*- 2,5- bis(2- thienyl- 2- cyanovinyl)- 1- (2′- ethylhexyloxy)- 4- methoxy- benzene- 5″,5″- diyl]) with bandgaps of 2.21 and 1.95 eV, respectively [139].

These materials can be doped by reduction (*n*-type) or oxidation (*p*-type) to form the doped layers of the IBSC structure shown in Figure 6.3.

6.4.2 Core/shell colloidal quantum dots

Colloidal chemistry allows the fabrication of quantum dots having a core/shell structure; i.e. semiconductor nanoparticles of approximately spherical shape (the core) surrounded by a thin shell of a semiconductor or insulating material. The shell around the QDs core is usually employed for passivation of the nanoparticle surface, and to improve its chemical and opto-electronic stability. However, in CQD-IBSCs the shell

coating can also be important to improve the absorption properties of the quantum dots, as shall be explained in this section.

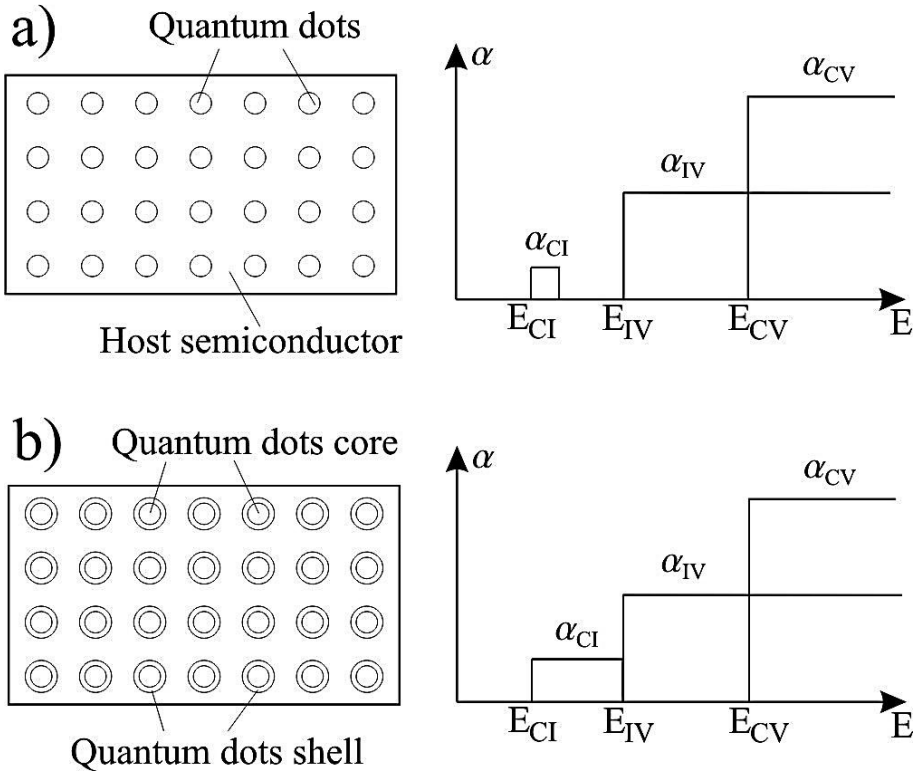

Figure 6.4: **a)** *Left* – top view of an IB layer with a QD array composed by typical semiconductor QDs without shell. *Right* – corresponding absorption spectrum. The transitions from the IB to the CB can only occur in a limited energy range close to E_{CI}. **b)** Same as (a) but with QDs coated with a shell material that provides a potential barrier for the conduction electrons, as shown below in Figure 6.5.

As described in Section 1.2, a typical IB material, formed by an array of QDs, exhibits three absorption coefficients related to the three electronic transitions – from the VB to the CB (α_{CV}), from the VB to the IB (α_{IV}) and from the IB to the CB (α_{CI}). These coefficients are schematically represented in Figure 6.4a. The first absorption coefficient (α_{CV}) is associated to the host semiconductor and is typically on the order of magnitude of $10^4 cm^{-1}$ (the case of GaAs or amorphous Si). The coefficient α_{IV} is usually one or two orders below ($\sim 10^{2-3} cm^{-1}$), as experimentally observed in prototype IBSCs [30]. However, the absorption of photons from the IB to the CB (α_{CI}) is estimated to be much lower than the previous two coefficients. The reason being that it implies a transition from a confined (localized) state within the QD to an extended (delocalized) state in the host material CB [31, 140]. The localized-to-delocalized character of the

transition leads to a low wavefunction overlapping between the two states, which results in a small matrix element for such optical transition. Besides, quantum selection rules determine that such matrix element is only non-zero if the confined and extended states differ only in one quantum number (n_x, n_y or n_z associated, respectively, to confinement along the x, y and z directions) [141]. Thus, an electron in the IB can only transition to a state close to the minimum of the CB, so it can only absorb photons having energy higher but close to E_{CI}. As such, α_{CI} not only has a small magnitude but also has a narrow spectral width close to E_{CI}, not allowing the IB material to absorb most of the photons with energies below E_{IV} (see Figure 6.4a).

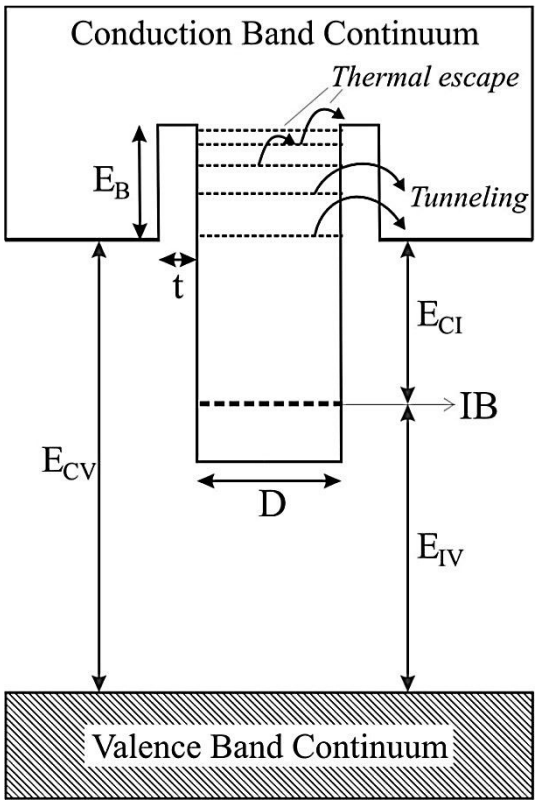

Figure 6.5: Energy band diagram of a colloidal quantum dot with diameter D coated with a thin shell material of thickness t, embedded in the host semiconductor material. The lowest confined level (ground-state) of the QD provides the IB. The shell acts as a potential barrier of height E_B for the conduction electrons, which produces additional localized levels above the minimum of the CB. Excited electrons can escape to the host material CB by thermal hoping or by tunneling across the thin barrier walls.

One of the innovations employed in the IBSC design described in this chapter [114] is aimed at increasing the spectral width of α_{CI} and extend it up to $E=E_{IV}$. This can be

accomplished by using a thin shell material, having a bandgap higher than that of the host semiconductor, enclosing the QDs core (see Figure 6.4b). The shell material acts as a potential barrier for the excited electrons, as depicted in Figure 6.5. We denote as E_B the energy difference between the top of the shell potential barrier and the minimum of the CB. This potential barrier extends the QD confinement to energies above the CB minimum, creating localized bound states between the CB minimum and the top of the barrier walls to which electrons from the ground state (the IB) can jump. Since such transitions are from a localized state to another localized state their associated absorption coefficient is high compared to transitions to CB extended states. Thus, this solution allows the electrons in the IB to better absorb photons with energies higher than E_{CI} (up to $E_{CI}+E_B$). The excited electrons in the localized states of the barrier then transition to the host material CB by thermal escape or tunneling across the thin shell barrier, as illustrated in Figure 6.5.

The parameters required for the CQD (core diameter, shell thickness, core and shell materials) are those that optimize the absorption coefficients of the IBSC associated to the electronic transitions to (α_{IV}) or from (α_{CI}) the IB, as shall be described next.

The position of the confined levels of the QDs can be calculated using quantum mechanical models of a particle (an excited electron and its hole counterpart) in a three-dimensional spherical box (the QD) [141]. As the particle diameter is reduced the separation between the energy of the excited levels increases, due to the quantum-confinement effect, and the energy gap between the QD valence states and its first excited ground state also increases (an effect known as the bandgap blue-shift).

In view of the above, two requirements can be formulated relative to the QD core material and diameter *D*:

1) The diameter has to be sufficiently small to allow only one excited level, which forms the IB, below the CB minimum, as shown in Figure 6.5.

2) The energy gap between the CB minimum and the QD ground state (the IB) has to be close to the optimum value of E_{CI}=0.71eV. Considering that the host semiconductor has an optimal bandgap of E_{CV}=1.95eV, this is the same as to require that the energy gap between the QD valence band and its first excited ground state is E_{IV}=1.24eV (see Figure 6.5)[3]. This limits the number of semiconductor materials that can compose the QDs core to only those that have bulk bandgaps below 1.24eV. Semiconductors with bulk bandgaps above

[3] Assuming that there is an alignment of the valence bands of the QD and host material

1.24eV have to be discarded for the dots, since in these materials the quantum-confined IB level can only occur at an energy E_{IV}(E_{CI}) above(below) the optimal energy. For instance, all the materials represented in Figure 6.1, with the exception of GaAs, can be eligible for the QDs.

In view of these requirements, and attending to the values in Figure 6.1, the QDs core should have a diameter *D* in the range of 1-10 nanometers. The preferred semiconductors that can compose the QDs core are the lead chalcogenide materials, particularly PbS or PbSe, due to their remarkable properties listed in Section 6.2.

The optimal shell material to be used around the QDs core is that which provides a potential barrier height equal to $\mathbf{E_B=E_{IV}-E_{CI}}$ (=0.53eV for the optimal gaps). Such optimum value allows the spectral width of α_{CI} to extend from E_{CI} to E_{IV}, without overlapping with α_{IV}, as shown on the right plot of Figure 6.4b. No overlap should occur between α_{CI} and α_{IV} since that would reduce the achievable cell efficiency [142]. In this way, the present IBSC device is able to generate photo-current from a broader range of photon energies than the conventional QD-IBSCs whose α_{CI} (see Figure 6.4a) is limited to energies close to E_{CI}.

The shell can be formed in solution phase during the colloidal synthesis or by controlled modification of the CQD surface; and it can be composed by a heterophase of oxide or nitride compounds alloyed with the core material. In the case of the preferential lead chalcogenide CQDs, the shell can be formed by controlled oxidation of the particle surface, forming a layer of oxides (of the type $PbXO_4$) together with PbX (where X stands for S, Se or Te) around the PbX core [143]. The shell thickness (*t*) should be about 1-2 nanometers, which is sufficiently high to allow quantum confinement in its interior, but also thin enough to enable electron tunneling across its potential walls.

Another important contribution of the QD shell, apart from enabling the spectral extension of α_{CI}, is the passivation of the dangling bonds existing at the QD surface. Such surface bonds create impurity states that act as traps for the photo-generated free carriers and cause electron-hole recombination, which reduces the photocurrent supplied by the solar cell. The carrier trapping and recombination at the QD surface is prevented when the dot is enclosed in a passivating shell material, with a higher bandgap than that of the host medium, which provides a potential barrier (wall) for the carriers. Besides, the shell also improves the chemical stability of the QDs over a long period of time and their optical stability for many illumination cycles. A similar solution has already been

incorporated in a patent by S. Forrest (U.S. Pat No. 7,414,294). However, the patent only considers the passivating effect of the QD shell material, and does not account for the important optimization of the shell potential barrier E_B to increase the spectral width of α_{CI}, as described in this section.

6.4.3 Colloidal metal nanoparticles sustaining surface plasmons

Another improvement introduced in the IBSC design detailed in this chapter is the implementation of a near-field light trapping structure to further increase the amount of photo-current generated by the intermediate band effect [114].

The light trapping structure is realized with an array of metallic nanoparticles (MNPs) that act as antennas for the incident light, bringing the incident energy from the surroundings and focusing it in their localized near-field. Such concentration effect is used here to increase the absorption in the CQDs placed close to the MNPs surface. As described in Chaper 2, the scattered near-field around an MNP can achieve particularly pronounced magnitudes for a MNP size well below the wavelength of the illuminating light, i.e. in the so called electrostatic scattering regime [23]. In this regime, the region of highest light intensity occurs at the MNP surface, in the direction of the incident electric field (normal to the incident light propagation direction), and is significant within a small region of about the MNP size outside the particle. Therefore, the MNPs should be positioned on the same plane as the QDs with an arrangement such as that sketched in Figure 2.2c and Figure 5.1.

When inserting metallic particles inside the active region of a solar cell they act as traps for the photo-generated free carriers causing electron-hole recombination and photo-current degradation. This recombination can be suppressed by coating the MNPs with a passivating semiconductor or insulating material having a higher bandgap than the host medium. The high bandgap of this passivating coating creates a potential barrier around the MNPs, such as the shell around the CQDs, which prevents carriers from reaching the metal surface and recombine. However, this coating should be thin enough to avoid quenching the light scattered by the MNPs; i.e. it should have a minimal thickness (on the order of the nanometer) just sufficient to prevent carrier tunneling across it.

The presence of the passivating shell around the MNP affects its polarizability and, thus, its SP frequency. For core/shell nanoparticles the polarizability is given by eq. (2.4).

As shown in Chapter 2, the peak intensity of the light scattered by an MNP occurs at the frequency of the illuminating light that matches its SP resonance. That is the frequency that maximizes (2.4), and thus allows the highest absorption enhancement by the receiving material in the MNPs near-field; in this case by the QDs. Therefore, the MNPs should have a shape, particularly an aspect ratio, that sets their SP resonance at an energy within the spectral width of α_{CI} or α_{IV}; i.e., in between E_{CI} and E_{CV}.

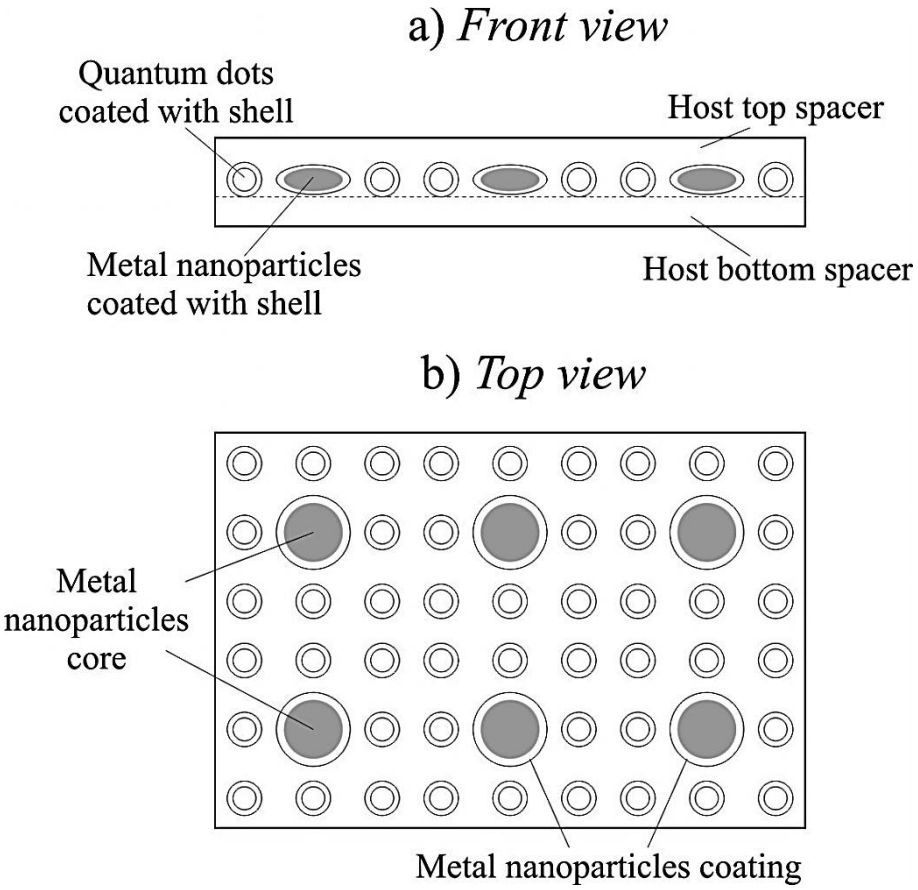

Figure 6.6: **a)** Front view of a binary array of CQDs and MNPs deposited on top of a layer of host material (bottom spacer) and then covered with another layer of host material (top spacer) that embeds the nanoparticles in the host medium. **b)** Top view of the binary array of CQDs and MNPs, both coated with a shell material.

The SP frequency is independent of the MNP size; however, the size has to be much lower than the wavelength of the illuminating light, according to conditions (2.1),

to remain in the electrostatic scattering regime. Since the wavelengths of interest are on the order of the micrometer, the preferential MNP sizes are in the range of tens of nanometers, therefore of the same order of magnitude as the CQD sizes.

As for the MNP material, it should be composed by a noble metal such as gold (Au) or silver (Ag). Previous experimental and theoretical literature studies confirm that nanoparticles composed by these metals are those that exhibit the strongest plasmonic response [42], mainly due to the relatively low imaginary part and high real part of their dielectric function in the infrared frequency range. Besides, both silver and gold metals can be synthesized in colloidal aqueous solution with remarkable uniformity in size and shape, as described in Section 5.2.

The inclusion of an array of optimally shaped MNPs, coated with a passivating shell, side-by-side with the QDs (illustrated in Figure 6.6) can increase the QDs absorption by a factor of about 10 or, in special cases of 100; as demonstrated in Section 2.3 and in [21, 38]. This may allow the magnitude of the sub-bandgap absorption coefficients of the IBSC (α_{CI} and α_{IV}) to approach that of the host medium coefficient (α_{CV}) for the appropriate photon energies.

Besides, on a more practical note, both core/shell MNPs and QDs can be synthesized in colloidal solution; so the fabrication of the proposed array of MNPs and CQDs can be achieved by low-cost wet-coating techniques able to pattern large-scale devices.

The most typical shell material used to coat colloidal nanoparticles of silver and gold is silicon dioxide (silica). If silica is used for the MNP shell it should have a thickness of a few nanometers, as indicated in Section 2.3. Such shell thickness should be sufficiently thick to prevent carrier tunneling but also thin enough to avoid shading the light intensity scattered by the MNP core.

6.4.4 Deposition of binary arrays of colloidal QDs and MNPs

The region where the light scattered by an MNP is more intense is at the point of intersection between its surface and the direction of the incident electric field vector which rotates in the plane orthogonal to the light propagation direction. So, the MNPs should be inserted side-by-side with the CQDs on the same plane, as sketched in Figure 6.6.

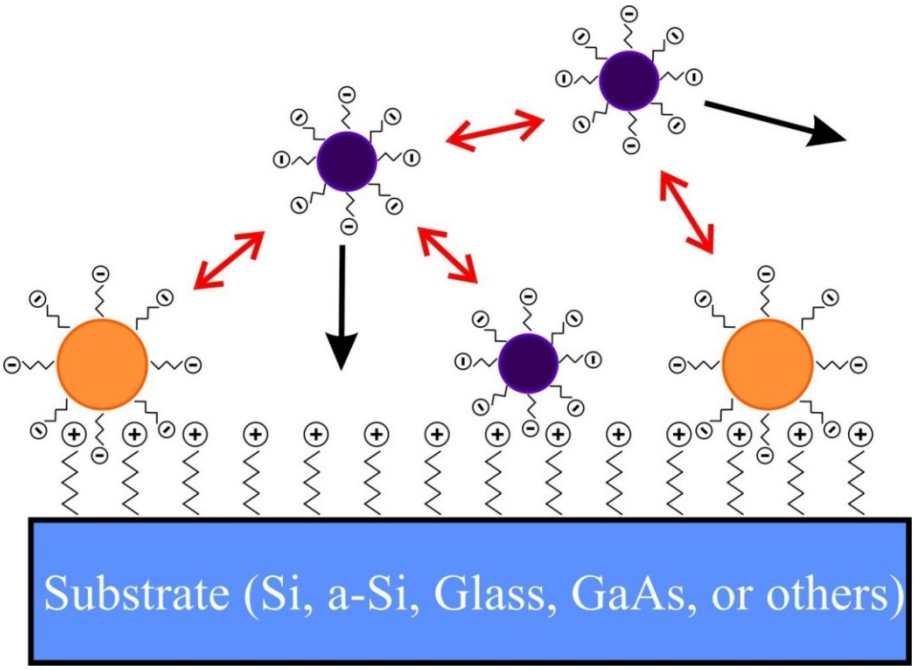

Figure 6.7: Self-assembled deposition of colloidal QDs in the spaces between the MNPs. The negative surface charge of the MNPs' and CQDs capping agent causes the particles to repeal each other (red arrows). They are attracted to the substrate (black arrows) if its surface is functionalized with molecules that have a positive charge on their end group.

[*Image not to scale* - the length of the organic molecules (zig-zag lines) is exaggerated for better visualization]

To deposit the MNPs and CQDs in a pattern similar to that of Figure 6.6 it is preferable to use wet-coating deposition techniques (e.g. spin-casting, dip-coating, ink-jet printing) so that all the steps involved in the assembly of the solar cell can be accomplished with inexpensive and large-scale processes [144]. One method to pattern a binary array of MNPs and CQDs in this way is by chemically functionalizing the surface of the host material before deposition, following the procedures described in Appendix C. First, the surface of the bottom host layer (bottom spacer in Figure 6.6a) is functionalized with a monolayer of appropriately conjugated molecules containing an end group that binds to the dangling bonds of the host surface and another end group that binds to the ligands attached to the colloids surface (as represented in Figure 5.7 and Figure 5.8). The preferential compound to functionalize the surface of the host material is an organic amino-silane such as APTES (3-Aminopropyltriethoxysilane) or APTMS (3-aminopropyltrimethoxysilane) [145], as used in the experiments reported in Chapter 5. Secondly, the solution containing the MNPs is dip-coated onto the

functionalized host surface and the MNPs surface ligands anchor the MNPs to the amino-silane end groups. The electrostratic repulsion between the MNPs establishes a certain inter-particle separation distance on the surface. The CQD dispersion is then spin-casted onto the same surface of the bottom spacer layer and the molecular ligands on the CQDs surface anchor the CQDs to the free amino-silane end groups in the areas not covered by the MNPs. Since the CQDs are smaller than the MNPs they deposit in the space between the MNPs, as illustrated in Figure 6.7 and Figure 6.8.

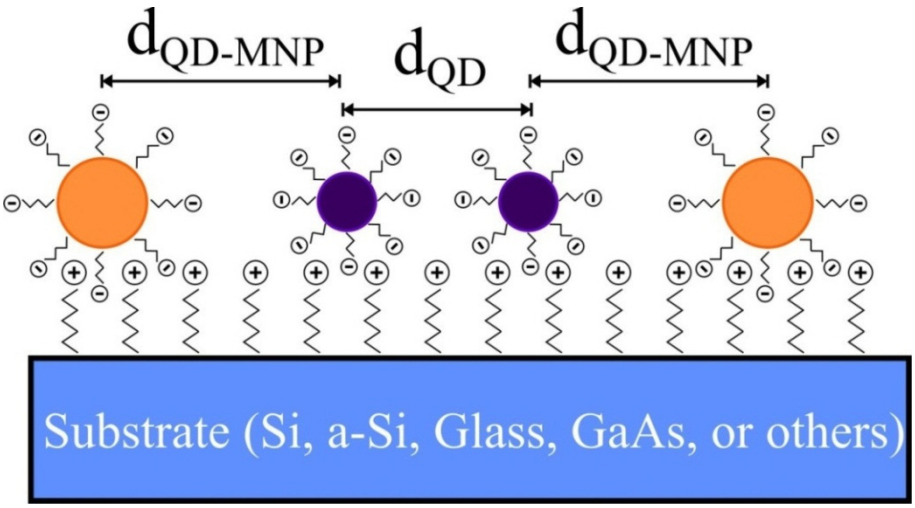

Figure 6.8: The electrostatic repulsion between the MNPs and CQDs keeps them separated by a certain distance upon deposition. The separation distance between the CQDs (d_{QD}) and between the MNPs and the CQDs ($d_{QD\text{-}MNP}$) depends on the surface charge density of the colloids and on the pH of the solution.

[*Image not to scale* - the length of the organic molecules (zig-zag lines) is exaggerated for better visualization].

Finally, a cleaning step is performed before depositing the top spacer layer of host material (see Figure 6.6a) over the array of MNPs and CQDs. The surface is cleaned from the organic compounds, or other contaminating species employed in the chemical functionalization of the surfaces, by heating the device at ~300 ^{o}C which evaporates the molecular compounds but should not affect the colloidal particles (nor the previously deposited layers of the IBSC structure in Figure 6.3). This should be followed by chemical cleaning (degreasing) in baths of acetone and isopropanol, to wash out the contaminants without removing the deposited colloids.

Figure 6.9 and Figure 6.10 show examples of AFM images revealing the obtained distributions of binary arrays of MNPs and CQDs, respectively in GaAs and Si samples. Similar depositions were also obtained on glass and a-Si films.

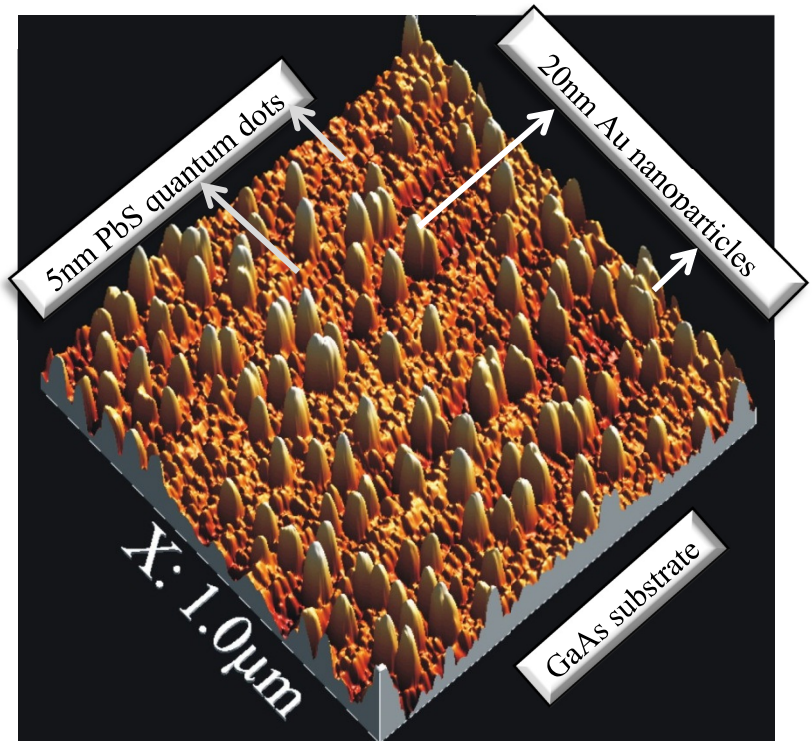

Figure 6.9: AFM image of a self-assembled binary array of Au MNPs (20nm diameter) and PbS CQDs (5.1nm diameter), patterned on a GaAs sample that was previously functionalized with APTMS. The CQDs (smaller dots) deposit in the areas between the MNPs (bigger particles).

It is possible to gain more control over the positioning of the patterned particles by coupling our previously described wet-coating method with a lithographic process, such as performed in [144]. This would consist in a first lithographic step to chemically engineer the spatial-selectivity of the host material surface at the nanoscale, by selectively functionalizing the surface at the spots where the colloids are intended to be located. Then, the following step would employ a wet-coating process to cast the colloidal particles onto the treated surface and make them adsorb onto the functionalized spots. Finally, a rinsing step would be performed to wash out all the colloids that did not get attached to the surface.

As an example, since APTMS binds preferentially to oxidized surfaces one could locally oxidize the host surface only at certain points distributed in a square lattice, using for instance scanning probe lithography [100]. This way the APTMS, and

afterwards the nanoparticles, would only deposit at the previously oxidized points allowing the formation of a square array such as depicted in Figure 6.6.

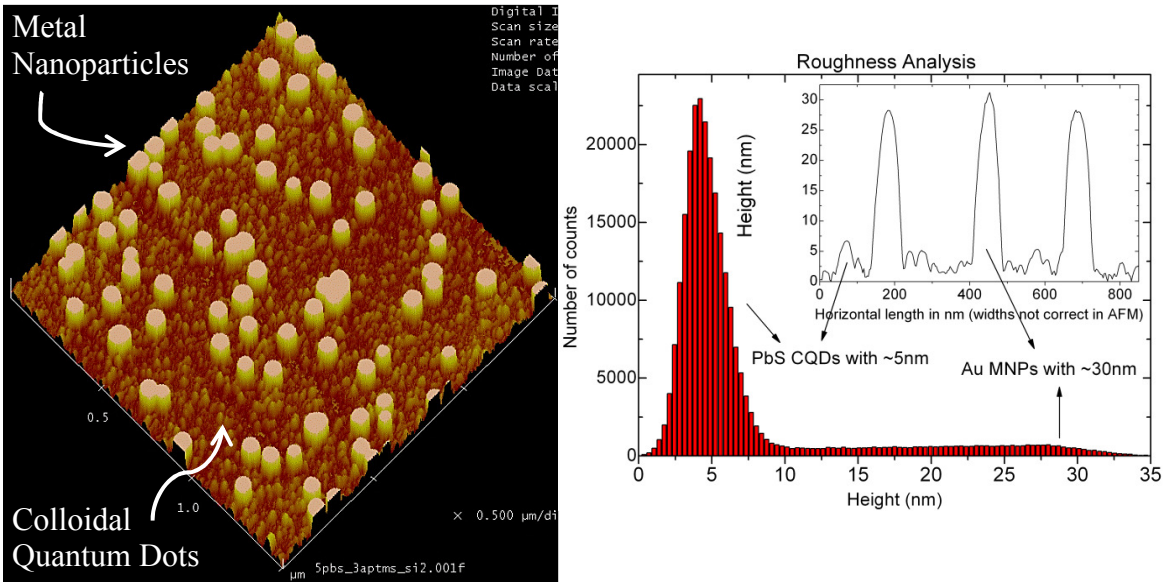

Figure 6.10: **Left** – AFM image similar to Figure 6.9 but with Au MNPs of 30nm and PbS CQDs of 5.1nm diameter, deposited on a functionalized Si sample. **Right** – Heights histogram of the left image performed with the *Nanoscope* software. The main peak of the histogram corresponds to the CQDs, exhibiting an average height (diameter) of 5±2nm; and the secondary peak close to 30nm corresponds to the MNPs. The inset in the plot is a cross-sectional profile at a spot on the left image, showing three MNPs and several CQDs deposited in between them. This profile reveals that no CQDs are deposited on top of the MNPs; the CQDs only deposit in the empty spaces between the MNPs with a certain separation distance dictated by their electrostatic repulsion. Such distance can be calculated by measuring the positions of the peaks in the profile[4]: on average we have $d_{QD\text{-}MNP}\approx55$nm and $d_{QD}\approx25$nm, as defined in Figure 6.8.

6.4.5 Construction steps of the intermediate band layer

To conclude the description of the CQD-IBSC design considered in this section, we summarize in the list below the main steps involved in the construction of the whole IB region of Figure 6.3 [114]:

[4] Note that in AFM the lateral dimensions of the particles main appear bigger than what they are in reality since the minimum lateral resolution of AFM (usually on the order of 100nm) is dictated by the size of the tip. Therefore, one can only rely on the measurements of the vertical heights which have a resolution of about 1nm.

1. Deposition of a thin (10-30 nanometers) layer of host semiconductor. This constitutes the bottom spacer layer of Figure 6.6a.
2. Deposition of the MNPs array, by controlled assembly using a colloidal wet-coating technique, on top of the previous layer of host material.
3. Deposition of the CQDs, by controlled assembly using a colloidal wet-coating technique, in between the spaces of the MNPs, forming an array such as that shown in Figure 6.6b. All the CQDs in the array should be located inside the near-field region of an MNP. Therefore, each CQD should be separated from an MNP surface by a distance shorter than the MNP size.
4. The array of patterned CQDs and MNPs is covered by a layer having the same material and thickness as the host layer beneath the array deposited in step 1). This corresponds to the top spacer layer of host material of Figure 6.6a.
5. On top of this spacer layer additional layers of CQD and MNP arrays can be added. This is accomplished by repeating steps 2) to 4) as many times as the number of desired QD layers. The more layers are stacked in this way the higher becomes the absorption of the IB material. However, the total number of layers is limited since the thickness of the whole IB region should not considerably exceed the carriers' diffusion length in the host material. Otherwise, the energy of the photo-generated electrons and holes can be lost by recombination before the carriers reach the contacts. As an example, the carrier diffusion length in hydrogenated amorphous silicon ranges from 0.1 to 0.3 micrometers, therefore in this case the maximum number of QD layers that can be incorporated in the IB region is of 5-15.

6.5 Advantages of CQD-IBSC relative to previous technology

The solar cell structure proposed in the previous section is analog to that described in the literature as a quantum-dot intermediate band solar cell (QD-IBSC) obtained from epitaxial growth of III-V compounds by the Stranski-Krastanov (SK) method (see Section 1.2). However, the device proposed here, denoted as colloidal quantum-dot

intermediate band solar cell (CQD-IBSC), has a number of advantages which are listed in the next lines [114, 125]:

1. **Allows the use of inexpensive materials**. A significant fraction of the overall production cost of wafer-based solar cells (such as the prototype IBSCs epitaxially grown by the SK method) is associated to the material requirements, in particular to the substrate which constitutes more than 97% of the cell volume. Unlike SK-grown QDs, CQDs do not require a lattice constant close to that of the host semiconductor since they are not formed epitaxially. So, CQDs may be integrated in a broad range of host semiconductors made of Earth-abundant materials. Three types of host materials were proposed in Section 6.4.1: hydrogenated amorphous silicon, multinary compounds of the chalcopyrite type and conjugated conductive polymers. Such host materials can be deposited by low-temperature techniques, gentle enough to preserve the integrity of the embedded QDs, which enables the fabrication of the cell structure on a wide range of low-cost substrates which can be rigid (e.g. glass, metal sheet), flexible (e.g. plastic) or roll-away types (e.g. polymer foil). Such substrates, apart from allowing the reduction in the device costs, may also provide physical flexibility and lightweight (especially important for space applications).

2. **Provides ease of fabrication and large scale processing.** All the colloidal nanostructures present in the proposed solar cell are solution-processed. The shell-coated CQDs and MNPs are synthesized in solution phase, and their assembly onto the device may be performed through standard wet-coating procedures (e.g. by spin or dip coating, or ink-jet printing) which can pattern an indefinitely large area in minutes. Therefore, the costs and time of fabrication are minimal when compared with the advanced technology and high number of hours required for the epitaxial growth of conventional QD structures by the SK method. The same advantages also apply to the fabrication of the proposed host materials. Both hydrogenated amorphous silicon and multinary compounds of the chalcopyrite type can be deposited by chemical vapor deposition techniques, which enable low temperature deposition over large areas. The deposition of

conjugated conductive polymers and the integration of colloidal nanoparticles in such host material is even more facilitated than in inorganic semiconductors, since organic polymers are synthesized in solution and the colloidal particles may be blended together with the polymer in solution-phase before deposition.

3. **Enables a higher control on the quantum dot geometry.** There is little control on the size and shape of the QDs that grow by strain unbalance with the SK method. Such dots grow in the form of pyramids with a significant dispersion in their dimensions, as can be seen in Figure 1.1a,b. However, QDs synthesized in colloidal solution are formed in batches with a much higher monodispersivity in size and shape. Such solutions contain spherical particles all with practically the same diameter in the range of 1-100 nanometers. Colloidal chemistry also allows the fabrication of core-shell QD structures with controlled shell growth at the monolayer level. The shell material can grow epitaxially on the surface of the core semiconductor, with the latter acting as a seed for the heterogeneous nucleation of the former.

4. **The QDs have stronger quantum confinement.** Since CQDs are not limited by strain requirements such as the SK QDs, they can be made much smaller, with diameters of a few nanometers, and spherical. CQDs can thus provide strong carrier confinement in all three dimensions, while SK QDs usually only have strong confinement along the layer growth direction. This is because SK QDs have a pyramidal shape whose base dimensions (on the order of tens of nanometers) are higher than the height.

5. **There is no wetting layer.** In the SK process the QDs nucleate on top of a thin wetting layer of the same material as the QDs. This wetting layer acts as a quantum well which disturbs the quantum confinement potential of the dots and reduces the voltage (quasi-Fermi level separation) of the cell. No such layer exists with CQDs since they are formed in solution and may be latter deposited by wet-coating over the host material surface.

6. **Structures can be analytically modeled**. The above advantages also facilitate modeling and comparison with quantum theory, which is important for the optimization of the physical parameters involved in the design of IBSCs. The fact that CQDs have a well-defined spherical geometry and monodisperse diameters allows their opto-electronic response to be modeled by analytically solving the Schrödinger equation in a spherical potential box. More complex numerical approaches have to be adopted for the modeling of SK QD geometries, since it is not possible to solve Schrödinger equation analytically for the case of a pyramidal potential box.

7. **There is a broader range of optimal dot/host material combinations.** CQDs are processed from solution independently of the host material, which allows their integration in any type of matrix material (crystalline or amorphous). This is not possible with SK QDs since they are grown epitaxially from a crystalline substrate whose lattice constant has to be close to that of the QD material. So, in the SK method the number of possible dot/host material combinations is severely limited by epitaxial constraints. The fact that no lattice requirements are needed between CQDs and host semiconductor greatly widens the set of possible dot/host material combinations that can be implemented in the solar cell. This is a major advantage for the construction of an optimal IBSC structure having the desired energy gaps (E_{CI}=0.71 eV, E_{IV}=1.24 eV and E_{CV}=1.95 eV), since in this way there is a broader range of materials that can be employed to fulfill such optimum conditions.

8. **CQDs may have higher delocalization of their wave functions.** Although there is no physical contact between adjacent QDs, exchange interactions can occur between them and their confined wavefunctions can overlap since they spill outside the QDs. The overlap of the wavefunctions can form a continuous mini-band, which allows carrier transport within the IB. This is advantageous for the IBSC, but not a necessary condition, since it can compensate for possible non-uniformities in the illumination or doping profiles. Besides, it also strengthens the absorption coefficients associated to below-bandgap transitions due to the delocalization of the QD ground states. The higher the QD Bohr

radius [eq. (6.1)] relative to its physical radius the more the wavefunctions spill outside the QD volume, and therefore the more delocalized the wavefunctions become. The fact that no lattice matching is required between quantum dot and host material allows the choice of more convenient materials for the QDs with a Bohr radius several times higher than that of the III-V SK QDs. For instance, with lead chalcogenide CQDs particle volume to Bohr radii ratios on the order of 0.01 are attainable, as opposed to ratios on the order of 0.1 with practically all the III-V and II-VI materials, with the possible exception of InSb.

9. **Allows QDs with higher radiative lifetimes.** Some of the semiconductors incorporated into CQDs can exhibit unusually long exciton lifetimes when the CQDs surfaces are well passivated. For example, lifetimes greater than 1 microsecond are observed in lead chalcogenide CQDs at room temperature, much slower than in III-V SK QDs whose lifetimes are typically sub-nanosecond [125]. The particularly high lifetimes observed in lead chalcogenide CQDs (particularly made of PbS and PbSe) are attributed to two factors. First, the weaker exchange interaction between the electron and hole in the excited state. Second, the large dielectric mismatch with the external medium which screens out the external electromagnetic field. The present CQD-IBSC strategy allows the use of QDs with lifetimes much higher than those of QDs formed by the SK technique, which is beneficial in two ways: 1) Higher lifetimes imply lower non-radiative current loss due to recombination, such as that assisted by midgap recombination centers created by QD surface states (dangling bonds) or other impurities. 2) It allows the photofilling of the IB, facilitating the absorption of photons that cause transitions from the IB to the CB. One of the requirements for the optimal performance of the IBCS is that the IB should be half-filled with electrons to provide a reasonable rate of electron promotion from the IB to the CB. This can be accomplished either through modulation doping of the region where the QDs are located [28] or by photo-generating an electron population in the IB (photofilling) sufficient for the two-step generation process to work properly [146]. An IB formed with CQDs having high carrier lifetimes, such as lead chalcogenide CQDs, may be photo-filled at moderate light concentration intensities, thus providing an absorption coefficient (and therefore

final efficiency) for the intermediate transitions similar to that achieved with doped QDs. This relieves the necessity of having a half-filled IB in thermal equilibrium by QD modulation doping.

10. **Provides access to the QDs surface.** Unlike SK QDs, the surface of CQDs is accessible for chemical modification when they are in solution phase, or after being deposited on the host material. As commented in Subsection 6.2.1, the surface treatment of CQDs improves the opto-electronic properties of the quantum dots and their stability over time. This can be accomplished through the growth of a shell material enclosing the CQDs or the attachment of molecular ligands that eliminate the trap states formed by the superficial dangling bonds of the QDs. The incorporation of a shell in the CQDs also allows the extension of the spectral response of the QD absorption associated with electronic transitions from the IB to the CB (α_{CI}), as previously described in Section 6.4.2.

11. **The assembly of QD lattices is facilitated**. With the SK method it is difficult to control the position where the QDs nucleate in the wetting layer; they either grow on random locations or on top of other QDs previously formed in bottom layers. Colloidal deposition processes by wet-coating can provide a better control over the positioning of the colloidal particles on a surface, allowing a self-assembled array of equally spaced CQDs to be formed on a surface with a remarkable degree of order. Such self-organization reduces the engineering requirements of high-cost technological equipment, such as that used in the epitaxial SK growth. Besides, other types of colloidal deposition procedures can be employed that are able to precisely engineer the deposition pattern and inter-particle spacing as required [144].

12. **Enables the assembly of QDs with other colloidal species, such as MNPs for light trapping.** The present method facilitates the integration of CQDs with any other type of colloidal particles required to improve the properties of the IB material. The proposed use of metal nanoparticles to trap light is particularly suited for implementation in the CQD-IBSC device presented here, because the MNPs are fabricated in colloidal solution, such as the CQDs, and may be

assembled together with the CQDs by wet-coating colloidal deposition techniques. Nonetheless, besides MNPs, any other type of colloidal specie can be incorporated in the CQD array using controlled wet-coating assembling procedures. As mentioned previously, colloidal deposition methods (e.g. spin-casting, dip-coating or ink-jet printing), apart from being low time consuming and inexpensive procedures, allow the scalability of the technology since they are able to pattern indefinitely large-area devices such as entire PV modules.

Besides the previously listed advantages of CQD-IBSCs relative to conventional SK-grown QD-IBSCs, the device detailed in this chapter also presents relevant advantages relative to current single-gap solar cells with an absorbing material made of a tridimensional closed-packed array of CQDs [116, 117], such as the cells referenced in the beginning of Section 6.2. In such cells there is no host material in the active region. The active layer is composed by a tightly-packed CQD superlattice, where the CQDs are spaced by organic capping ligands that passivate their surface dangling bonds but constitute potential barriers for the carrier transport. Therefore, in these devices, carriers are delivered to/from the electrodes by an inefficient hopping transport mechanism, through percolated networks across the CQDs and the capping ligands [117, 134]. This yields low carrier mobilities (10^{-4}-10^{-3} cm^2/Vs are typical) and poor environmental stability; which together limit the conversion efficiency of these cells to very low values (~5%). This constitutes a severe impediment to the practical application of this solar cell technology.

In the IBSC design, the volume between the CQDs is filled with a host semiconductor which constitutes a straightforward way to eliminate the mobility problems of these cells. In the CQD-IBSC, hopping transport is avoided due to the two-photon process in which a first photon is absorbed, promoting an electron from the host VB to the IB formed by the CQDs, followed by a second photon which promotes the electron from the IB to the host CB that conducts it to the contact. As such, the delivery of photo-excited carriers to/from the contacts is not performed by hopping across the CQDs but rather by typical conduction through a semiconductor material embedding the CQDs. In conventional semiconductors, mobilities are several orders of magnitude higher than those of percolated CQD networks (around 10 and 10^2 cm^2/Vs respectively for amorphous and crystalline silicon). Therefore, the incorporation of the CQDs in a

semiconductor host with well-established growth techniques, as proposed here, allows efficient injection and collection of charge carriers from the CQDs, with the added benefit of isolating the CQDs from the external environment which prevents their oxidation and greatly improves the device stability [118].

6.6 Measured plasmon-enhanced absorption in CQDs

Proof-of-concept experiments have been performed to verify in practise the increase of absorption in CQDs that can be provided by MNPs. The experiments consisted in measuring the light extinction of different samples containing MNPs and/or CQDs using the spectrophotometry technique described in Section 5.6.

First, we attempted to measure the extinction of monolayers of PbS CQDs deposited on several substrates, such as those shown in the AFM images of Fig. C.5 in the end of Appendix C. However, the amount of light absorbed by a single layer of dots is so small that it was not possible to measure with our spectrophotometer. Therefore, the experiments had to be performed using CQD films composed of several CQD layers stacked on top of each other, as in Section 6.2.2. The absorption peaks corresponding to the CQDs ground-state could only be clearly observed in the extinction spectra of films having thicknesses on the order of the micrometer (see Figure 6.2).

Several samples were prepared containing arrays of Au MNPs with 40, 60 or 80 nm diameter deposited onto glass slides and then covered by films of PbS CQDs with 2.3, 3.4 or 5.1 nm diameter. The example in Figure 6.11 shows the results obtained with one of such samples having 40nm MNPs embedded in a CQD film with 5.1nm dots (red curve). The figure also shows the extinction of only the MNPs over glass (blue curve), which is the same as that in Figure 5.18, and of only the CQDs film (in green). The thickness of the deposited CQDs film is small (~100nm), so it is not enough optically dense to allow the observation of their ground-state absorption peak (at λ=1330nm) as in Figure 6.2.

In Figure 6.11 a very pronounced enhancement is observed in the CQD film absorption due to the light scattered by the MNPs at their plasmon resonance. The height of the peak in the red curve (at λ=561nm), corresponding to the MNPs+CQD film, is almost 3 times higher than the height of the peak in the blue curve (at λ=513nm)

with only MNPs. An increase in the extinction peak intensity of embedded MNPs was also observed in the case of MNPs inside a-Si (see Figure 5.19), and it occurs because the medium surrounding the MNPs is effectively aborbing its scattered light which is particularly intense at their plasmon resonance.

It can also be realized in the red curve of Figure 6.11, that the dispersive lineshape peak (seen in the blue curve at ~730nm) almost disappears after covering the MNPs with the CQDs film. This feature is related with the interaction between the MNPs electric field and the substrate, as explained in Section 5.6. Here the CQDs film is acting as a dielectric medium surrounding the MNPs which reduces the refractive index contrast at the glass interface and, therefore, decreases the light that is backreflected from the substrate surface.

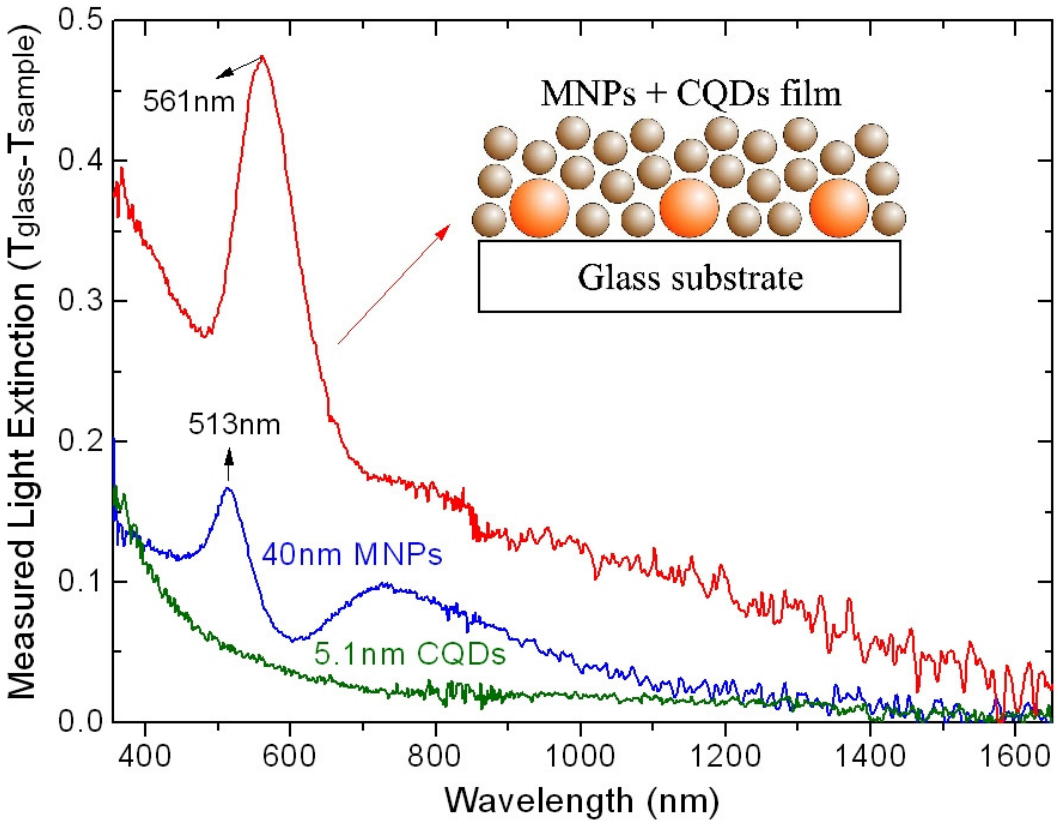

Figure 6.11: Extinction spectra of 40nm Au MNPs on glass before (*blue line*) and after (*red line*) being covered by a 5.1nm PbS CQD film with a thickness around 100nm. The *green line* shows, for comparison, the spectrum of a 5.1nm CQD film with a similar thickness deposited on glass (without MNPs). Such small film thickness does not allow the observation of the peak corresponding to the CQDs ground-state, which is present in Figure 6.2 with a thicker film.

Similar curves were obtained for the other samples containing 40nm Au MNPs covered by the other types of CQDs with 2.3 or 3.4nm diameter; and also for the three samples with 60nm Au MNPs. However, the plasmonic peaks of these MNPs occur at wavelengths (500-600nm) below the absorption peaks of the CQDs ground-state (shown in Figure 6.2). According to the authors, the best way to shift the SP resonances to the IR wavelengths of interest at the CQDs ground-state would be by using oblate or "flattened" MNPs, as referred in Section 5.6 and calculated in Section 2.3.

An alternative (but not so satisfactory) approach could be the use of bigger spherical MNPs, since the wavelengths of the scattering resonances increase with the particle size. For instance, the 80nm Au MNPs exhibit a broad lineshape resonance that can extend further in the infrared (as seen in Figure 5.19). So, only with these MNPs could we observe some evidence of enhancement of the CQDs peak absorption at their ground-state, as shown in Figure 6.12. The thickness of the CQD film deposited in this case is higher than that of Figure 6.11, because we wanted to make sure that the 80nm MNPs were completely covered by the CQDs.

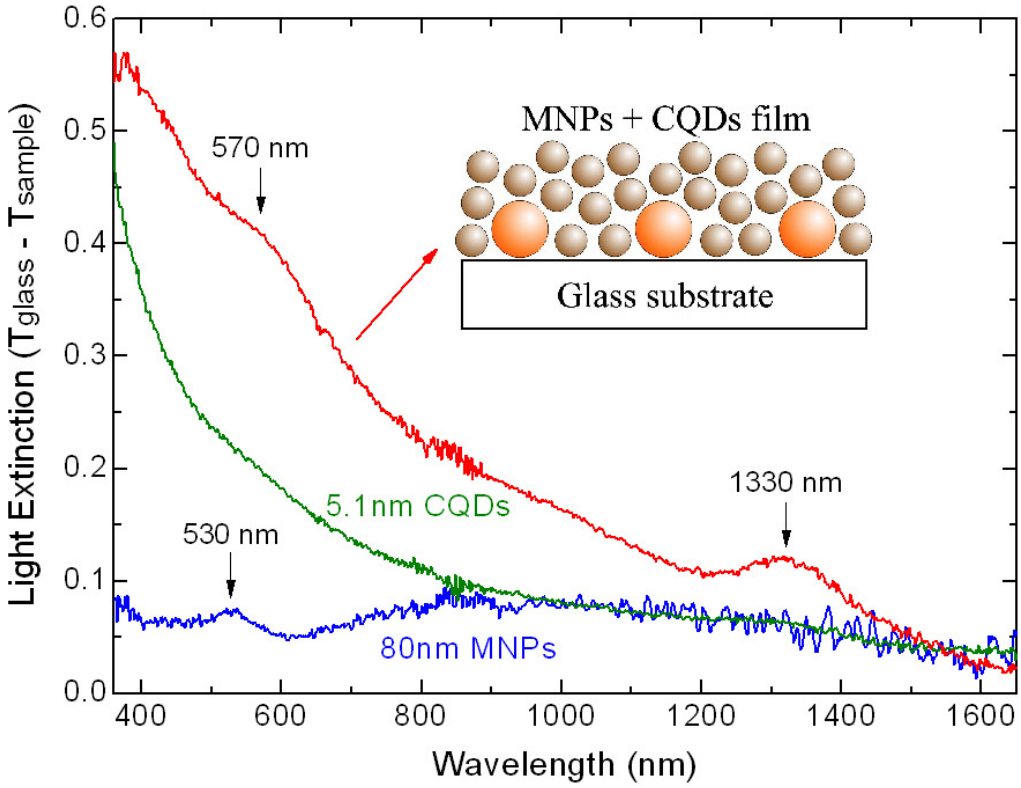

Figure 6.12: Same as Figure 6.11 but with 80nm Au MNPs and using a thicker (~300nm) CQD film deposited on top of the MNPs. Here the ground-state

absorption peak of the 5.1nm CQDs (at 1330nm, see Figure 6.2) was enhanced due to the presence of the MNPs.

The approach of using big (>60nm diameter) spherical MNPs is not so satisfactory because for these larger particles the plasmon-enhanced absorption is less effective [68]. As seen in Figure 5.17a and Figure 5.20, particles with sizes above 60nm exhibit higher order modes (quadrupolar, octopolar, etc.) but a reduced scattering efficiency at the dipolar SP mode. This is because the induced field inside these particles is no longer totally uniform and in phase with the incident light, as would be the case in smaller particles. So, in short, the bigger the MNP the less pronounced its resonant scattering behaviour becomes.

The wavelengths of the plasmonic peaks (within 500-600nm) are indicated in the curves of Figure 6.11 and Figure 6.12 by black arrows. It can be seen that the peaks of the MNPs+CQDs curves are redshifted relative to the peaks of only MNPs on glass. This occurs because the medium surrounding the MNPs covered by CQDs has a higher effective refractive index than that surrounding the MNPs that are just deposited on glass. The values of the redshifts in the peaks of the MNPs+CQDs samples indicate that the 5.1nm CQDs films have an effective refractive index of about N_m=1.8-1.9.

6.7 Conclusions

There are two direct advantages of the IBSC devices described in this chapter: the increase of light absorption by intermediate band solar cells, and the reduction of their fabrication costs by using solution-processed nanostructures [114].

The conventional QD-IBSC technology, employing SK epitaxial growth, is costly both in economical and temporal terms. Therefore, such approach would hardly support the desired cost reduction of PV production. The present chapter is intended to contribute in this respect, whereby a manufacturing method for the realization of a new IBSC is proposed, based on a simple and low-cost solution-based process able to fabricate regularly spherical QDs that can be incorporated in a broad range of semiconductor host materials with bandgaps close to the IBSC optimum.

The presented way of realization shows an unprecedented QD-IBSC design using solution-processed nanostructures made by colloidal chemistry. The use of such method is promising, not only for the significant price reduction of the previous inherently

expensive cells constructed with epitaxial techniques, but also for the elimination of undesirable effects that reduce the reachable cell voltage.

In addition, a method is presented to incorporate in the cell a near-field light trapping structure composed by an array of metal nanoparticles sustaining surface plasmons, also solution-processed. This has the potential to highly increase the light intensity of the appropriate photons in the quantum dots volume, allowing the enhancement of the cell absorption below the forbidden bandgap of the host semiconductor and, therefore, developing the performance theoretically promised by this kind of cell, but not yet reached in practice.

Several of the components and methods described in this chapter can be interesting solutions to enhance light harvesting in many other types of opto-electronic applications.

6.8 Ongoing work

The group is now engaged in the construction of the first test devices incorporating CQDs and colloidal MNPs, in collaboration with *Universidad Politécnica de Cataluña* (UPC). These experiments constitute the beginning of a new research line that the group will pursue based on the work developed in this PhD.

The incorporation of colloidal particles inside a solar cell structure is not a trivial task in practice. The QD-IBSCs that have been fabricated up to now with the SK method are processed in a single growth run, since the QDs are formed epitaxially together with the deposition of the cell material. The embedment of colloids in the cell, as proposed in this chapter, implies using more than one growth run to construct its layer structure. This is because these particles are synthesized in solution phase, separately from the deposition of the cell material. So, to insert the colloids inside any of the cell's layers its growth has to be interrupted, the samples removed from the deposition chamber, the colloids patterned by wet-coating methods such as described in Appendix C and D, and then the samples have to re-inserted back into the chamber to continue the deposition of the materials on top.

The main drawback of this fabrication process is an inevitable increase in the amount of defects present in the cell material, particularly at the interfaces where the growth has been interrupted to deposit the colloidal particles. Therefore, the primary

goal of the experiments referred in this section is to verify if operational PV devices can be constructed in this way, having arrays of CQDs and/or MNPs inserted in the middle of the *p-n* junction of solar cells. The devices are currently being fabricated in the cleanroom facilities of UPC and consist in HiT-type solar cells [147, 148] composed of the layer structure depicted in Figure 6.13. The substrate is a *p*-type Si wafer, all the a-Si layers are deposited by plasma-enhanced chemical vapour deposition (PECVD), the ITO contact deposited by sputtering and the metallizations performed by thermal evaporation. A HiT cell structure was chosen for these preliminary tests because it can allow good conversion efficiencies (23% is the present record), and all the processing is performed under low-temperature conditions (<200ºC), so there is no risk of affecting the deposited nanoparticles. It was verified that CQDs can withstand temperatures up to ~300ºC and MNPs up to ~700ºC, as referred in Section 5.4, without suffering significant deformation.

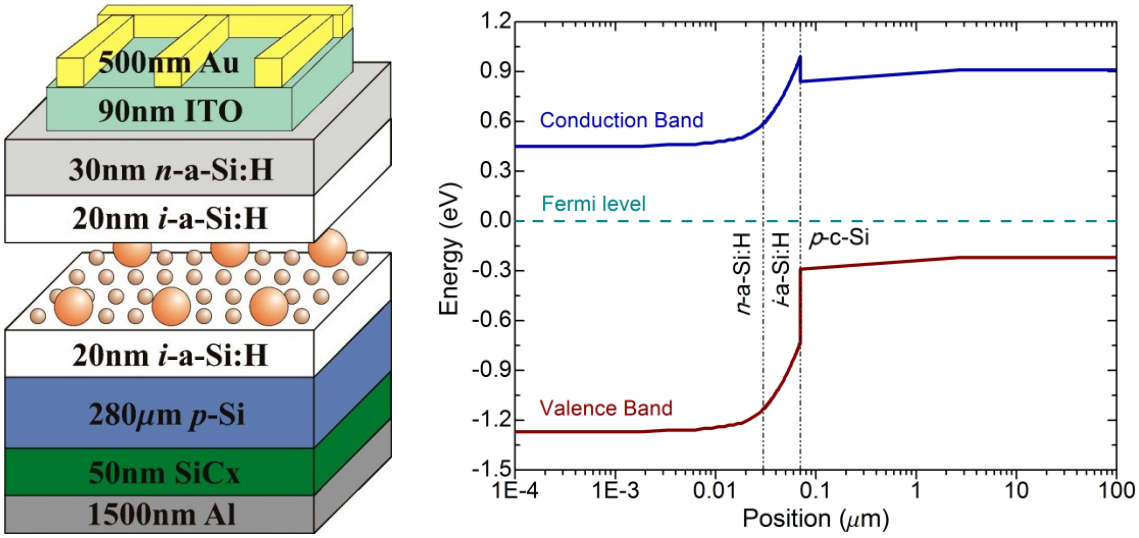

Figure 6.13: **Left** – Layer structure of the first batch of test devices grown on a *p*-doped Si substrate. Self-assembled arrays of MNPs (big spheres) and/or CQDs (small spheres) are inserted in the middle of the intrinsic a-Si layer (*i*-a-Si:H). This structure is identical to a HiT solar cell architecture but with a much thicker intrinsic region (40nm of *i*-a-Si:H, whereas in conventional HiT cells usually only 5-10nm are used) to isolate the colloidal particles from the doped layers. **Right** – Band diagram of the cell *p-i-n* junction simulated using the AFORS-HET program of *Helmholtz Zentrum Berlin*, not taking into account the presence of the colloidal particles.

Figure 6.14 shows the I(V) and $J_L(V_{OC})$ curves of the first few devices that have completed fabrication. The anomalous "S" shape of the I(V) curves is characteristic of HiT-type cells and is generally attributed, among other factors, to the offsets in the valence and conduction bands between the crystalline Si wafer (c-Si) and the a-Si (see band diagram of Figure 6.13) which constitute energy barriers respectively for hole and electron transport [147, 148].

Not much conclusions can be drawn from the results of Figure 6.14 yet, since we still need to analyze other reference devices that are still under construction. However, it is verified that operational devices, having a reasonable photocurrent response, can be constructed with the present method.

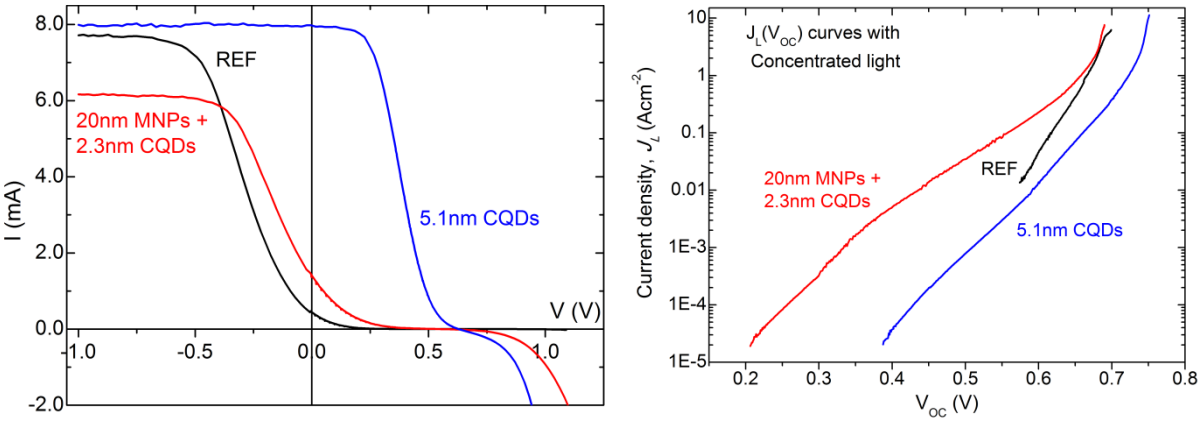

Figure 6.14: **Left** – One sun I(V) curves of three solar cells fabricated with the structure of Figure 6.13 containing an array of 5.1nm PbS CQDs (*blue line*), a binary array of 20nm Au MNPs and 2.3nm CQDs (*red line*), and no particles (*black*). **Right** – Photocurrent density J_L vs. open-circuit voltage V_{OC} under different levels of light concentration (up to ~500 suns), for the same samples as the left plot. The area of the cells is 0.25 cm^2.

Chapter 7

Final remarks and future work

There is much theoretical and experimental work to be done in the field of near-field optics applied to photovoltaics. In the following sections, we suggest a few research ideas to further develop the topics presented in this thesis.

7.1 Metal nanoparticles sustaining surface plasmons

In terms of fundamental physics, it is important to understand in more detail the principles of light-matter interaction with the longitudinal near-field scattered by MNPs. Section 1.4 described a semi-classical formalism, derived by our group, that is able to determine the amount of absorption enhancement that is produced in a medium (electronic system) surrounding an MNP sustaining SPs. Such formalism dictates that the absorption from a longitudinal field is chiefly determined by the intensity of the electrostatic scalar potential. Whereas with a classical transverse field, the absorption is (as is well known) determined by the electric field intensity. It would be important to link our semi-classical formalism to quantum-electrodynamics (QED) theories, as attempted by O. Keller [37, 65]. This would not only allow the verification of our derivation, but would also shed additional physical meaning to the idea of the scalar potential being an operator that generates photons (such as the electric field) and transmits electrostatic energy.

It would be also interesting to use a scanning near-field optical microscopy (SNOM) technique to directly measure the absorption produced from a longitudinal field, so that we could experimentally verify the results of the previously referred semi-classical formalism.

In terms of computational modeling, the numerical studies presented in Chapter 2 can be developed by considering:

- inter-particle effects on the SP frequency and on the absorption enhancement produced by the MNPs
- an inhomogeneous ambient medium around the MNPs, taking into account the quantum dots inclusions present close the particles.
- illuminating light at oblique incidence, particularly at the sunlight incidence angles.

7.2 Mesoscopic dielectric spheroids

In Chapters 3 and 4 we studied scattering by wavelength-sized dielectric spheroids (DMPs) and realized that they can provide considerable near-field light concentration in a mesoscopic scale, which provides attractive solutions for novel PV devices. When the illuminating light flows through the scattering particles it originates distinct regions of constructive and destructive interference of the electromagnetic waves. The region of peak constructive interference is the focus of the particle, where the highest electric field enhancement occurs. Conceptually, one knows that the bigger the scatterer the more intense can its focus be, because there can be more interference of the internal and external waves. However, a general formalism able to determine the fundamental limits of such light enhancement is still lacking. It would be interesting to think of a theoretical model that could determine the maximum field intensity that would be physically possible to obtain by any type of scatterer; and that could predict how that maximum value would decrease with the increase of the volume of the focal spot.

In terms of the computational analysis performed in this work, it could be extended in the following ways:

- Axial incidence was assumed; i.e., the spheroids symmetry axis was taken to be parallel to the incoming light direction. Such studies should be extended to the case of non-axial incidence, to account for the oblique sunlight rays.
- One could also consider an heteregoneous medium surrounding the DMPs; for instance the simple case of a spheroid lying on the surface of a certain PV substrate, which can be computed with FDTD or FEM methods.
- Our numerical code written in Mathematica7.0 would perform faster if it were converted to a standard non-symbolic programming language such as Fortran, Pascal, C/C++, etc. In this thesis we only used Mathematica due to its built-in package of spheroidal functions. For future work, it would be important to write these functions in a standard programming language. Once that is done, the rest of the code should be easily converted.

Besides, no experimental work was performed so far with DMPs since we haven't yet come across any efficient method that is able to produce them. So, it would be important to find a way of constructing arrays of DMPs with sizes close to the

wavelength (on the order of the micrometer) and pattern them in PV materials. It may be possible to synthesize DMPs in colloidal solution, similarly to the latex spheres used in nano-sphere lithography. Otherwise, one could try to fabricate arrays of spheroidal (or coin-shaped) DMPs by hole-mask colloidal litography (HCL) [83], or any other kind of lithographic strategy.

Another promising project that should be explored, is the possibility of applying the near-field produced by DMPs to spectral splitting strategies in third-generation solar cells. The results of Chapters 3 and 4 reveal that DMPs act as mesoscopic lenses and focus the light at different spots in front of the particle for distinct wavelengths. The UV light originates a focus further away from the particle than the IR light. So, for example, one could consider placing an array of spheroids on the bottom of a multi-junction cell, as sketched in Figure 7.1, so that they can focus the IR light in the bottom layers, the VIS light in the intermediate layers, and the UV light in the top layers.

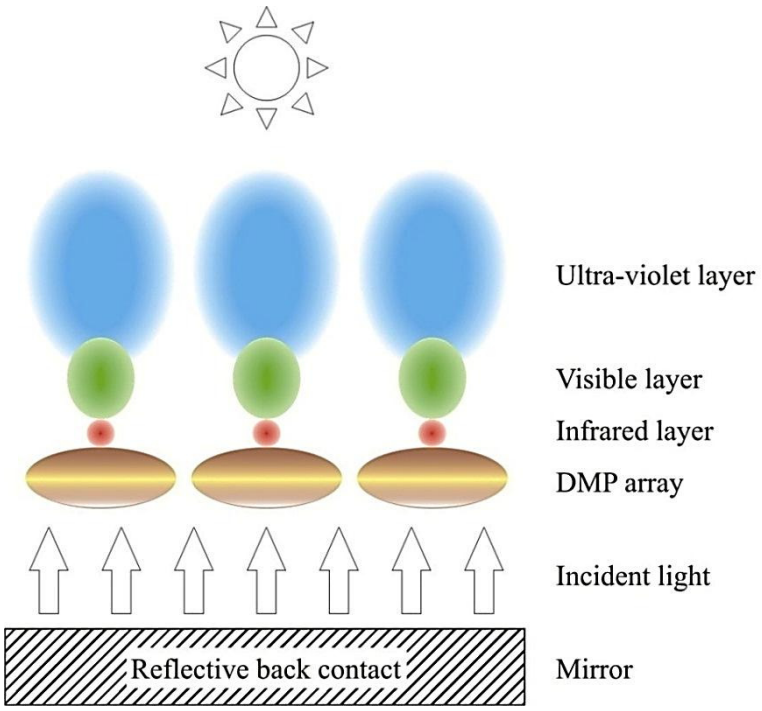

Figure 7.1: Possible strategy to implement dielectric mesoscopic spheroids for spectral splitting in a thin-film multi-junction solar cell.

7.3 Colloidal quantum-dot IBSCs

This is a very recent idea, and much has still to be done in this new line of research of IBSCs to achieve in practice the device proposed in Chapter 6.

Firstly, it is important to model the opto-electronic response of the colloidal quantum dots (CQDs) in order to guide the experiments and understand the measured results. For that, we refer to the latest computational work of Luque *et al.* [31, 141] where the band structure and absorption coefficient of InAs QDs in a GaAs matrix are determined, using a $k \cdot p$ multiband method. A similar analysis should be performed for PbS CQDs [149] in the matrix materials proposed in Section 6.4.1., with the aim of optimizing the CQDs size (and perhaps shape) for optimal performance of the IBSC.

Another interesting idea that should be explored, is the possibility of having different intermediate bands, located at distinct energies, along the active region of the solar cell. With CQD-IBSCs it is feasible to construct a solar cell having layers of quantum dots of different sizes. The top layer would have smaller CQDs to position the IB closer to the host material conduction band, and the bottom layer would have bigger CQDs to position the IB closer to the valence band. In between these layers, several other CQD layers can be constructed having a gradient of dot diameters, as represented in Figure 7.2. Such dot diameters, and hence the energetic positions of the corresponding IB levels, would of course be optimized to allow the highest possible cell conversion efficiency when illuminated by the AM1.5 solar spectrum.

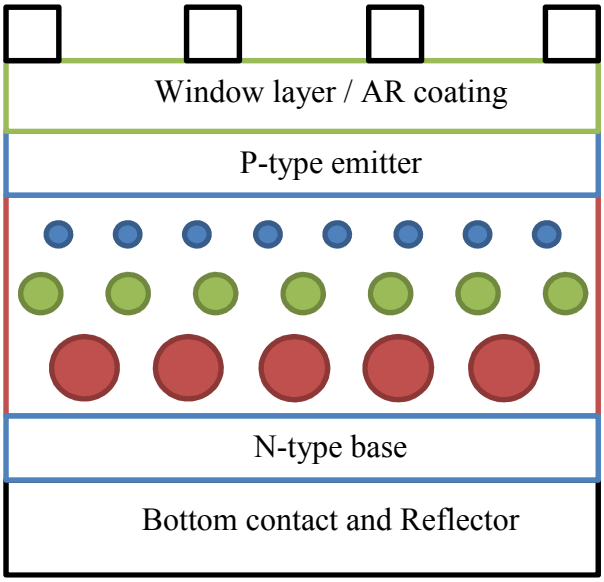

Figure 7.2: CQD-IBSC composed of a gradient of QD sizes/bandgaps. This produces a gradient of intermediate band positions that should be optimized for maximum cell efficiency under the AM1.5 solar spectrum.

The absorption of this cell can be further increased by incorporating in each CQD layer an MNP array with MNPs optimally shaped to produce an SP resonance at one (or both) of the transition energies of the CQDs in that layer, as proposed for the CQD-IBSC of Chapter 6.

APPENDIXES

Appendix

A. Spheroidal vector wave functions

Spheroidal wave functions have found many important applications in mathematical physics and engineering where the prolate or the oblate spheroidal coordinate system is used. In the evaluation of electromagnetic fields in spheroidal structures, spheroidal wave functions are often encountered, especially when boundary value problems are solved using full-wave analysis. By applying the separation-of-variables to the Maxwell's equations (1.5), satisfied by either an electric or magnetic field, the spheroidal harmonics of electromagnetic waves can be obtained [53]. This separability is analogous to that of solving Laplace equation in spherical coordinates.

The spheroidal coordinates (η, ξ, ϕ) are related to the Cartesian coordinates by the following transformations:

$$\begin{aligned} x &= \frac{\mathrm{d}}{2}\sqrt{(1-\eta^2)(\xi^2 \pm 1)}\cos\phi, \\ y &= \frac{\mathrm{d}}{2}\sqrt{(1-\eta^2)(\xi^2 \pm 1)}\sin\phi, \\ z &= \frac{\mathrm{d}}{2}\eta\xi, \end{aligned} \tag{A.1}$$

where the upper and lower signs pertain to oblate and prolate spheroidal coordinates, respectively, and d is the interfocal distance. Prolate and oblate spheroidal coordinate systems are formed by rotating the two-dimensional elliptic coordinate system, consisting of confocal ellipses and hyperbolas, about the major and minor axes of the ellipses, respectively. The domains of the spheroidal coordinates are:

$$-1 \le \eta \le 1, \qquad \varepsilon \le \xi < \infty, \qquad 0 \le \phi < 2\pi$$

where ϵ=0 in the oblate case and ϵ=1 in the prolate.

The expressions of the spheroidal vector wave functions used in eqs. (3.2)-(3.4) are given below [1, 53]:

$$\underline{\mathbf{M}_{e0n}^{x(i)}(C;\eta,\xi,\phi):}$$

$$M_{e0n,\eta}^{x(i)} = -\frac{2(\xi^2 \pm 1)^{1/2}}{\mathrm{d}(\xi^2 \pm \eta^2)^{1/2}} S_{0n} \frac{d}{d\xi} R_{0n}^{(i)} \sin\phi,$$

$$M_{e0n,\xi}^{x(i)} = \frac{2(1-\eta^2)^{1/2}}{\mathrm{d}(\xi^2 \pm \eta^2)^{1/2}} \frac{d}{d\eta} S_{0n} R_{0n}^{(i)} \sin\phi,$$

$$M_{e0n,\phi}^{x(i)} = \frac{2}{\mathrm{d}(\xi^2 \pm \eta^2)} \left[\xi(1-\eta^2) \frac{d}{d\eta} S_{0n} R_{0n}^{(i)} + \eta(\xi^2 \pm 1) S_{0n} \frac{d}{d\xi} R_{0n}^{(i)} \right] \cos\phi;$$

$$\underline{\mathbf{N}_{e0n}^{x(i)}(C;\eta,\xi,\phi):}$$

$$N_{e0n,\eta}^{x(i)} = \frac{4}{K\,\mathrm{d}^2(\xi^2 \pm \eta^2)^{1/2}} \left[\eta S_{0n} \frac{\partial}{\partial\xi} \left(\frac{(\xi^2 \pm 1)^{3/2}}{(\xi^2 \pm \eta^2)} \frac{d}{d\xi} R_{0n}^{(i)} \right) - \frac{1}{(\xi^2 \pm 1)^{1/2}} \frac{d}{d\eta} S_{0n} R_{0n}^{(i)} \right.$$
$$\left. + (1-\eta^2) \frac{d}{d\eta} S_{0n} \frac{\partial}{\partial\xi} \left(\frac{\xi(\xi^2 \pm 1)^{1/2} R_{0n}^{(i)}}{\xi^2 \pm \eta^2} \right) \right] \cos\phi,$$

$$N_{e0n,\xi}^{x(i)} = -\frac{4}{K\,\mathrm{d}^2(\xi^2 \pm \eta^2)^{1/2}} \left[\xi \frac{\partial}{\partial\eta} \left(\frac{(1-\eta^2)^{3/2}}{(\xi^2 \pm \eta^2)} \frac{d}{d\eta} S_{0n} \right) R_{0n}^{(i)} + \frac{1}{(1-\eta^2)^{1/2}} S_{0n} \frac{d}{d\xi} R_{0n}^{(i)} \right.$$
$$\left. + (\xi^2 \pm 1) \frac{\partial}{\partial\eta} \left(\frac{\eta(1-\eta^2)^{1/2} S_{0n}}{\xi^2 \pm \eta^2} \right) \frac{d}{d\xi} R_{0n}^{(i)} \right] \cos\phi,$$

$$N_{e0n,\phi}^{x(i)} = \frac{4(1-\eta^2)^{1/2}(\xi^2 \pm 1)^{1/2}}{K\,\mathrm{d}^2(\xi^2 \pm \eta^2)} \left[\frac{1}{(\xi^2 \pm 1)^{1/2}} \frac{\partial}{\partial\eta} \left((1-\eta^2)^{1/2} \frac{d}{d\eta} S_{0n} \right) R_{0n}^{(i)} \right.$$
$$\left. + \frac{1}{(1-\eta^2)^{1/2}} S_{0n} \frac{\partial}{\partial\xi} \left((\xi^2 \pm 1)^{1/2} \frac{d}{d\xi} R_{0n}^{(i)} \right) \right] \sin\phi;$$

$\underline{\mathbf{M}_{e1n}^{z(i)}(C;\eta,\xi,\phi):}$

$$M_{e1n,\eta}^{z(i)} = \frac{2\eta}{\mathrm{d}(\xi^2 \pm \eta^2)^{1/2}(1-\eta^2)^{1/2}} S_{1n} R_{1n}^{(i)} \sin\phi,$$

$$M_{e1n,\xi}^{z(i)} = -\frac{2\xi}{\mathrm{d}(\xi^2 \pm \eta^2)^{1/2}(\xi^2 \pm 1)^{1/2}} S_{1n} R_{1n}^{(i)} \sin\phi,$$

$$M_{e1n,\phi}^{z(i)} = \frac{2(\xi^2 \pm 1)^{1/2}(1-\eta^2)^{1/2}}{\mathrm{d}(\xi^2 \pm \eta^2)} \left[\eta \frac{d}{d\eta} S_{1n} R_{1n}^{(i)} - \xi S_{1n} \frac{d}{d\xi} R_{1n}^{(i)} \right] \cos\phi;$$

$\underline{\mathbf{N}_{e1n}^{z(i)}(C;\eta,\xi,\phi):}$

$$N_{e1n,\eta}^{z(i)} = \frac{4(1-\eta^2)}{K\,\mathrm{d}^2(\xi^2 \pm \eta^2)^{1/2}} \left[\eta \frac{d}{d\eta} S_{1n} \frac{\partial}{\partial\xi} \left(\frac{\xi^2 \pm 1}{\xi^2 \pm \eta^2} R_{1n}^{(i)} \right) - S_{1n} \frac{\partial}{\partial\xi} \left(\frac{\xi(\xi^2 \pm 1)}{\xi^2 \pm \eta^2} \frac{d}{d\xi} R_{1n}^{(i)} \right) + \frac{\xi}{(1-\eta^2)(\xi^2 \pm 1)} S_{1n} R_{1n}^{(i)} \right] \cos\phi,$$

$$N_{e1n,\xi}^{z(i)} = \frac{4(\xi^2 \pm 1)^{1/2}}{K\,\mathrm{d}^2(\xi^2 \pm \eta^2)^{1/2}} \left[\xi \frac{\partial}{\partial\eta} \left(\frac{1-\eta^2}{\xi^2 \pm \eta^2} S_{1n} \right) \frac{d}{d\xi} R_{1n}^{(i)} - \frac{\partial}{\partial\eta} \left(\frac{\eta(1-\eta^2)}{\xi^2 \pm \eta^2} \frac{d}{d\eta} S_{1n} \right) R_{1n}^{(i)} + \frac{\eta}{(1-\eta^2)(\xi^2 \pm 1)} S_{1n} R_{1n}^{(i)} \right] \cos\phi,$$

$$N_{e1n,\phi}^{z(i)} = -\frac{4(1-\eta^2)^{1/2}(\xi^2 \pm 1)^{1/2}}{K\,\mathrm{d}^2(\xi^2 \pm \eta^2)} \left[\frac{\xi}{\xi^2 \pm 1} \frac{d}{d\eta} S_{1n} R_{1n}^{(i)} + \frac{\eta}{1-\eta^2} S_{1n} \frac{d}{d\xi} R_{1n}^{(i)} \right] \sin\phi;$$

Note that these expressions are in simplified form, applicable only to the particular case of axial incidence considered here. For the general case of oblique incidence the full expressions of the vector wave functions can be found in the books [1, 53].

Appendix

B. Nelder and Mead optimization algorithm

The optimization routine used in Chapter 4 consists of a multidimensional direct search algorithm known as the Nelder and Mead or downhill simplex method [150, 151]. This method has found widespread use in the optimization of nonlinear functions whose gradient is very expensive (or practically impossible) to calculate.

The method determines the set of n variables that maximize (or minimize) a certain function F. The n variables are treated as the coordinates of a n-dimensional space in which F is defined. The algorithm starts by picking n+1 initial points inside the n-dimensional domain. These points are regarded as the vertices of an n-simplex (n-dimensional analogue of a triangle). Function F is evaluated at each of these vertices and then the algorithm moves and/or redimensions the n-simplex in the n-dimensional space towards the vertex with better F value. Function F is again evaluated at the new n-simplex points and the procedure is iteratively repeated as better F values are found, until some desired bound is obtained.

It is important to define well the domain (lower and upper limits) of each n variable, in order to avoid searching in physically forbidden regions, or where it is known a-priori that F has undesired values. The optimizations performed in this work use up to 3 variables, the spheroid parameters: R_{eq}, b/a and n_r. The domain allowed for the simplex was defined according to a set of lower limits ($a,b>0$ and $n_r>1$) and upper limits ($n_r \leq 4.0$ and $|C_i|<60$). The upper limit for n_r was taken to be 4.0 for the reasons mentioned in Section 4.6. The upper bound set for $|C_i|$ is due to computational constraints, as referred in Section 4.3.

To restrict the searching direction of the algorithm inside our chosen domain, the function F is simply set to a low value at any point outside the allowed region, so that out-of-bounds points are not considered for the new simplex in the next iteration.

The points chosen for the initial simplex were picked randomly inside the allowed domain. The algorithm then moves and redimensions the simplex towards the regions of highest *F* until it shrinks at the maximum point found.

With this method, a maximum is reached within about 30-50 iterations. However, this can be a local maximum in the search domain. To ensure that a global maximum is reached, the algorithm is sequentially run with different initial point sets until the results converge to a single overall maximum. Table 4.1 and Table 4.2 present the values of the overall maximum values obtained for the optimizations of $|\mathbf{E}_S|^2$ and P [eq. (4.3)], respectively.

Appendix

C. Procedures for nanoparticle self-assembly on various substrates

This appendix describes in detail all the experimental steps involved in the patterning of a monolayer of colloidal nanoparticles on the surface of distinct materials such as Si, a-Si, GaAs and glass. The first experimental procedure (A) that is presented corresponds to the patterning of metal nanoparticles, used in the experiments of Chapter 5 and 6. Then we describe the procedure (B) used in the experiments of Chapter 6 for the patterning of lead-sulfide (PbS) colloidal quantum dots.

A) Patterning arrays of metal nanoparticles (MNPs):

MNP aqueous solutions were bought from specialized companies, such as *nanoComposix* and *British Bio Cells*. These solutions should be stored under dark at a temperature around 5^{o}C. A fridge is a good place to keep them.

The standard procedure used to construct self-assembled monolayer arrays of MNPs on various substrates is composed of the following steps:

A.1) Wafer cutting

First of all, the substrate wafers are cut to the appropriate dimensions. If the samples are made of Si or GaAs, then the wafers of these materials are cut with a typical diamond-tip pen. If the samples' material is glass, or a-Si over a glass substrate, it cannot be cut with a diamond tip, instead it is cut with a mechanical rotating saw. In most of our experiments the samples were cut to a dimension of about 1x1 cm^2, because that is the maximum dimension that can be used for atomic force microscopy (AFM) measurements. For optical measurements the samples were a bit bigger, up to 2x2 cm^2.

A.2) Degreasing

After the cutting, the samples are cleaned from organic impurities, and other common debris, with a standard degreasing procedure. This involves submerging the samples in heated baths (~60 ^{o}C) of acetone, then isopropanol and finally methanol; for approximately 3 minutes in each bath. The samples are then dried under an air or nitrogen flux.

A.3) RCA1 clean

The RCA clean is a standard set of wafer cleaning steps developed to clean silicon before high temperature processing steps. In our experiments we apply the first part of this procedure, known as RCA1, which removes all organic contaminants and leaves a thin oxide layer (thickness on the order of the nanometer) on the surface. The RCA1 is performed with a 1:1:5 (by volume) solution of ammonium hydroxide [NH_4OH (25%)] + hydrogen peroxide [H_2O_2] + water [H_2O] at 75 or 80°C, typically for 10-15 minutes. The samples are rinsed in water afterwards, and then dried under an air or nitrogen flux.

Another reason for performing this RCA1 clean, is that it is a pre-requisite for the functionalization of the surface with APTMS (performed on the next step). Previous works [103, 152] claim that the organic linker molecules attach preferentially to oxidized surfaces. In fact, in [103] the authors were able to selectively functionalize Si surfaces by locally oxidizing them using an AFM nano-oxidation technique. Therefore, in view of these results, it is recommended to perform an RCA1 clean prior to the APTMS functionalization in order to leave an oxidized surface.

Care must be taken when performing RCA1 cleans in materials other than Si. This is because this solution can etch certain materials such as GaAs [153], so the immersion of GaAs in the RCA1 solution should be performed in a short time and without heating, as indicated in Table C.1.

Material	Temperature	Immersion Time
Si or Glass	80 ºC	15 min
a-Si films	60-70 ^{o}C	10 min
GaAs	Room temperature (no heating)	30 s

Table C.1: Conditions applied to the surfaces of Si, glass, a-Si and GaAs during the RCA1 clean. This solution does not cause any damage to the surface of Si nor glass, but it rapidly etches GaAs materials [153]. Therefore, it is not advisable to immerse the GaAs wafer in it for more than 1 min.

Alternatively (or additionally) to the RCA1, the samples can also be treated with a "Piraña solution" which also cleans and oxidizes their surface for APTMS functionalization. This consists in immersing the sample for 10-15 minutes at about 80^{o}C in a solution of H_2SO_4(98%):H_2O_2(30%) in 3:7 by volume.

A.4) Functionalization with APTMS

As referred in Section 5.3, the material used to produce a positive surface charge on the sample surface (represented in Figure 5.7 and Figure 5.8) is APTMS [(3-Aminopropyl)-trimethoxysilane], bought from *Sigma Aldrich*. This surface charge attracts and binds the negatively charged colloids dispersed in solution to the sample.

The functionalization involves three steps:

A.4.1) Immersion in aqueous APTMS dilution – the samples are immersed in APMTS diluted in water (or ethanol) at a concentration of 10% by volume. In principle, much lower concentrations, such as 0.1-1%, would suffice to cover the samples surfaces; but we choose to use an excess of APTMS concentration to make sure that the coverage is complete. The immersion time is of 1-1.5 hours.

A.4.2) Cleaning excess APTMS – the samples are then rinsed in water and ethanol to remove the excess amount of APTMS that is not in direct contact with the sample. This leaves, in principle, a monolayer of APTMS molecules attached to the surface.

A.4.3) APTMS curing – the APTMS monolayer is cured by baking the samples in oven at 110-115 ^{o}C during one hour.

A.5) MNP deposition by dip-coating

Prior to the deposition of the nanoparticles, the colloidal solution should always be bath-sonicated for about 10 minutes. This helps to re-disperse the particles and disrupt some agglomerates that are naturally formed when the solutions are stored for several days.

After bath-sonicating the colloidal solution, the sample is immersed in it (see Fig. C.1) so that the dispersed colloids get deposited on the positively charged surface of the sample, as illustrated in Figure 5.7. The number of deposited particles increases with the immersion time, and saturates when the total negative charge of the deposited MNPs becomes equal to the positive charge of the APTMS-terminated sample surface. When this occurs, the repelling force of the deposited MNPs shields the electrostatic attracting

force that drives the colloids to the functionalized surface, and the deposition stops. This evolution is schematically plotted in Fig. C.2.

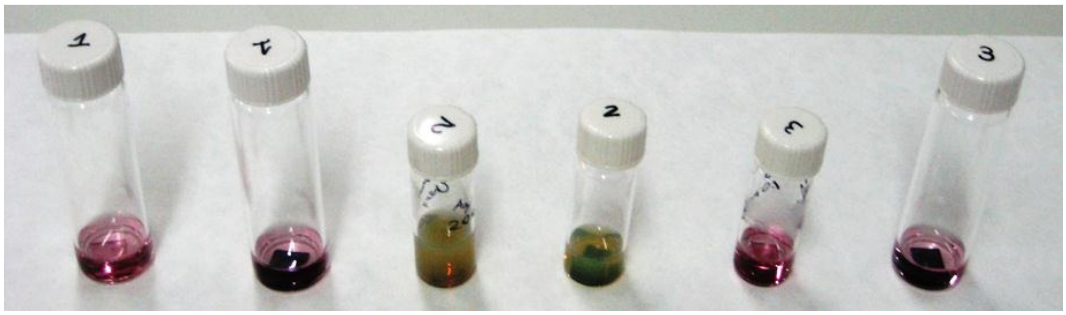

Fig. C.1: Photo of a typical set of samples immersed in MNP solutions. In each set of experiments we usually worked with 6 samples at a time, to optimize our processes in a faster way. The red-pink solutions contain Au MNPs and the yellow ones have Ag MNPs.

We do not know what is the exact minimum time required to achieve the maximum surface coverage (t_0), so in the experiments performed in this work the samples were left overnight (for about 10-13 hours) submerged in the MNP solution. This way it is guaranteed that the samples are immersed for a time longer than t_0 (shown in Fig. C.2) and their surfaces completely covered with MNPs up to saturation.

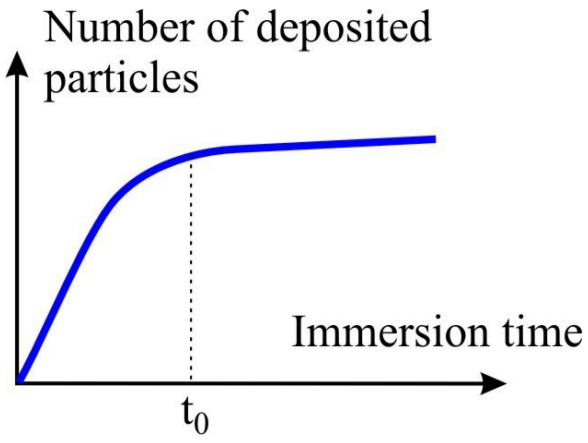

Fig. C.2: Schematic plot of the number of deposited colloidal particles as a function of the time of immersion in the solution. The time it takes to reach saturation (t_0) is usually of a few hours.

After removing the samples from the MNP solution, they should be rinsed in water (see Fig. C.3) to remove the deposited MNPs that are not in direct contact with the sample surface. This leaves a monolayer of MNPs uniformly covering the entire

surface, such as shown in the SEM images of Fig. C.4. Finally the samples are dried in an air or nitrogen flux.

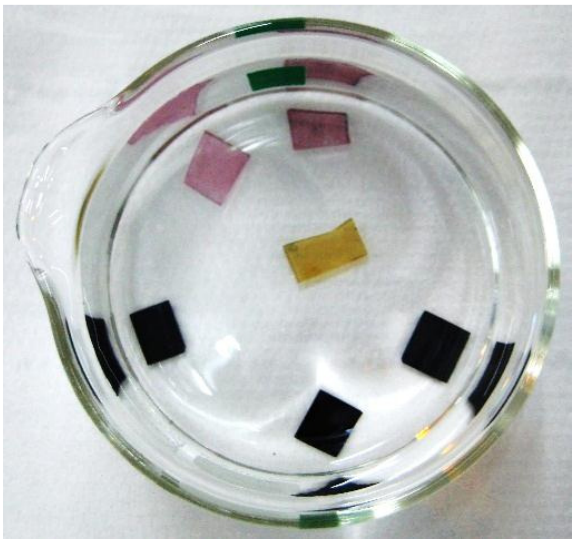

Fig. C.3: Batch of 6 samples being rinsed in water after the dip-coating process shown in Fig. C.1. The coloured samples are glass slides that were immersed overnight in Au (red-pink) or Ag (yellow) colloidal solutions. The other 3 dark samples are pieces of Si and GaAs that have also been immersed in the same solutions.

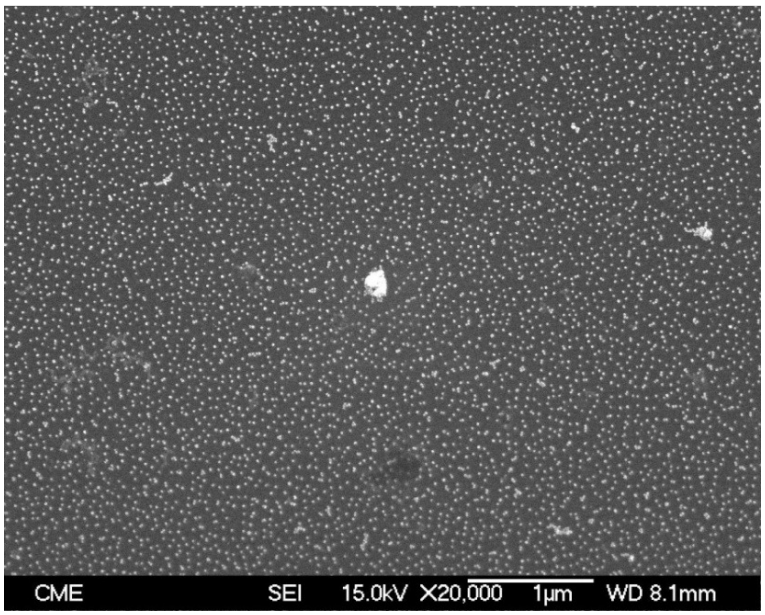

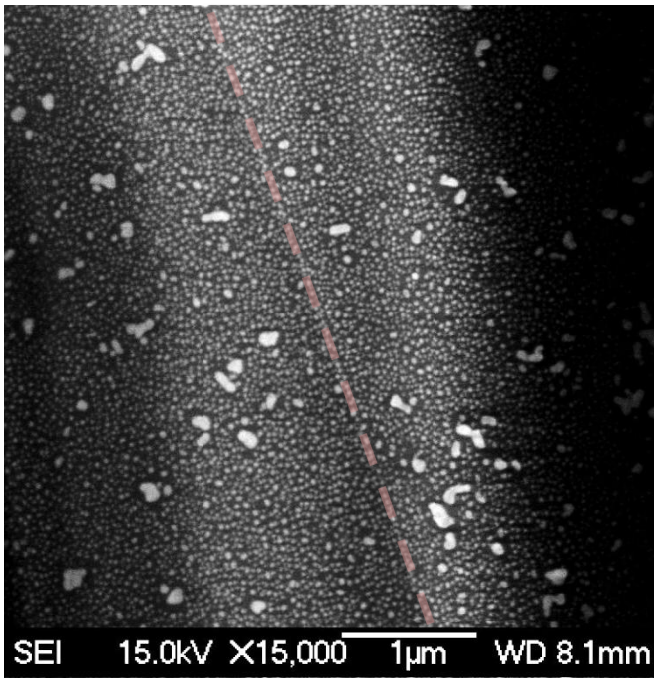

Fig. C.4: Examples of SEM images of self-assembled Au MNPs with 20nm diameter. The distribution of particles is uniform throughout the samples' surface.

Top – Au MNP array on Si. A few MNP clusters, or other impurities, are inevitably present. These are actually helpful in SEM analysis for the focusing of the image.

Bottom – This image shows the deposition of MNPs on the interface (marked by the dashed line) between an a-Si layer (left side) and glass (right side). It can be seen that there is no difference between the distribution of MNPs on a-Si or on glass, which shows that our deposition method is quite substrate-independent. The big MNP agglomerates observed in this sample are due to the bad quality of the colloidal solution used in this particular test. This bad solution was not used in any other experiment.

A.6) Final cleaning

After depositing the MNPs, it is necessary to effectively clean the samples' surface without affecting the attached particles. This cleaning step should be able to remove any contaminants coming from the MNP solution, the organic species involved in the deposition process (APTMS and capping molecules), and the superficial oxides produced by the RCA1 in step 3). This may be particularly important if the deposited MNP array is going to be embedded inside the active region of a solar cell. In that case the removal of any impurities is crucial, since they cause recombination of the photo-generated carriers in the cell material.

To that end, a series of chemical tests have been conducted to study the robustness

and adhesion strength of the deposited MNPs on Si and GaAs samples. After each test the sample surface was inspected by AFM to check if there was any size reduction or adsorption of the nanoparticles. It was observed that the relevant processes listed in Table C.2 do not cause any considerable changes to the deposited particles.

	Process	**Solvents**	**Time**	**Temp.**
1	Degreasing with organic solvents	Acetone Isopropanol Methanol	3 min in each solvent	60 ºC
2	Bath Sonication	Acetone or DI water	1 hour	Room Temp.
3	Etching of GaAs oxides	NH_4OH (25% solution)	10 min	80 ºC
4	Etching of SiO_2	HF (0.14% solution)	1 min	Room Temp.

Table C.2**:** Tested cleaning procedures that do not remove nor etch the deposited MNPs

Processes 1 and 2 should be able to remove contaminants coming from the colloidal solution. Whereas processes 3 and 4 remove, respectively, the surface oxides and the organic species in GaAs [153] and Si [154]. The times used for the tests listed in Table C.2 are above the minimum times required for each cleaning process. This way we can be sure that the MNPs do not suffer any change even if the process takes longer than the minimum necessary time.

Another way of removing the organic species present on the surface can be by annealing the samples in an inert atmosphere of forming gas (90% nitrogen + 10% hydrogen) at about 500^{o}C, for 15 minutes. At such temperature all the organic substances present on the samples should be evaporated, and the MNPs should not be affected since they can withstand temperatures up to 700-800 ^{o}C, as explained in Section 5.4.

B) Patterning colloidal quantum dot (CQD) arrays

The experimental tests mentioned in Section 6.4.4 with CQDs used solutions of PbS nanoparticles dispersed in 1-octanol, bought from *Evident Technologies*. The organic capping agent used to stabilize the CQDs in octanol is oleic acid. The CQD

solutions should be stored in dark at a temperature around 5^{o}C, for instance in a fridge such as the MNP solutions.

CQDs deposit quite easily in Si materials, without requiring the functionalization of the surface with an organic monolayer, such as the APTMS treatment performed for the deposition of MNPs. The standard procedure used to construct self-assembled close-packed arrays of PbS CQDs in Si is composed of the following steps:

B.1) Wafer cutting

Same as step A.1) in the patterning of MNPs.

B.2) Degreasing in heated baths of acetone + isopropanol + methanol

Same as step A.2) in the patterning of MNPs.

B.3) Bath sonication of CQD solution for 10 minutes

This helps to disrupt some of the colloid agglomeration that occurs when the solutions were stored for long time.

B.4) Hydrofluoric (HF) acid treatment

The Si samples are dipped for 30s in an aqueous dilution of HF containing HF(50%):H_2O in 2:75 by volume. After dipping the samples in the HF dilution they are rinsed in water and then dried in a flux of air or nitrogen.

This step is important because, as observed by [118], the HF converts the naturally oxidized surface of silicon to an hydrogen-terminated surface (hydrophobic) which is suited for the attachment of the CQDs. Alternatively, a functionalizing (glue) layer can be deposited on the substrate surface, such as the APTMS used for the patterning of MNPs. In [134] the substrates were treated with hexamethyldisilazane (HMDS) prior to QD deposition by immersing them in HDMS and then baking them at 130^{o}C for 2h in a closed vessel. This procedure replaces the polar silanol-terminated SiO_2 surface (native oxide in Si) with a hydrophobic trimethylsilyl-terminated surface (trimethylsiloxylated).

It was found that the PL intensity measured from QD films on HF-treated silicon was 3 times stronger than films on HMDS-treated silicon. For that reason, we use the HF treatment of Si and a-Si samples for the CQD patterning instead of the HDMS functionalization.

B.5) Spin coating of CQDs

Immediately after the previous step, the samples are placed in the spinner and a small amount of CQD solution is dropped on top. As explained in Appendix D, one of the requirements for a successful spin-coating is that the deposited drop should wet all the sample surface. Since octanol wets fairly well most semiconductor surfaces, a small drop of about 10 μl is enough to cover the entire surface of a typical 1x1cm^2 sample.

After that, the sample is rotated at 1500 rpm for 1 minute.

B.6) Rinsing and oven drying

The sample is then rinsed in the same solvent as the CQD solution, in this case octanol. This removes the excess layers of CQDs that are not in direct contact with the sample surface, leaving a compact monolayer of CQDs covering the entire surface.

The octanol is then evaporated by drying the sample in oven at 120^{o}C for about 15 minutes.

B.7) Final cleaning

The samples can finally be cleaned by rinsing in DI water, isopropanol and/or acetone. However, it was observed than they cannot be degreased, following the procedure described in step 2), since the methanol removes the oleic acid capping agent around the CQDs causing them to aggregate into clusters.

The experimental procedure composed of the previous steps should be applied when depositing PbS CQDs in Si or a-Si. Nevertheless, we have found that these CQDs can also be patterned onto glass or GaAs by functionalizing the surface of these materials with APTMS (instead of the HF treatment in step B.4), following the procedure described for the patterning of MNPs. The results of the CQDs patterning performed in this way can be analyzed by AFM, as shown in the examples of Fig. C.5.

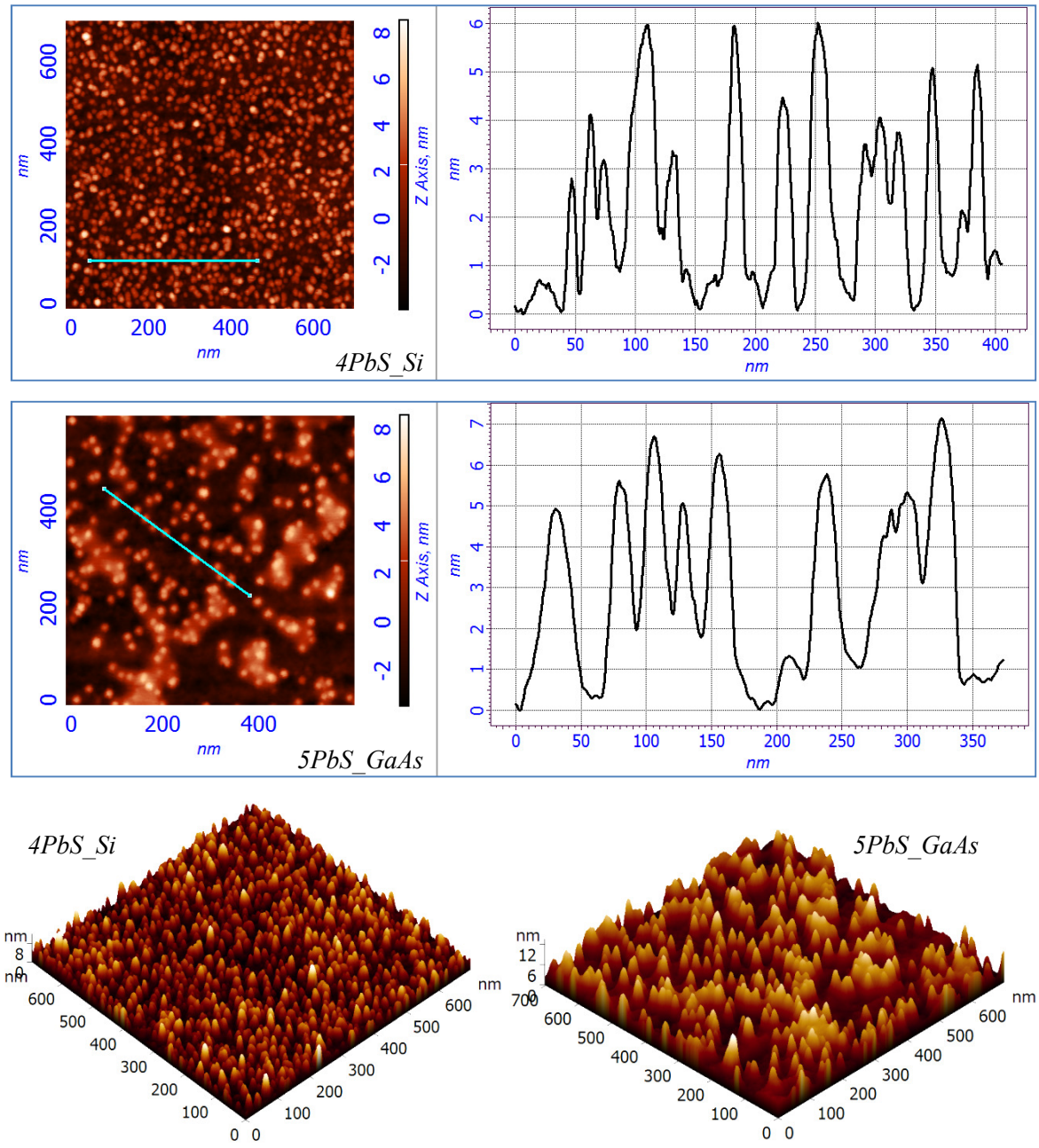

Fig. C.5: Examples of AFM images of self-assembled PbS CQDs with ~5.1nm diameter. These images were taken with an Ntegra Prima AFM system of the *NT-MDT* company.

Here we show the results of two samples containing CQDs deposited in Si (*4PbS_Si*) and GaAs (*5PbS_GaAs*). The top images show the topography (*left side*) and the cross section profile (*right side*) along the blue line. It can be seen that the deposited CQDs have the expected heights (diameters), attending to the fact that the blue line may not pass by the exact top point of all the particles. The bottom images show the 3D topography of the samples, where the uniformity of the distribution can be appreciated. It was verified that this distribution is the same throughout the entire samples' surface, since similar images were taken at distinct spots on the samples.

Appendix

D. Notes about colloidal spin-coating and surface hydrophilization

One of the main advantages of spin-coating relative to dip-coating is that it allows a fast deposition with a controlled amount of liquid solution in contact with the sample. In the course of the experimental work performed in this PhD, we performed hundreds of spin-coating runs on distinct samples and with different spinning conditions. This allowed us to learn some practical ideas about this technique, which are described in this appendix and can be regarded as a set of practical advices to achieve a successful spin-coating.

The first condition for a uniform spin-coating over the entire sample is that the solvent of the colloidal solution must wet the surface. Wetting means, in this sense, that when a drop of the solvent is placed on the surface it spreads to form a thin layer covering an area of the surface much larger than the drop. This can be quantified by measuring the equilibrium contact angle formed between the sample and the drop surface: the higher the contact angle the less the liquid "wets" the sample surface.

For instance, when attempting to spin-coat metal nanoparticles (MNPs) dispersed in aqueous solution, it is necessary that the surface can be wetted by water. In other words, the surface must be hydrophilic. Unfortunately, the surfaces of most common semiconductor materials, such as Si and GaAs, are naturally hydrophobic; so they repeal water [155]. Therefore, to spin-coat MNPs dispersed in aqueous solutions on the surface of Si or GaAs it is essential to chemically treat these surfaces appropriately to make them hydrophilic.

A certain surface can be made hydrophilic by passivating it with hydroxyl (OH^-) groups. These groups have the ability to form hydrogen bridges with the water molecules, causing the surface to attract water instead of repealing it. Such passivation treatment can be achieved with different types of solutions; but, according to our tests, that which seemed to work best was the solution employed in the RCA1 process

[NH_4OH(25%):H_2O_2:H_2O in 1:1:5 by volume] described in the previous appendix. The conditions that should be applied for the case of Si, a-Si, glass and GaAs materials are indicated in Table C.1.

Silicon surfaces become perfectly hydrophilic after cleaning with the standard RCA1 procedure [154]. This solution leaves on the Si surface an hydroxylated oxide with OH^- groups [156]. Such surface is easily wetted by aqueous solutions, as required for spin-coating. The hidroxylated oxide can later be removed after spin-coating by dipping the Si sample in a dilute HF solution, as shall be explained below.

With GaAs we have to be more careful, since the RCA1 solution etches the material [153]. So the wafer cannot be immersed in this solution for more than 1 min, and no heating can be applied. This treatment is therefore not so effective in GaAs and its hydrophilicity disappears after some minutes. Other solutions have been tried to hydrophilize GaAs in a better way; in particular solutions containing NH_4OH since it is expected to passivate the GaAs surface with hydrophilic groups (OH^-) [157]. If a simple NH_4OH dilution is used (without the H_2O_2) no hydrophilization is observed. So some amount of H_2O_2 has to be present, and the best solution that we have worked so far is the RCA1.

After hydrophilizing the surface, the MNP colloidal dispersion can effectively be deposited by spin-coating if the surface charge is opposite to that of the MNPs capping agent. If that does not occur, then the surface has to be functionalized with appropriate molecular linkers that provide the desired surface charge to attract the particles electrostatically, as explained in Section 5.3 and in the previous appendix.

The spin-coating procedure starts by placing a drop of solution on top of the treated surface. The drop should be large enough to cover the entire surface area. Then the spinner accelerates to the desired rotation speed (usually on the order of 1000 rpm) and remains at that speed for a few minutes. The spin-coating conditions (rotation time, speed, number of spin steps, etc.) should be optimized for each particular colloidal solution according to the solution concentration, solvent viscosity, etc.

Finally the samples should be rinsed in the solvent liquid (water for aqueous MNP solutions) and then dried in oven (~120^{o}C) for about 10-15 minutes. This evaporates all the solvent and leaves only the colloids deposited on the sample surface. The density and uniformity of the deposited particles can then be examined, for instance, by taking atomic force microscopy (AFM) images at several spots along the wafers. Fig. D.1 is an

example of one such AFM image, showing a distribution of Au MNPs on the surface of GaAs obtained by spin-coating. Similar distributions have been obtained with Ag MNPs in GaAs, and also on the surface of Si with Au and Ag MNPs.

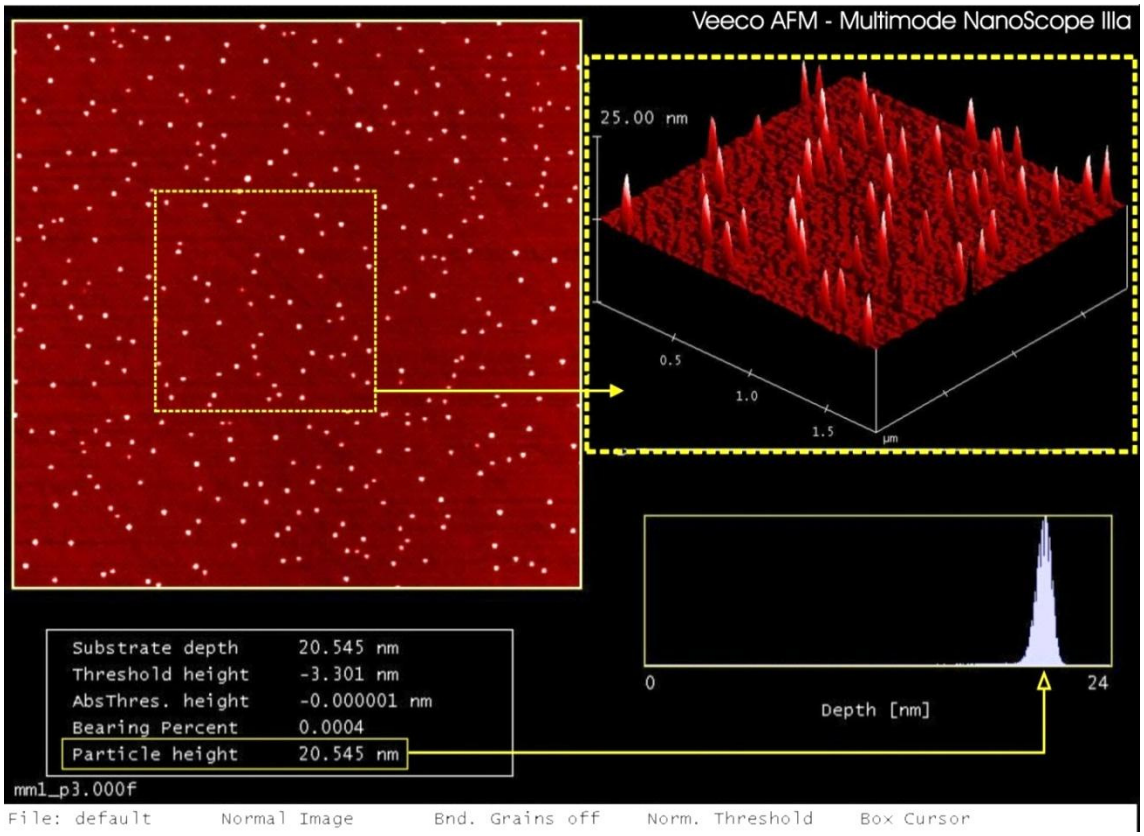

Fig. D.1: AFM image of Au nanoparticles deposited by spin-coating on the surface of a GaAs wafer. The particles have a diameter distribution of 20±2nm, as shown on the bottom right graph.

References

1. Li, L.-W., X.-K. Kang, and M.-S. Leong, *Spheroidal Wave Functions in Electromagnetic Theory*. 2002: John Wiley & Sons, Inc.

2. Asano, S. and G. Yamamoto, *Light-scattering by a spheroidal particle.* Applied Optics, 1975. **14**(1): p. 29-49.

3. Morrison, J.A. and M.J. Cross, *Scattering of a plane electromagnetic-wave by axisymmetric raindrops.* Bell System Technical Journal, 1974. **53**(6): p. 955-1019.

4. Sinha, B.P. and R.H. Macphie, *Electromagnetic scattering by prolate spheroids for plane-waves with arbitrary polarization and angle of incidence.* Radio Science, 1977. **12**(2): p. 171-184.

5. Sebak, A.R. and B.P. Sinha, *Scattering by a conducting spheroidal object with dielectric coating at axial incidence.* Ieee Transactions on Antennas and Propagation, 1992. **40**(3): p. 268-274.

6. Novotny, L. and B. Hecht, *Principles of Nano-Optics*. 2006, Cambridge, UK: Cambridge University Press.

7. Girard, C. and A. Dereux, *Near-field optics theories.* Reports on Progress in Physics, 1996. **59**(5): p. 657-699.

8. Munzer, H.J., et al., *Local field enhancement effects for nanostructuring of surfaces.* Journal of Microscopy-Oxford, 2001. **202**: p. 129-135.

9. O'Neal, D.P., et al., *Photo-thermal tumor ablation in mice using near infrared-absorbing nanoparticles.* Cancer Letters, 2004. **209**(2): p. 171-176.

10. Kofler, J. and N. Arnold, *Axially symmetric focusing as a cuspoid diffraction catastrophe: scalar and vector cases and comparison with the theory of Mie.* Physical Review B, 2006. **73**(23): p. 16.

11. Richard, N., *Analysis of polarization effects on nanoscopic objects in the near-field optics.* Physical Review E, 2001. **63**(2): p. art. no.-026602.

12. Chen, Z., A. Taflove, and V. Backman, *Photonic nanojet enhancement of backscattering of light by nanoparticles: a potential novel visible-light ultramicroscopy technique.* Opt. Express, 2004. **12**(7): p. 1214-1220.

13. Blanco, L.A. and F.J. García de Abajo, *Spontaneous emission enhancement near nanoparticles.* Journal of Quantitative Spectroscopy and Radiative Transfer, 2004. **89**(1-4): p. 37-42.

14. Li, C.H., et al., *Electric and magnetic energy density distributions inside and outside dielectric particles illuminated by a plane electromagnetic wave.* Optics Express, 2005. **13**(12): p. 4554-4559.

15. Barton, J.P., *Internal and near-surface electromagnetic fields for a spheroidal particle with arbitrary illumination.* Appl. Opt., 1995. **34**(24): p. 5542-5551.

16. McNeil, L.E., A.R. Hanuska, and R.H. French, *Near-field scattering from red pigment particles: absorption and spectral dependence.* Journal of Applied Physics, 2001. **89**(3): p. 1898-1906.

17. Devilez, A., N. Bonod, and B. Stout, *Near field dielectric microlenses*, in *Proc. SPIE*. 2010, Spie-Int Soc Optical Engineering: Bellingham. p. 771708.

18. Tom, D.M., *Near-field optical data storage: avenues for improved performance.* Optical Engineering, 2001. **40**(10): p. 2255-2260.

19. Girard, C., et al., *Shaping and manipulation of light fields with bottom-up plasmonic structures.* New Journal of Physics, 2008. **10**: p. 22.

20. Devilez, A., B. Stout, and N. Bonod, *Compact metallo-dielectric optical antenna for ultra directional and enhanced radiative emission.* Acs Nano, 2010. **4**(6): p. 3390-3396.

21. Mendes, M.J., et al., *Plasmonic light enhancement in the near-field of metallic nanospheroids for application in intermediate band solar cells.* Applied Physics Letters, 2009. **95**(7): p. 071105.

22. Grandidier, J., et al., *Thin-film solar cells: light absorption enhancement in thin-film solar cells using whispering gallery modes in dielectric nanospheres.* Advanced Materials, 2011. **23**(10): p. 1171-1171.

23. Bohren, C.F. and D.R. Huffman, *Absorption and scattering of light by small particles*. 2004, Weinheim: Wiley-VCH.

24. Shockley, W. and H.J. Queisser, *Detailed Balance Limit of Efficiency of p-n Junction Solar Cells*. Vol. 32. 1961: AIP. 510-519.

25. Luque, A. and A. Marti, *Increasing the efficiency of ideal solar cells by photon induced transitions at intermediate levels.* Physical Review Letters, 1997. **78**(26): p. 5014-5017.

26. Luque, A., A. Marti, and A.J. Nozik, *Solar cells based on quantum dots: Multiple exciton generation and intermediate bands.* Mrs Bulletin, 2007. **32**(3): p. 236-241.

27. Luque, A., et al., *Operation of the intermediate band solar cell under nonideal space charge region conditions and half filling of the intermediate band.* Journal of Applied Physics, 2006. **99**(9): p. 094503.

28. Marti, A., L. Cuadra, and A. Luque, *Quantum dot intermediate band solar cell*, in *Conference Record of the Twenty-Eighth Ieee Photovoltaic Specialists Conference - 2000*. 2000, Ieee: New York. p. 940-943.

29. Marti, A., L. Cuadra, and A. Luque, *Quasi-drift diffusion model for the quantum dot intermediate band solar cell.* IEEE Transactions on Electron Devices, 2002. **49**(9): p. 1632-1639.

30. Luque, A., et al., *General equivalent circuit for intermediate band devices: Potentials, currents and electroluminescence.* Journal of Applied Physics, 2004. **96**(1): p. 903-909.

31. Luque, A., et al., *New Hamiltonian for a better understanding of the quantum dot intermediate band solar cells.* Solar Energy Materials and Solar Cells, 2011. **95**(8): p. 2095-2101.

32. Antolin, E., et al., *Low temperature characterization of the photocurrent produced by two-photon transitions in a quantum dot intermediate band solar cell.* Thin Solid Films, 2008. **516**(20): p. 6919-6923.

33. Born, M. and E. Wolf, *Principles of Optics: Electromagnetic Theory of Propagation, Interference and Diffraction of Light (7th Edition)*. 1999: Cambridge University Press.

34. Jackson, J., *Classical Electrodynamics*. 1998: Wiley.

35. Cohen-Tannoudji, C., J. Dupont-Roc, and G. Grynberg, *Photons and Atoms - Introduction to Quantum Electrodynamics*. 1997, New York: Wiley-Interscience.

36. Mellor, A., et al., *Upper limits to absorption enhancement in thick solar cells using diffraction gratings.* Progress in Photovoltaics: Research and Applications, 2011. **19**(6): p. 676-687.

37. Keller, O., *Near-field optics and quantum optics: an assignation arranged by four kinds of photons.* Journal of Microscopy, 2003. **209**: p. 272-276.

38. Luque, A., et al., *Light absorption in the near field around surface plasmon polaritons.* Journal of Applied Physics, 2008. **104**(11): p. 8.

39. Maier, S., *Plasmonics: Fundamentals and Applications*. 2007: Springer, Berlin.

40. Somsikov, V.V. and N.V. Voshchinnikov, *On the applicability of the Rayleigh approximation for coated spheroids in the near-infrared.* Astronomy and Astrophysics, 1999. **345**(1): p. 315-320.

41. Palik, E., *Handbook of Optical Constants of Solids (5 Volume Set)*. 1997, San Diego, CA: Academic Press.

42. Atwater, H.A. and A. Polman, *Plasmonics for improved photovoltaic devices.* Nat Mater, 2010. **9**(3): p. 205-213.

43. Woodall, J.M. and H.J. Hovel, *HIGH-EFFICIENCY GA1-XALXAS-GAAS SOLAR CELLS.* Applied Physics Letters, 1972. **21**(8): p. 379-&.

44. Zhang, J., et al., *Design optimization of stacked layer dielectrics for minimum gate leakage currents.* Solid-State Electronics, 2000. **44**(12): p. 2165-2170.

45. Luque, A., A. Martí, and L. Cuadra, *Impact-ionization-assisted intermediate band solar cell.* IEEE Transactions on Electron Devices, 2003. **50**(2): p. 447–454.

46. Schaller, R.D., et al., *Seven excitons at a cost of one: Redefining the limits for conversion efficiency of photons into charge carriers.* Nano Letters, 2006. **6**(3): p. 424-429.

47. Mendes, M.J., et al., *Near-field scattering by dielectric spheroidal particles with sizes on the order of the illuminating wavelength.* J. Opt. Soc. Am. B, 2010. **27**(6): p. 1221-1231.

48. Mendes, M.J., et al., *Light concentration in the near-field of dielectric spheroidal particles with mesoscopic sizes.* Optics Express, 2011. **19**(17): p. 16207-16222.

49. Mie, G., *Articles on the optical characteristics of turbid tubes, especially colloidal metal solutions.* Annalen Der Physik, 1908. **25**(3): p. 377-445.

50. Thiele, E.S. and R.H. French. *Light-scattering properties of representative, morphological rutile titania particles studied using a finite-element method*. in *99th Annual Meeting of the American-Ceramic-Society*. 1997. Cincinnati, Ohio: Amer Ceramic Soc.

51. Barton, J.P., *Internal, Near-Surface, and Scattered Electromagnetic Fields for a Layered Spheroid with Arbitrary Illumination.* Appl. Opt., 2001. **40**(21): p. 3598-3607.

52. Oguchi, T., *Attenuation and phase rotation of radio-waves due to rain - calculations at 19.3 and 34.8 GHz.* Radio Science, 1973. **8**(1): p. 31-38.

53. Flammer, C., *Spheroidal Wave Functions*. 1957, Stanford, CA: Stanford University Press.

54. Falloon, P.E., P.C. Abbott, and J.B. Wang, *Theory and computation of spheroidal wavefunctions.* Journal of Physics a-Mathematical and General, 2003. **36**(20): p. 5477-5495.

55. Li, L.W., et al., *Computations of spheroidal harmonics with complex arguments: a review with an algorithm.* Physical Review E, 1998. **58**(5): p. 6792-6806.

56. Abramowitz, M. and I.A. Stegun, *Handbook of Mathematical Functions*. 1970: Dover Publications.

57. Hodge, D.B., *Eigenvalues and eigenfunctions of spheroidal wave equation.* Journal of Mathematical Physics, 1970. **11**(8): p. 2308-&.

58. Press, W., et al., *Numerical Recipes in FORTRAN 77: The Art of Scientific Computing*. 1992: Cambridge University Press.

59. Joo, K.S. and M.F. Iskander, *A new procedure of point-matching method for calculating the absorption and scattering of lossy dielectric objects.* Ieee Transactions on Antennas and Propagation, 1990. **38**(9): p. 1483-1490.

60. Farafonov, V.G. and V.B. Il'in, *Scattering of light by axially symmetric particles: modification of the point-matching method.* Optics and Spectroscopy, 2006. **100**(3): p. 437-447.

61. Boyde, L., K.J. Chalut, and J. Guck, *Interaction of Gaussian beam with near-spherical particle: an analytic-numerical approach for assessing scattering and stresses.* Journal of the Optical Society of America a-Optics Image Science and Vision, 2009. **26**(8): p. 1814-1826.

62. Nishimura, M., S. Takamatsu, and H. Shigesawa, *A numerical analysis of electromagnetic scattering of perfect conducting cylinders by means of discrete singularity method improved by optimization process.* Electronics Communications of Japan, 1984. **67**: p. 75-81.

63. Ludwig, A.C., *A comparison of spherical wave boundary-value matching versus integral-equation scattering solutions for a perfectly conducting body.* Ieee Transactions on Antennas and Propagation, 1986. **34**(7): p. 857-865.

64. Ravey, J.C. and P. Mazeron, *Light-scattering in the physical optics approximation - application to large spheroids.* Journal of Optics-Nouvelle Revue D Optique, 1982. **13**(5): p. 273-282.

65. Keller, O., *Near-field photon wave mechanics in the Lorenz gauge.* Physical Review A, 2007. **76**(6): p. 11.

66. Xu, F., et al., *Generalized Lorenz-Mie theory for an arbitrarily oriented, located, and shaped beam scattered by a homogeneous spheroid.* Journal of the Optical Society of America a-Optics Image Science and Vision, 2007. **24**(1): p. 119-131.

67. Lee, J.Y. and P. Peumans, *The origin of enhanced optical absorption in solar cells with metal nanoparticles embedded in the active layer.* Optics Express, 2010. **18**(10): p. 10078-10087.

68. Mertens, H., A.F. Koenderink, and A. Polman, *Plasmon-enhanced luminescence near noble-metal nanospheres: comparison of exact theory and an improved Gersten and Nitzan model.* Physical Review B, 2007. **76**(11): p. 115123.

69. Mendes, M.J., et al. *Near-field light focusing by wavelenght-sized dielectric spheroids for photovoltaic applications*. in *Optical Nanostructures and Advanced Materials for Photovoltaics - Concepts of Light Trapping and Photon Transport*. 2011. Austin, Texas (USA): Optical Society of America.

70. Lecler, S., Y. Takakura, and P. Meyrueis, *Properties of a three-dimensional photonic jet.* Optics Letters, 2005. **30**(19): p. 2641-2643.

71. Devilez, A., et al., *Three-dimensional subwavelength confinement of light with dielectric microspheres.* Optics Express, 2009. **17**(4): p. 2089-2094.

72. Itagi, A.V. and W.A. Challener, *Optics of photonic nanojets.* J. Opt. Soc. Am. A, 2005. **22**(12): p. 2847-2858.

73. Devilez, A., et al., *Spectral analysis of three-dimensional photonic jets.* Optics Express, 2008. **16**(18): p. 14200-14212.

74. Ferrand, P., et al., *Direct imaging of photonic nanojets.* Optics Express, 2008. **16**(10): p. 6930-6940.

75. Lecler, S., *Light scattering by sub-micrometric particles*. 2005, Louis Pasteur University: Strasbourg.

76. Hecht, E., *Optics (4th Edition)*. 2001: Addison Wesley.

77. Purcell, E.M. and Pennypac.Cr, *Scattering and absorption of light by nonspherical dielectric grains.* Astrophysical Journal, 1973. **186**(2): p. 705-714.

78. Barton, J.P., *Internal and near-surface electromagnetic fields for an absorbing spheroidal particle with arbitrary illumination.* Appl. Opt., 1995. **34**(36): p. 8472-8473.

79. Kirby, P., *Calculation of spheroidal wave functions.* Computer Physics Communications, 2006. **175**(7): p. 465-472.

80. Kirby, R., *Calculation of radial prolate spheroidal wave functions of the second kind.* Computer Physics Communications, 2010. **181**(3): p. 514-519.

81. Hägglund, C. and B. Kasemo, *Nanoparticle plasmonics for 2D-photovoltaics: mechanisms, optimization, and limits.* Opt. Express, 2009. **17**(14): p. 11944-11957.

82. Borgstrom, M.T., et al., *Nanowires With Promise for Photovoltaics.* Ieee Journal of Selected Topics in Quantum Electronics, 2011. **17**(4): p. 1050-1061.

83. Fredriksson, H., et al., *Hole-mask colloidal lithography.* Advanced Materials, 2007. **19**(23): p. 4297-+.

84. Moon, J.H., et al., *High-throughput synthesis of anisotropic colloids via holographic lithography.* Advanced Materials, 2007. **19**(18): p. 2508-+.

85. Mazeron, P. and S. Muller, *Dielectric or absorbing particles: EM surface fields and scattering.* Journal of Optics-Nouvelle Revue D Optique, 1998. **29**(2): p. 68-77.

86. Akimov, Y.A., W.S. Koh, and K. Ostrikov, *Enhancement of optical absorption in thin-film solar cells through the excitation of higher-order nanoparticle plasmon modes.* Optics Express, 2009. **17**(12): p. 10195-10205.

87. Beck, F.J., et al., *Asymmetry in photocurrent enhancement by plasmonic nanoparticle arrays located on the front or on the rear of solar cells.* Applied Physics Letters. **96**(3): p. 3.

88. Beck, F.J., A. Polman, and K.R. Catchpole, *Tunable light trapping for solar cells using localized surface plasmons.* Journal of Applied Physics, 2009. **105**(11): p. 7.

89. Kim, S.S., et al., *Plasmon enhanced performance of organic solar cells using electrodeposited Ag nanoparticles.* Applied Physics Letters, 2008. **93**(7): p. 3.

90. Watanabe, R. and K. Miyano, *Metal nanoparticles in a photovoltaic cell: Effect of metallic loss.* AIP Advances, 2011. **1**(4): p. 042154.

91. Beck, F.J., S. Mokkapati, and K.R. Catchpole, *Plasmonic light-trapping for Si solar cells using self-assembled, Ag nanoparticles.* Progress in Photovoltaics: Research and Applications, 2010. **18**(7): p. 500-504.

92. Mendes, M.J., et al. *Embedment of metal nanoparticles in GaAs and Si for plasmonic absorption enhancement in intermediate band solar cells*. in *25th European Photovoltaic Solar Energy Conference and Exhibition - 5th World Conference on Photovoltaic Energy Conversion*. 2010. Valencia, Spain.

93. Temple, T.L. and D.M. Bagnall, *Optical properties of gold and aluminium nanoparticles for silicon solar cell applications.* Journal of Applied Physics, 2011. **109**(8).

94. Pillai, S. and M.A. Green, *Plasmonics for photovoltaic applications.* Solar Energy Materials and Solar Cells, 2010. **94**(9): p. 1481-1486.

95. Tan, B.J.Y., et al., *Fabrication of Size-Tunable Gold Nanoparticles Array with Nanosphere Lithography, Reactive Ion Etching, and Thermal Annealing.* The Journal of Physical Chemistry B, 2005. **109**(22): p. 11100-11109.

96. Romo-Herrera, J.M., R.A. Alvarez-Puebla, and L.M. Liz-Marzan, *Controlled assembly of plasmonic colloidal nanoparticle clusters.* Nanoscale, 2011. **3**(4): p. 1304-1315.

97. Frens, G., *Controlled nucleation for regulation of particle-size in monodisperse gold suspensions.* Nature-Physical Science, 1973. **241**(105): p. 20-22.

98. Liu, F.K., et al., *Rapid fabrication of high quality self-assembled nanometer gold particles by spin coating method.* Microelectronic Engineering, 2003. **67-8**: p. 702-709.

99. Bigioni, T.P., et al., *Kinetically driven self assembly of highly ordered nanoparticle monolayers.* Nat Mater, 2006. **5**(4): p. 265-270.

100. Sheu, J.T., et al., *Selective deposition of gold nanoparticles on SiO2/Si nanowire.* Microelectronic Engineering, 2005. **78-79**: p. 294-299.

101. Wang, J., et al., *Gold nanoparticulate film bound to silicon surface with self-assembled monolayers.* Thin Solid Films, 1998. **327**: p. 591-594.

102. Leu, C.C., S.T. Chen, and F.K. Liu, *Spin-Coating-Derived Gold-Nanoparticle Memory.* Journal of the American Ceramic Society, 2010. **93**(10): p. 3142-3147.

103. Zheng, J.W., et al., *Nanopatterned assembling of colloidal gold nanoparticles on silicon.* Langmuir, 2000. **16**(10): p. 4409-4412.

104. Yamada, M. and Y. Ide, *Anomalous Behaviors Observed in the Isothermal Desorption of Gaas Surface Oxides.* Surface Science, 1995. **339**(3): p. L914-L918.

105. Lou, C.Y. and G.A. Somorjai, *Studies of Vaporization Mechanism of Gallium Arsenide Single Crystals.* Journal of Chemical Physics, 1971. **55**(9): p. 4554-&.

106. Castro, T., et al., *Size-Dependent Melting Temperature of Individual Nanometer-Sized Metallic Clusters.* Physical Review B, 1990. **42**(13): p. 8548-8556.

107. Lu, H.M., et al., *Size-, Shape-, and Dimensionality-Dependent Melting Temperatures of Nanocrystals.* Journal of Physical Chemistry C, 2009. **113**(18): p. 7598-7602.

108. Chen, C.L., et al., *In situ observations of crystalline-to-liquid and crystalline-to-gas transitions of substrate-supported Ag nanoparticles.* Applied Physics Letters, 2010. **96**(25): p. 3.

109. Chen, Y.S., et al., *Enhanced thermal stability of silica-coated gold nanorods for photoacoustic imaging and image-guided therapy.* Optics Express, 2010. **18**(9): p. 8867-8877.

110. Temple, T.L., et al., *Influence of localized surface plasmon excitation in silver nanoparticles on the performance of silicon solar cells.* Solar Energy Materials and Solar Cells, 2009. **93**(11): p. 1978-1985.

111. Mertz, J., *Radiative absorption, fluorescence, and scattering of a classical dipole near a lossless interface: a unified description.* J. Opt. Soc. Am. B, 2000. **17**(11): p. 1906-1913.

112. Zhang, Q.B., et al., *Colloidal Synthesis of Plasmonic Metallic Nanoparticles.* Plasmonics, 2009. **4**(1): p. 9-22.

113. Antolin, E., et al., *Reducing carrier escape in the InAs/GaAs quantum dot intermediate band solar cell.* Journal of Applied Physics, 2010. **108**(6): p. 064513.

114. Mendes, M.J., et al., *INTERMEDIATE BAND SOLAR CELL HAVING SOLUTION-PROCESSED COLLOIDAL QUANTUM DOTS AND METAL NANOPARTICLES*, in *Patent request # 61/547,312*, U.P.d. Madrid, Editor. 2011: USA.

115. Rogach, A.L., et al., *Infrared-Emitting Colloidal Nanocrystals: Synthesis, Assembly, Spectroscopy, and Applications.* Small, 2007. **3**(4): p. 536-557.

116. Talgorn, E., et al., *Unity quantum yield of photogenerated charges and band-like transport in quantum-dot solids.* Nat Nano, 2011. **6**(11): p. 733-739.

117. Emin, S., et al., *Colloidal quantum dot solar cells.* Solar Energy, 2011. **85**(6): p. 1264-1282.

118. Sun, B., et al., *Hybrid Photovoltaics Based on Semiconductor Nanocrystals and Amorphous Silicon.* Nano Letters, 2009. **9**(3): p. 1235-1241.

119. Pattantyus-Abraham, A.G., et al., *Depleted-Heterojunction Colloidal Quantum Dot Solar Cells.* ACS Nano, 2010. **4**(6): p. 3374-3380.

120. McDonald, S.A., et al., *Solution-processed PbS quantum dot infrared photodetectors and photovoltaics.* Nat Mater, 2005. **4**(2): p. 138-142.

121. Konstantatos, G. and E.H. Sargent, *Colloidal quantum dot photodetectors.* Infrared Physics & Technology, 2011. **54**(3): p. 278-282.

122. Konstantatos, G. and E.H. Sargent, *Nanostructured materials for photon detection.* Nat Nano, 2010. **5**(6): p. 391-400.

123. Talapin, D.V. and C.B. Murray, *PbSe Nanocrystal Solids for n- and p-Channel Thin Film Field-Effect Transistors.* Science, 2005. **310**(5745): p. 86-89.

124. Brumer, M., et al., *Nanocrystals of PbSe core, PbSe/PbS, and PbSe/PbSexS1-x core/shell as saturable absorbers in passively Q-switched near-infrared lasers.* Appl. Opt., 2006. **45**(28): p. 7488-7497.

125. Guyot-Sionnest, P., *Colloidal quantum dots.* Comptes Rendus Physique, 2008. **9**(8): p. 777-787.

126. Levina, L., et al., *Efficient infrared-emitting PbS quantum dots grown on DNA and stable in aqueous solution and blood plasma.* Advanced Materials, 2005. **17**(15): p. 1854-+.

127. Beard, M.C., et al., *Multiple Exciton Generation in Colloidal Silicon Nanocrystals.* Nano Letters, 2007. **7**(8): p. 2506-2512.

128. Tang, J. and E.H. Sargent, *Infrared Colloidal Quantum Dots for Photovoltaics: Fundamentals and Recent Progress.* Advanced Materials, 2011. **23**(1): p. 12-29.

129. Nozik, A.J., *Multiple exciton generation in semiconductor quantum dots.* Chemical Physics Letters, 2008. **457**(1-3): p. 3-11.

130. Wehrenberg, B.L., C. Wang, and P. Guyot-Sionnest, *Interband and Intraband Optical Studies of PbSe Colloidal Quantum Dots.* The Journal of Physical Chemistry B, 2002. **106**(41): p. 10634-10640.

131. Lee, M.-H. and et al., *Structural and optical characterizations of multi-layered and multi-stacked PbSe quantum dots.* Nanotechnology, 2005. **16**(8): p. 1148.

132. Barkhouse, D.A.R., et al., *Thiols Passivate Recombination Centers in Colloidal Quantum Dots Leading to Enhanced Photovoltaic Device Efficiency.* ACS Nano, 2008. **2**(11): p. 2356-2362.

133. Hinds, S., et al., *Smooth-Morphology Ultrasensitive Solution-Processed Photodetectors.* Advanced Materials, 2008. **20**(23): p. 4398-4402.

134. Luther, J.M., et al., *Structural, Optical, and Electrical Properties of Self-Assembled Films of PbSe Nanocrystals Treated with 1,2-Ethanedithiol.* ACS Nano, 2008. **2**(2): p. 271-280.

135. Luque, A. and S. Hegedus, *Handbook of Photovoltaic Science and Engineering*. 2003: Wiley.

136. Fuertes Marrón, D., et al., *Optoelectronic evaluation of the nanostructuring approach to chalcopyrite-based intermediate band materials.* Solar Energy Materials and Solar Cells, 2010. **94**(11): p. 1912-1918.

137. Ojajarvi, J., et al., *Tetrahedral chalcopyrite quantum dots for solar-cell applications.* Applied Physics Letters, 2011. **99**(11): p. 111907.

138. Bundgaard, E. and F.C. Krebs, *Low band gap polymers for organic photovoltaics.* Solar Energy Materials and Solar Cells, 2007. **91**(11): p. 954-985.

139. Lee, S.K., et al., *New low band-gap alternating polyfluorene derivatives for photovoltaic cells.* Thin Solid Films, 2006. **511-512**: p. 157-162.

140. Martí, A., C.R. Stanley, and A. Luque, *Chapter 17 - Intermediate Band Solar Cells (IBSC) Using Nanotechnology*, in *Nanostructured Materials for Solar Energy Conversion*, S. Tetsuo, Editor. 2006, Elsevier: Amsterdam. p. 539-566.

141. Luque, A., et al., *Intraband absorption for normal illumination in quantum dot intermediate band solar cells.* Solar Energy Materials and Solar Cells, 2010. **94**(12): p. 2032-2035.

142. Cuadra, L., A. Martí, and A. Luque, *Influence of the overlap between the absorption coefficients on the efficiency of the intermediate band solar cell.* IEEE Transactions on Electron Devices, 2004. **51**(6): p. 1002-1007.

143. Galat, J., et al., *Studies on the interaction between oxygen and lead chalcogenide surfaces.* Oxidation of Metals, 1975. **9**(6): p. 497-506.

144. Li, J.-R., et al., *Engineering the Spatial Selectivity of Surfaces at the Nanoscale Using Particle Lithography Combined with Vapor Deposition of Organosilanes.* ACS Nano, 2009. **3**(7): p. 2023-2035.

145. Zheng, J., et al., *Nanopatterned Assembling of Colloidal Gold Nanoparticles on Silicon.* Langmuir, 2000. **16**(10): p. 4409-4412.

146. Strandberg, R. and T.W. Reenaas, *Photofilling of intermediate bands*. Vol. 105. 2009: AIP. 124512.

147. Das, U., et al. *Investigation of hetero-interface and junction properties in silicon heterojunction solar cells*. in *Photovoltaic Specialists Conference (PVSC), 2010 35th IEEE*. 2010.

148. Lu, M., et al., *Optimization of interdigitated back contact silicon heterojunction solar cells: tailoring hetero-interface band structures while maintaining surface passivation.* Progress in Photovoltaics: Research and Applications, 2011. **19**(3): p. 326-338.

149. Kang, I. and F.W. Wise, *Electronic structure and optical properties of PbS and PbSe quantum dots.* J. Opt. Soc. Am. B, 1997. **14**(7): p. 1632-1646.

150. Lagarias, J.C., et al., *Convergence properties of the Nelder-Mead simplex method in low dimensions.* Siam Journal on Optimization, 1998. **9**(1): p. 112-147.

151. Mendes, M.J., H.K. Schmidt, and M. Pasquali, *Brownian dynamics simulations of single-wall carbon nanotube separation by type using dielectrophoresis.* Journal of Physical Chemistry B, 2008. **112**(25): p. 7467-7477.

152. Wu, B., et al., *Direct deposition and assembly of gold colloidal particles using a nanofountain probe.* Langmuir, 2007. **23**(17): p. 9120-9123.

153. Bryce, C. and D. Berk, *Kinetics of GaAs dissolution in H2O2-NH4OH-H2O solutions.* Industrial & Engineering Chemistry Research, 1996. **35**(12): p. 4464-4470.

154. Muhlhoff, L. and T. Bolze, *Surface Analytical Characterization of Oxide-Free Si(100) Wafer Surfaces.* Fresenius Zeitschrift Fur Analytische Chemie, 1989. **333**(4-5): p. 527-530.

155. Dorrer, C. and J. Ruhe, *Wetting of silicon nanograss: From superhydrophilic to superhydrophobic surfaces.* Advanced Materials, 2008. **20**(1): p. 159-+.

156. Reinhardt, K.A. and W. Kern, *Handbook of Silicon Wafer Cleaning Technology (2nd Edition)*. 2008, William Andrew Publishing.

157. Xuan, Y., H.C. Lin, and P.D. Ye, *Simplified surface preparation for GaAs passivation using atomic layer-deposited high-kappa dielectrics.* Ieee Transactions on Electron Devices, 2007. **54**(8): p. 1811-1817.